

# Multi-Finger Haptic Devices Integrating Miniature Short-Stroke Actuators

THÈSE N° 5485 (2012)

PRÉSENTÉE LE 28 SEPTEMBRE 2012

À LA FACULTÉ DES SCIENCES ET TECHNIQUES DE L'INGÉNIEUR

LABORATOIRE D'ACTIONNEURS INTÉGRÉS

PROGRAMME DOCTORAL EN SYSTÈMES DE PRODUCTION ET ROBOTIQUE

ÉCOLE POLYTECHNIQUE FÉDÉRALE DE LAUSANNE

POUR L'OBTENTION DU GRADE DE DOCTEUR ÈS SCIENCES

PAR

Grégory SAVIOZ

acceptée sur proposition du jury:

Prof. P. Ryser, président du jury  
Prof. Y. Perriard, directeur de thèse  
Dr F. Mondada, rapporteur  
Prof. B. Semail, rapporteur  
Dr S. Urben, rapporteur



ÉCOLE POLYTECHNIQUE  
FÉDÉRALE DE LAUSANNE

Suisse  
2012



*Mais vous savez, moi je ne crois pas qu'il y ait de bonnes ou de mauvaises situations. Moi, si je devais résumer ma vie, aujourd'hui avec vous, je dirais que c'est d'abord des rencontres, des gens qui m'ont tendu la main peut-être à un moment où je ne pouvais pas, où j'étais seul chez moi. Et c'est assez curieux de se dire que les hasards, les rencontres forment une destinée. Parce que quand on a le goût de la chose, quand on a le goût de la chose bien faite, le beau geste, parfois on ne trouve pas l'interlocuteur en face, je dirais le miroir qui vous aide à avancer. Alors ce n'est pas mon cas, comme je disais là, puisque moi au contraire j'ai pu, et je dis merci à la vie, je lui dis merci, je chante la vie, je danse la vie, je ne suis qu'amour. Et finalement quand beaucoup de gens aujourd'hui me disent : "Mais comment fais-tu pour avoir cette humanité ? " et bien je leur réponds très simplement, je leur dis : "C'est ce goût de l'amour", ce goût donc, qui m'a poussé aujourd'hui à entreprendre une construction mécanique, mais demain qui sait ? Peut-être simplement à me mettre au service de la communauté, à faire le don, le don de soi.*

— Edouard Bear

Ceux à qui je dois ce travail,  
et bien plus encore,  
se reconnaîtront.





# Remerciements

L'aboutissement du labeur qui vous est présenté dans ce document n'aurait certainement pas été envisageable sans l'appui apporté par moult personnes que je tiens à remercier ici. En commençant par le Prof. Yves Perriard pour son soutien, ainsi que l'indépendance et la confiance qu'il m'a accordées. En sus de l'aspect professionnel, il a su créer au laboratoire un environnement agréable qui m'a permis de passer quatre années merveilleuses, ne rechignant pas à nous offrir le couvert et parfois même le gîte lorsque le besoin s'en faisait sentir.

Je tiens également à exprimer ma gratitude envers les membres du jury: Prof. Betty Semail, Dr. Francesco Mondada et Prof. Peter Ryser pour avoir gracieusement pris la peine de s'intéresser à mon travail et d'y ajouter une touche éclairée à travers leurs remarques avisées. Une distinction particulière va au Dr. Sébastien Urben du CHUV avec qui j'ai pu développer une enrichissante collaboration écartant mes œillères scientifiques et qui n'a pas eu peur d'affronter le monde de l'ingénieur en se joignant à mon jury de thèse.

Rien n'aurait été pareil sans la présence de mes collègues au sein du LAI, notamment grâce à l'aide apportée par les sages anciens: André, Christian, Mika, Paolo et Omar, jamais avares en conseils. Merci également à la plupart des onze étudiants que j'ai pu suivre durant leur projet de semestre ou de Master et qui ont su apporter une touche de fraîcheur et de curiosité à mon travail. Je remercie bien évidemment tous les collègues que j'ai pu côtoyer durant ces quelques années, ceux partis plus tôt et ceux encore présents, avec une mention particulière pour Dr. Pascal avec qui j'ai passé plus de temps qu'avec l'intégralité de mes proches durant ces neuf dernières années. Sans oublier Richard Milhé, Olivier Campiche et les autres employés de chez Logitech avec qui j'ai eu le plaisir de collaborer, toujours dans la bonne humeur, durant plus de deux ans et demi.

Le travail n'étant de loin pas tout, je tiens à terminer ces remerciements par les personnes qui comptent plus que tout à mes yeux: mes parents, tout d'abord, qui ont toujours cru en moi et ont tout mis en œuvre pour me permettre d'atteindre mes objectifs, mes trois *petits* frères qui, malgré leur grande taille, m'acceptent toujours comme je suis et finalement la plus belle, Cynthia, avec qui j'apprends chaque jour bien plus qu'au cours de n'importe quel cursus. Pour terminer, un gros *big up* à tous mes potos, les Johns, les moustachus et tous les autres sans qui la vie manquerait cruellement de sel, de raclette et de pinard.

*Neuchâtel, 28 Septembre 2012*

G. S.



# Abstract

The omnipresence of electronic devices in our everyday life goes together with a trend that makes us always more immersed during their utilization. By immersion, we mean that during the development of a new product, it is more and more required to stimulate several senses of the user so as to make the product more attractive. The sense of touch does not escape the rule and is more and more considered. Definitely democratized by its integration in smartphones with touchscreens, the haptic feedback allows enhancing the human-machine interactions in many ways. For instance by improving the comfort of use of a button through the modification of its force feedback. It can also offer an interactive experience during the manipulation of digital information and even improve the communication, particularly through the internet and for blind people, with the introduction of non-verbal signals.

For these reasons, the present thesis focuses on the conception of multi-finger haptic devices, a new kind of peripherals integrating multiple actuators and capable of providing a fully programmable force feedback to the user's fingers. A global methodology is presented, outlining the different constituents necessary for their conception: actuator, sensor, control, communication and software user interface. Then, generic tools corresponding to the two first elements are presented.

An accurate modeling of miniature electromagnetic short-stroke actuators is made possible thanks to the combination of 3D finite element modeling (FEM) and design of experiments (DOE). The non-usual behavior of magnetic flux lines in miniature actuators with relatively large airgaps imposes to avoid simplified analytical models and to use the reliable results of finite elements. The long computation times required by 3D FEM are balanced by the use of selective DOE making the modeling methodology easily adaptable, rapid and accurate. The parametrical model of the force provided by the modeling methodology is then integrated in a full parametrical setup allowing for the optimization of the actuator force using a conventional algorithm. The advantage of the parametrical optimization is that complementary non-linear constraints such as weight and temperature can be added, making the model multi-physic.

Then, several original position measurement techniques using existing sensors are developed including a low-cost custom single-photointerrupter sensor allowing for direction discrimination for fast-prototyping and a hybrid sensing method using tiny Hall sensors and taking advantage of the leaks of the main actuator magnet. Two innovative self-sensing methods are then presented, allowing for the measurement of the mover position of linear short-stroke

## Remerciements

---

actuators. The first solution estimates the position of the coil by measuring the acceleration through the back emf. However in this case, a constant acceleration is required, which strongly restrains the application scope. The second solution allows for a real-time measurement of the position thanks to a passive oscillating RLC circuit influenced by the variation of the coil impedance. All the solutions presented are low-cost, compact and require few computation resources.

Finally, in order to illustrate the methodology proposed along the thesis, several prototypes are fabricated, giving an overview of the possibilities offered by multi-finger haptic devices. A haptic numeric pad is notably used in an experiment made in collaboration with the University Service of Child and Adolescent Psychiatry in Lausanne with the aim of improving the impaired emotional processing of psychotic adolescents. Moreover, the successful identification of several touch sensations on the same haptic pad lays the first stones of a new tactile language.

**Keywords:** Multi-finger haptic devices, force feedback, design of experiments, 3D finite element modeling, miniature short-stroke actuators, position detection, self-sensing, tactile language, emotional processing, human hand physiology.

# Résumé

L'engouement actuel pour les appareils électroniques en tout genre s'accompagne d'une tendance à l'immersion des utilisateurs. En effet, de plus en plus de produits tentent d'intégrer des fonctionnalités stimulant plusieurs de nos sens afin de les rendre plus attractifs. Bien évidemment, le sens du toucher n'échappe pas à la règle. Définitivement démocratisé grâce à son intégration dans les téléphones à écran tactile, le retour haptique permet d'améliorer les interactions homme-machine de nombreuses manières. Il permet par exemple d'augmenter le confort de frappe en modifiant le retour de force généré par un bouton-poussoir. Il ouvre également la voie vers une expérience interactive lors de la manipulation d'informations digitales ainsi qu'à l'enrichissement de la communication, notamment à travers internet et pour les personnes aveugles, grâce à l'introduction de nouveaux langages non-verbaux.

Pour les raisons mentionnées, cette thèse se concentre sur la conception de systèmes haptiques multi-numériques, un nouveau genre de périphériques intégrant de multiples actionneurs et capable de fournir un retour de force entièrement programmable aux doigts de l'utilisateur. Une méthodologie globale est présentée, mettant en avant les différents constituants nécessaires à leur conception, à savoir actionneur, capteur, contrôle, communication et interface utilisateur. Puis, des outils génériques correspondant à ces deux premiers éléments sont développés.

La modélisation d'actionneurs électromagnétiques miniatures à faible course est rendue possible grâce à la combinaison de modélisation à éléments finis 3D (MEF) et des plans d'expériences. Le comportement non-conventionnel des lignes de champ magnétique, caractéristique des actionneurs miniatures possédant de relativement grands entrefers, empêche l'utilisation de modèles analytiques simplifiés au profit des résultats fiables des éléments finis. Les longs temps de calcul propres aux simulations 3D sont compensés par l'utilisation de plans d'expériences sélectifs rendant la méthodologie facilement adaptable, rapide et précise. Quant au modèle paramétrique de la force généré par la méthode de modélisation, il est ensuite intégré dans un programme général englobant toutes les étapes, y compris l'optimisation de la force de l'actionneur à l'aide d'un algorithme conventionnel. L'avantage de l'optimisation paramétrique est qu'elle permet d'y inclure des contraintes non-linéaires additionnelles (poids, température, etc...), afin de devenir multi-physique.

Par la suite, plusieurs techniques originales de mesure de la position utilisant des capteurs existants sont développées, incluant un capteur optique pour le prototypage rapide à photo-

## Remerciements

---

interrupteur unique permettant de distinguer le sens de déplacement ainsi qu'une méthode de détection hybride utilisant les fuites magnétiques de l'aimant principal de l'actionneur. Deux méthodes de détection de la position sans capteur sont ensuite présentées pour des actionneurs linéaires à faible course. La première solution permet l'interpolation de la position en mesurant l'accélération à travers la tension induite de mouvement. Cependant, cette méthode nécessite une accélération constante, ce qui limite fortement le champ d'application. La seconde solution permet une mesure en temps réel grâce à un circuit RLC oscillant influencé par la variation de l'impédance de la bobine avec la position. Toutes les solutions développées dans cette section sont compactes, bon marché et nécessitent peu de ressources de calcul.

Enfin, afin d'illustrer la méthodologie présentée tout au long de la thèse, plusieurs prototypes ont été fabriqués, donnant un aperçu des possibilités offertes par les systèmes haptiques multi-digitaux. Un pad numérique haptique est notamment utilisé par la suite dans une expérience en collaboration avec le Service Universitaire de Psychiatrie de l'Enfant et de l'Adolescent de Lausanne avec l'objectif d'améliorer le traitement émotionnel altéré d'adolescents psychotiques. De plus, le succès rencontré lors de l'identification d'une série de sensations tactiles sur le même pad numérique pose les bases d'un nouveau langage tactile.

**Mots-clés :** Systèmes haptiques multi-digitaux, retour de force, plans d'expériences, modélisation éléments finis 3D, actionneurs miniatures à faible course, détection de la position sans capteur, langage tactile, traitement de l'émotion, physiologie de la main humaine.

# Contents

<b>Remerciements</b>	<b>v</b>
<b>Abstract</b>	<b>vii</b>
<b>Contents</b>	<b>xi</b>
<b>List of figures</b>	<b>xv</b>
<b>List of tables</b>	<b>xxiii</b>
<b>1 Introduction</b>	<b>1</b>
<b>2 The sense of touch</b>	<b>5</b>
2.1 Touch sense tasks and sensitivities . . . . .	6
2.2 Human hand physiology . . . . .	8
2.2.1 Mechanoreceptors . . . . .	9
2.2.2 From nerve endings to the central nervous system: the tactile units . . .	10
2.2.3 Location and spatial resolution of tactile units . . . . .	12
2.2.4 Frequency and temporal resolution of tactile units . . . . .	13
2.3 State of the art . . . . .	16
2.3.1 Haptics: Roles and implications in the daily life . . . . .	16
2.3.2 Kinesthetic sensitivity and force feedback . . . . .	18
2.3.3 Cutaneous sensitivity and vibrotactile stimulation . . . . .	23
2.3.4 Thermal sensitivity and heat transfer . . . . .	28
2.4 Motivations . . . . .	29
2.4.1 Repetitive strain injuries . . . . .	29
2.4.2 Gaming and virtual reality: a new touch experience . . . . .	31
2.5 Summary . . . . .	32
<b>3 Multi-finger haptic systems</b>	<b>35</b>
3.1 Key elements . . . . .	36
3.2 Actuator . . . . .	37
3.3 Sensor . . . . .	40
3.4 Control . . . . .	41
3.5 Communication . . . . .	42
3.6 Software user interface . . . . .	43

<b>4</b>	<b>Design methodology for linear short-stroke actuators</b>	<b>45</b>
4.1	Design . . . . .	47
4.1.1	Case study: Square electrodynamic actuator . . . . .	47
4.1.2	Finite element modeling for rapid analysis . . . . .	49
4.2	Optimization tools . . . . .	52
4.2.1	Analytical modeling . . . . .	52
4.2.2	Hybrid alternatives . . . . .	57
4.3	Design of experiments and parametrical modeling . . . . .	61
4.3.1	Experimental domain . . . . .	61
4.3.2	Building the matrix of experiments . . . . .	61
4.3.3	Parameterization . . . . .	63
4.3.4	Results . . . . .	64
4.3.5	Statistical analysis . . . . .	69
4.4	Design improvement . . . . .	72
4.4.1	Linearization of the force profile . . . . .	72
4.4.2	Prototype . . . . .	76
4.5	Full parametrical setup . . . . .	77
4.6	Actuators . . . . .	80
4.6.1	Cylindrical actuator . . . . .	80
4.6.2	Square actuator II . . . . .	87
4.6.3	Fixed magnet actuators . . . . .	92
4.6.4	Vibrotactile button . . . . .	95
4.7	Thermal analysis . . . . .	98
4.7.1	Limiting elements . . . . .	98
4.7.2	FEM steady state thermal analysis . . . . .	99
4.8	Summary . . . . .	103
<b>5</b>	<b>Position sensing of compact actuators for multi-finger haptic devices</b>	<b>105</b>
5.1	Reassignment of existing sensors . . . . .	106
5.1.1	Independent sensing method . . . . .	106
5.1.2	Hybrid sensing method . . . . .	109
5.2	Self-sensing approach . . . . .	112
5.3	Back emf for position interpolation . . . . .	113
5.3.1	Physiological considerations . . . . .	113
5.3.2	Back emf . . . . .	114
5.3.3	Free fall study . . . . .	115
5.3.4	Results . . . . .	117
5.4	Oscillating RLC circuit . . . . .	120
5.4.1	Coil properties . . . . .	120
5.4.2	Oscillating RLC circuit . . . . .	123
5.4.3	Simulation and numerical validation of the phenomenon . . . . .	126
5.4.4	Frequency adaptation . . . . .	130



5.4.5 Measurement method . . . . .	130
5.4.6 Results . . . . .	133
5.4.7 Improvements and design for self-sensing . . . . .	137
5.5 Summary . . . . .	138
<b>6 Multi-finger haptic applications</b>	<b>141</b>
6.1 Haptic Keyboard . . . . .	142
6.1.1 Actuator . . . . .	142
6.1.2 Control . . . . .	144
6.1.3 Communication . . . . .	147
6.1.4 Prototypes . . . . .	149
6.1.5 Software user interface . . . . .	152
6.2 VibKey Pad . . . . .	155
6.2.1 Capacitive touch sensor . . . . .	156
6.2.2 Vibrator . . . . .	157
6.2.3 Control . . . . .	158
6.2.4 Prototypes . . . . .	160
<b>7 Impact study of haptic feedback on emotional processing</b>	<b>163</b>
7.1 Context . . . . .	163
7.2 Objectives . . . . .	167
7.3 Method . . . . .	168
7.3.1 Participants and apparatus . . . . .	168
7.3.2 Procedure and experimental design . . . . .	168
7.4 Results . . . . .	171
7.4.1 Identification part . . . . .	171
7.4.2 Effect on emotional processing . . . . .	174
7.5 Discussion . . . . .	179
<b>8 Conclusion and outlook</b>	<b>183</b>
8.1 Main results and innovative contributions . . . . .	183
8.2 Outlook . . . . .	185
<b>A Actuators</b>	<b>187</b>
A.1 Optimization tools . . . . .	187
A.1.1 Design of experiments . . . . .	187
A.2 Actuators . . . . .	190
A.2.1 Cylindrical actuator . . . . .	190
A.2.2 Square actuator II . . . . .	191
A.2.3 Fixed magnet actuators . . . . .	194
A.2.4 Vibrotactile button . . . . .	195

## Contents

---

<b>B</b>	<b>Sensors</b>	<b>197</b>
B.1	Hybrid sensing method . . . . .	197
B.1.1	Linear Hall sensors for position measurement . . . . .	197
B.2	Self-sensing approach . . . . .	199
B.2.1	Oscillating RLC circuit . . . . .	199
B.2.2	RLC circuit with parallel capacitor . . . . .	199
B.2.3	RLC circuit with parallel inductor . . . . .	200
<b>C</b>	<b>Applications</b>	<b>205</b>
C.1	Haptic Pad and Haptic Keyboard . . . . .	205
C.1.1	Actuator . . . . .	205
C.1.2	Prototypes . . . . .	207
<b>D</b>	<b>Impact study of haptic feedback on emotional processing</b>	<b>209</b>
D.1	Results . . . . .	209
D.1.1	Effect on emotional processing . . . . .	209
	<b>Bibliography</b>	<b>211</b>
	<b>Curriculum Vitae</b>	<b>227</b>

# List of Figures

2.1	Penfield Homunculus . . . . .	6
2.2	Exploratory procedures . . . . .	7
2.3	Hand components . . . . .	8
2.4	Mechanoreceptors . . . . .	9
2.5	Types of tactile afferent units . . . . .	11
2.6	Location of receptive field centers in the human hand glabrous skin . . . . .	12
2.7	Spatial tactile discrimination over human body . . . . .	13
2.8	Threshold-frequency characteristics . . . . .	14
2.9	Human finger bandwidths . . . . .	15
2.10	Electromechanical force feedback peripherals . . . . .	19
2.11	Commercially available haptic displays . . . . .	20
2.12	Haptic systems used in minimally invasive surgery simulation or teleoperation . . . . .	21
2.13	Haptic music instruments . . . . .	21
2.14	Haptic music instruments . . . . .	22
2.15	Haptic systems for finger rehabilitation . . . . .	22
2.16	Haptic gloves . . . . .	23
2.17	Haptic gloves . . . . .	24
2.18	Eccentric motor vibrators . . . . .	24
2.19	Tactile touchscreens . . . . .	25
2.20	Influence of kinesthetic vs. tactile . . . . .	26
2.21	Tactile display (kinesthetic and tactile feelings) . . . . .	27
2.22	Tactuator principle . . . . .	27
2.23	Material Rubik Cube . . . . .	28
2.24	Repetitive strain injuries trend in US businesses . . . . .	30
3.1	General configuration of a haptic system for multi-finger applications with its main components . . . . .	36
3.2	Control principle of a single key . . . . .	41
3.3	Single and mutli-DSP control principles . . . . .	42
3.4	Closed loop of information in usual computer operations . . . . .	43
4.1	Initial electrodynamic actuator . . . . .	47
4.2	Underhung and overhung coil principles . . . . .	48
4.3	2D FEM issues with 3D objects. . . . .	50

## List of Figures

---

4.4	3D FEM flux density analysis . . . . .	50
4.5	Magnetic flux path in 2D cut . . . . .	50
4.6	Force provided by the initial actuator for different current values . . . . .	51
4.7	FEM force is proportional to the current and varies with the position of the coil . . . . .	51
4.8	Similarly for the measured force . . . . .	51
4.9	When the section crossed by the flux is small compared to the airgap width, the fringes/flux ratio becomes critical . . . . .	52
4.10	2D version of the actuator . . . . .	53
4.11	Equivalent magnetic circuit . . . . .	53
4.12	Flux path with ideal iron . . . . .	55
4.13	Saturation at 1 T . . . . .	55
4.14	Classic model vs FEM for different magnet heights with the coil in its down position (0 mm) . . . . .	56
4.15	Force profiles comparison between classic and loops models and FEM for different magnet heights . . . . .	57
4.16	General experimental system with input factors $\vec{X}$ and output answers $\vec{Y}$ . . . . .	58
4.17	Linear model for two factors and corresponding 2D projection . . . . .	60
4.18	Linear model with interactions for two factors . . . . .	60
4.19	Quadratic model with interactions for two factors . . . . .	60
4.20	Composite design for three factors with $\alpha = 1$ (sphere radius) . . . . .	62
4.21	Parameters $a_i$ for the linear model without interaction obtained with different designs . . . . .	65
4.22	Parameters in % of the average $a_0$ . . . . .	65
4.23	Linear model without interaction obtained with different designs vs FEM . . . . .	66
4.24	Linear model with interactions obtained with factorial design and quadratic model with interactions obtained with composite design vs FEM . . . . .	66
4.25	Parameters $a_i$ for the linear model with interactions obtained with factorial design . . . . .	66
4.26	Parameters in % of the average $a_0$ . . . . .	66
4.27	Parameters $a_i$ for the quadratic model with interactions obtained with the composite design . . . . .	67
4.28	Parameters in % of the average $a_0$ . . . . .	67
4.29	Comparison between the quadratic model of the force (Table 4.7) and FEM simulations for different magnet heights . . . . .	68
4.30	Parameters $a_i$ for the quadratic model with interactions obtained with the composite design . . . . .	69
4.31	Parameters in % of the average $a_0$ . . . . .	69
4.32	Linear model without interaction obtained with different designs vs FEM with saturation . . . . .	69
4.33	Linear model with interactions obtained with factorial design and quadratic model with interactions obtained with composite design vs FEM with saturation . . . . .	69
4.34	Probability distribution of absolute discrepancies between the quadratic model and FEM . . . . .	70

4.35 Cumulative distribution function of absolute discrepancies . . . . .	70
4.36 Probability distribution of absolute discrepancies between quadratic model and FEM with saturation . . . . .	71
4.37 Cumulative distribution function of absolute discrepancies with saturation . .	71
4.38 Cumulative distribution function of relative discrepancies without saturation .	71
4.39 Cumulative distribution function of relative discrepancies with saturation . . .	71
4.40 Geometry improvements for linearization and new factors . . . . .	73
4.41 Force profile corresponding to the optimal force geometry (4.3.5) . . . . .	73
4.42 Force profile shift provoked by a "mechanical offset" $w_3$ . . . . .	74
4.43 Force profile shift provoked by an enlargement of the housing bottom $w_2$ . . .	75
4.44 Actuator force characteristic after linearization process . . . . .	75
4.45 Second prototype with embedded force sensor . . . . .	76
4.46 Exploded view of the second prototype with guiding system . . . . .	76
4.47 Measurements vs FEM for the second prototype at 0.5 A . . . . .	77
4.48 Block diagram of the full parametrical setup . . . . .	78
4.49 Graphic user interface for the experimental domain definition . . . . .	79
4.50 Cylindrical actuator principle . . . . .	81
4.51 Quadratic model parameters for 3 factors . . . . .	82
4.52 Parameters in % of the average $a_0$ . . . . .	82
4.53 Quadratic model vs FEM (48 simulations) . . . . .	82
4.54 Quadratic model parameters in % of the average $a_0$ for 5 factors . . . . .	83
4.55 Surface comparison between model and FEM when varying pairs of factors . .	84
4.56 FEM validation of the quadratic model when varying pairs of factors . . . . .	84
4.57 Quadratic model parameters in % of the average $a_0$ for 7 factors . . . . .	85
4.58 FEM validation of the quadratic model when varying pairs of factors . . . . .	86
4.59 Square actuator principle . . . . .	87
4.60 Quadratic model parameters in % of the average $a_0$ for 5 factors . . . . .	88
4.61 Quadratic model parameters in % of the average $a_0$ for 7 factors . . . . .	89
4.62 Star validation principle for 3 factors (• = optimum) . . . . .	90
4.63 Average force of the star validation around the optimum (•) obtained respectively with the 5 factors model and FEM . . . . .	91
4.64 Average force of the star validation around the optimum (•) obtained respectively with the 7 factors model and FEM . . . . .	91
4.65 Prototype of the cylindrical actuator . . . . .	93
4.66 Force profile comparison between FEM and measurements . . . . .	93
4.67 Adaptation of iron saturation to 1.1 T and of magnetic remanence to 1.37 T . .	94
4.68 Prototype of the square actuator . . . . .	94
4.69 Force profile comparison between FEM and measurements . . . . .	94
4.70 FEM simulation of the square actuator with a 1 mm shorter coil and an iron saturation of 0.95 T . . . . .	95
4.71 Principle of the vibrotactile button . . . . .	95
4.72 Free factors for the vibrotactile button optimization . . . . .	96

## List of Figures

---

4.73	Force characteristic of the vibrotactile button . . . . .	96
4.74	Quadratic model parameters for 3 factors in % of the average $a_0$ . . . . .	97
4.75	Surface obtained with the quadratic model II for different base heights . . . . .	98
4.76	Steady state thermal analysis of seven optimal actuator geometries for the two extreme positions of the coil (in and out) at full power ( $j = 8 \text{ A/mm}^2$ ) . . . . .	100
4.77	Temperature of the actuator corresponding to different usage rates (coil in) . . . . .	102
4.78	Temperature of the actuator corresponding to different current levels (coil in) and comparison with measurements on the RA5fix prototype ( $\Delta$ ) . . . . .	102
5.1	Miniature photointerrupter from Omron Electronics Inc. . . . .	107
5.2	Single-photointerrupter principle . . . . .	107
5.3	Signal processing of the sensor output. At each pulse-triggered interrupt, the values of the two comparators (CMP1 and CMP2) are read and translated into a binary code . . . . .	108
5.4	Functional demonstrator of the single-photointerrupter optical sensor . . . . .	108
5.5	Representation of the flux density $B$ above the actuator initial square design . . . . .	110
5.6	Projections of the flux density characteristic along the $z$ -axis . . . . .	110
5.7	Vertical component of the flux density above the actuator center with probe . . . . .	111
5.8	Miniature Hall sensor board embedded in a square actuator . . . . .	111
5.9	Hall sensor measurements with linear interpolations and quadratic polynomial . . . . .	112
5.10	Flux crossing the coil vs position . . . . .	115
5.11	Back emf measurement principle . . . . .	116
5.12	Velocity vs back emf during a free fall . . . . .	116
5.13	Zoom on back emf from instrumentation amplifier output . . . . .	117
5.14	Position interpolated from back emf data with different $\Delta t$ vs position measured with a precision CCD laser sensor . . . . .	118
5.15	Discrepancies between position measurement and interpolation and corresponding moving average . . . . .	118
5.16	Real time interpolated position from back emf data vs position measured with a precision CCD laser sensor . . . . .	119
5.17	Comparison between interpolated position and laser sensor data . . . . .	119
5.18	Equivalent circuit of a wound coil . . . . .	120
5.19	Frequency characteristic of the inductance of a cylindrical short-stroke actuator coil at two extreme positions . . . . .	122
5.20	Frequency characteristic of the resistance of a cylindrical short-stroke actuator coil at two extreme positions . . . . .	122
5.21	Oscillating RLC circuit behavior . . . . .	123
5.22	Drive circuit principle for actuator and electrical model of a coil . . . . .	124
5.23	Self-sensing measurement circuits for the simulation of the variable inductance effect . . . . .	125
5.24	Current decrease in RL circuit . . . . .	126
5.25	Low frequency current decrease in RLC circuit . . . . .	128

---

5.26 High frequency oscillations in RLC circuit . . . . .	128
5.27 Low frequency current decrease in RLC circuit (numerical) . . . . .	129
5.28 High frequency oscillations in RLC circuit (numerical) . . . . .	130
5.29 Influence on the coil inductance caused by an additional capacitor in parallel .	131
5.30 Influence on the coil resistance caused by an additional capacitor in parallel . .	131
5.31 Drain voltage characteristic with a 33 nF capacitor in parallel with the coil . . .	132
5.32 Self-sensing measurement principle . . . . .	132
5.33 Drain voltage after voltage limiter $u_{lim}$ (5.1 V), low-pass filter $u_{lp}$ (12 kHz) and comparator $u_{comp}$ (4.5 V) . . . . .	133
5.34 Drain voltage measurements $u_d$ and the corresponding signals triggering the microcontroller external interrupt $u_{comp}$ for high and low positions of the coil .	134
5.35 Dynamic measurements of the coil position with a reference laser sensor and the self-sensing algorithm output supplied with a PWM duty cycle of 50 % . . .	135
5.36 Detailed comparison between self-sensing and laser sensor values during dy- namic displacements of the coil (PWM 50 %) . . . . .	135
5.37 Residual oscillations on the drain voltage for high positions (red) . . . . .	136
5.38 Influence of the PWM duty cycle on the position detection during dynamic displacements of the coil . . . . .	136
5.39 Values of the counter at the lowest actuator position (sensor offset) for different duty cycles . . . . .	137
6.1 Electromagnetic actuators array with the coils fixed on the main board . . . . .	143
6.2 Guideway of MX™ 5500 keys . . . . .	144
6.3 Key adapters with and without slit . . . . .	144
6.4 O-rings mounted on actuators . . . . .	144
6.5 Preparation for the gluing of the coils . . . . .	144
6.6 Block control strategy and closed-loop principle for a single key . . . . .	145
6.7 Detailed view of the Hall sensors . . . . .	145
6.8 Sensors insulation and supporting springs . . . . .	145
6.9 DSP control principle for a single key . . . . .	146
6.10 Distribution of the groups of keys . . . . .	147
6.11 Communication between keyboard and computer . . . . .	147
6.12 Passive priority selector composed of a cascade of OR gates for the characters transmission . . . . .	148
6.13 Microcontroller selector for force profile upload . . . . .	149
6.14 Haptic Pad electronic board . . . . .	150
6.15 The Haptic Pad and its user interface . . . . .	150
6.16 Top case of the Haptic Keyboard with actuators plugged in . . . . .	151
6.17 Assembled bottom case of the Haptic Keyboard . . . . .	151
6.18 Haptic Keyboard front view with travel modification mechanism . . . . .	152
6.19 Software User Interface for Haptic Keyboard . . . . .	153
6.20 Constant force mode . . . . .	154

## List of Figures

---

6.21	Keyboard height modification mode . . . . .	154
6.22	Software User Interface for Haptic Pad . . . . .	155
6.23	Touch feedback . . . . .	156
6.24	Prototype of a vibrotactile button (VibKey) . . . . .	156
6.25	Capacitive effect on fingertip . . . . .	156
6.26	Charge circuit principle of a capacitive touch surface . . . . .	157
6.27	Effect of the presence of a finger on the capacitor charge . . . . .	157
6.28	Control circuit for the vibrotactile button . . . . .	158
6.29	Block diagram detailing the execution of the vibrotactile button program . . . . .	159
6.30	Simple square control . . . . .	159
6.31	Enhanced sinusoidal control . . . . .	160
6.32	Rigid VibKey Pad prototype . . . . .	160
6.33	Back side of the VibKey Pad . . . . .	160
6.34	Flexible VibKey Pad prototype . . . . .	161
7.1	Some emoticons and proposed hapticons . . . . .	165
7.2	The wearable HaptiHug imitates a realistic hugging . . . . .	166
7.3	The HaptiHeart simulates different heartbeat patterns . . . . .	166
7.4	VITAL vibrotactile interface . . . . .	166
7.5	Force profiles implemented on keys 1-8 of the Haptic Pad for identification . . . . .	169
7.6	Example of faces displayed during the emotional experiment . . . . .	170
7.7	Haptic Pad setup for the recognition of emotions . . . . .	170
7.8	Correspondence between emotions, visual and haptic clues . . . . .	170
7.9	Block diagram presenting the four parts of the experiment: 1. without clue, 2. visual clue, 3. visuo-tactile clues and 4. tactile clue only (• = start) . . . . .	171
7.10	Percentage of correct profiles drawing per participant . . . . .	173
7.11	Percentage of correct drawing of each profile for the distinct groups (all, engineers and psychologists) . . . . .	173
7.12	Percentage of correct profiles matching per participant during and after the experiment . . . . .	174
7.13	Percentage of correct matching of each profile for the distinct groups (all, engineers and psychologists) . . . . .	174
7.14	Results of the ranking of the five more memorable touch sensations . . . . .	174
7.15	Weighted ranking of the five more memorable touch sensations . . . . .	174
7.16	Average accuracy of emotions recognition during the four conditions with standard errors . . . . .	175
7.17	Detail per emotion . . . . .	175
7.18	Average response time during the four conditions with standard error bars . . . . .	176
7.19	Detail per emotion . . . . .	176
7.20	Detail of the answers given for the four different haptic clues during the tactile part	178
A.1	Two and three-level factorial designs for two factors $x_1$ and $x_2$ . . . . .	188
A.2	Doehlert hexagonal matrix for two factors $x_1$ and $x_2$ . . . . .	189



A.3 Composite design for two factors $x_1$ and $x_2$ . . . . .	189
A.4 Cylindrical actuator parts . . . . .	194
A.5 Square actuator parts . . . . .	194
B.1 Flux density on a 2D grid overhanging a cylindrical actuator . . . . .	198
B.2 Flux density vectors above the actuator . . . . .	198
B.3 Hall sensor output variation related to PWM duty cycle . . . . .	198
B.4 Test circuit with parallel capacitor . . . . .	200
B.5 Measurements made on the circuit of Figure B.4 with a prototype of actuator . . . . .	200
B.6 Effect on the capacitor impedance connected in parallel with the coil . . . . .	201
B.7 Output characteristic of the LM358 operational amplifier . . . . .	203
B.8 Measured time variation $\Delta t$ versus position measured with an external laser sensor	203
B.9 Current versus duty cycle characteristic measured on the complete self-sensing setup and its linear interpolation between 15 and 95 % . . . . .	204
B.10 Current behavior and drain voltage oscillations during normal PWM operations	204
C.1 Top view of the Haptic Pad electronic board . . . . .	207
C.2 Back side of the Haptic Keyboard electronic board . . . . .	208
C.3 Detailed view of the microcontrollers . . . . .	208
C.4 Driver circuits and position sensor filters . . . . .	208
D.1 Detail of the answers given for the four different haptic clues during the visuo- tactile part . . . . .	210



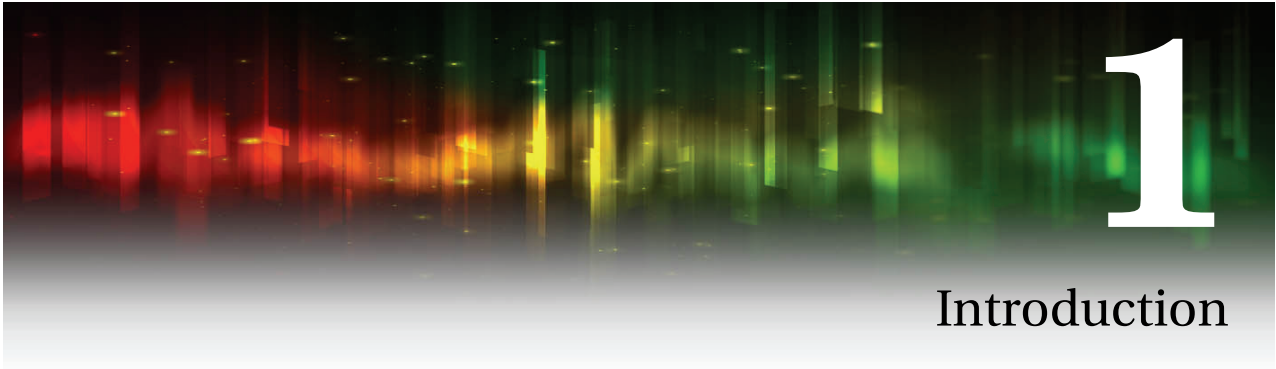
## List of Tables

2.1	Main characteristics of the four tactile unit types . . . . .	11
2.2	Frequency characteristic and temperature sensitivity of the four tactile unit types	14
2.3	Human finger bandwidths and corresponding functions . . . . .	15
2.4	Distribution of selected cases of injuries involving days away from work . . . . .	31
3.1	Qualitative comparison of existing actuating principles . . . . .	39
4.1	Actuator specifications . . . . .	46
4.2	Actuator advantages . . . . .	49
4.3	Free factors for the optimization of the initial square actuator geometry . . . . .	61
4.4	Model matrix of a composite design for quadratic model with interactions for three factors . . . . .	63
4.5	Model matrix of a Hadamard design for linear model without interaction for three parameters . . . . .	64
4.6	Model matrix of a factorial design for linear model with interactions for three parameters . . . . .	65
4.7	Parameters $\bar{a}$ of the quadratic model obtained with the composite design presented in Figure 4.20 . . . . .	67
4.8	Parameters $\bar{a}$ of the quadratic model obtained with the composite design presented in Figure 4.20 taking saturation into account . . . . .	68
4.9	Discrepancy analysis of the quadratic models . . . . .	71
4.10	Maximums and discrepancies with FEM of the quadratic models . . . . .	72
4.11	Actuator dimensions after linearization process [mm] . . . . .	76
4.12	Free factors for optimization . . . . .	81
4.13	Free factors for optimization . . . . .	83
4.14	Free factors for optimization . . . . .	85
4.15	Optimal actuator configurations . . . . .	86
4.16	Average force resulting from the optimization process and comparison with FEM	87
4.17	Free factors for optimization . . . . .	88
4.18	Free factors for optimization . . . . .	89
4.19	Optimal actuator configurations . . . . .	90
4.20	Average force resulting from the optimization process and comparison with FEM	90
4.21	Dimensions [mm] and results of the star validation with a radius of 0.2 mm for the square actuator with 5 factors . . . . .	91

## List of Tables

---

4.22	Free factors for optimization . . . . .	92
4.23	Optimal actuator configurations . . . . .	92
4.24	Average force resulting from the optimization process and comparison with FEM . . . . .	93
4.25	Free factors for optimization . . . . .	96
4.26	Optimal actuator configurations . . . . .	97
4.27	Force resulting from the optimization process and comparison with FEM . . . . .	97
4.28	Optimal actuators characteristics with $N$ the number of turns, $R$ the coil resistance, $P$ the Joule losses and $T/F$ the coil temperature over force ratio when the coil is inside the actuator . . . . .	100
4.29	Typing characteristics and usage rates for the most frequently used keys for different kind of users . . . . .	101
5.1	Parameters values for low and high frequency configurations of the RLC circuit based on measurements . . . . .	127
5.2	Measured values of the components used in the final test bench . . . . .	134
7.1	Summarized results of the descriptive part of the force profiles identification . . . . .	172
7.2	Overall accuracy of emotions recognition averaged on the four conditions [%] . . . . .	175
7.3	Detailed accuracy of emotions recognition during the four conditions [%] and corresponding improvements relatively to the first condition . . . . .	176
7.4	Detailed response times during the four conditions [ms] and corresponding improvements relatively to the first condition . . . . .	177
7.5	Overall accuracy of force profiles recognition under different conditions [%] . . . . .	178
A.1	Quadratic model of the cylindrical actuator for 3 factors . . . . .	190
A.2	Quadratic model of the cylindrical actuator for 5 factors . . . . .	190
A.3	Quadratic model of the cylindrical actuator for 7 factors . . . . .	190
A.4	Quadratic model of the square actuator with first order interactions for 5 factors . . . . .	191
A.5	Quadratic model of the square actuator with first order interactions for 7 factors . . . . .	191
A.6	Dimensions [mm] and results of the star validation with a radius of 0.5 mm for the square actuator with 5 factors . . . . .	192
A.7	Dimensions [mm] and results of the star validation with a radius of 0.2 mm for the square actuator with 7 factors . . . . .	192
A.8	Dimensions [mm] and results of the star validation with a radius of 0.5 mm for the square actuator with 7 factors . . . . .	193
A.9	Quadratic model of the cylindrical actuator with first order interactions for the fixed magnet configuration . . . . .	194
A.10	Quadratic model of the square actuator with first order interactions for the fixed magnet configuration . . . . .	194
A.11	Quadratic model I of the vibrator with interactions for 3 factors . . . . .	195
A.12	Quadratic model II of the vibrator with interactions for 3 factors . . . . .	195
C.1	Dynamics of electrodynamic and electromagnetic configurations . . . . .	206



The relation between man and machine saw a spectacular evolution throughout the ages. The technology greatly contributed to this evolution towards what we can call a full usage of the human sensory apparatus. It started with hearing and the appearance of novel sound storage methods in the 18<sup>th</sup> century. Vision then, with the beginning of image projection with the Lumière brothers and the first televisions in the end of the following century and finally touch, with the first electrically actuated teleoperator to remotely handle radioactive substances in the 1950s. Naturally, all these domains have undergone important technological improvements to reach the current level of applications that have become a part of our everyday life. The present thesis continues this way and particularly focuses on the sense of touch, commonly related to as haptics.

The word haptics comes from the Greek *haptein*, "to touch". It was first used in the world of art by A. Riegel in Austria and then by G. Deleuze in France who described the art as a progression between haptics and optics, from the touch sensation of the painter to the single visual sense of the viewer [1]. Deleuze notably inspired numerous researchers in the United States who started the virtual reality movement. From that point, the importance given to the sense of touch has been growing in different domains: from the simple game controller to professional environments such as surgery, virtual reality and robotics. Force feedback devices slowly appeared to be useful even in the daily life.

More and more, the human being is confronted to the digital world and uses one electronic device after the other. It begins with an electric toothbrush in the morning, an mp3 player on the way to work, a computer here, a tablet there. A short call to your friend who, while

## Chapter 1. Introduction

---

driving his car, presses on the central console to answer the phone and mute the sound of the radio. Once back home, the kids are playing video games and after cooking dinner in your brand-new kitchen, you fall on the couch and manipulate the TV remote control before going to bed, your alarm clock on the bedside table, ready to wake you up the next morning. Nowadays, it becomes obviously difficult to voluntarily avoid using electronic devices. All those mentioned in the typical day presented above however require a human-machine interaction. The buttons, generally used to communicate with the device, can have various shapes and functionalities and the sensation they provide to the user gains in importance.

Man-machine interactions assume two main features. On one hand is the haptic sensation itself. Indeed, more and more efforts are put to improve the comfort provided by the interfaces in response to actions of the user's fingers. On the other hand, the interface can be aimed to convey physical information to the user. It can be done either by acknowledging a hit or by communicating information through the sense of touch, using for instance new haptic languages, enlarging thus the richness of information. The communication through the internet, for example, suffers from a lack of content usually attribute to non-verbal signals.

In response to the current concerns regarding the relation between the electronic devices and the humans, the present thesis aims to propose a methodology for the development of multi-finger haptic devices. Under the form of peripherals integrating networks of actuators, these devices will offer the possibility to the user to freely adapt the force feedback to his needs for various tasks involving the use of up to his ten fingers.

The following work addresses all the steps towards the elaboration of multi-finger haptic devices and starts with a large introduction to the sense of touch in order to have a better comprehension of the fantastic sensory-motor apparatus that is the human hand. An overview of the current state of research is then presented and the elements motivating the present thesis are exposed.

In a second block, the proper methodology for the conception of multi-finger haptic devices is studied. Chapter 3 first outlines the problem by describing the key components constituting a multi-finger haptic device. From there, focus is put on two main components essential to the generation of a reliable haptic feedback, namely the actuators and the sensors. For both of them, generic tools are provided, offering the possibility for future developers to use them for different kinds of multi-finger haptic applications. Chapter 4 proposes a novel methodology specifically designed for the modeling and optimization of miniature electromagnetic short-stroke actuators requiring a precise modeling of three-dimensional flux paths and material characteristics. A full parametrical optimization setup using the design of experiments combined with 3D finite element modeling is implemented and validated with several configurations of actuators. Then, in order to be able to accurately control different kinds of miniature short-stroke actuators, chapter 5 presents a panel of innovative solutions to measure their position. Taking advantage of existing sensors or tailor-made self-sensing techniques, the solutions developed offer low-cost and compact alternatives, easily embeddable in networks

---

of miniature actuators.

In order to illustrate the global methodology for multi-finger haptic devices, chapter 6 presents two applications developed and manufactured within the framework of the thesis. The Haptic Keyboard is a force feedback computer keyboard integrating 64 fully programmable actuators allowing the user to enhance his typing experience by finely defining the force feedback generated by each key in response to his strokes. Besides that, a VibKey Pad integrating four vibrotactile buttons is developed. The main role of this small remote control is to improve the touch feeling provided by tactile buttons. Indeed, the lack of physical acknowledgement of most devices with tactile buttons can be an issue, which is solved by the addition of a haptic feedback integrated in the form of a vibration.

Finally, in order to enlarge the scope of multi-finger haptic applications, a pilot study is run in collaboration with the University Service of Child and Adolescent Psychiatry in Lausanne, with the aim of improving the perception of emotions of psychotic adolescents with the help of tactile information. Using the Haptic Pad, a smaller version of the Haptic Keyboard integrating 16 keys, the identification of various touch sensations by a sample of healthy subjects is studied, laying the first stones for a novel haptic language. Then, these results are used to influence the recognition of emotions on human faces, a common weakness affecting psychotic adolescents.







**Contents**

---

<b>2.1 Touch sense tasks and sensitivities . . . . .</b>	<b>6</b>
<b>2.2 Human hand physiology . . . . .</b>	<b>8</b>
2.2.1 Mechanoreceptors . . . . .	9
2.2.2 From nerve endings to the central nervous system: the tactile units . . .	10
2.2.3 Location and spatial resolution of tactile units . . . . .	12
2.2.4 Frequency and temporal resolution of tactile units . . . . .	13
<b>2.3 State of the art . . . . .</b>	<b>16</b>
2.3.1 Haptics: Roles and implications in the daily life . . . . .	16
2.3.2 Kinesthetic sensitivity and force feedback . . . . .	18
2.3.3 Cutaneous sensitivity and vibrotactile stimulation . . . . .	23
2.3.4 Thermal sensitivity and heat transfer . . . . .	28
<b>2.4 Motivations . . . . .</b>	<b>29</b>
2.4.1 Repetitive strain injuries . . . . .	29
2.4.2 Gaming and virtual reality: a new touch experience . . . . .	31
<b>2.5 Summary . . . . .</b>	<b>32</b>

---

The scientific community and beyond agree to say that from a sensory-motor point of view, the human being is a fantastic machine. Endowed of five complementary senses, namely hearing, sight, smell, taste and touch, the human body is able to perceive and interact with its

## Chapter 2. The sense of touch

---

environment in a manner that we do not even notice it. The present work focuses on the most spread out of all which covers the whole body from head to toe: the sense of touch.

Broadly speaking, touch is usually referred to as *somesthesia*, which is the faculty of body perception including various sensory systems like skin, tendons, joints, viscera, etc... [2]. Not all body parts are equal regarding their density in nerve endings and motor skills; the hands, and the fingers particularly, are among the most elaborated parts. Figure 2.1 (a) shows the size of each body part, scaled relatively to the amount of cortex dedicated to it, either from the sensory or motor point of view. Despite its actual size, the hand represents an important feature on both sides. Not surprisingly, it becomes a major part of a distorted representation of the human body relatively to its sensory functions called the *Penfield homunculus* (Figure 2.1 (b)) from the name of an American neurosurgeon who mapped the sensory-motor areas of the human brain [3].

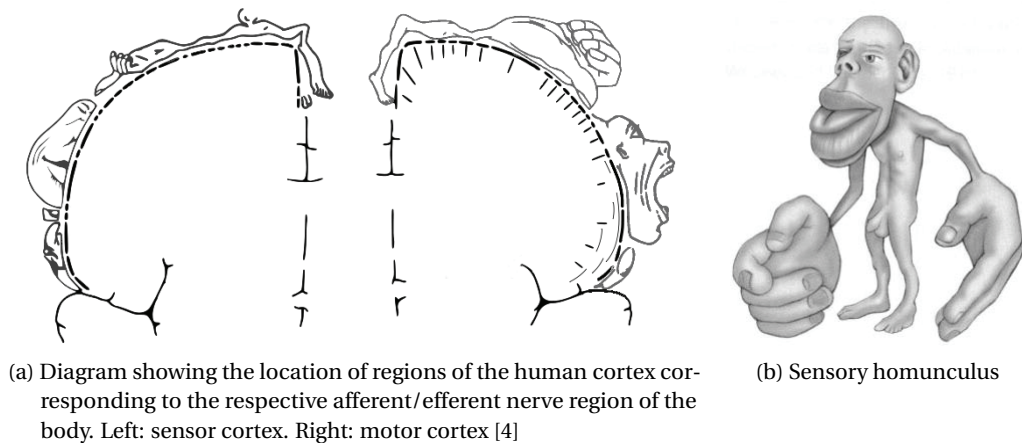


Figure 2.1 – Penfield Homunculus

In the present chapter, attention is given to the nature and role of the touch perception in human hands and fingers. After a brief enumeration of the functionalities attributed to the sense of touch, a detailed analysis of the global somesthetic system is provided bringing three sub-categories into light, namely cutaneous, kinesthetic and thermal. In order to have a sufficient comprehension of the mechanisms in play, physiological aspects of the hand are presented, linking both mechanical and nervous systems. We then outline interactions that touch might have with other senses before considering how it can enter our daily life with various applications and developments in a non-exhaustive state of the art. Finally, the elements that motivated the present work on multi-finger haptic devices will be exposed.

### 2.1 Touch sense tasks and sensitivities

Touch can be used in various ways depending on the task to be executed and the properties to be extracted from an object. The present section, without going into detail, gives an overview

of the different touch procedures developed by the human body and the information resulting from these procedures.

A first distinction appears between active and passive touch. As stated by Gibson [5], being passively touched by an object, focuses the subject on his own body sensation whereas an active exploration provides information about the environment itself. Within the active touch category, a second distinction comes with the way an object is touched depending on the property aimed to be identified. Six main exploratory procedures are proposed by Lederman and Klatzky [6] allowing the subject to determine the shape, softness, temperature, texture, volume or weight of an object (Figure 2.2).

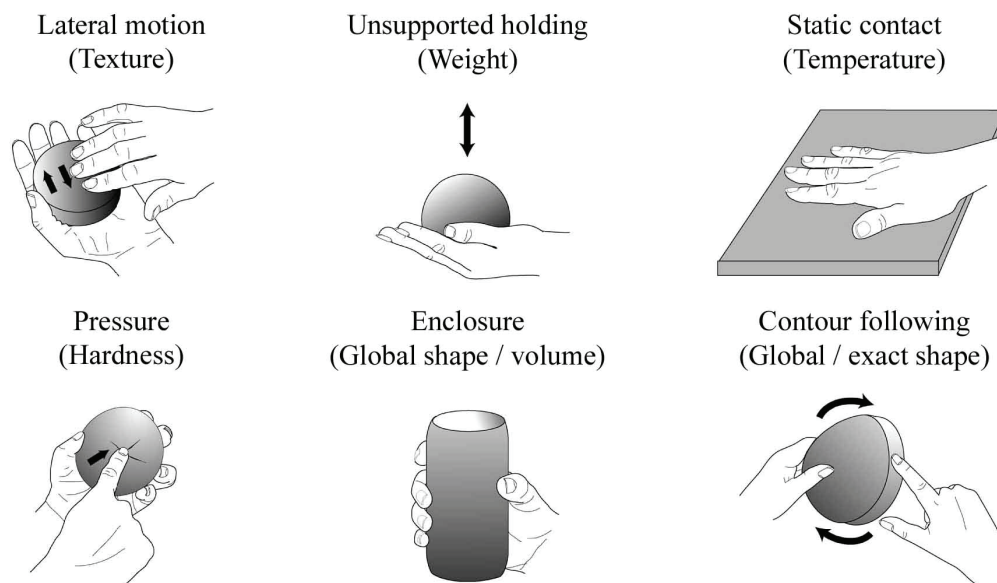


Figure 2.2 – Exploratory procedures and associated object properties adapted from [6]

In order to efficiently gather the above-cited properties from the environment, the somesthetic system is split in four sensibilities, each responding to specific stimuli. These four categories of touch can be summarized as follows:

- **The kinesthetic sense** is related to joints, muscles and tendons. The information transmitted is essentially proprioceptive, meaning that it informs the person about his own mechanical state. Forces acting on the joints are taken into account as well.
- **The tactile or cutaneous sense** allows us to perceive textures and surfaces roughness. It also plays a role in shape and orientation identification during exploration phases and is sensitive to vibrations.
- **The thermal sense** allows not only sensing the apparent temperature of an object, but also the nature of this object (e.g. metal is "colder" than wood due to a better heat conduction).

- **The nociception** monitors the pain which can be cutaneous, muscular or articular and eventually has a function of alarm that can trigger reflexes.

In order to get a better comprehension on the manner with which the human body monitors and interprets the characteristics of an object, it seems important to explain the inner behavior of the human touch tools, especially the hand and fingers. The next section thus proposes an introduction to the hand physiology, bringing its mechanical and sensory constitution to light. It will help the reader to understand how information is gathered by a person to finally provide an intelligible feeling. The following overview results from several readings to which the reader is encouraged to refer for further information [7–9].

### 2.2 Human hand physiology

The human hand is the sensory-motor limb by excellence. The great number of mechanical degrees of freedom associated to the innumerable nerve endings make it one of the most sophisticated mechatronic systems on earth. Despite its complexity, the motor part of the hand is composed of three main elements namely bones or phalanges, tendons and muscles. The muscles, located either in the hand itself or in the forearm, drive the joints movements through tendons (Figure 2.3).

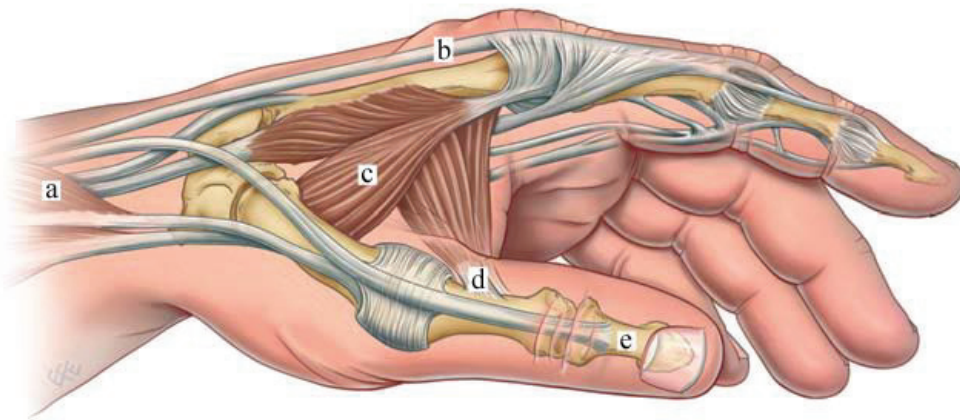


Figure 2.3 – Contractions of muscles whether in the forearm (a) or in the hand (c) pull on the tendons (b,d), themselves attached to the phalanges (e) [7]

This complex mechanics would be of no use without a dense network of sensors and a centralized control. The sensors are nothing else than nerve endings differentiable by their roles. On one hand are the mechanoreceptors, responsible for measuring the stretching, vibration or pressure applied to the hand. They are located whether in the skin and tissues, serving the cutaneous sense, or directly associated to joints and muscles, serving the kinesthetic sense. On the other hand, one find free nerve endings distributed throughout the skin and locomotor apparatus. Called either thermoreceptors or nociceptors, these sensors allow for the detection

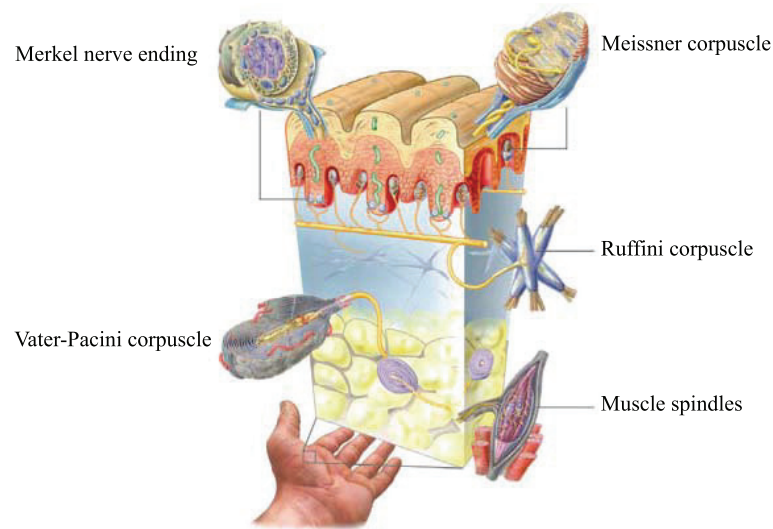


Figure 2.4 – Schematic drawing of mechanoreceptors in the skin and muscles of the hand [7]

of changes in temperature and pain respectively [10].

### 2.2.1 Mechanoreceptors

In his book [7], Grunwald lists six kinds of mechanoreceptors presented in Figure 2.4. Both Ruffini and Vater-Pacini corpuscles are located nearby joints, in the connective tissue forming the joint capsule as well as between the skin and the fibrous membrane surrounding the muscle. The former, composed of one or several cylinders (0.2-0.3 mm long) oriented in different directions, present a high sensitivity to the stretching of the fibers composing them. The latter, also called Pacinian corpuscles, are slightly bigger (up to 1 mm diameter) and respond to vibration stimuli.

The muscle spindles (2-10 x 0.2 mm), as indicated by their name, find themselves in the muscles and deform with the latter, giving information about the change in length. Then, at the interface between skeletal muscles and tendons lay the Golgi tendon organs (up to 1.6 x 0.1 mm, not visible in Figure 2.4). They monitor the tension developed by the muscle and are capable of triggering protective reflexes. These two mechanoreceptors are dedicated to the locomotion apparatus.

Merkel cells and Meissner corpuscles belong to the cutaneous mechanoreceptors. The former are located close to the surface, in the epidermis, and the latter lay in the dermis, but very close to the epidermis. Both are sensitive to small indentations of the skin but differ in the rapidity of their response. Finally, Ruffini corpuscles, similar to those found nearby joints complete the set of cutaneous receptors.

When a mechanoreceptor detects a stress or a vibration, it creates an electric potential that

has to be encoded and transmitted to the central nervous system. This operation is performed using a propagation of action potentials, similar to a train of pulses [11]. The electric impulse starts from the receptor, goes through the primary afferent axon to the spinal cord and terminates in the brain where signals are centralized and computed. The complex encoding of the information necessitates the introduction of a higher level characterization of the system: the tactile units. Also called mechanoreceptive units, their function is to assess directly the relation between impulse discharges and perceptive experiences [12]. A tactile unit can be summarized as a nervous fiber innervating the glabrous skin (hairless skin) carrying the electrical information and whose end-organ is a mechanoreceptor.

### 2.2.2 From nerve endings to the central nervous system: the tactile units

In order to understand how information is encoded, Vallbo and Hagbarth [13] developed a technique to measure the discharges of single mechanoreceptive units by sticking a tiny tungsten electrode in the median nerve just above the elbow. At that time, they managed to measure neural impulses of 40  $\mu\text{V}$  of amplitude in response to mechanical stimuli on awake human subjects. The study resulted in numerous papers explaining how information is encoded [11–15]. The result is a classification of the tactile units in four categories: FA I, FA II, SA I and SA II depending on their adaptation rapidity (fast or slow) and spatial resolution (small or large). Fast adapting units are highly reactive and more dedicated to dynamic phases. On the contrary, slow adapting units are more likely to respond during steady state phases [11]. Types I and II are related to the size of the receptive field; confined to a small region for I or larger and less defined for II. The function of each type during touch operations is detailed in [12].

- FA I: fast adapting with small receptive fields. Formerly RA for rapidly adapting.
- FA II: fast adapting with large receptive fields. Formerly PC for Pacinian corpuscle.
- SA I: slow adapting with small receptive fields.
- SA II: slow adapting with large receptive fields.

Figure 2.5 shows the typical response of the four types of tactile unit during skin indentations. The tactile units with small receptive fields, FA I and SA I, are more reactive when touched by a sharp object, making them ideal for a detailed spatial resolution [16]. This characteristic is of great importance in motor control and exploration of the environment. The receptors of the FA II and SA II units are located deeper in the skin which decreases their spatial resolution. The FA II units react only during abrupt changes in indentation. In fact, they appear to be highly sensitive to vibrations with a peak at 250-300 Hz [17]. As for the SA II units, additionally to their sensitivity to indentation of the skin, they exhibit a directional sensitivity during stretching of the skin [18]. The position of the joints as well as shear forces applied to the skin can thus be monitored, which is highly useful in motor control processes.

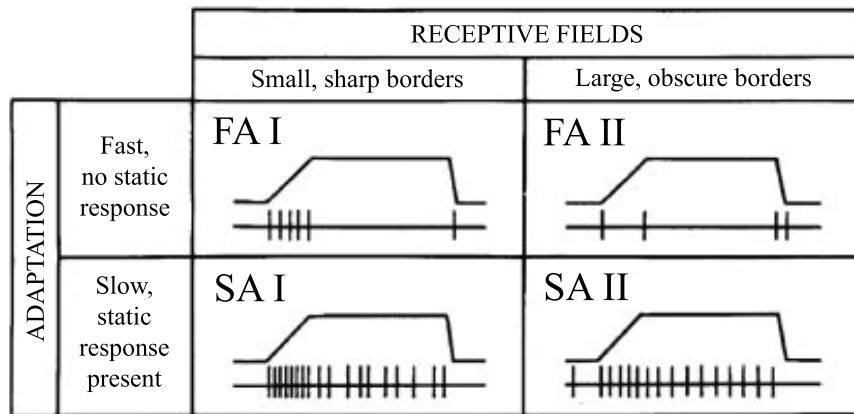


Figure 2.5 – Types of tactile afferent units in the glabrous skin of the human hand. The graphs show the impulses discharge (lower trace) to perpendicular ramp indentation of the skin (upper trace) for each category [19]

A study of Wrestling and Johansson [11] confirmed the role of the different tactile units during precision grip operations. The subject had to lift a small cylinder between his fingers and thumb, position it in the air and replace it. FA I and SA I were highly active during the initial period of grip force increase and during the very release of the object. The FA II, in addition to initial touch and release, fired at the start of the vertical movement and the contact with the table. These periods are indeed favorable to high frequency vibrations spreading through tissues. Finally, SA II units responded more strongly while the object was held in the air, subjecting the skin to shear forces. Table 2.1 summarizes the properties of the four tactile units and closes the loop by linking them to their corresponding mechanoreceptors.

Table 2.1 – Main characteristics of the four tactile unit types

Tactile unit	Mechanoreceptor <sup>1</sup>	% <sup>2</sup>	Size of field <sup>3</sup>	Main functions
FA I	Meissner corpuscle	43%	12.6 mm <sup>2</sup>	Response to small skin indentations and slow vibrations
FA II	Pacinian corpuscle	13%	101 mm <sup>2</sup>	High frequency vibrations
SA I	Merkel cell	25%	11.0 mm <sup>2</sup>	Static discrimination of shapes
SA II	Ruffini corpuscle, spindle	19%	59 mm <sup>2</sup>	Discrimination of skin stretching and position of joints

After answering the question "How it works", a zoom out is now necessary to understand how the sensing principles presented previously are applied to the whole hand so as to be meaningful at the human scale. In order to do so, it is important to locate where the mechanoreceptive units are placed in the human hand.

<sup>1</sup>Various studies allowed to link each tactile unit to a specific mechanoreceptor [18, 20–22]

<sup>2</sup>Percentage of the total number of tactile units[14]

<sup>3</sup>The median values presented are still very dependent on the kind of mechanical stimuli [15]



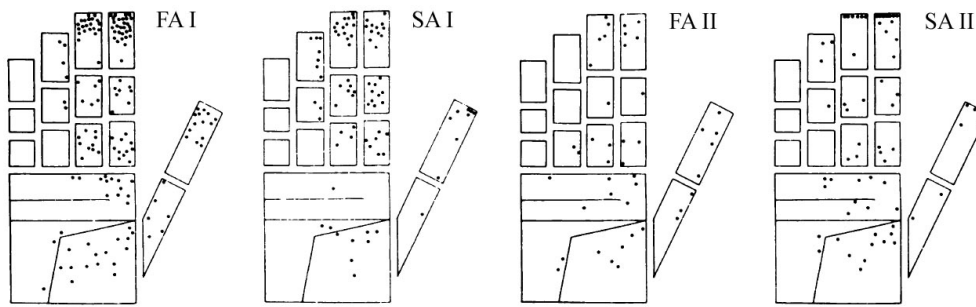


Figure 2.6 – Location of receptive field centers of 334 tactile units in the human hand glabrous skin classified by type [14]

### 2.2.3 Location and spatial resolution of tactile units

In their study of 1979, Johansson and Vallbo recorded single unit impulses, using the same method as Vallbo and Hagbarth, by percutaneously inserting a tungsten needle electrode in the median nerve in conscious human subjects while palpating their hand with a small glass rod. A sample of 334 tactile units were identified and classified in the four categories: FA I, FA II, SA I and SA II. The results are reported in Figure 2.6 which shows the localization of the receptive field centers identified in the glabrous skin of the human hand.

The almost even distribution of type II units can be explained by their large receptive fields. Neither the detection of vibrotactile stimuli nor the state of the locomotor apparatus necessitates a high spatial resolution. However, an exception has to be noticed with the cluster of SA II units visible at the top of the index and middle fingers. These receptors respond vigorously to forces applied to the nail and seem more related to the nail itself than to the skin [22]. As mentioned in Table 2.1, the number of type I units and especially FA I is much higher than type II. Indeed, as their receptive fields are smaller, numerous of them are needed to provide the high spatial resolution desired for exploration and fine motor control.

The overall density of mechanoreceptive units shows a marked increase towards the finger tips, mainly due to the FA I units. The relative densities in the three regions, namely palm, fingers and finger tips are 1, 1.6 and 4.2. Based on the sample of 334 units and the number of myelinated fibers in the median nerve, the total number of tactile units innervating the glabrous skin of the human hand is estimated at 17'000 [14]. The fingers are thus, with 85% of the hand tactile units, one of the most sensitive parts of the human body.

To demonstrate the high spatial sensitivity of the fingers compared with the rest of the body, two methods are used: two-point touch threshold and point localization threshold. In the former, subjects are asked to discriminate the minimum distance between two simultaneous stimuli, at which they still feel two distinct points and not only one. In the latter, the two stimuli are applied successively on the skin. Again, the subject is asked to say whether the two stimuli are applied at the same location or not. The results show a much better sensitivity of the second method with ~1-2 mm on the finger tips compared to ~2-4 mm for the two-point



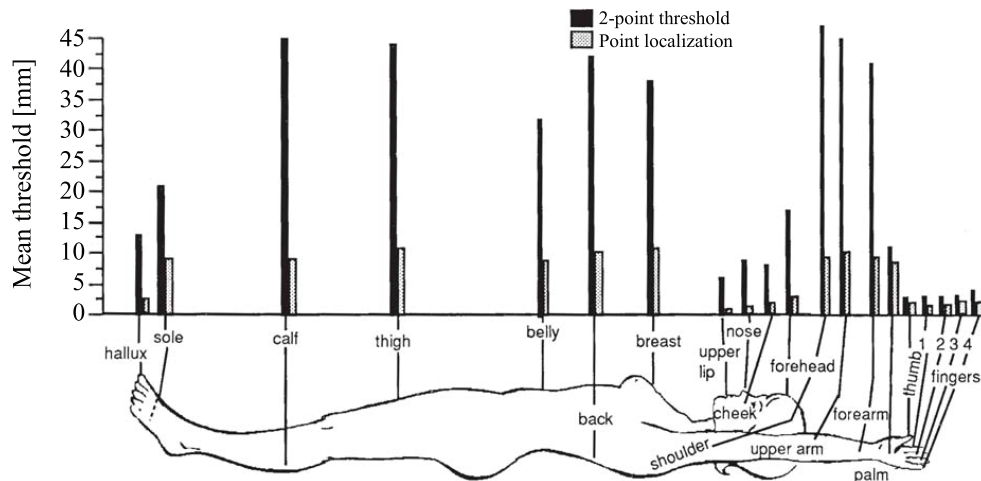


Figure 2.7 – Two-point touch and point localization thresholds over the human body [27], adapted from [23]

touch threshold method [23]. Both tests were performed on entire bodies giving the graph presented in Figure 2.7. Fingers clearly appear to offer the best resolution which makes them perfect candidates for force feedback and vibrotactile systems. A decline of almost 1% per year is however to be expected in tactile spatial acuity due to aging [24, 25]. Finally, it has to be noted that the most sensitive body part is the tip of the tongue (not presented here), with a minimum threshold of  $\sim 1$  mm [26].

So far, spatial resolution has been studied in a plan which is parallel to the skin. This resolution is of importance during exploration phases where the shape or orientation of an object needs to be determined. However, these results were obtained using stimuli provided perpendicularly to the plan of the skin with sufficient amplitude to be sensed by the subject. In a second approach, the minimum perceptible displacement of an object in contact with the skin is investigated. The following subsection proposes to link the tactile units with the indentation thresholds, showing a strong dependency on the excitation frequency.

### 2.2.4 Frequency and temporal resolution of tactile units

A psychophysical study of Bolanowski et al. [28] analyzed the sensitivity of the skin to vibratory stimuli. The goal was to generate sinusoidal vibratory displacements of the skin and detect the minimum detection threshold for a frequency range from 0.4 to 500 Hz. The stimuli were applied on the thenar eminence (part of the palm located at the base of the thumb) and the results are given in decibel with a  $1 \mu\text{m}$  reference (Figure 2.8). Three main parts appear on the graph. The first part, between 0.4 and 3 Hz, is insensitive to frequency with a threshold approaching 0.3 mm. Then, a linear portion decreases by 5 dB/oct. between 3 and 40 Hz and finishes with a U-shaped portion up to 500 Hz. The maximum sensitivity is reached at 300 Hz corresponding to a displacement of  $\sim 15$  nm. Arguments persist on the frequency of maximum

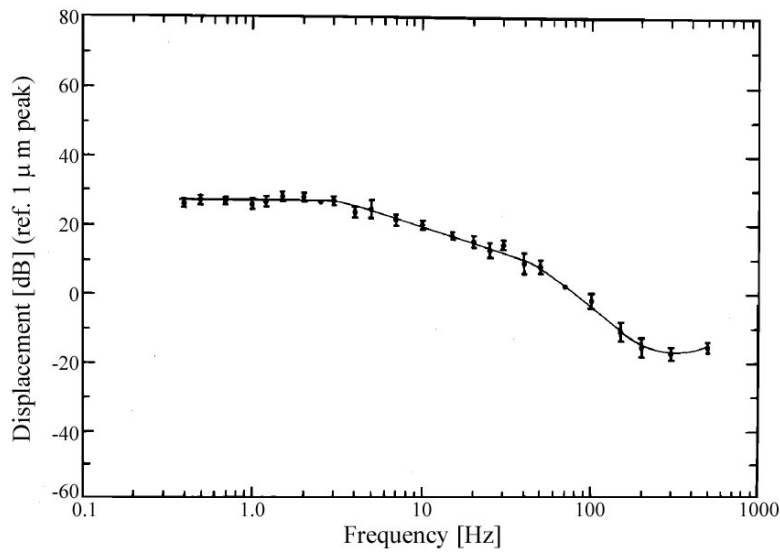


Figure 2.8 – Threshold-frequency characteristic obtained with a stimulus contactor of 2.9 cm<sup>2</sup> applied on the thenar eminence [28]

sensitivity which is frequently given at 250 Hz in literature (e.g. for both children and adults in [29]).

In addition, Verrillo [30] showed that the sensitivity level also depends on the size of the contactor. A decreasing sensitivity for areas smaller than ~3 cm<sup>2</sup> confirms the capacity of spatial (and temporal) summation of the Pacinian corpuscles [28]. We can thus retain that the sensitivity threshold is much higher for lower frequencies and that vibrotactile stimulations should be produced between 250-300 Hz with a contact area approaching 3 cm<sup>2</sup> for a maximum efficiency.

In order to be consistent with the previous subsections, Table 2.2 summarizes the frequency characteristics of the four tactile units by giving the specific frequency range related to each mechanoreceptor type. The table is completed by additional hints on the temperature sensitivity of each type.

Table 2.2 – Frequency characteristic and temperature sensitivity of the four tactile unit types

T. unit	Mechanoreceptor	Frequency	Shape vs. freq.	Temperature sensitivity
FA I	Meissner corpuscle	10-100 Hz	Flat	Not affected
FA II	Pacinian corpuscle	40-800 Hz	U-shape	Highly affected
SA I	Merkel cell	0.4-100 Hz	~FA I	Affected
SA II	Ruffini corpuscle, spindle	15-400 Hz	~FA II with lower sensitivity	Affected

Besides the previous frequency sensitivity analysis, Shimoga [31] summarizes the key bandwidths used by the human finger in dexterous telemanipulation (Figure 2.9 and Table 2.3).

## 2.2. Human hand physiology

It is interesting to note that the human finger cannot react to unexpected force/position events more than one or two times per second. As for the control, the human finger is slightly faster and can operate until 16 Hz for tasks like force and position control and adaptation of grasping force. Above, the human being is only able to feel displacements or forces acting on his own body. 320 Hz constitutes the upper limit, beyond which the human finger sensitivity to discriminate two consecutive force input signals starts declining.

This classification is helpful in a sense that it defines the two main sensitivities of touch: the so-called kinesthetic and tactile senses. At low frequency, a person is able to distinctly feel the forces applied on the fingers, knowing their position and react to them, contrarily to higher frequencies, at which the person just feels vibrations. The border between these categories is however quite vague and changes from one application to another.

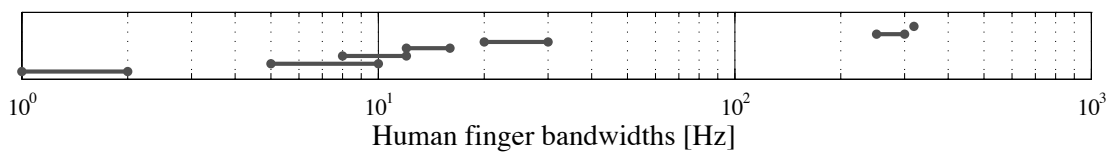


Figure 2.9 – The human finger uses different bandwidths depending on the task (See Table 2.3), adapted from [31]

Table 2.3 – Human finger bandwidths and corresponding functions, adapted from [31]

Bandwidth	Function of the human fingers
1-2 Hz	The maximum bandwidth with which the human fingers can react to unexpected force/position signals [32].
5-10 Hz	The maximum bandwidth with which the human fingers can apply force and motion commands comfortably [32].
8-12 Hz	The bandwidth beyond which the human fingers cannot correct for its positional disturbances
12-16 Hz	The bandwidth beyond which the human fingers cannot correct their grasping forces if the grasped object slips [33].
20-30 Hz	The maximum bandwidth with which the human fingers demand the force input signals to be presented for meaningful perception [32].
250-300 Hz	The bandwidth at which the skin has maximum sensitivity to vibrations [28, 30].
320 Hz	The bandwidth beyond which the human finger sensitivity to discriminate two consecutive force input signals declines [32].

This frequency analysis terminates the introduction on the human hand physiology and opens the way for their utilization in research and its applications.

### 2.3 State of the art

With a better comprehension of the human hand sensitive apparatus, we can now investigate the categories of touch introduced in section 2.1. Kinesthetic and cutaneous senses were largely discussed in the previous section and it comes naturally that applications related to these senses represent a paramount part of the present section. The role of haptic devices being often the enhancement of the user's experience and comfort, nociception becomes uninteresting and is left aside. Similarly, thermal sensitivity is only briefly discussed.

From the point of view of a haptic system, the major function consists in stimulating one or several tactile (or eventually thermal) units presented in section 2.2. Devices are thus required to generate mechanical stimuli; either a displacement, a force or a vibration, that activates the desired mechanoreceptors. Touch sensitivities are thus paired with their matching mechanical terms as follows: kinesthetic with force feedback, cutaneous with vibration or surface roughness and thermal with heat transfer. Before considering the numerous domains explored by the scientific community to develop new devices, it seems important to introduce the different roles of haptic devices and their implications in the daily life.

#### 2.3.1 Haptics: Roles and implications in the daily life

The growing interest given to the sense of touch enlarges the field of application almost every day. However, despite the numerous technologies, the main functions fulfilled by haptic devices can be reduced to four:

- In virtual reality (VR), the trend pushes towards software interfaces that create a universe which is to be closer and closer to reality. Haptic systems represent the link between this virtual world and reality (e.g. [32, 34, 35]). They try to give a physical consistency to virtual objects. Indeed, exciting a maximum number of senses, together with vision, increases the degree of immersion. Even if the sense of touch is slower than vision for certain features like shape, size and distance recognition, it is equivalent or better for textures perception [26]. It becomes even more important for the perception of forces, vibrations and temperature where sight is not useful at all. Compared to audition, despite a lower temporal resolution, the spatial resolution of touch is more precise [6]. Touch can thus be compared to other senses in terms of pros and cons, but finally represents an excellent complement to all of them.

VR goal is always to recreate specific environments using a computer. From video games to surgery simulation tools, the haptic feeling is more and more important. It becomes even vital when it comes to real-time surgery using telemanipulators where the surgeon has to feel what he is doing and what tissue he is cutting through (e.g. [36, 37]). Teleoperation, i.e. master-slave systems, is considered as the mother discipline of haptics [38]. Its position, either in the present or in the next sub-category, is not well defined. Indeed, teleoperation whose first role is to recreate forces sensed by the slave

end-effector [39], slowly transformed to a purely virtual simulation tool without physical slave, generally used for training [40]. Thus, data used to generate the force sensation comes either from analytical models (geometry, texture, viscosity) or from real-time measurements.

- The second domain of haptic applications attempts to reproduce mechanical feelings of devices that evolved and lost the physical feedback that used to be given to the user. Two simple examples to help the comprehension are the *click* of the computer mouse buttons and the vibration of the phone with touchscreen. In old computer mice, the contact of the buttons was made thanks to a buckling blade characterized by a specific noise and force feedback. As new switches do not do this *click* anymore, a mechanical element had to be added to recreate physical acknowledgement. Same for mobile phones with touchscreen, where the sensation of hitting a key is faked by a vibration as for physical response.

Moreover, in a close future with the end of the legislation imposing a mechanical link between the steering wheel and the wheels in cars, all the systems called "steer by wire" or "drive by wire" will come up (e.g. [41–43]). With that, and it is already the case in planes ("fly by wire" [44]), force feedback is necessary for the driver to keep a kinesthetic perception of the vehicle behavior. This category distinguishes itself by the fact that the visual perception is no more virtual, but well and truly real.

- The third category does not content itself with reproducing feelings known and experienced by the user. New sensations are created, improving the user's comfort. Applications such as massage armchairs and other vibrating devices already exist but are limited in terms of function and flexibility. In this domain, possibilities are infinite, similarly to the human imagination, but the chances of an application to succeed reside in its acceptance by eventual users. Indeed, as most devices falling in the present category are new to people, their effect on touch sensation is unknown. A learning phase is thereby required in order to take advantage of the novelty. Inevitably, this last category requires research on human physiology so as to better understand and fit his needs.
- The last category gathers devices designed for rehabilitation together. Recover from a fracture, a broken bone or a ligament tear can be long and painful for the patient. Unfortunately, the struggle continues after the removal of the cast or splint, when the muscle is atrophied and needs to be redeveloped. Haptic devices shorten recovery time by proposing an adaptable program, generally based on impedance control. Research is active in this domain going from applications for fingers [45, 46] to larger orthoses destined to hip and legs rehabilitation [47]. Another promising field of application is the stroke recovery. Indeed, when the issue is not only muscular but touches motion abilities, it becomes necessary to develop systems that stimulate more than just the kinesthetic apparel. Global VR environments are developed using visual interfaces (e.g. for finger [48, 49]) and even electrical stimulation (e.g. for lower limbs [50, 51]).

The above presentation of the four main roles aimed to be fulfilled by haptic devices does not exhibit well-defined borders between each other. The fact that an application, classified in one category, possesses characteristics of other categories shows the possibility for a technology to be used for different aims. For this reason, the following subsections propose a state of the art of the research on haptic systems for hands and fingers sorted regarding the sensitivity they stimulate. Works are so numerous and cover so many various domains that this non-exhaustive list only pretends to give an overview of the research activities.

### 2.3.2 Kinesthetic sensitivity and force feedback

Kinesthetics is the ability of the human being to sense the position of his body and limbs. For instance, it allows a person to know if his arms are stretched in front of him or simply laying along his hips. As this function is unconscious, it seems completely natural to us and is often underestimated. However, in his book, J. Cole follows the tracks of I. Waterman, a nineteen-year-old butcher who completely lost proprioception [52]. The latter explains how strange it can be to wake up and be terrified by the presence of a hand on his face, not realizing for a while that the hand belonged to him. Similarly, Mr. Waterman tends to use excessive force to grasp objects, easily breaking plastic cups. This last example shows that, in addition to position, forces acting on each and every joint of the body are monitored by mechanoreceptive units. Both position and force information are thus complementary and necessary to interact with force feedback devices.

Force feedback devices are precisely applications that affect the kinesthetic sense. As indicated by its name, force feedback provides a force in response to a displacement applied by the user. This "displacement in - force out" control is called impedance control (opposite to admittance control) [53].

The most accessible domain when talking about force feedback is probably gaming. Products like force feedback steering wheels and joysticks are already available on the market since years. They usually use low-cost DC or brushless DC motors coupled to the output with belts or gears (Figure 2.10 (a)). Encouraged by these successes, research is still active, notably in the development of new 1 or 2 degrees of freedom (DOF) actuators. The Laboratory of Integrated Actuators (LAI-EPFL) has developed a joystick with two electrodynamic actuators, each controlling one axis providing either a spring or viscous feeling to the user (Figure 2.10 (b)).

Classic computer peripherals like the mouse are also improved to provide an enhanced experience. The version of Kudo et al. [55] uses two DC motors each coupled to a differential mechanism in contact with the mouse ball (Figure 2.10 (c)). The omni-travelling system is able to counter displacements of the mouse with a force of 4.8 N for 2.5 W giving, by example, the impression of touching the screen limits. A similar effect is obtained by attaching an electromagnet under the mouse moving on a ferromagnetic pad [57].

Electromechanical systems are the most commonly used in force feedback applications.

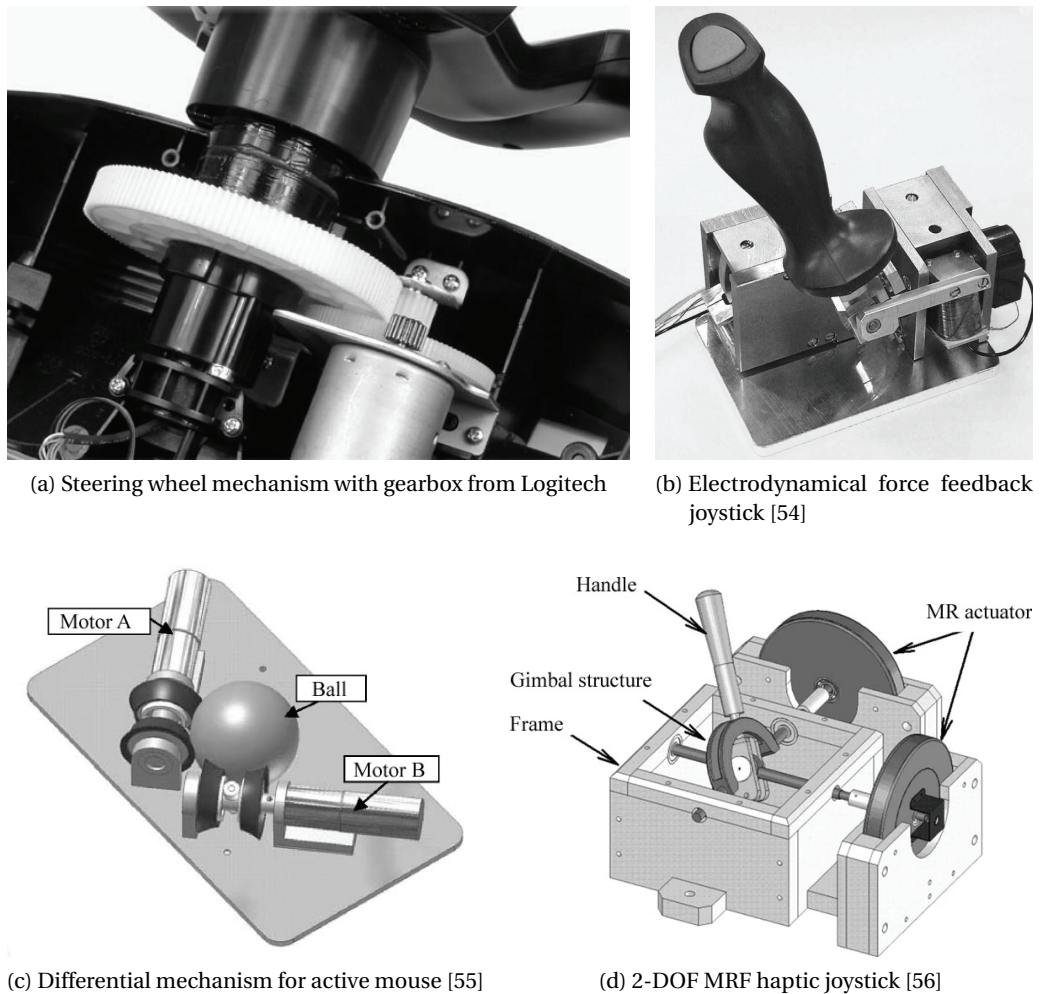


Figure 2.10 – Electromechanical force feedback peripherals

However, a growing interest in smart materials naturally led researchers to investigate new solutions for haptic devices. There are many kinds of smart materials like piezoelectric ceramics, electroactive polymers (EAPs), shape memory alloys (SMAs), electrorheological and magnetorheological fluids (ERFs and MRFs). Basically, all of them change their form or properties when subjected to heat, electrical or magnetic field. This section will however not explain all of them in detail and let the user go further in his research in related literature. Not all smart materials really match requirements for haptic applications, but ERFs and MRFs do. Their main characteristic is to change their rheological properties when subjected to an electric or magnetic field respectively. The fact that these fluids can quickly pass from a liquid to a very viscous state make them ideal candidates to build strong and compact brakes. Two prototypes of 2-DOF joysticks were developed using respectively electro and magnetorheological fluids (Figure 2.10 (d)) for vehicular instrument control and virtual reality [56, 58].

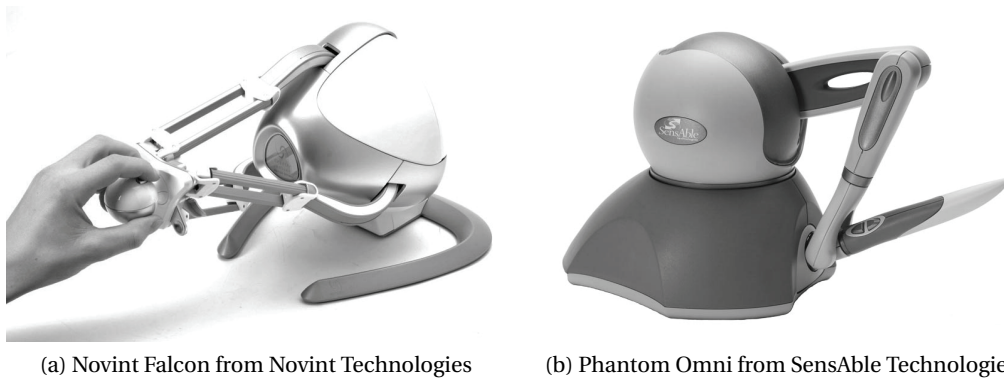


Figure 2.11 – Commercially available haptic displays

With the evolution of software, notably in graphics and computer-aided design, it became important to improve haptic devices and propose the so-called haptic displays. Their function is to generate a three-dimensional (3D) force feedback related to the information displayed on the screen. Rotations are often implemented as well giving 5 to 6 DOF to the end-effector [59]. The sensation of grasping a virtual object or exploring a surface can then be simulated [60, 61]. Developments led to the commercialization of two products: the Novint Falcon and the Phantom Omni (Figure 2.11). Similarly to gaming, the force feedback is generated by DC or brushless DC motors. A popular trend in the scientific community is to take advantage of existing hardware, characterize it and adapt it to fulfill different requirements. For instance the Novint Falcon is at first characterized for an application as a robot manipulator (impedance control [62]) and then turned into a tool to transmit a force to an immobilized fingertip (admittance control [63]).

Also used for the simulation of minimally invasive surgery [64], these haptic displays obviously evoke their predecessors, namely master-slave systems, mainly used in surgical teleoperations. Indeed both simulation and teleoperation domains require a high-fidelity haptic feedback, the main difference laying in the control. A lot of applications were thus developed for minimally invasive surgery like endoscopy, laparoscopy and tumor localization (Figure 2.12) [36, 37, 40, 65].

In parallel to computer peripherals were developed some applications for musicians. The aim is to give more attractiveness to digital instruments which deprive the user of the original touch while saving space. Cadoz et al. [66] first developed a modular feedback keyboard composed of a row of sliced motors, actually electrodynamical actuators providing peak forces up to 80 N (Figure 2.13). The keyboard first aim was musical creation, with each actuator corresponding to a piano key. Further studies used the device for real-time computer animation by coupling several keys together so as to have multi-DOFs end-effectors like joysticks and scissors [67].

In the same lines, a compact haptic music keyboard capable of providing three touch sensations namely piano, harpsichord and organ was designed at LAI-EPFL (Figure 2.14 (a)). Then,



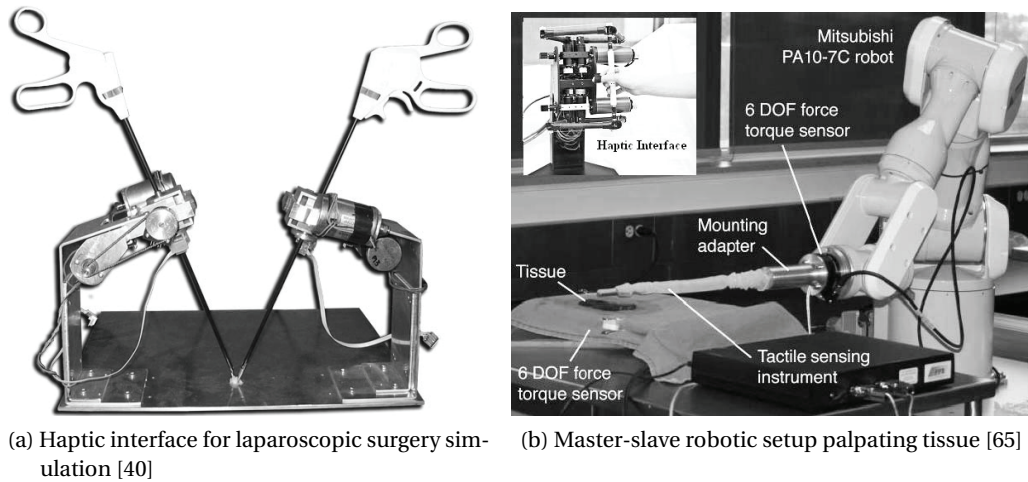


Figure 2.12 – Haptic systems used in minimally invasive surgery simulation or teleoperation

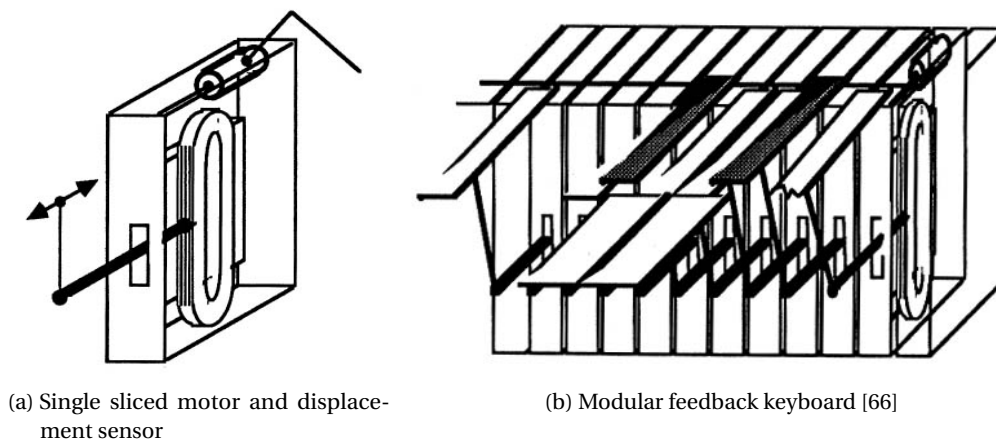


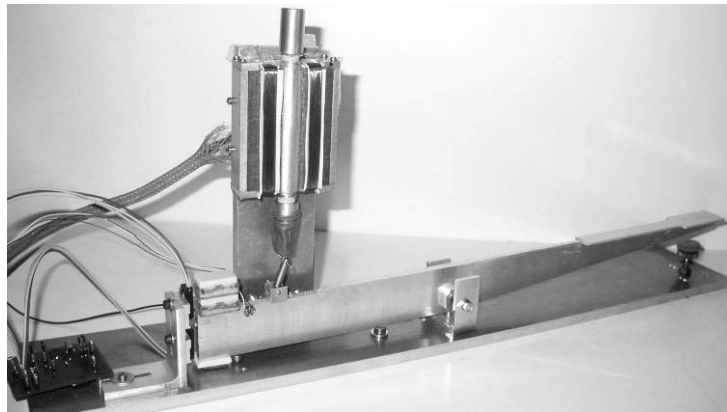
Figure 2.13 – Haptic music instruments

as for the joysticks, a magnetorheological version of the haptic piano key has been developed in France (Figure 2.14 (b)).

A recent study using electromagnetic linear motors, from the market this time, is called Inverse Piano [71]. It consists of 4 keys, controlled in position and force by actuators placed directly under the fingers. The Inverse Piano proposes to study fingers interactions in non-isometric pressing tasks. It is also claimed to be used as a rehabilitation device for patients suffering from a loss of dexterity and finger strength. As mentioned in the previous subsection, rehabilitation represents a promising field of application for haptics, particularly for the hand and fingers. The limit between rehabilitation and virtual reality in this domain is hard to be determined as most systems can be used both ways. A first category of rehabilitation devices is considered as not portable in a sense that the whole system is often very heavy and fastened to the ground. An example is the haptic interface for finger exercise embedding two brushed DC motors and



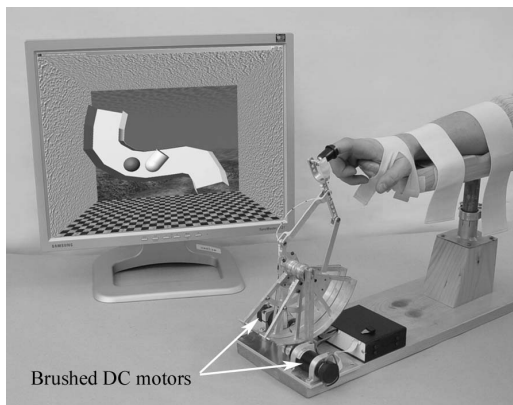
(a) Haptic music keyboard [68, 69]



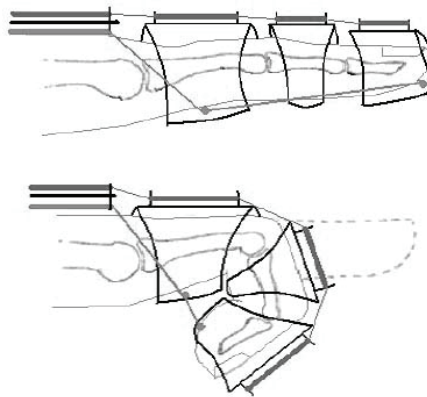
(b) Single MR piano key [70]

Figure 2.14 – Haptic music instruments

a tendon-driven transmission allowing the finger to move in a vertical plan (Figure 2.15 (a)). Forces reaching 10 N give consistency to the images displayed by the graphic user interface and help the patient to exercise [66].



(a) Haptic interface for finger exercise and graphic user interface [66]



(b) Design concept for wire-driven finger flexion and extension [46]

Figure 2.15 – Haptic systems for finger rehabilitation

The evolution towards compact and lightweight haptic systems for the fingers, generally using wire driven mechanisms (Figure 2.15 (b)) pushes towards fully or semi-portable devices [45, 46]. It results in the design of numerous haptic gloves embedding servo motors, pneumatic actuators or magnetorheological fluid brakes (linear or rotating) providing forces between 5 and 12 N to the fingers (Figure 2.16). The applications for such gloves go from rehabilitation [72] to virtual reality [73] via robot teaching [74] and master-slave systems [75]. Following this trend, we developed a haptic glove designed for three fingers (index, middle finger and

thumb) and integrating custom magnetorheological linear brakes [76] (Figure 2.17 (a)). The latest version of the actuator weighs 56 g and generates a force of 14.4 N for 1.5 W.

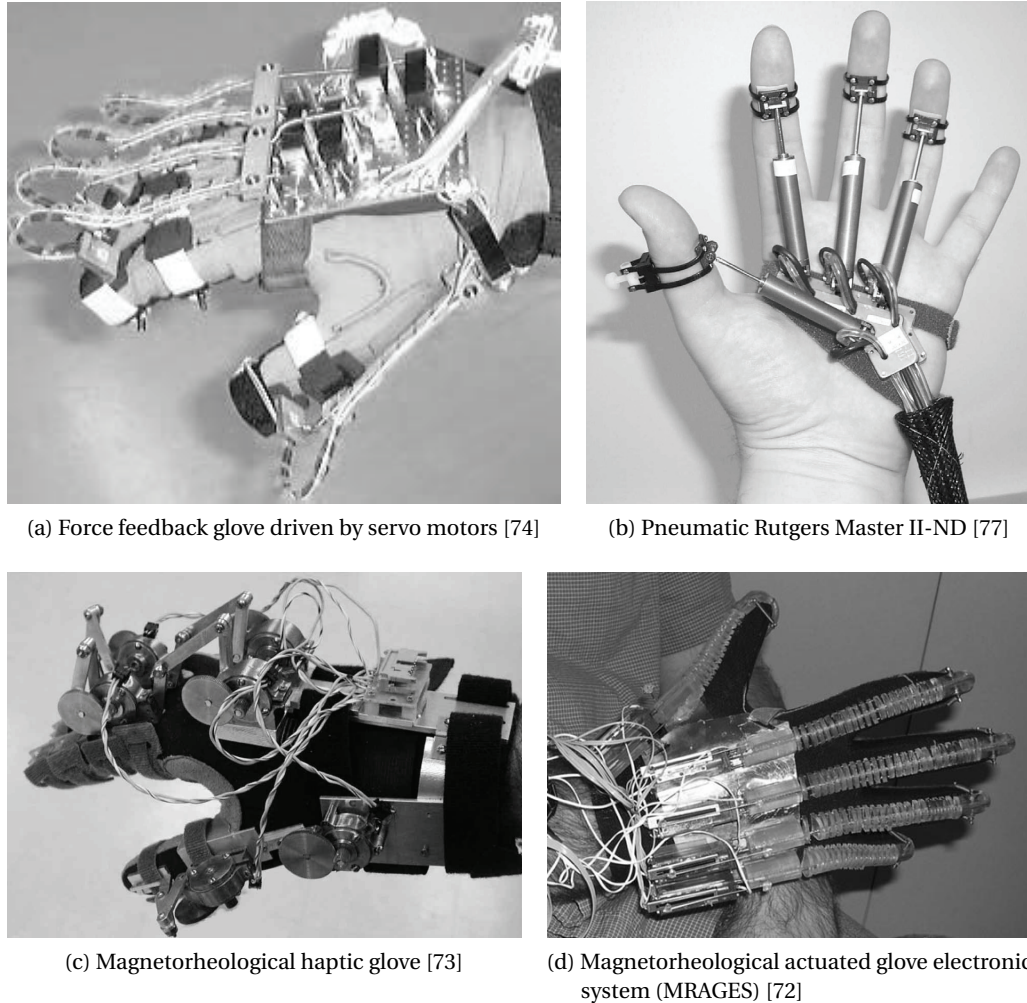


Figure 2.16 – Haptic gloves

The only commercialized force feedback glove, called CyberGrasp, is sold by Immersion (Figure 2.17 (b)). Despite excellent behavioral properties, its main disadvantage resides in the fact that the driving actuators are locked in a remote box weighting 20 kg.

### 2.3.3 Cutaneous sensitivity and vibrotactile stimulation

Section 2.2 presented the Pacinian corpuscles, end-organs of the FA II tactile units, as sensitive to high frequency vibrations. Their even distribution over the human hand as well as their large receptive fields make them ideal sensors for vibrotactile stimulation. Moreover, thanks to spatial and temporal integration [28, 78], vibrations do not have to be generated very precisely, allowing for multiple applications to be imagined.



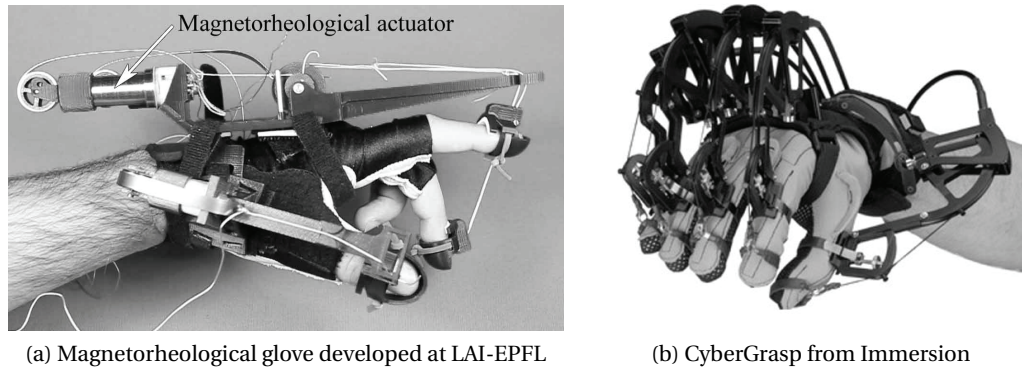


Figure 2.17 – Haptic gloves

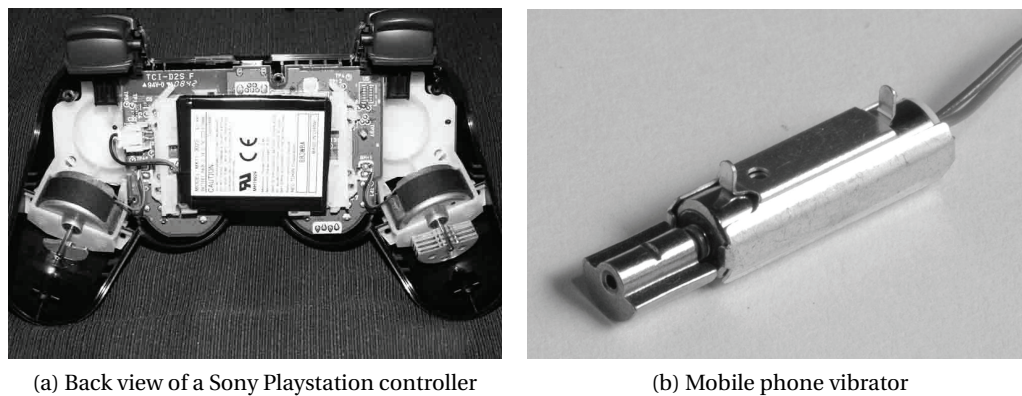


Figure 2.18 – Eccentric motor vibrators

Vibrations can be seen as information that enhances the touch feeling. Similarly to kinesthetics, gaming is one of the first domains to integrate vibrotactile feedback. Today, rare are the game controllers not to offer this kind of feedback to the user (Figure 2.18 (a)). As a mass production object, vibrators have to be cheap. The solution is to use a brushed DC motor coupled to an eccentric mass which rotation causes the vibration. The integration of this kind of vibrators in mobile phones largely contributed to their miniaturization (Figure 2.18 (b)). The emergence of the touchscreen in smart phones and tablets sometimes troubles the user as he is not able to physically feel the clicks. A tactile feedback is thus needed to replace the keys. From now on, vibrations are present everywhere and the user can feel when he is being shot by another player or when he is driving on the side of the road and he can get a click acknowledgement from his smart phone.

Besides the traditional eccentric motor, other technologies point the tip of their nose. For larger screens, Immersion developed a linear actuator capable of adding tactile feedback for screen diagonals up to 15 inches (Figure 2.19 (a) left). Piezoelectric ceramics also represent an interesting alternative as they are silent and generate high frequency vibrations when

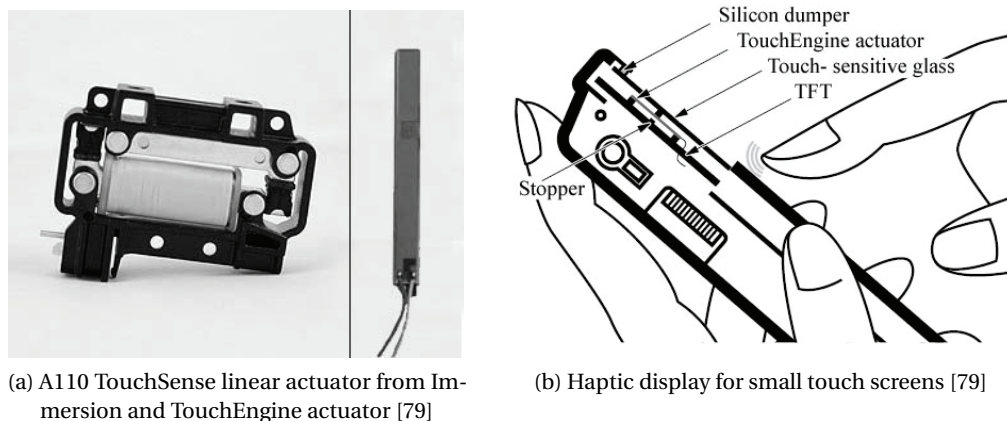


Figure 2.19 – Tactile touchscreens

subjected to an alternating voltage. The TouchEngine actuator is a multilayer sandwich of piezoceramic films that either shrink or expand depending on the polarity of the signal (Figure 2.19 (a) right). Once placed under a touch-sensitive glass, vibrations are transmitted to the user's finger (Figure 2.19 (b)). Using different modes of vibration, the user can feel snaps, crackles or pops depending on whether he opens, drags or drops a document [79, 80].

Vibrotactile feedback also finds applications in computer peripherals in order to enhance the user's experience. Hughes and Forrest [81] embedded small audio speakers on a conventional mouse to generate the vibrations. During an experiment, subjects were asked to pass the cursor over a map, whose color was representative of the altitude. The altitude data was translated into vibration magnitude in order to give a tactile feedback to the user. Finally, stereo vibration was implemented to allow for two-dimensional localization. Lindeman et al. [82] went further by developing wearable modules capable of handling up to 16 vibrators each. The aim is to improve the perception of contact with purely virtual objects in virtual environments by covering the user's body with eccentric motors.

In addition to their work on virtual contact, Lindeman et al. noticed that kinesthetic and tactile systems can be highly interdependent according to the task (Figure 2.20). Rincon-Gonzales et al. [83] corroborated this argument in their research in neuroprosthetics by showing through experiments that tactile and proprioceptive information is processed simultaneously and they concluded that both feedbacks should be provided together. It is notably the case in haptic search, where blinded subject are asked to discriminate the shape and orientation of objects placed in front of them [84]. One of the main differences between both sensory systems resides in the fact that cutaneous sensors are not affected by a decrease in size of the presented objects and show better performances than kinesthetics in this situation [85]. Following the idea of cross-influence, Akamatzsu et al. [86] improved the tactile mouse by embedding a solenoid driving a small pin and an electromagnet to simulate respectively tactile and force feedbacks which resulted in a reduction of targets selection and clicking times.

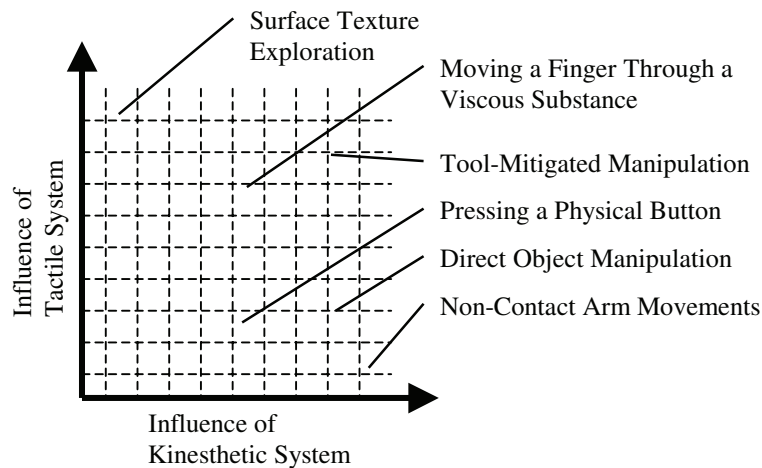
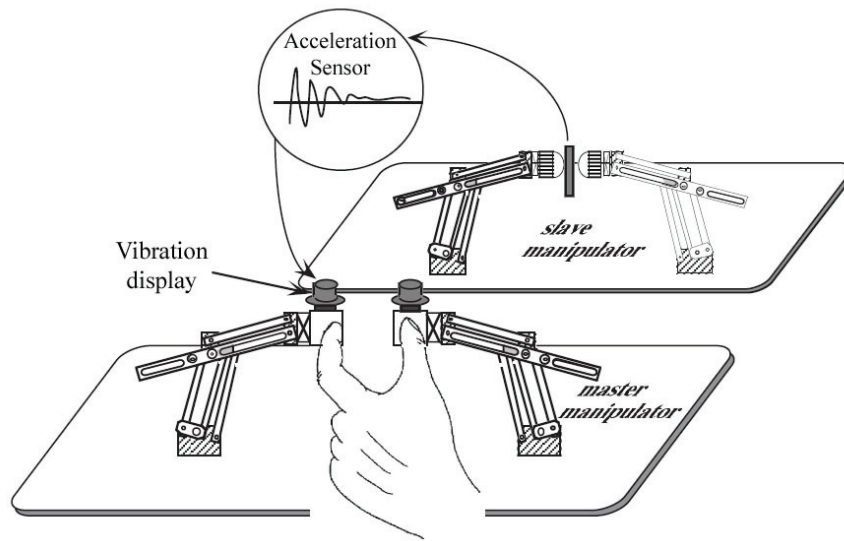


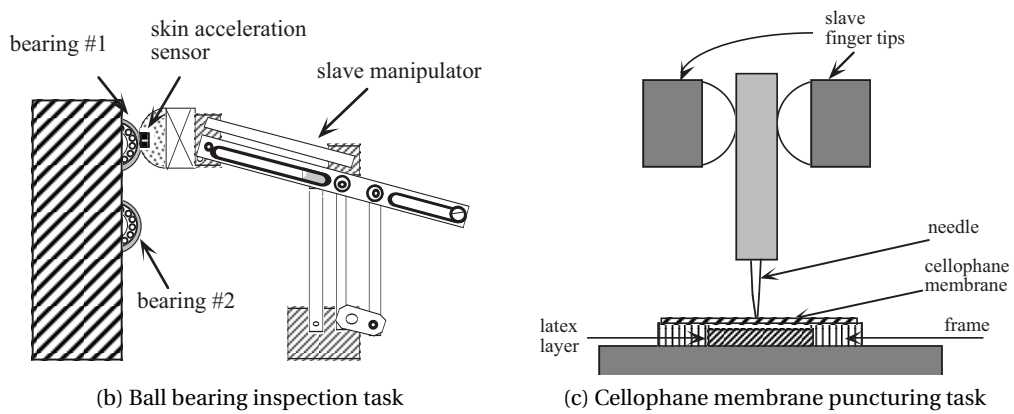
Figure 2.20 – Influence of tactile and kinesthetic systems in haptic tasks [82]

A second stage in the merging of kinesthetic and tactile feedbacks is obtained by upgrading force feedback devices with vibrotactile elements. For instance, miniature loudspeakers were mounted on a master-slave haptic display (Figure 2.21 (a)). Both master and remote slave manipulators are identical two-fingered hands with two degrees of freedom in each finger. Kontarinis and Howe [87] confirmed that the addition of vibrotactile information directly related to the acceleration measured on the slave manipulator plays an important role in manipulation. It however depends on the task. For example, it greatly helps when the user is asked to determine if a ball bearing is damaged or not by rubbing the finger on it (Figure 2.21 (b)). Force and reaction time used to pierce a cellophane membrane with a needle are also reduced (Figure 2.21 (c)). Vibrotactile feedback is finally useless in assembly tasks involving a precise control of contact forces (e.g. peg-in-hole insertion). In conclusion, vibrations are better in indicating transitions and represent a complement to force feedback.

The ultimate stage consists in developing devices directly capable of providing a feedback on the entire frequency range, from continuous to 300 Hz (maximum sensitivity to vibrations). With the aim of transmitting information through the fingers, Tan et al. [88] developed the Tactuator (principle in Figure 2.22), a multi-finger tactual display composed of three single-DOF actuators, driven by disk drive motors, stimulating the index, middle finger and the thumb. It is inspired from the Tadoma method, used by deaf and blind people, where the person perceives the mechanical actions associated with speech production by placing a hand on the face and neck of the person who speaks. The goal of the Tactuator is an artificial aid for communication of acoustic signals through the sense of touch. A frequency and amplitude analysis using the Tactuator concluded that low and high frequency signals do not interfere with each other, making thus information transmission through touch possible. However, the large discrimination thresholds prevent encoding more than a few speech features [89]. Israr et al. [90] finally managed to transmit up to sixteen consonant, discriminated by pairs with an average discriminability of 88 %.



(a) Two-fingered master-slave system with embedded vibrotactile feedback



(b) Ball bearing inspection task

(c) Cellophane membrane puncturing task

Figure 2.21 – Tactile display (kinesthetic and tactile feelings) [87]

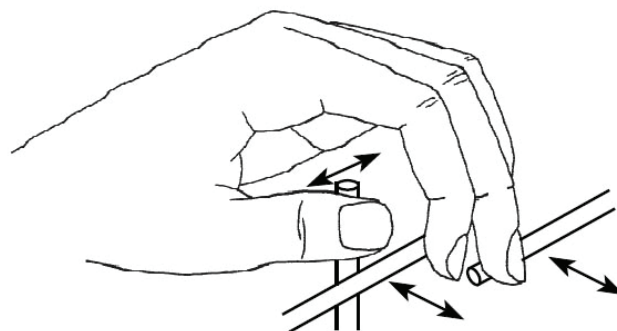


Figure 2.22 – Schematic drawing illustrating fingers placement on the Tactuator [88]

Finally, we would like to mention a domain of the cutaneous sensitivity which is barely

## Chapter 2. The sense of touch

---

represented in the present work, namely the tactile surface sensitivity. Indeed, numerous research and applications, not addressed in this work, are dedicated to simulate, sense and fake surface textures using actuated pins or artificial roughness [9, 91–94]. The tactile sensitivity however focuses here on the utilization of vibrations only.

### 2.3.4 Thermal sensitivity and heat transfer

Thanks to its thermoreceptors, the human hand can determine the apparent warmth or coolness of an object in contact with the skin within a range of 5° - 45° C [6]. Moreover, the human being possesses the ability to distinguish the nature of the touched surface. In fact, a single physical interaction governs the whole thermal sensitivity: the thermal diffusivity [95]. Indeed, as the skin temperature on the human hand is within 25° - 36° C and the ambient temperature is generally lower [96], the action of touching an object creates a temperature gradient leading the heat to diffuse towards the object. By monitoring the thermal time constant thanks to the thermoreceptors, it is possible to differentiate materials solely by their differences in thermal properties. Bergmann Tiest and Kappers [97] demonstrated that a difference of 43% in thermal diffusivity constitutes the minimum threshold necessary to discriminate between two materials based on thermal properties only. Wood and Plexiglas or glass and steel are thus distinguishable contrarily to aluminum and copper for instance.

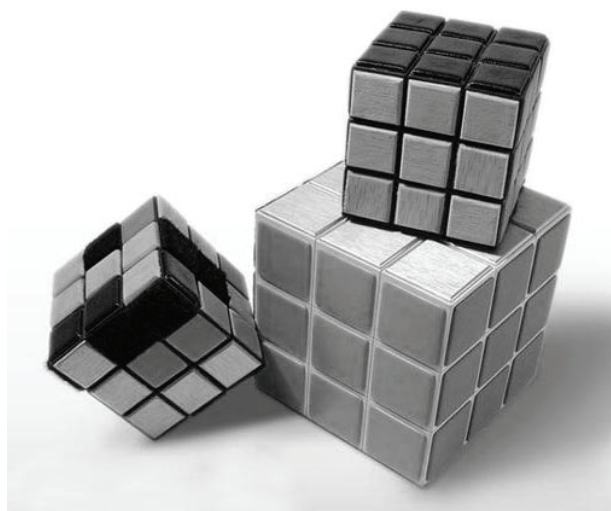


Figure 2.23 – Material Rubik Cube by Zhiliang Chen

Nowadays, thermal sensation is mostly related to comfort and is hardly used in haptics. Indeed, numerous are the applications like heated seats for automotive or heated pillows, but it is difficult to find applications dedicated to the sense of touch. We can nevertheless mention the Material Rubik Cube by Zhiliang Chen<sup>4</sup> in which the faces of the cube are covered with different materials (rubber, wood, metal, textile and plastic) designed for blind people (Figure

---

<sup>4</sup><http://www.coroflot.com/saliang999/if>



2.23). In this case, thermal sensitivity allows the user to distinguish one material from the other. Tactile sensitivity obviously plays a complementary role in the user's judgment.

Research involving thermal sensitivity together with the sense of touch is rare and as it does not fit the aim of the present work, investigations will not be furthered this way.

In conclusion, the state of the art presented in this section gives a general survey of existing applications developed in haptic systems used by hand. The domain is obviously extremely wide and it is not possible to cover it entirely in a few paragraphs. Interested readers are encouraged to further the search in literature if desired. However, it gives a good idea of on-going research and will help understand the context of the present work.

## 2.4 Motivations

The inevitable emergence of haptics represents a great opportunity to improve people's comfort. Within the framework of this thesis, two main channels are considered in order to provide a new touch experience to the peripherals user. On one hand, we aim to fight one of the silent plagues of the modern era which are the repetitive strain injuries. Indeed, as it will be developed below, repetitive tasks, notably involving computer peripherals, can provoke insidious diseases causing personal and economic issues. The first goal of the present research points toward solutions to potentially improve the situation. On the other hand, it comes out of the state of the art that the major part of the existing haptic applications is related to gaming and communication, the idea being often to integrate low-cost actuators providing either a force feedback or a vibration to the user. Indeed, people are fond of new sensations, new feelings, which opens the way for a multitude of new applications, either to communicate with the user, by example by marking a transition in the execution of an action, or to reproduce existing or made-up feelings. The field of application of haptic devices becomes thus as wide as imagination is.

In order to get a better comprehension of the need for haptic devices that enhance comfort, a brief description of repetitive strain injuries from a medical and statistical point of view is presented.

### 2.4.1 Repetitive strain injuries

Repetitive strain injuries (RSI) are injuries of the musculoskeletal and nervous systems affecting various structures like tendons, muscles, joints, nerves and vascular system. Also called cumulative trauma disorders (CTD) or repetitive motion disorders (RMD), they may be caused by repetitive tasks, forceful exertion, vibrations, mechanical compression or sustained and awkward positions [98, 99]. These disorders differ from workplace injuries in the sense that they develop gradually with time and effort. RSIs affect three main distinctive parts of the human body, namely lower limbs, back and upper limbs, computer peripherals affecting

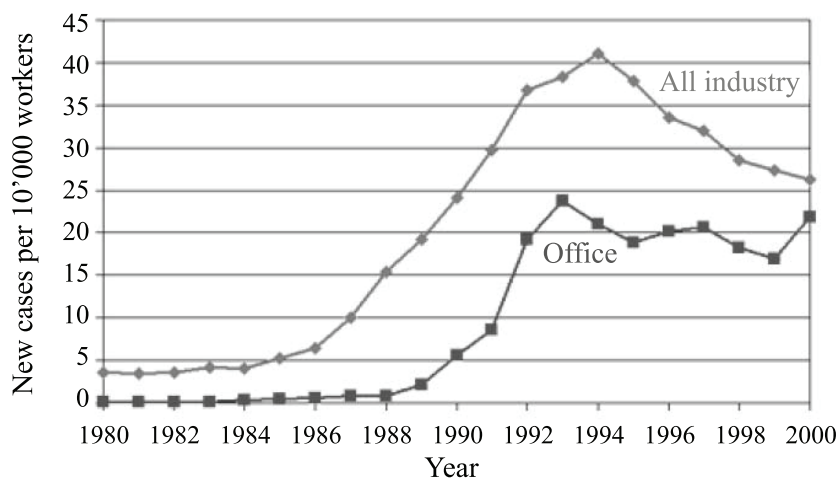


Figure 2.24 – Repetitive strain injuries trend in US businesses (adapted from [101])

principally the latter.

An example of peripheral responsible for the development of RSI is the computer keyboard. In 1974 already, researchers suspected the keyboard to be the source of disorders suffered by telegraphists [100]. The phenomenon affecting office workers, aka computer users, saw a dramatic rise in the early 1990's corresponding to a rapid growth of personal computer use, like shown by a study of the Bureau of Labor Statistics in U.S. businesses (Figure 2.24). The reason is that the keyboard constrains the user to adopt awkward postures and overcome unadapted keyswitch activation forces which reduces blood flow and restricts nerves and ligaments movements.

Resulting RSIs are numerous and include notably tendinitis, tenosynovitis, carpal tunnel syndrome (CTS) and bursitis [98, 102]. Most of them are or follow from a tendons inflammation. As treatment, doctors often prescribe rest so as to let the disorder resolve spontaneously. Massages, braces and anti-inflammatory medications can help accelerating healing, but RSIs tend to come back if no ergonomic adjustment of the working posture is undertaken.

### The British example

Recent studies performed at the UK Health and Safety Executive showed that in 2009/10, 198'000 people, working in the UK in the 12 months preceding the survey, had a musculoskeletal upper limb or neck disorder caused or made worse by work [103]. Obviously, only a part of these cases can be attributed to repetitive typing. Proper administrative and secretarial occupations represent 9.6% of the cases. However, this proportion can certainly be widened to domains like associate professional and technical (14.1%) and many others.

According to the Chartered Society of Physiotherapy and the UK Health and Safety Executive

[103, 104], an estimated 2.9 million working days were lost in the UK in 2010/11 with an average of 14.5 days per case. It represents a cost of ~£300 million<sup>5</sup> per year in lost working time, sick pay and administration attributed to musculoskeletal disorders mainly affecting upper limbs and neck.

**The American example**

Similarly a survey of the US Bureau of Labor Statistics [105] evaluated the number of nonfatal occupational injuries and illnesses involving days away from work in the private industry of all United States in 2008. 30'920 cases are attributed to repetitive motion and 4'670 to typing or keyentry activities, representing together more than 3% of the injuries and illnesses in the whole private industry. The nature of the illness or injury as well as the proportion affecting upper extremities for both activities are summarized in Table 2.4.

Table 2.4 – Distribution of selected cases of injuries and illnesses involving days away from work according to the activity, nature of injury and part of the body affected. Data from [105]

Activity	Carpal tunnel	Tendonitis	Soreness	Upper extremities affected
Repetitive motion	32.5%	5.6%	15.7%	66.7%
Typing or keyentry	57.2%	4.3%	11.6%	90.4%

The number of people affected by RSI is often underestimated, especially because these diseases are neither popular in the medical world due to a lack of treatments, nor in today's society because not considered as something serious. However, both examples presented previously, representing solely the tip of the iceberg, show the extent of the phenomenon and the necessity of preventing it. Solutions to prevent RSI are, on the one hand, to adopt a correct posture during repetitive tasks like typing. Numerous studies, brochures and websites propose advices to adjust chair level and joints angle to decrease body strains. On the other hand, research is pushing towards hardware improvements and introduction of haptics.

**2.4.2 Gaming and virtual reality: a new touch experience**

The second main target aimed to be reached is to propose new touch experiences in various domains going from gaming to virtual reality. Consumers are more and more demanding for new technologies as long as they can satisfy their curiosity. Feeling new feedbacks and tuning them following our wishes can be made possible thanks to the design of new haptic devices. Contrarily to robotics where the trend is to build always more complex systems, the sense of touch is already able to experience new sensations with simple actuators with only one degree of freedom. This simplification also goes with realities of the mass market in which it is inconceivable to propose ultra-sophisticated devices reaching unacceptable prices. Indeed, despite niche markets like medical and research, the main obstacle to the democratization of

<sup>5</sup>Data interpolated from 2007/08 data.

haptic devices stays the ratio between the added value that they bring and their price. The idea is thus to propose a methodology to design various compact actuators characterized by a high modularity and flexibility. Reactivity becomes a real advantage compared to sophisticated systems, allowing for quick adaptations to the customer needs.

Gamers, for example, are fond of all kinds of peripherals that offer the possibility to be tuned in accordance with their own preferences. Proposing a device capable of adapting its force feedback and sensitivity would thus appear as appealing. Similarly, it could be interesting for computer users to get a feedback from their keyboard enriching the man-machine interaction; either by transmitting extra information through the sense of touch, for instance by blocking a key that does not have to be pressed, or by adapting the keyswitch activation force depending on the finger force. It is also valid for all kinds of media control (video, sound editing, etc...) [106]. More largely, one can imagine knobs and buttons that imitate physical sensations like buckling, roughness or viscosity. Resulting applications would be likely to enter the domain of virtual reality and more indirectly psychology, especially in cognitive studies where a lot still is to be discovered on interactions between the sense of touch and the brain in general. And why not imagining to link touch sensations to emotions similarly to emoticons (☺ ☹) in online chats?

Actuators could finally help learning about human preferences in terms of touch. The automotive industry, for example, places importance on the tactile feedback of all switches and latches within a vehicle and always looks towards improvements. One option is, as mentioned above, to directly integrate haptic devices mimicking desired feedback (example of a haptic knob for instruments control [107]). An indirect approach would be to use the same haptic system, define the most comfortable force profile thanks to experiments on a sample of population and then reproduce the obtained force profile with a purely mechanical system. An advantage of this method is a lowering of the production costs. Another is that the haptic devices are used to study the human hand physiology which can eventually result in lumped models of the motor apparatus [108].

## 2.5 Summary

Different aspects of the sense of touch are approached in this chapter which is a global state of the art of existing haptic technologies specifically dedicated to the human hand and fingers. After a brief definition of the sense of touch, the physiology of the human hand is detailed in order to get a better comprehension of the sophisticated tool that it represents. Understanding the behavior of the sensory part of the hand is necessary to design effective haptic interfaces. That is the reason why the four kinds of tactile unit innervating the hand are presented, namely FA I, FA II, SA I and SA II. Each of them is characterized by a specific end-organ, called mechanoreceptor, allowing a person to sense the surrounding environment as well as his own position and the position of his limbs. The tactile units, either fast or slow and with large or small receptive fields, provide information to the central nervous system which

monitors the different signals and provides an intelligible message to the motory apparatus. These sensors monitor all kinds of mechanical data including small skin indentations, high frequency vibrations, discrimination of shapes and force-position information of the skin, joints and muscles and translate them into trains of electrical impulses travelling through the nerves. Then, the distribution of tactile units within the hand is exposed. Finally, spatial and temporal resolutions are described, terminating the introduction on the fantastic system that is the human hand.

The proper state of the art starts with the enumeration of the four main roles of haptics. The first function, highly related to virtual reality, proposes to increase the degree of reality by giving a physical consistency to virtual objects. Secondly, some systems reproduce mechanical feelings that used to be provided by old-fashioned devices in order to help the user to face his reticence to new touch technologies (e.g. touchscreens, drive-by-wire). Then, haptics goes one step further by providing new sensations to the user. The fact of materializing sensations not yet known by the user can improve his comfort if well accepted. Finally, rehabilitation in case of accident or stroke represents a promising field of application for force feedback. However, as the limit between the different roles of haptics is not well defined depending on the application, it is decided to classify existing research examples regarding the sensitivity they stimulate.

The sense of touch is composed of four sub-categories named sensitivities. The kinesthetic sensitivity monitors the position of the limbs and the force acting on them. The cutaneous sensitivity is more closely related to the skin. It is capable of fine spatial discrimination and is especially sensitive to high frequency vibrations. The two last sensitivities, namely thermal and nociceptive, are only briefly outlined. The former can determine the apparent temperature of an object and also helps discriminating its material using thermal diffusion. The latter responds to pain and plays the role of an alarm triggering safety reflexes.

Force feedback systems are known to excite the kinesthetic sense. Gaming is a popular domain with applications like force feedback joysticks and steering wheels. Then, with the requirements of virtual reality to work in a three-dimensional environment, appear the haptic displays; a sort of robotic arm rendering force feedback on three to six degrees of freedom. Similarly, a lot of professional master-slave systems were developed. Initially used in teleoperation, these devices are more and more used for simulations in the domains of surgery and mechanical assembly. Force feedback systems also find their utility in music (digital keyboard) and rehabilitation. Rehabilitation is composed of two sub-categories, whether the system is portable or not. Portable systems naturally take the shape of haptic gloves, well represented in the current research and used either in rehabilitation or in virtual reality.

The cutaneous sensitivity is here strongly related to vibrotactile stimulation. As for kinesthetics, gaming represents a large part of the applications. Indeed, many remote controllers provide vibrations to the user enhancing his immersion in the game. In the same lines, the absence of tactile feedback in mobile phones and tablets with touchscreens pushed towards the

## Chapter 2. The sense of touch

---

development of various kinds of vibrators so as to fake mechanical feelings. Different studies concluded that a haptic feedback provides better results when both kinesthetic and cutaneous senses are stimulated simultaneously. It is either the case by adding acceleration-related vibrations to a force feedback system or by designing devices capable of covering the entire frequency range, for example to transmit information through the fingers.

Finally, motivations for the development of a methodology to design compact actuators and corresponding haptic systems are exposed. Generally looking towards an improvement of the user's comfort, force feedback devices are aimed to decrease repetitive strain injuries. Indeed, repetitive tasks, notably involving computer peripherals, can provoke insidious diseases causing personal and economic issues. We thus aim to design new actuators to be embedded in peripherals allowing the user to adapt the force feedback following his preferences and needs with the hope of decreasing musculoskeletal disorders. Two statistics made in the United Kingdom and United States show the extent of the problem touching particularly office workers.

Beside the ergonomic aspect, new touch experiences are aimed to be provided. In virtual reality and gaming, people are always looking for new sensations to enhance their immersion in the digital world. Attempts have already been made to give consistency to objects or actions for example in media control. The goal is to match a tactile feeling with an object or an action either by mimicking or making-up a force feedback. Multi-finger haptic devices embedding short-stroke linear actuators go this way and propose a fully adaptable force feedback that possesses the ability to fit either the user preferences or the application requirements. On the other hand, these systems represent an excellent opportunity for researchers to learn about the human hand physiology, behavior and preferences, notably useful for the design of innovative products.



**Contents**

---

<b>3.1 Key elements . . . . .</b>	<b>36</b>
<b>3.2 Actuator . . . . .</b>	<b>37</b>
<b>3.3 Sensor . . . . .</b>	<b>40</b>
<b>3.4 Control . . . . .</b>	<b>41</b>
<b>3.5 Communication . . . . .</b>	<b>42</b>
<b>3.6 Software user interface . . . . .</b>	<b>43</b>

---

As indicated by its name, a multi-finger haptic device represents a subcategory of haptic devices that aims to provide an active interface for two to ten fingers depending on the application. Force or tactile feedbacks are generated in response to actions of the user which can be a displacement, a force or simply a contact. As introduced in subsection 2.3.1, the final role of multi-finger haptic devices is to enhance the human touch experience. It can be achieved by simply imitating and improving existing feelings (e.g. a haptic keyboard) or by creating new sensations inspired from nature and mechanics (e.g. programmable buttons) or even by transmitting information to the human finger through touch (e.g. physical acknowledgement of a vibrotactile surface).

### 3.1 Key elements

The general configuration encountered by multi-finger haptic devices can be summarized as in Figure 3.1. From the five main components presented, the first three namely actuation, sensing and control are inevitably present in all devices. Then, as multi-finger devices often take the form of peripherals, they need to be connected to a master unit and communicate with it. Finally, when connected to a computer, the need for a graphic user interface is generally demanded, either to offer the possibility to the user to adapt the touch sensation to his wishes or simply to provide a visual feedback to the finger actions. It should be noted that the function of visual feedback usually precedes the touch feedback and the latter is used as complementary information.

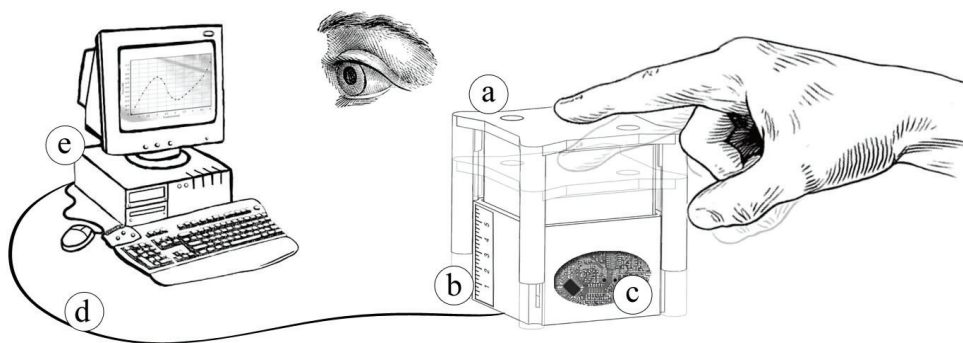


Figure 3.1 – General configuration of a haptic system for multi-finger applications with its main components: a) actuator/motor, b) sensor, c) control electronics and software, d) communication and e) software user interface

Different kinds of haptic devices can be labeled as multi-finger as long as they can interact with at least two fingers. However, in some cases, devices integrating multiple actuators can be handled with either one or several fingers depending on the application and the user's preferences. These devices will thus be considered as multi-finger as well in this work as they allow for a possible interaction with several fingers. A classification is here proposed regarding the relation between finger and actuator. According to its relative position, the actuator can indeed be defined as finger-related or not. A finger-related device is generally portable in a sense that each actuator is dedicated to a single finger, the most representative example being the haptic glove like those presented in Figures 2.16 and 2.17. In that case, a constant control of all actuators is necessary.

On the other hand, some applications integrate several actuators that are not necessarily linked to a single finger. It is notably the case of computer keyboards and other tactile pads where each finger can randomly press on several keys. The actuators, usually more numerous than the number of involved fingers, are fixed on a board independent from the user's hand. A variable control, switching between a standby mode waiting for an action of the user and an active mode, thus has to be implemented for each actuator. The following chapters of the



work precisely focus on the second category and expose a global methodology for the design of such kind of devices.

The need for this kind of multi-finger applications is motivated by the fact that the human being is more and more surrounded by electronic devices such as computers, tablets, video on demand and game consoles, aimed to improve his daily life. The need for the user to feel immersed in a virtual environment increases. A representative example is the success encountered by the new generation of game consoles like the Wii from Nintendo and the Kinect from Microsoft. The user is always demanding for more reality in what he feels. The present work thus proposes to broaden his experience by integrating the dimension of touch in the peripherals. Novel haptic buttons indeed allow improving the comfort of the user and transmitting a new kind of information through his fingers.

With that in mind, the sections of the present chapter introduce the different elements composing the universal multi-finger device presented in Figure 3.1. For each of them, a global definition is proposed and the direction followed in the thesis is outlined.

### 3.2 Actuator

The actuation block is directly responsible for the creation of the touch sensation. Two kinds of feedbacks are considered for multi-finger haptic boards, namely force and vibrotactile, respectively reacting to a displacement or a contact with the finger. Generally obtained from rotating DC and brushless DC motors as shown in the state of the art of section 2.3, the trend followed in the present thesis is to design specific miniature linear actuators to generate either a force or a vibration depending on the final application requirements.

The first crucial decision in the development of a haptic device is the choice of the actuating system. The fact that a multi-finger device possibly embeds a multitude of actuators influences their specifications. Indeed, for questions of cost and ease of assembly, the preferred geometry has to be clean, limiting the number of mechanical parts and manufacturing operations. Considering the limited space generally at disposal for each actuator, it has to be compact with a sufficient force density. Table 3.1 presents a general qualitative comparison of technologies available in today's actuators. This comparison results from several research works of Hollerbach et al. [109], Madden et al. [110] and McBean and Breazeal [111]. Most of the technologies listed are however not able to fulfill the requirements. Each of the proposed solution is briefly analyzed and rejected if not suitable.

For practical reasons, hydraulic and pneumatic solutions are left aside because of their need for a compressor. Despite satisfying force and response time, it would not be realizable to have a compressor annexed to each device [111].

As mentioned earlier, many haptic products are driven by rotating motors coupled to the load with belts or gears. Building a complete system with reduction plus rotary to linear

transformation is inappropriate for such confined dimensions. In order to save space and avoid useless mechanical complexity, conventional motors are not kept as potential winners.

Further on is a group of emerging smart materials. Some of them, like electroactive polymers [112] and shape memory alloys (SMA) are very interesting despite short displacements, but are unfortunately too slow to provide a meaningful feedback to the user. Indeed, a relaxing time of the order of magnitude of the second for SMA [113] is not adapted to match with the human hand sensitivity characteristics (Table 2.3). For example, the downstroke average time during normal typing operations (keyswitch compression) approaches ten milliseconds [114]. Electro and magnetorheological fluids could be suitable and represent a great challenge in terms of miniaturization and sealing. Nevertheless, high voltages required by electrorheological fluids [115] represent a major safety issue for desktop applications and will therefore not be considered. Magnetorheological fluids could be convenient for one or a few keys, but as mechanical tolerances and assembly represent a big challenge to avoid fluid leakage without adding a significant friction [76], it is not feasible to consider such a solution for multi-finger haptic devices without spending most of the time in fine tuning. However, magnetorheological fluids can still be an interesting technology for haptic devices considering their high force density.

Piezoelectric actuators present the advantage of having a strong holding force when not powered. This advantage becomes a drawback in the present case because the key would have to be driven down and then up, following the finger stroke making the control and electronics more expensive and bulky. In addition, the low speeds usually reached by these actuators definitely eliminate this solution [110].

Finally, electromechanical actuators are considered [116]. The best trade-off between high force density, low reluctant force and easy control is obtained with electrodynamic actuators (i.e. voice coils). Moreover, the low inertia of the moving coil allows for a better dynamic response. On the other hand, electromagnetic actuators are similar to electrodynamic actuators but have the coil at the stator and the mover contains the magnet. Fortunately, the increase in inertia is limited when considering miniature actuators and reasonably influences the dynamics. In conclusion, electrodynamic and electromagnetic systems represent the best option to succeed in the task of providing a fast, adaptable and strong enough feedback to the user within the pre-defined space. Chapter 4 will thus be entirely dedicated to their design and optimization.

Table 3.1 – Qualitative comparison of existing actuating principles

Actuator	Force	Response time	Power	Applications
Electrodynamic	$F=f(I)$ prop. to current	up to 25 kHz over 20 G of acceleration	Good efficiency	Voice coils, linear motors, 2-way actuators
Electromagnetic	$F=f(I)+F_R$ (reluctant forces)	Slower than electrodynamic due to magnet inertia	High efficiency	Linear motors, sensors
Hybrid (polarized reluctant)	$F=f(I)+g(I^2)+F_R$ (High force density)	Slower than electrodynamic due to iron inertia	High efficiency	Percussion hammer, electro-magnets
Variable reluctance	$F=f(I^2)$ (Low force density)	Slower than electrodynamic due to iron inertia (moving part)	Low efficiency	Electro-magnets, valves
Piezoelectric	High off-state forces	Up to 1 m/s (typ. 0.05 m/s)	High voltage for great forces	Linear motors, bimorphs, sensors, cutting tools
Shape memory alloys (SMA)	$F=f(T^*)$ short displacements	Relaxing time $\approx 1s$	High current densities	SMA wires, glasses frames, robot muscles
Magnetorheological fluids (MRF)	50-100 kPa	Milliseconds	2-24 V 1-2 A	Pistons, seismic and railcar dampers, valves
Electrorheological fluids (ERF)	2-5 kPa (130 for GER)	Milliseconds	High voltages (1 kV/mm, 1-10 mA)	Hydraulic valves, brakes, tactile displays
Electroactive polymers (EAP)	Very low forces, short displacements	Slow	High voltage, low current (dielectric) or inversely (ionic)	Lens positioners, artificial muscles
Rotating motors	Rotating motors are bulky for miniature applications and the conversion in a linear displacement even more			
Pneumatic/ Hydraulic	Great forces and good response time, however these systems require a compressor			

### 3.3 Sensor

Basically, a haptic interface is supposed to react to a specific action of the user. For that, an input, which can be a force, a displacement or simply a contact, is required from the user and needs to be detected so as to trigger a physical response. Among the three possible inputs, the present work concentrates on the position detection which is indispensable for an accurate control of the touch sensation when using linear actuators. The general requirements for the design of position sensors for multi-finger haptic devices are outlined hereinafter.

The detection of the position is essential in force feedback mechanisms if one wants to accurately respond to displacements of the user's finger. In the case of miniature systems, it becomes necessary for the sensor to be integrable without affecting the behavior or the geometry of the mechanical unit. Numerous types of sensors are capable of detecting the position of a mover; however, most of them are not adapted for small haptic systems for the following reasons:

- Firstly, as the forces in play are relatively small, all position sensors involving a contact should be prohibited to avoid affecting the human finger sensitivity. Parasitic forces have to be reduced to the minimum to guarantee a realistic and sharp feeling to the user.
- Compared to vision, a fluid haptic feedback requires a much higher update rate. A frequency of 1 kHz is often mentioned so as to guarantee a good illusion [38]. Knowing that, position sensors have to be fast, moreover for multi-finger applications where several actuators may have to be driven simultaneously and still fit above 1 kHz.
- Actuators and motors responsible for the force feedback are often aimed to be integrated in complex devices leading to very narrow available spaces. In this case, the geometry of the electromechanical part is optimized to fit within a certain volume and so, integrating bulky sensors becomes very tricky. A smart approach is to take advantage of intrinsic variables already present within or around the system. Position can, for example, follow from a measurement of voltage, current or magnetic flux to reduce the volume required by the sensor.
- The cost of the sensor also needs to be considered. Indeed, multi-finger applications by definition integrate multiple actuators requiring as many position sensors. In addition, these devices are aimed to target a large public and thus cannot afford to embed expensive measurement systems. The global sensing part including the sensor itself and its signal processing thus needs to be designed with an eye to decreasing hardware and software complexity.

In summary, the requirements for the choice of a position sensor are to be fast, small, low-cost and contactless. Knowing that, solutions using existing sensors as well as novel methods involving self-sensing are exposed in chapter 5.

### 3.4 Control

The integration of actuators and sensors represents an important step in the process of the development of a haptic system. They would however be useless without an efficient control managing them. Indeed, the feeling provided to the user directly depends on the way the actuator is driven. Multi-finger haptic devices, as presented in this thesis, represent a special category of haptic devices characterized by their own requirements. Indeed, the great number of actuators or vibrators embedded necessitates a redefinition of the global specifications. Contrarily to robotics and its always growing complexity, the trend pushes towards a simplification of the control hardware in order to offer a greater scalability without rocketing the final bulk and cost. In order to efficiently distribute computational and electrical resources, everything must be smartly fined down, from the single actuator to drive the entire multi-finger system. The focus is here put on the control hardware. Recommendations are given so as to guide the designer towards a simplification of the electronics and an improvement of its performance relatively to the tasks to be fulfilled. As an illustration, the example of a haptic keyboard embedding numerous linear actuators is analyzed.

First, the control principle of a single actuator is presented in Figure 3.2. Before designing the control circuit of a subsystem, it is necessary to think in terms of functions and keep only those that are required by the application. In the case of a haptic key, the actuator is aimed to counter the force produced by a human finger. The term impedance control is generally used to describe the creation of a force in response to a displacement [53]. As the user pushes downwards, the force feedback acts against it, in one direction. A single transistor circuit driven by only one pulse width modulation signal (PWM) is thus sufficient. The potential number of actuators controlled by one DSP is thus increased compared to the case of a bidirectional H-bridge drive with four transistors. Ideally in such a case, the closed-loop control should require only one output for the control instruction and one input for the measurement of the position.

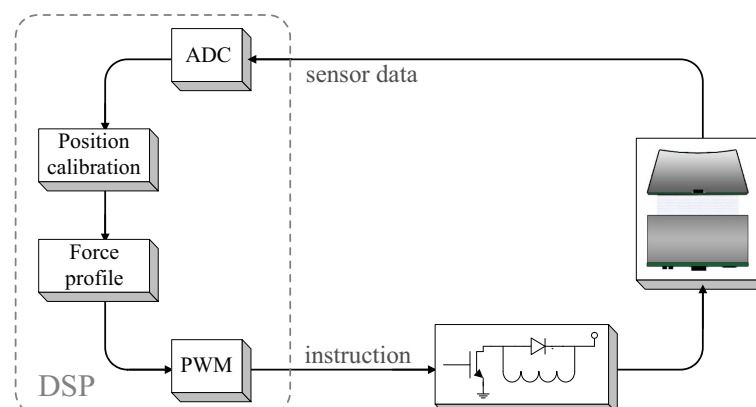


Figure 3.2 – Control principle of a single key

Then, once placed in an array, the independent control of each actuator represents a real challenge due to their number. The example of the computer keyboard containing up to hundred keys is very representative and facilitates the understanding. Indeed, rare are the applications where more subsystems have to be controlled simultaneously. Microcontrollers with as many available pins (ADC conversion and PWM outputs) do not exist up to now<sup>1</sup>. An interesting strategy consists in putting multiple microcontrollers in parallel, each of them controlling a subgroup of keys (Figure 3.3). This solution represents a trade-off between an expensive configuration where each actuator is controlled by a single dedicated microcontroller and the hypothetical version in which a single microcontroller drives all keys simultaneously.

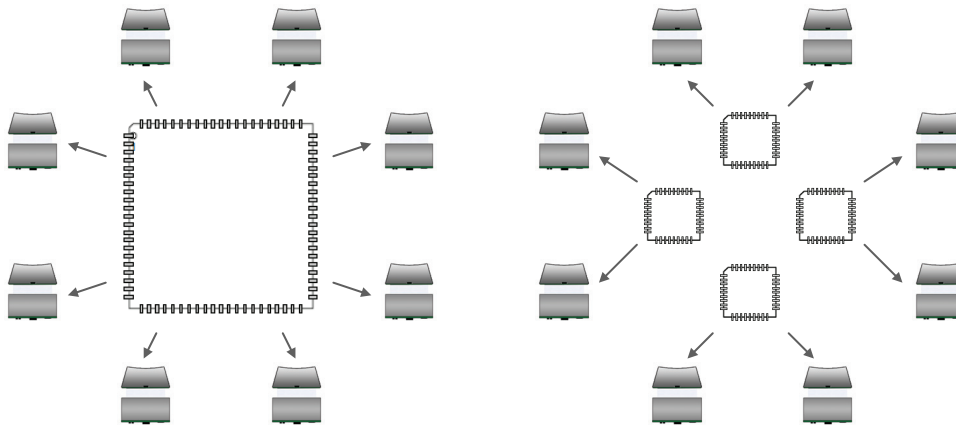


Figure 3.3 – Single and multi-DSP control principles

In conclusion, the key word when designing an electronic drive for multi-finger haptic systems is simplicity. As control does not represent a central part of the present work, the brief analysis stops here and we leave it to the reader to further it in accordance to his needs. Likewise, the proper software part including controllers is not addressed here. Complements are however given in chapter 6, dedicated to the applications.

### 3.5 Communication

The number and variety of peripherals requiring a communication with a central console, generally a computer, do not stop increasing with the advances in technology and multi-finger devices are not an exception to the rule. Most of the time, the data flow is unidirectional and informs the computer about the state of the device itself (position, temperature, etc. . .) or its environment. It is notably the case of computer peripherals like mice and keyboards where data obtained from arms and fingers movements are translated for the computer. From a global point of view, it is nothing else but a point-to-point transmission of electrical stimuli between the human brain and the computer. The signal passes through several

<sup>1</sup>FPGAs are not considered in this work.

transducers like muscles, keys and switches before being reconstituted and interpreted by the computer (Figure 3.4). In that case, the loop is usually closed using visual and auditory feedbacks provided by the screen and speakers. The idea behind multi-finger haptic devices is to enhance that feedback by adding a tactile dimension to the relation between the human being and the machine.

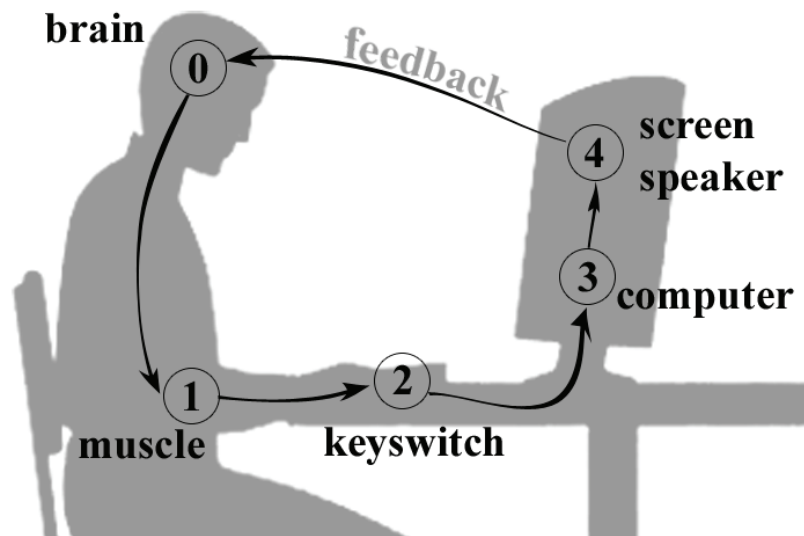


Figure 3.4 – Closed loop of information in usual computer operations

A haptic feedback, entirely pre-programmed and embedded within the peripheral can content itself with a unidirectional communication towards the computer (e.g. for characters transmission). However, with the aim of increasing the device performance and provide new functionalities, a two-way communication is proposed. Indeed, a transfer of information towards the haptic device allows for two major improvements. First, the opportunity can be given to fine-tune the touch sensation anytime depending on the task or user, increasing thus the comfort. Then, additional information can be conveyed to the user through the sense of touch opening the way to a novel mean of communication.

In conclusion, the implementation of the communication circuit can differ depending on the final application but a bidirectional connection appears as a must for a greater flexibility. No chapter is specifically dedicated to communication but solutions developed within the framework of applications are presented in chapter 6.

### 3.6 Software user interface

The software user interface is considered as the last part of a multi-finger haptic device even if it does not physically form a part of it. Following the characteristics outlined in the previous section, a graphic interface can fulfill two distinct functions. On one hand, an interactive

### **Chapter 3. Multi-finger haptic systems**

---

window displaying the main properties of the haptic feedback helps adjusting the tactile sensation provided by the device. The user can for instance decide to opt for one or another force profile to improve his typing comfort. On the other hand, the graphic interface fulfills its original role which is to provide a visual feedback to embody the actions of the user (e.g. by displaying typed characters or following a path on the screen).

Similarly as for the communication module, each software user interface strongly depends on the application and some examples will be presented together with their corresponding device (chapter 6).





# Design methodology for linear short-stroke actuators

## Contents

---

- 4.1 Design . . . . . 47**
  - 4.1.1 Case study: Square electrodynamic actuator . . . . . 47
  - 4.1.2 Finite element modeling for rapid analysis . . . . . 49
- 4.2 Optimization tools . . . . . 52**
  - 4.2.1 Analytical modeling . . . . . 52
  - 4.2.2 Hybrid alternatives . . . . . 57
- 4.3 Design of experiments and parametrical modeling . . . . . 61**
  - 4.3.1 Experimental domain . . . . . 61
  - 4.3.2 Building the matrix of experiments . . . . . 61
  - 4.3.3 Parameterization . . . . . 63
  - 4.3.4 Results . . . . . 64
  - 4.3.5 Statistical analysis . . . . . 69
- 4.4 Design improvement . . . . . 72**
  - 4.4.1 Linearization of the force profile . . . . . 72
  - 4.4.2 Prototype . . . . . 76
- 4.5 Full parametrical setup . . . . . 77**
- 4.6 Actuators . . . . . 80**
  - 4.6.1 Cylindrical actuator . . . . . 80

## Chapter 4. Design methodology for linear short-stroke actuators

---

4.6.2	Square actuator II . . . . .	87
4.6.3	Fixed magnet actuators . . . . .	92
4.6.4	Vibrotactile button . . . . .	95
<b>4.7</b>	<b>Thermal analysis . . . . .</b>	<b>98</b>
4.7.1	Limiting elements . . . . .	98
4.7.2	FEM steady state thermal analysis . . . . .	99
<b>4.8</b>	<b>Summary . . . . .</b>	<b>103</b>

---

As introduced in the previous chapters, the aim of the thesis is to propose a methodology to design haptic peripherals embedding multiple actuators. The central part of every haptic device being the one responsible for the creation of the tactile feedback, a method for the optimization of linear short-stroke actuators is presented. As the comparison of section 3.2 pointed out that electrodynamic actuators are the best candidates for this kind of applications, the present chapter focuses on their optimization. The particularity of these actuators is that at the small-size scale, which is required by multi-finger haptic devices, airgaps and displacements are large relatively to the entire structure. A standard modeling using a simplified behavior of the magnetic flux lines neglecting fringes and leakage thus loses its efficiency and an alternative design methodology becomes necessary. It should be precise, fast and being able of easily integrating materials characteristics.

Table 4.1 – Actuator specifications

<i>Parameter</i>	<i>Value</i>
Available ground surface	18 x 18 mm <sup>2</sup>
Actuator height (indicative)	10 mm
Travel	5 mm
Maximum force	min. 1 N
DC voltage	5 V

In order to facilitate the comprehension of the approach, a miniature electrodynamic actuator aimed to be integrated under a computer key is taken as example. Its specifications are given in Table 4.1. First of all, the initial design is given, based on general requirements for narrow available spaces. In addition, it is shown how to take advantage of finite element modeling for a rapid initial analysis of the magnetic behavior for early stages of the actuator design. Then, three major tools used for the optimization are outlined: analytical model, genetic algorithm and design of experiments. After dismissing the two firsts, the method of the design of experiments coupled with finite element modeling is detailed and applied to the example actuator. Once the method is validated, design modifications are made on the sample actuator,

improving the linearity of the force characteristic along the travel. A full parametrical setup is then presented merging the entire optimization process into a unique program integrated behind a single user-friendly graphic interface. This full parametrical setup is then used to optimize several actuators showing the range of potential applications. Finally, a brief thermal analysis is performed on the optimized geometries for more safety.

## 4.1 Design

### 4.1.1 Case study: Square electrodynamic actuator

In order to fit the actuator under a computer key, force density, mechanical simplicity and dynamic considerations have to be taken into account during the design. Electrodynamic actuators intrinsically fulfill these requirements; however, not all configurations are suitable for miniaturization. The geometry initially designed is presented in Figure 4.1 and emphasis is made on its key advantages in the rest of the subsection.

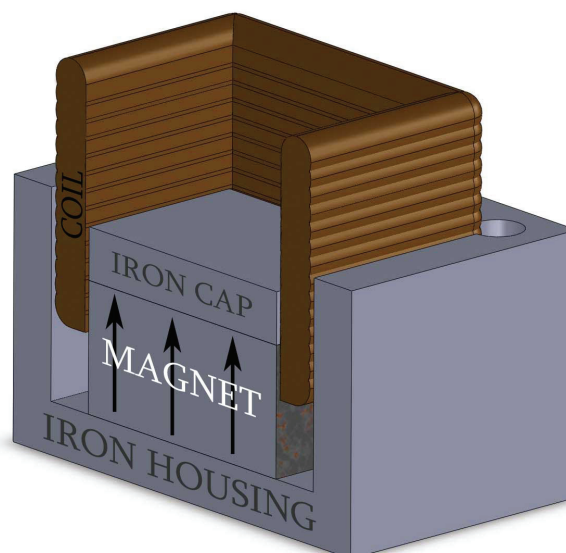


Figure 4.1 – Initial electrodynamic actuator

The electrodynamic actuator, also called voice coil, is a kind of electromechanical actuator characterized by a fixed magnetic circuit and a moving coil. The coil lightweight gives the big advantage of reducing the inertia of the moving part which improves the dynamics. It is the reason why this actuator kind is used in most loudspeakers to cover the entire audible bandwidth and in PC hard disks heads to rapidly scan data. The second advantage of voice coils is their simplicity. One or several permanent magnets are fixed to the housing and generate a constant magnetic flux in the airgap. When a magnetic flux crosses a conductor supplied with current, Laplace's force is generated. This force is directly proportional to the

current which simplifies the control algorithm:

$$d\vec{F} = I d\vec{l} \times \vec{B} \quad (4.1)$$

where  $I$  is the current,  $l$  the conductor length and  $B$  the flux density crossing the coil.

In order to miniaturize the actuator and minimize the number of magnets and their complexity, it is decided to place a single magnet, vertically polarized, in the center, with the coil sliding along it. The trick is to use an iron cap to "bend" the flux horizontally in the airgap in order to create a vertical force. This configuration involves using an overhung coil (Figure 4.2). Contrarily to the underhung coil where the gap is much larger than the coil, the entire gap always faces the same number of turns for any position of the coil allowing for a constant force along the travel. This last assertion requires the hypothesis of magnetic flux lines that are perpendicular to the surface they leave or enter. Moreover, the force density is improved despite an increase of power consumption. Indeed, depending on the travel, many turns carry current without participating to the force creation. It is however necessary if one wants to guarantee a sufficient force and still minimize the magnetic circuit volume. In the case of an underhung coil, the flux density in the airgap would not be sufficient unless building a bigger structure around the coil, which would not fulfill the specifications.

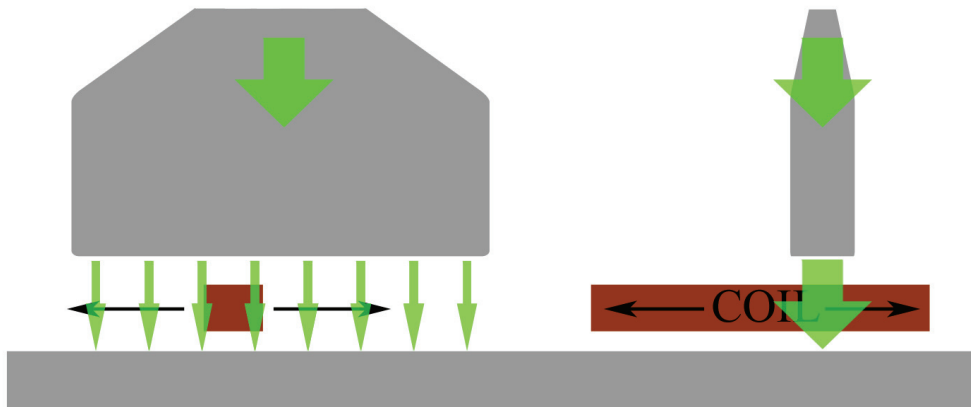


Figure 4.2 – Underhung and overhung coil principles

The tight dimensions available under a computer key impose to take advantage of the maximum volume at disposal. With a square configuration, which fits the contour of a key, the coil is longer and its four sides contribute to the force. Finally, the external iron housing suppresses any leakage that could affect the surroundings and disturb neighboring keys.

The advantages characterizing the designed geometrical configuration are summarized in Table 4.2.

Table 4.2 – Actuator advantages

Geometrical feature	Advantage
Square geometry	The entire volume at disposal is used, increasing thus the force density.
Single magnet with vertical magnetization	Ease of assembly, low cost. The fringes created by the vertical magnetization above the iron cap could be used with a Hall sensor to measure the position.
Iron cap (responsible for the bending of the flux)	The flux crosses the entire length of the turns, increasing thus the force. A single magnet can be used and geometry is simplified.
Overhung coil	The force is constant all along the stroke if the flux is correctly confined in the narrow gap.
Electrodynamic system	Dynamics and reactivity are improved thanks to the low inertia of the coil. Moreover, force is directly proportional to the current.
External iron housing	Surrounding the magnet magnetically isolates the actuator from neighboring actuators.
Self-supporting coil	The possibility to use such kind of coils increases the number of turns and so the force by avoiding an additional frame.

#### 4.1.2 Finite element modeling for rapid analysis

The beginning of any electromechanical development consists in the understanding of the phenomena prevailing in the system. Finite element modeling (FEM) represents an excellent means of analysis in the first steps of a project. Indeed, the user can enter his first drafts and quickly get a feeling of their performance. Without much effort, this tool permits to quickly assess the behavior and performance of the geometry. Formerly in two dimensions (2D), FEM is now capable of computing three-dimensional objects. Despite a significantly increased computation time, 3D programs give a visual rendering of extruded shapes and complete systems, making them somehow comparable to computer aided design (CAD).

FEM is also very useful during the design phase and helps highlighting and improving assets of the geometry. Regularly used for the design of rotating motors and actuators, 2D FEM becomes limited when the geometry requires a variation of the magnetic flux path in the three dimensions. In the case of the present actuator, the entire volume cannot be built with an extrusion of a single 2D cut (Figure 4.3). 3D implementation is thus required to model it properly.

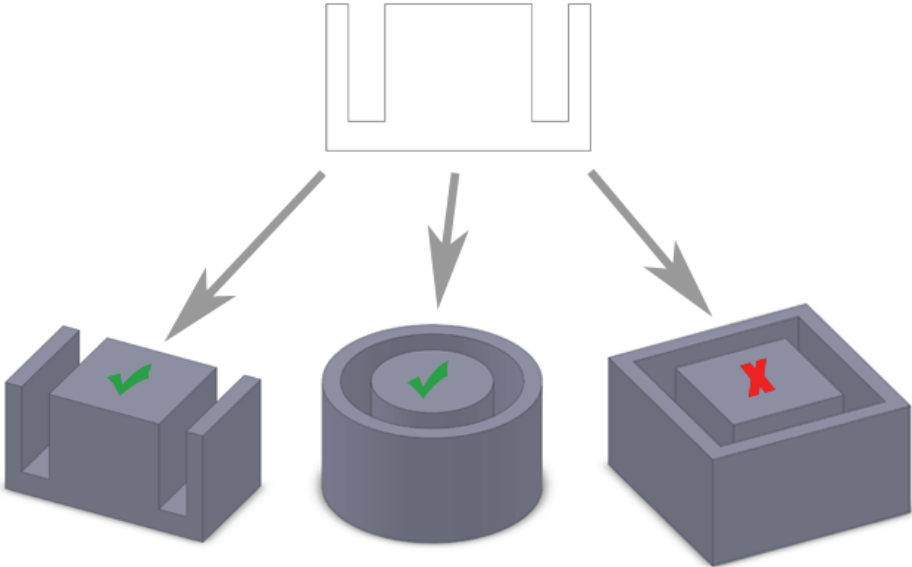


Figure 4.3 – 2D FEM issues with 3D objects.

To illustrate the previous points, the magnetic flux density of the initial geometry obtained with FEM is presented in Figure 4.4. The path followed by the magnetic flux clearly appears and shows the leaks within and around the actuator (Figure 4.5).

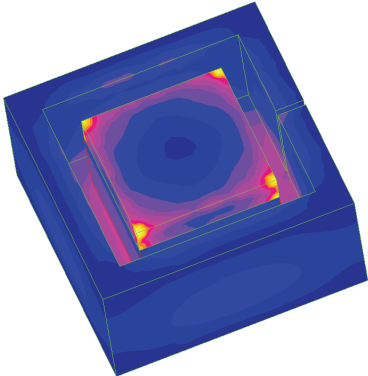


Figure 4.4 – 3D FEM flux density analysis

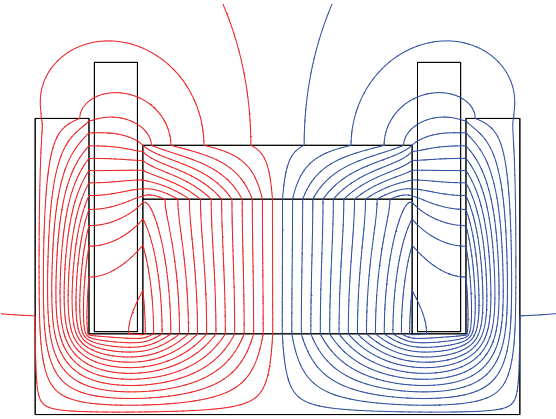


Figure 4.5 – Magnetic flux path in 2D cut

Supplying a current in the coil allows for the calculation of Laplace's force (4.1) and rapidly gives a first impression of its magnitude and profile along the travel (Figure 4.6). The first observation that can be made is that the force decreases with the position of the coil. The higher the coil position, the lower the force is due to diagonal fringes that close themselves in the housing below the cap. These fringes do not participate to the force anymore above

a certain coil position confirming thus the issue mentioned in introduction and requiring a specific modeling method (Figure 4.5). The fringes are notably related to the iron saturation level and permeability that bend the flux lines. FEM offers the possibility to enter the magnetic characteristic of a material, which represents a big advantage in terms of modeling. Saturation can immediately be detected and rough improvements applied to the geometry, giving a better idea of the overall dimensions of the structure. However, the user has to be careful. Indeed, a small difference in iron properties between simulations and reality leads to discrepancies of the force profile (Figure 4.6). A lot of parameters like material and meshing properties are not trivial to implement and can compromise the quality of the results if not implemented with precaution.

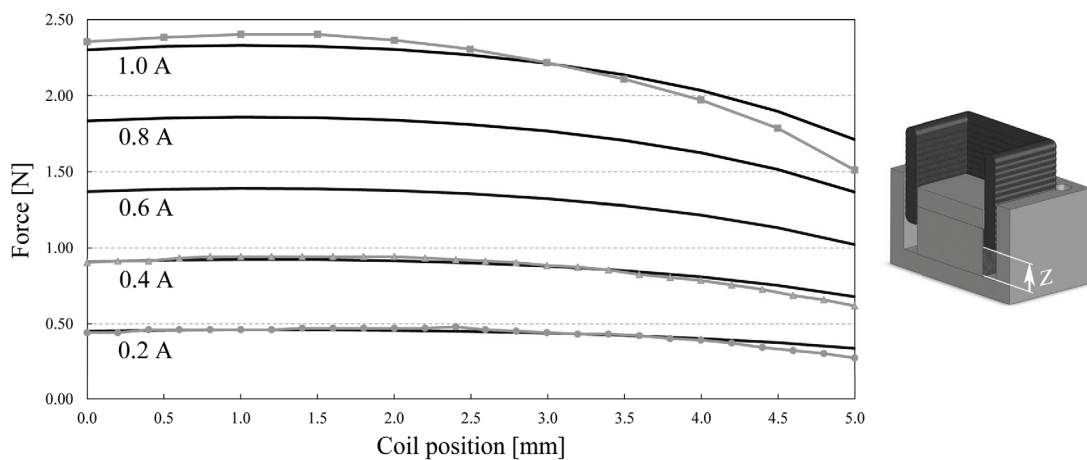


Figure 4.6 – Force provided by the initial actuator for different current values (black lines: FEM, grey dotted lines: measurements)

The second information to be brought to light by the FEM preliminary analysis is the confirmation of the direct proportionality between force and current (Figure 4.7).

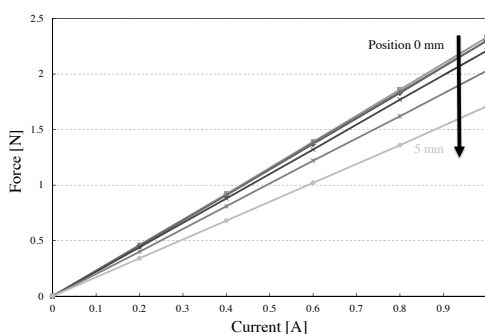


Figure 4.7 – FEM force is proportional to the current and varies with the position of the coil

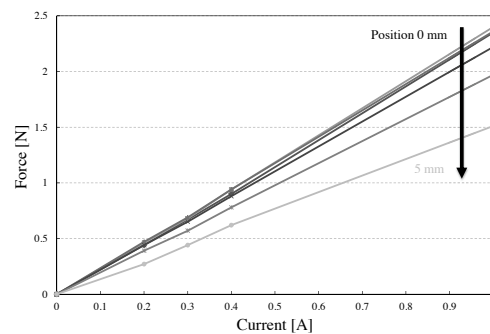


Figure 4.8 – Similarly for the measured force

This affirmation is doubly confirmed by the measurements shown in Figure 4.8 where the slope varies with the position of the coil. This issue will be addressed in subsection 4.4.1.

From now on, FEM simulations will be run with a normalized current of 1 A in order to simplify the comparisons. However, the heat generated by such current is unacceptable for continuous operations and will have to be scaled down later.

### 4.2 Optimization tools

The challenge of scaling down a system is to still guarantee performances fulfilling the specifications for given geometrical constraints. In the present example, the actuator must fit under a computer key and provide at least 1 N. The objective function of the optimization will thus be the force provided by the actuator for a fixed value of current. The advantage behind this method is that power can be minimized indirectly for the desired performance. Indeed, as the force is directly proportional to the current (4.1), if the force provided by the optimum is greater than the specifications, a downward adaptation of the current decreases the power consumption, which goes together with today's ecological and economic trends.

#### 4.2.1 Analytical modeling

The utility of analytical models in optimization processes, especially in the electromechanical domain, is well known. This technique allowed for numerous motors and actuators optimizations to succeed. However, implementing a complete analytical model that fits reality can be a long and painful way depending on the configuration. Certain geometries can be described as "preferable" for an analytical approach when the airgap is narrow relatively to the overall size. Practically, it means that magnetic circuits that are likely to generate fringes and leaks of the same order of magnitude as the useful flux will represent an issue during the flux path modeling (Figure 4.9).

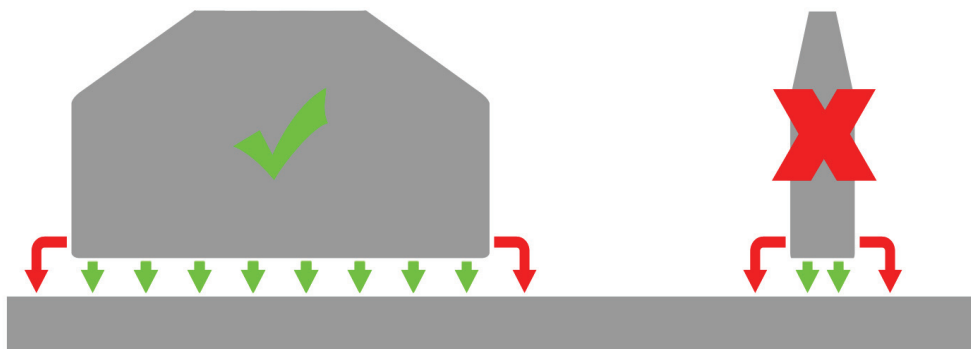


Figure 4.9 – When the section crossed by the flux is small compared to the airgap width, the fringes/flux ratio becomes critical



In the present case of actuator miniaturization, a large airgap is required to combine mechanical simplicity and multi-turns windings, which naturally leads to important fringes that can follow irregular paths (Figure 4.5). Modeling the flux lines by arcs and straight lines, very useful for toothed structures [117], becomes problematic due to large airgaps. Indeed, small dimensional or material variations lead to significant perturbations of the flux behavior.

### 2D analytical model

In order to demonstrate the difficulties mentioned above, the model of a simplified version of the actuator (Figure 4.10) is implemented with the following hypothesis [116, 118]:

- The flux is equally distributed within the crossed section.
- A mean path is used to define the travel of the flux lines.
- Eddy current losses and hysteresis effect are neglected.
- The flux leaves and enters the surface perpendicularly.
- Saturation level is considered as constant within each subpart.

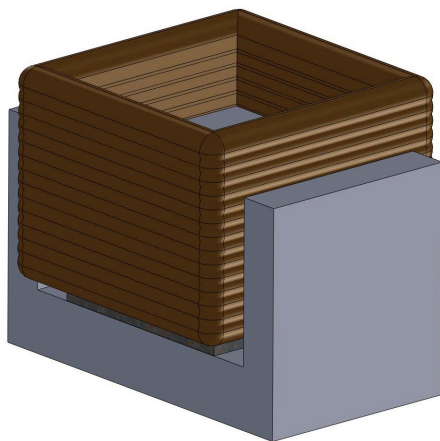


Figure 4.10 – 2D version of the actuator

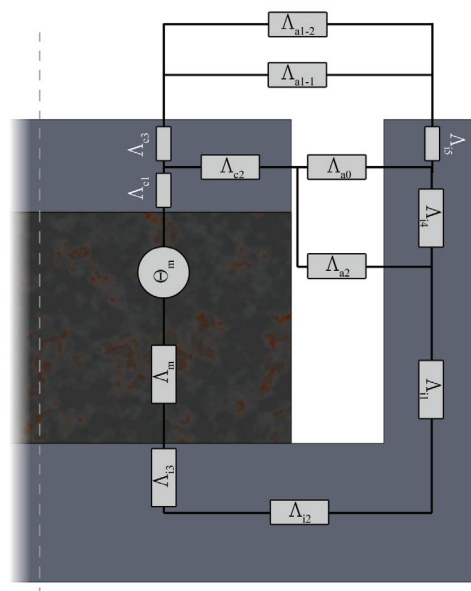


Figure 4.11 – Equivalent magnetic circuit

## Chapter 4. Design methodology for linear short-stroke actuators

---

The first step consists in translating the geometry into a magnetic circuit as shown in Figure 4.11. The flux path is divided into permeances  $\Lambda$  given by:

$$\Lambda = \int \frac{\mu \cdot ds}{l} \quad (4.2)$$

where  $\mu$  is the magnetic permeability of the material,  $ds$  a surface element crossed by the flux and  $l$  the length of the flux path.

The potential created by the magnet  $\Theta_m$  is:

$$\Theta_m = \frac{B_0}{\mu_0 \cdot \mu_{rm}} \cdot l_m \quad (4.3)$$

with  $B_0$  the magnet remanence,  $\mu_0$  the vacuum magnetic permeability,  $\mu_{rm}$  the magnet relative permeability and  $l_m$  the magnet length.

Kirchhoff's first and second laws applied to the magnetic circuit allow for the reduction of the circuit to an equivalent permeance  $\Lambda_{eq}$  in series with  $\Theta_m$ , hence the magnetic flux  $\Phi$  becomes:

$$\Phi = \Theta_m \cdot \Lambda_{eq} \quad (4.4)$$

Going back to the original circuit (Figure 4.11) determines the flux crossing every parts of the airgap. With the relation linking the flux density  $B$  and the flux  $\Phi$  (4.5), every element of Laplace's equation (4.1) is assembled to calculate the force.

$$\Phi = \int B \cdot ds \quad (4.5)$$

Two different approaches are usually used to set up an analytical model with the intention of optimizing a motor or an actuator. The first method consists in implementing the model with ideal iron. Saturation is therefore not considered during the optimization phase, but the thickness of iron parts (especially external housing) is adapted afterwards so as to avoid saturation. This is only possible when the outer volume is not constrained, which is not the case here. The second approach calculates the flux density within the permeances of the equivalent circuit and limits it if higher than the saturation level, in accordance with iron characteristics. Unfortunately, for certain geometries, saturation does not only limit the magnitude of the flux but deviates it, causing unwanted behaviors. The actuator studied in this work is a good example of this effect. In Figure 4.12, when the iron is considered as ideal, the coil bottom is

crossed by lines going towards the housing with a strong horizontal component participating to the force. On the other hand, when the iron is subjected to saturation, the bottom of the housing vertical walls gets saturated and some flux lines tend to close themselves directly towards the bottom (Figure 4.13). In this case, the horizontal component of the flux crossing the coil is negligible, or even negative with respect to the force. As a result, when the coil moves along the vertical axis, non-linearity appears. Modeling the behavior of the flux for such actuators would necessitate a huge effort to become as precise as FEM could be. This is the reason why, in projects that are not purely academic, an alternative has to be found to save time and still guarantee accurate results.

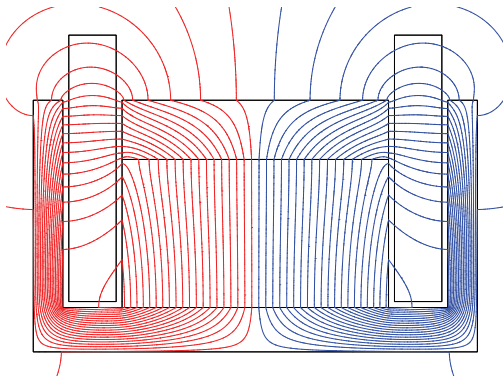


Figure 4.12 – Flux path with ideal iron

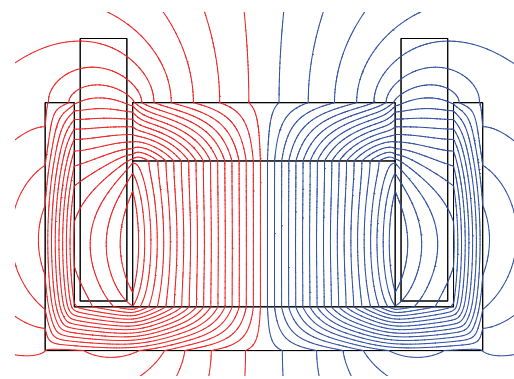


Figure 4.13 – Saturation at 1 T

To illustrate the issue of the flux behavior, results of the analytical model corresponding to Figure 4.10 are compared with FEM simulations. Two versions of the model are implemented, namely *classic* and *loops*.

The first model labeled as *classic* is a straightforward application of equations (4.1) to (4.5). The flux crossing the airgap is considered as horizontal. In order to ease the understanding, a single parameter, namely the magnet height, varies in the presented example. Saturation is not considered in the analytical model yet.

A first comparison is made with the coil in down position (Figure 4.14). With a maximum relative error of 3.7%, results are quite close, except for the 0.8 mm height where it is shorter for the flux to close below the magnet instead of crossing the airgap making the configuration singularly different (the effect is comparable to the one shown in Figure 4.13 and the force thus decreases rapidly for low positions). A second observation could be the fact that the model characteristic is more linear than FEM. It can be fully explained by the fact that non-horizontal components of the flux produce a horizontal force which is not useful.

While discrepancies are limited for low positions at which all leaks contribute to the force, regardless of the direction of the flux in the airgap, errors increase when one look along the travel (Figure 4.15). It becomes thus necessary to be able to precisely predict the path followed by every flux line, which would represent an important work of fundamental research. Two

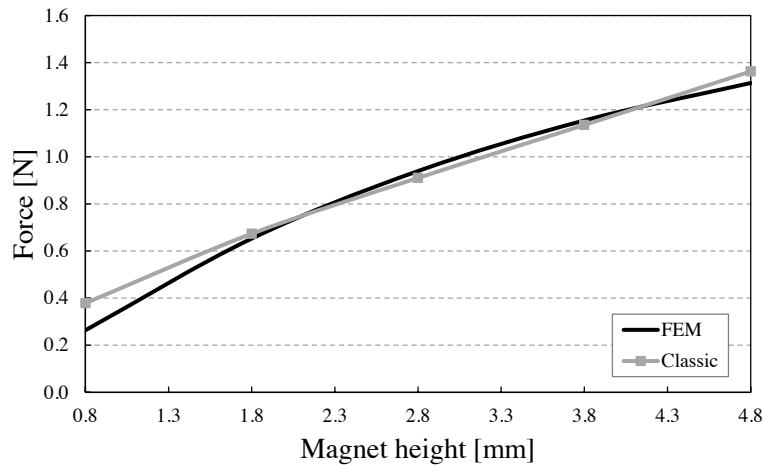


Figure 4.14 – Classic model vs FEM for different magnet heights with the coil in its down position (0 mm)

main effects are responsible for model discrepancies:

- During an upward displacement, the coil starts losing bottom fringes, which results in a decrease of the force. The effect is limited for the first millimeters where these losses are compensated by the gain of fringes passing above the actuator (Figure 4.15 (a) and (b)). On the contrary, for thin magnets, the flux prefers to close below the magnet like in Figure 4.13. The bottom flux lines decrease the force and so, losing them makes the force increase. This effect clearly appears in Figure 4.15 (c) and (d).
- The error appearing at the upper end of the travel (3-5 mm) can be explained by a missing permeance above the actuator ( $\Lambda_{a1-2}$  in Figure 4.11). Indeed, the higher the magnet, the higher are the fringes above the actuator. When the coil is up, this leakage participates to the force.

The *classic* model approaches FEM simulations but not sufficiently to permit considering using it for optimization. As mentioned before, some error sources are identified and could be solved with an adaptation of the model.

The *loops* model is an evolution of the *classic* model created to take the loops made by the flux lines under the magnet into account using an additional permeance in the airgap lower part. As expected, Figure 4.15 shows an improvement of the fit in the first half of the travel. The maximum relative error stays below 4.5% between 0 and 2.5mm and goes up to 13% at 5mm. This second implementation shows the possibility to improve the model step by step until getting a reasonable accuracy. A reasonable accuracy yes, but for what experimental domain? What is the range of admissible parameters variations that still guarantees a model match?

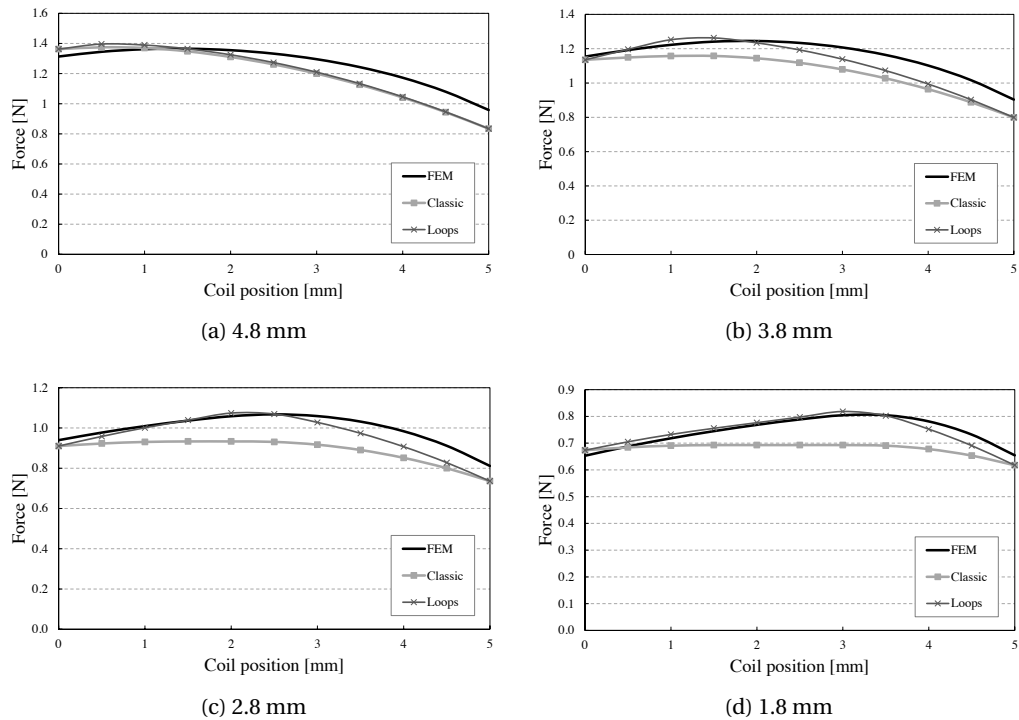


Figure 4.15 – Force profiles comparison between classic and loops models and FEM for different magnet heights

#### 4.2.2 Hybrid alternatives

The analytical modeling of small actuators with no confined flux path presents an issue of application area. Indeed, the validation of the model necessitates comparisons with numerous FEM simulations or measurements on different geometries to make sure that it is accurate on the entire experimental domain. Even once the model is labeled as *ready for optimization*, a last FEM validation is operated on the optimal design to make sure it corresponds to reality before manufacturing the first prototype. In addition, there is no chance for the model to be used as is to optimize a different kind of actuator. This method can be described as case-related. The question can now be asked about the legitimacy of such optimization process. Why not finding a quicker and more precise way to obtain the optimal geometry?

As FEM is used for the verification of analytical models, one can imagine getting rid of the analytical part and take advantage of FEM solely. Clearly, FEM software cannot be used alone without a strategy. Empirical step-by-step optimizations are indeed time consuming and do not necessarily lead to a global optimum. This is the point where hybrid methods come into play.

### Genetic algorithms

The first technique combines FEM with genetic algorithms. It is a stochastic method of optimization where mutations and crossover operators are applied on a population of random geometries called individuals. During a step, all individuals are simulated via FEM and evaluated. The best individuals are kept and labeled as *parents*. *Children* are generated to fill the population and many iterations are operated until obtaining an optimum. Genetic algorithms already proved to be efficient for the design of linear actuators [119]. However, as tens of thousands of simulations are necessary to converge towards a solution, 2D FEM, with simulation steps completed in a few seconds, is mandatory. 3D modeling is unimaginable with current computation power. This point thus eliminates genetic algorithms as a potential solution.

Contrarily to genetic algorithms, it is preferable to limit the number of simulations to the strict minimum. This is exactly what design of experiments does.

### Design of experiments

Design of experiments (DOE) is a statistical method to model a system in its entire experimental domain using a limited data set. More largely, DOE links an output vector  $\vec{Y}$ , the responses, to an input vector  $\vec{X}$ , the factors, using a controlled number of experiments (Figure 4.16). It is applicable to numerous domains and industries where empirical knowledge has to be gathered based on the analysis of limited experimental data.

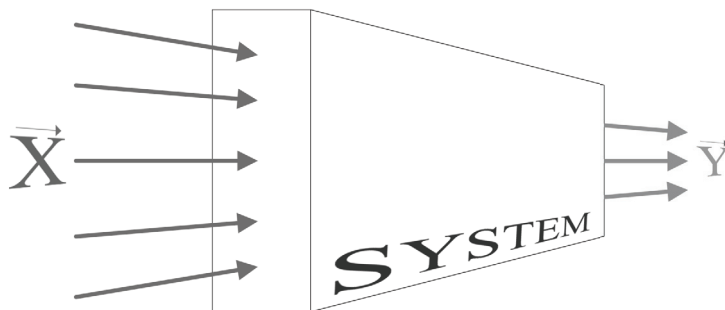


Figure 4.16 – General experimental system with input factors  $\vec{X}$  and output answers  $\vec{Y}$

The input factors can represent a multitude of parameters like time, material, operator and many others but they are generally assimilated to geometrical dimensions in the case of mechanical systems design. Each factor varies inside a pre-defined range and all factors boundaries define the experimental domain. Let us take the simple example of the tensile strength test applied to aluminum cylindrical rods. The output is the force at which the rod breaks. For this example, two factors, namely the rod diameter and its length are taken, varying between 2 and 4 mm and from 100 to 150 mm respectively. These dimensions are defined before planning the experiments, in accordance with the project specifications and constitute

the experimental domain. DOE aims to gather the behavior of each possible rod within the domain with a limited number of experiments. In industry, it is obviously not feasible to build a prototype corresponding to every single possible configuration to determine the optimum. Thus, FEM simulations represent an excellent alternative to replace real experiments, saving time, work and money.

In any case, the success of DOE resides in the careful choice of the design of experiments. A design is obtained by picking in a "normalized" experimental domain (1 and -1 standing for the upper and lower boundaries respectively), a set of configurations that will constitute the base of the analysis. Each design is characterized by a number of experiments and their position within the experimental domain. Old-fashioned designs used in laboratories consisted in varying one factor at a time, losing de facto interaction effects. In response to this lack of efficiency, structured designs were invented.

Five existing designs directly taken from literature are presented for purpose of information in appendix A.1.1 in order to help understand the functioning of the design of experiments first invented by R. Fisher [120].

Once the design of experiments is chosen and applied to the system, the data obtained from those experiments needs to be processed. In an utilization of DOE called *response surface methodology* (RSM), a polynomial function is obtained from the experimental data to model the system behavior on the whole experimental domain. The interpolation is generally either linear or quadratic and integrates or not interactions between factors in order to fit reality. Examples of such surfaces are presented for 2 factors (Figures 4.17 to 4.19) and their corresponding equations are:

$$y = a_0 + a_1 \cdot x_1 + a_2 \cdot x_2 \tag{4.6}$$

$$y = a_0 + a_1 \cdot x_1 + a_2 \cdot x_2 + a_{12} \cdot x_1 \cdot x_2 \tag{4.7}$$

$$y = a_0 + a_1 \cdot x_1 + a_2 \cdot x_2 + a_{12} \cdot x_1 \cdot x_2 + a_{11} \cdot x_1^2 + a_{22} \cdot x_2^2 \tag{4.8}$$

$x_i$  being the geometrical factors and  $a_i$  the constant parameters to determine.

The advantages of RSM are multiple. First, the information contained in the parameters  $a_i$  allows for a rapid analysis in order to determine what are the prevailing factors of the system. Interactions between factors are revealed as well, which helps understand the behavior and additionally clearly separate the effect of single inputs. Secondly, as the output of the system

is known for the entire domain, it is possible to find the optimum. Quadratic polynomials are excellent candidates for optimization as shown in Figure 4.19.

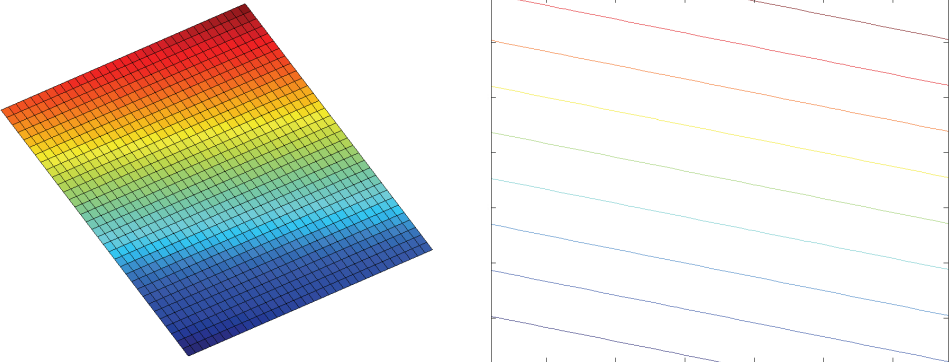


Figure 4.17 – Linear model for two factors and corresponding 2D projection

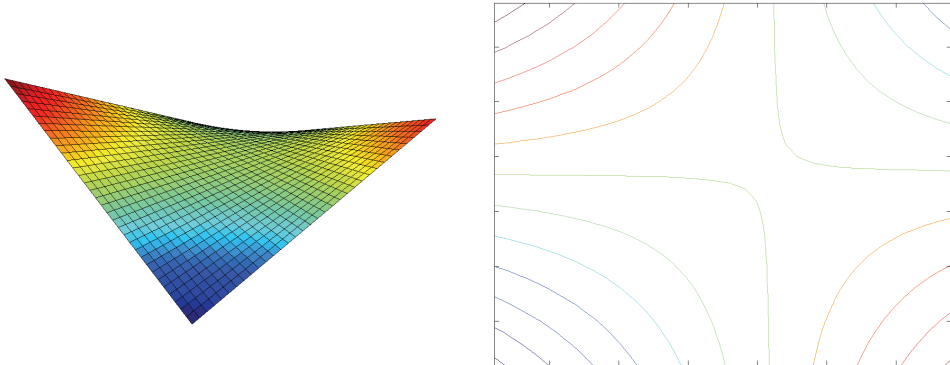


Figure 4.18 – Linear model with interactions for two factors

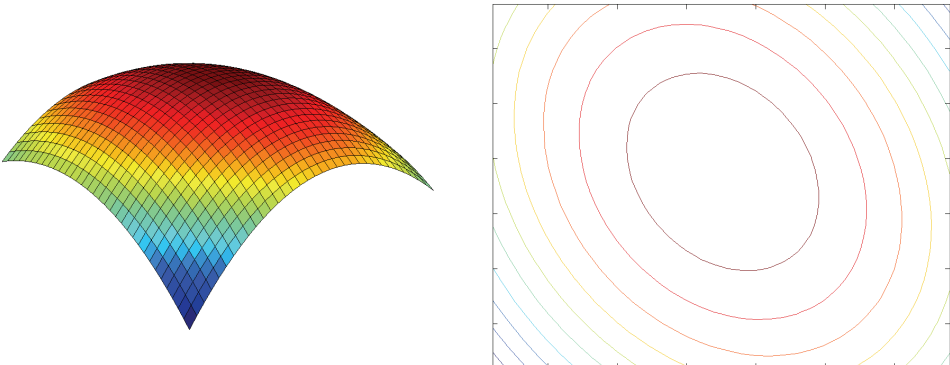


Figure 4.19 – Quadratic model with interactions for two factors



### 4.3 Design of experiments and parametrical modeling

The first task of a DOE process is to carefully select a design that could fit the specifications. A trade-off has to be made between a high number of simulations and a good accuracy. By definition, experimental designs strongly decrease the necessary number of simulations. Among the examples presented in appendix A.1.1, some like the fractional design, propose to save even more simulations by replacing interactions by new factors. This would be useful for experiments requiring the construction of prototypes, but not for simulations. Saving an hour of computation and losing efficiency caused by the appearance of parameters bias is not worth it. It is thus better to orient the choice on more elaborated designs, developed for optimization and not only for parameters comparison.

#### 4.3.1 Experimental domain

In the example of the square actuator presented to illustrate the method (Figure 4.1), the number of free factors is fixed to three. They are presented in Table 4.3 with their assumed boundaries defining the experimental domain.

Table 4.3 – Free factors for the optimization of the initial square actuator geometry

Factor	Geometrical dimension	Range [mm]
$x_1$	magnet height	[3-7]
$x_2$	magnet length	[8-12]
$x_3$	housing thickness	[1-2.1]

As the force is directly proportional to the current (4.1), it is not considered as a parameter and the normalization is obtained by fixing it to 1 A. In order to guarantee a high force density, NdFeB magnets are used. They are characterized by a high remanent flux density of 1.26 T and a relative permeability of 1.15. The wire diameter is fixed to 0.2 mm, which represents a compromise between thermal dissipation and electric time constant. A thermal convection model and tests on fabricated coils showed that 0.2 mm is the minimal wire diameter to fit the requirements. The number of turns depends on the available space in the airgap and is hence not a free factor.

#### 4.3.2 Building the matrix of experiments

Once the factors are defined, they are normalized as follows:

$$x_{ni} = \frac{2 \cdot x_i - (x_{imax} + x_{imin})}{x_{imax} - x_{imin}} \quad (4.9)$$

## Chapter 4. Design methodology for linear short-stroke actuators

with  $x_{imax}$  and  $x_{imin}$  the maximal and minimal values of the factor  $x_i$ . For the rest of the work, the normalized value  $x_{ni}$  will be noted  $x_i$ .

The example of a two-level composite design is shown in Figure 4.20 to illustrate the principle. The rows of the corresponding model matrix are split in three blocks (Table 4.4). The first block represents the factorial design (8 experiments), the second the star design (6 experiments) and finally, at the very bottom, the central point experiment for a total of 15 simulations. Usually, several experiments are run at [0;0;0] for the characterization of the experimental error. In the case of FEM simulations, only one experiment is sufficient as the results would be the same.

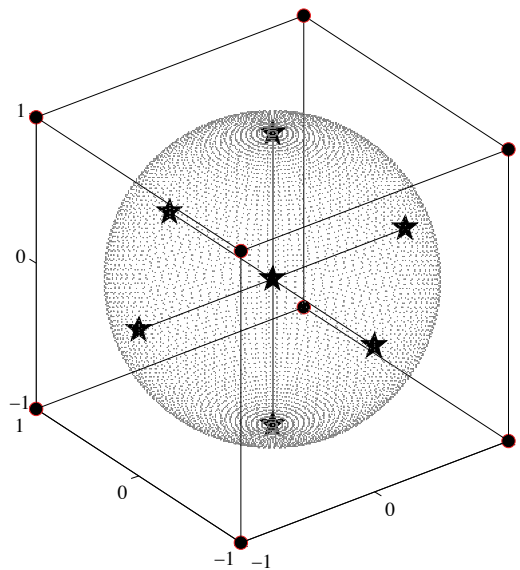


Figure 4.20 – Composite design for three factors with  $\alpha = 1$  (sphere radius)

Each row of the experimental matrix (grey columns in Table 4.4) corresponds to a set of normalized geometrical dimensions for one simulation. All of its columns are independent to each other in order to guarantee orthogonality. The matrix of experiments is then extended to the model matrix  $\mathbf{X}$  where each column stands for a parameter. The matrix  $\mathbf{X}$  shown in Table 4.4 stands for a quadratic model with interactions. The first column  $a_0$  corresponds to the average value,  $a_{1-3}$  to the linear effects,  $a_{11-33}$  to the quadratic effects and the rest represents first and second order interactions. The columns of the right part of the matrix are built by multiplying columns of the experimental matrix between each other. For instance,  $a_1 \cdot a_2$  gives  $a_{12}$  and so on. The radius of the star design  $\alpha$  is usually greater than one and related to the number of central experiments. Feneuille and al. [121] give an optimal  $\alpha$  of 1.215 for three factors and one central experiment. However, experiments run with  $\alpha = 1.22$  and  $\alpha = 1$  showed no significant difference (as it will be shown later in Figures 4.27 and 4.28). It will thus be kept equal to one.

For the square actuator, the non-linearity is neglected and the hypothesis of a constant force

### 4.3. Design of experiments and parametrical modeling

Table 4.4 – Model matrix of a composite design for quadratic model with interactions for three factors

	$a_0$	$a_1$	$a_2$	$a_3$	$a_{12}$	$a_{13}$	$a_{23}$	$a_{11}$	$a_{22}$	$a_{33}$	$a_{123}$
factorial	1	1	1	1	1	1	1	1	1	1	1
	1	1	1	-1	1	-1	-1	1	1	1	-1
	1	1	-1	1	-1	1	-1	1	1	1	-1
	1	1	-1	-1	-1	-1	1	1	1	1	-1
	1	-1	1	1	-1	-1	1	1	1	1	-1
	1	-1	1	-1	-1	1	-1	1	1	1	1
	1	-1	-1	1	1	-1	-1	1	1	1	1
	1	-1	-1	-1	1	1	1	1	1	1	-1
star	1	$-\alpha$	0	0	0	0	0	$\alpha^2$	0	0	0
	1	$\alpha$	0	0	0	0	0	$\alpha^2$	0	0	0
	1	0	$-\alpha$	0	0	0	0	0	$\alpha^2$	0	0
	1	0	$\alpha$	0	0	0	0	0	$\alpha^2$	0	0
	1	0	0	$-\alpha$	0	0	0	0	0	$\alpha^2$	0
	1	0	0	$\alpha$	0	0	0	0	0	$\alpha^2$	0
0	1	0	0	0	0	0	0	0	0	0	

along the travel is made. The force acting on the coil is thus only computed for its lowest position (0 mm). The 15 simulations of the composite design are run in 3D FEM and Laplace's force is computed.

#### 4.3.3 Parameterization

Finally, a polynomial is built out of the simulations data. Two models of the force  $F$ , namely linear (4.10) and quadratic (4.11), are generated:

$$F = a_0 + \sum_{i=1}^3 a_i x_i + \sum_{i \neq j}^3 a_{ij} x_i x_j + a_{123} x_1 x_2 x_3 \quad (4.10)$$

$$F = a_0 + \sum_{i=1}^3 a_i x_i + \sum_{i \leq j}^3 a_{ij} x_i x_j + a_{123} x_1 x_2 x_3 \quad (4.11)$$

## Chapter 4. Design methodology for linear short-stroke actuators

---

The least squares method is used to determine the vector of parameters  $\vec{a}$  characterizing the polynomial. First, the output vector  $\vec{Y}$  composed of force values  $F$  obtained with FEM can be written as:

$$\vec{Y} = \mathbf{X}\vec{b} + \epsilon \quad (4.12)$$

Then,

$$\vec{b} = (\mathbf{X}^T \mathbf{X})^{-1} \mathbf{X}^T \vec{Y} - (\mathbf{X}^T \mathbf{X})^{-1} \mathbf{X}^T \epsilon \quad (4.13)$$

By removing the error term with  $\epsilon$ , one gets the vector of coefficients  $\vec{a}$  which is an estimation of  $\vec{b}$  as the error is neglected.

$$\vec{a} = (\mathbf{X}^T \mathbf{X})^{-1} \mathbf{X}^T \vec{Y} \quad (4.14)$$

### 4.3.4 Results

#### Ideal iron characteristics

DOE starts with the choice of an appropriate design. Three designs are studied and compared in this section: Hadamard, factorial and composite designs. These three designs are characterized by different numbers of experiments: from only five for a Hadamard design (an extra row filled with 1 is aggregated to it (Table 4.5)) up to fifteen for a composite design (eight for a two-level full factorial). They were chosen so to show the importance of a sufficient number of simulations and bring limitations to light. For this first part of the analysis, saturation is not implemented in FEM, the iron is thus considered as ideal.

Table 4.5 – Model matrix of a Hadamard design for linear model without interaction for three parameters

$a_0$	$a_1$	$a_2$	$a_3$
1	1	1	1
1	-1	1	-1
1	1	-1	-1
1	-1	-1	1
1	-1	-1	-1

### 4.3. Design of experiments and parametrical modeling

Table 4.6 – Model matrix of a factorial design for linear model with interactions for three parameters

$a_0$	$a_1$	$a_2$	$a_3$	$a_{12}$	$a_{13}$	$a_{23}$	$a_{123}$
1	1	1	1	1	1	1	1
1	1	1	-1	1	-1	-1	-1
1	1	-1	1	-1	1	-1	-1
1	1	-1	-1	-1	-1	1	1
1	-1	1	1	-1	-1	1	-1
1	-1	1	-1	-1	1	-1	1
1	-1	-1	1	1	-1	-1	1
1	-1	-1	-1	1	1	1	-1

The comparison starts with the simplest polynomial: linear without interaction. With only four coefficients, the average  $a_0$  and three direct effects, it is difficult to predict precisely the behavior of the system for the entire domain unless it is purely linear. However, it represents an interesting tool to rank factors. As shown in Figure 4.21, the average  $a_0$  is much larger than the effects. It becomes thus preferable to compare the ratio between the parameters and the average (Figure 4.22). The iron housing thickness  $a_3$  is clearly the prevailing parameter and the magnet height  $a_1$  is almost negligible, except for the Hadamard design. Hadamard design is an excellent tool to estimate the main effects on condition that there is no interaction. Unfortunately, interactions do appear in the present system as shown in the following validation.

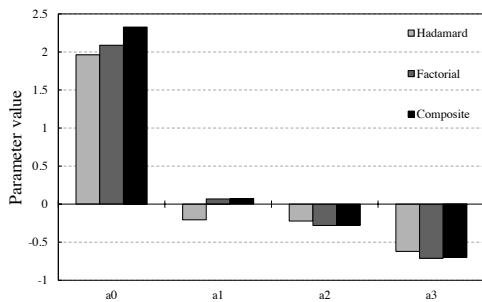


Figure 4.21 – Parameters  $a_i$  for the linear model without interaction obtained with different designs

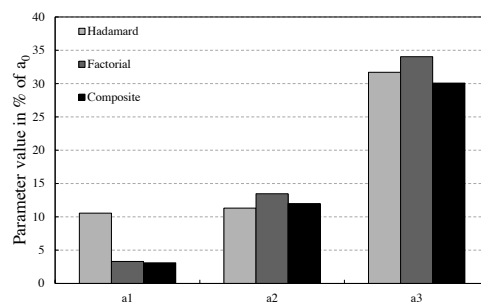


Figure 4.22 – Parameters in % of the average  $a_0$

The goal of the surface response methodology is to interpolate the behavior of the system on the entire experimental domain. Validation will thus be executed by comparing a large number of FEM simulations evenly distributed within the entire domain, with corresponding

## Chapter 4. Design methodology for linear short-stroke actuators

values obtained with the different models. For this first part, 567 geometries were computed for a total of more than hundred hours of simulations with an Intel Core 2 Duo CPU at 3.00 GHz and 3.25 GB of RAM. The results of the linear models without interaction are presented in Figure 4.23 where the oblique line stands for the reference. All linear models present a lack of accuracy. Their force characteristics are curved and dispatched which demonstrates the necessity of increasing the number of parameters.

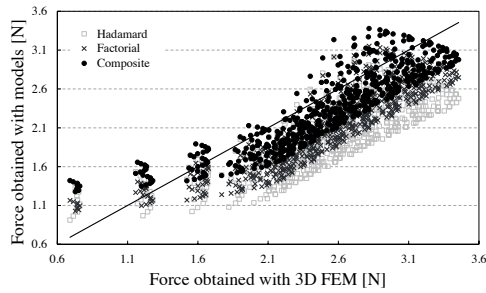


Figure 4.23 – Linear model without interaction obtained with different designs vs FEM

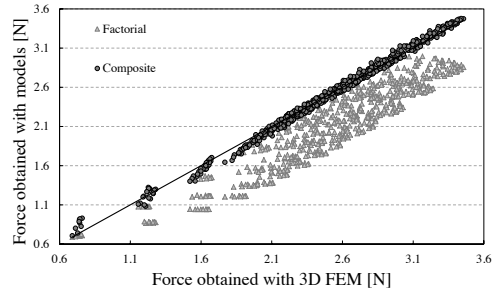


Figure 4.24 – Linear model with interactions obtained with factorial design and quadratic model with interactions obtained with composite design vs FEM

To prove the presence of interactions, the factorial design is used to generate a linear model taking first and second order interactions into account (Table 4.6 and (4.10)). The repartition of the direct effects stays similar and one remarks a peak at  $a_{23}$  corresponding to the interaction between magnet length and housing thickness (Figures 4.25 and 4.26). The force characteristic is straightened but still spread and shifted (light gray in Figure 4.24). A quadratic model thus seems necessary to increase accuracy.

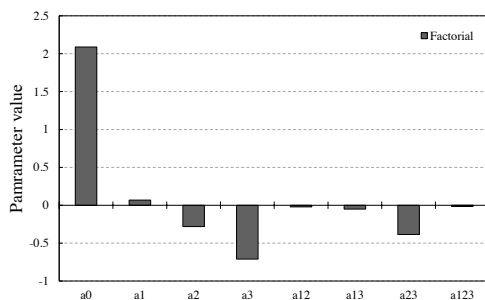


Figure 4.25 – Parameters  $a_i$  for the linear model with interactions obtained with factorial design

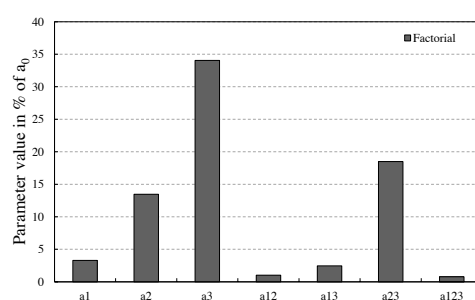


Figure 4.26 – Parameters in % of the average  $a_0$

With only eight simulations, a factorial design cannot generate the eleven parameters of a quadratic model with interactions for 3 factors (4.11). A quadratic model matrix is thus created

### 4.3. Design of experiments and parametrical modeling

from the composite set of experiments. The obtained vector  $\vec{a}$  corresponding to the model matrix  $\mathbf{X}$  of Table 4.4 is presented in Table 4.7.

Table 4.7 – Parameters  $\vec{a}$  of the quadratic model obtained with the composite design presented in Figure 4.20

average	linear effects			interactions			quadratic effects			inter.
$a_0$	$a_1$	$a_2$	$a_3$	$a_{12}$	$a_{13}$	$a_{23}$	$a_{11}$	$a_{22}$	$a_{33}$	$a_{123}$
2.81	0.07	-0.28	-0.70	-0.02	-0.05	-0.39	-0.21	-0.46	-0.05	-0.02

As already mentioned in subsection 4.3.2 the difference between the composite designs using  $\alpha=1$  or 1.22 is negligible (Figures 4.27 and 4.28). It will thus be set to 1 for the rest of the section. Linear parameters and interactions are proportionally similar to the previous models but additional quadratic terms justify the utilization of this polynomial. Without surprise,  $a_{22}$  corresponding to the magnet length is important. It comes from the square shape of the magnet: indeed, doubling the magnet length quadruples the area crossed by the flux. The force characteristic is greatly improved and fits the reference line (dark grey in Figure 4.24).

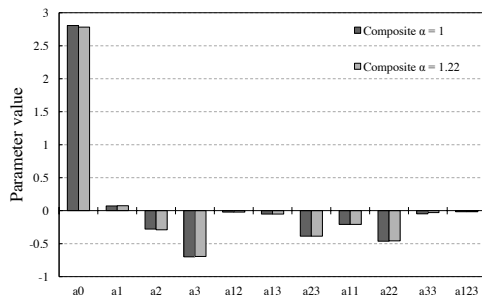


Figure 4.27 – Parameters  $a_i$  for the quadratic model with interactions obtained with the composite design

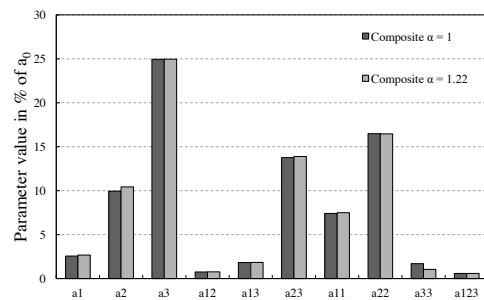


Figure 4.28 – Parameters in % of the average  $a_0$

Finally, to illustrate the good fit obtained with the quadratic model in Figure 4.24, three surfaces are plot for three different heights of the magnet giving thus an insight of the model accuracy (Figure 4.29).

#### Real iron characteristics

FEM offers the possibility to enter the magnetic properties of materials such as saturation level and magnetic permeability. It represents an advantage, especially for compact systems for which it is not possible to enlarge iron surfaces affected by saturation. Properly dealing with saturation allows for volume and performance improvement. The analysis of the parameters  $\vec{a}$  for the quadratic model obtained with the composite design (Table 4.8 and Figures 4.30 and

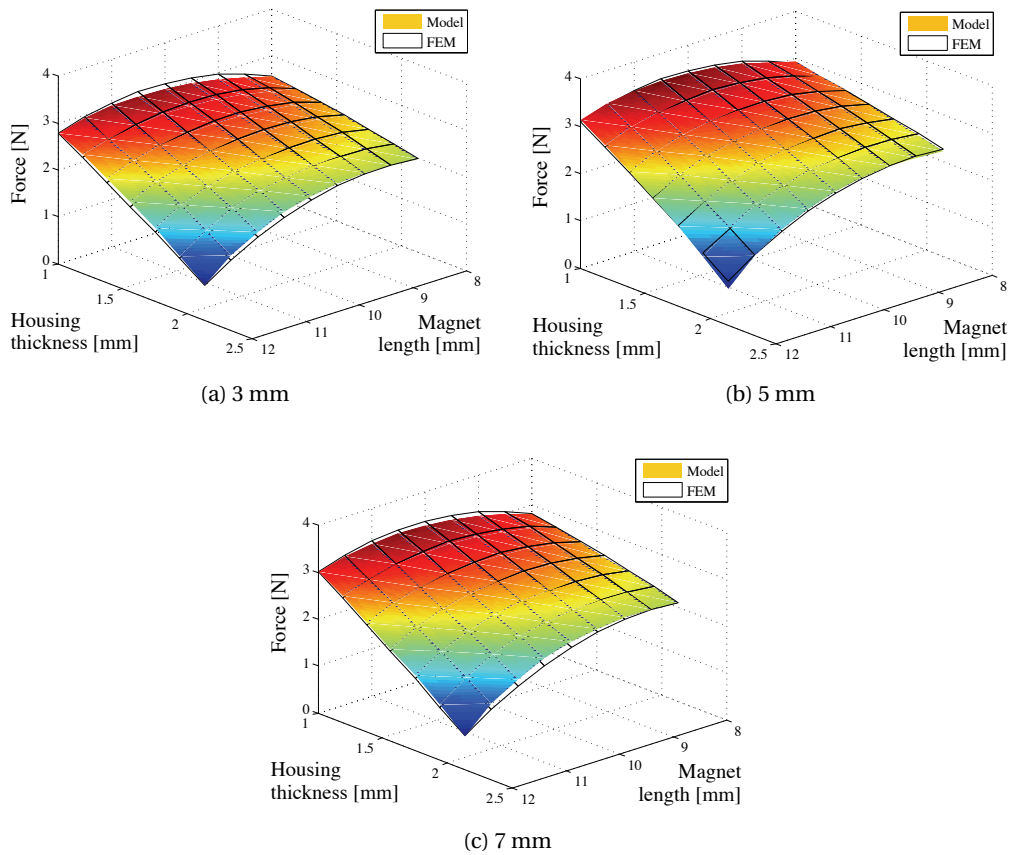


Figure 4.29 – Comparison between the quadratic model of the force (Table 4.7) and FEM simulations for different magnet heights

4.31) shows a behavior similar that of the model neglecting saturation. The main difference is the reinforcement of quadratic effects generated by the saturation affecting the iron housing.

Table 4.8 – Parameters  $\vec{a}$  of the quadratic model obtained with the composite design presented in Figure 4.20 taking saturation into account

average	linear effects			interactions			quadratic effects			inter.
$a_0$	$a_1$	$a_2$	$a_3$	$a_{12}$	$a_{13}$	$a_{23}$	$a_{11}$	$a_{22}$	$a_{33}$	$a_{123}$
2.77	0.03	-0.37	-0.35	-0.03	0.02	-0.21	-0.22	-0.39	-0.19	0.00

Once again, the models are validated using a comparison with FEM simulations evenly distributed within the experimental domain. 75 simulations are computed for geometries taking saturation into account. Linear models with or without interaction are still not sufficient (Figures 4.32 and 4.33) and a quadratic model is required (dark grey in Figure 4.33). An important observation is the decrease of the maximum FEM force from 3.46 N to 2.86 N between ideal



### 4.3. Design of experiments and parametrical modeling

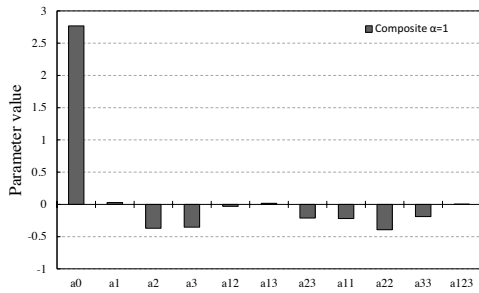


Figure 4.30 – Parameters  $a_i$  for the quadratic model with interactions obtained with the composite design

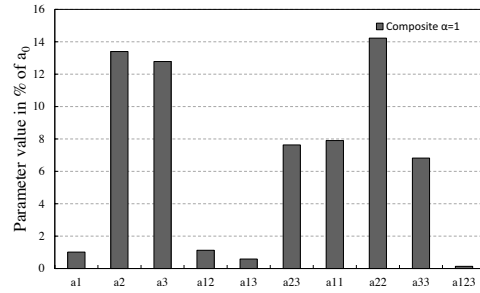


Figure 4.31 – Parameters in % of the average  $a_0$

and real iron characteristics for the quadratic model.

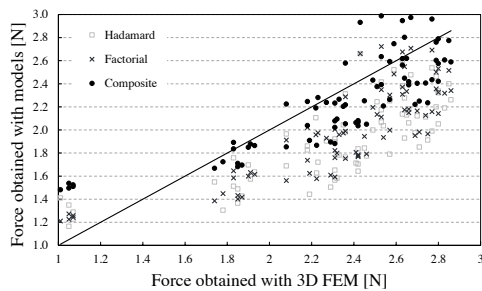


Figure 4.32 – Linear model without interaction obtained with different designs vs FEM with saturation

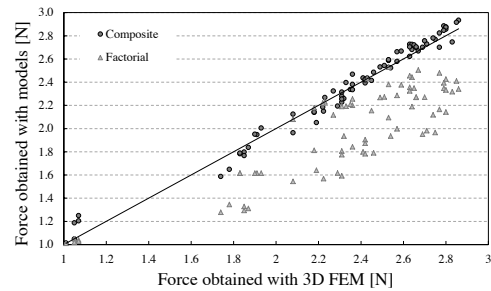


Figure 4.33 – Linear model with interactions obtained with factorial design and quadratic model with interactions obtained with composite design vs FEM with saturation

#### 4.3.5 Statistical analysis

A probability analysis is performed for a detailed interpretation of the results. The quadratic model being the best candidate for an optimization (Figures 4.24 and 4.33), it is studied in this subsection taking, or not, saturation into account. A straightforward tool showing the repartition of model errors is to divide their range into fixed length intervals and count the number of experiments falling in each division. For both cases, the cumulative histogram is compared to the normal distribution  $n$  obtained with the mean  $\mu$  and standard deviation  $\sigma$  of

the error vector.

$$n(x) = \frac{1}{\sqrt{2\pi\sigma^2}} e^{-\frac{(x-\mu)^2}{2\sigma^2}} \tag{4.15}$$

The normal distribution, as indicated by its name, is accepted by the scientific community to describe the way a cluster of points would naturally arrange around a mean. In industry, it is used to measure the dimensions of parts coming out of a production line in order to detect the number of defects. In the case of the actuator modeling without saturation, the histogram approaches a normal behavior (Figure 4.34). It comes out that 96.7% of the absolute errors are spread between -0.1 N and 0.1 N. Another way to represent the accuracy is the cumulative distribution function (Figure 4.35). Few off-centered errors going down to -0.18 N mainly affect weak force values. For these cases, the coil is so slim that a lack of FEM nodes reduces computation accuracy. However, as it only affects low forces, it does not disturb the optimization process.

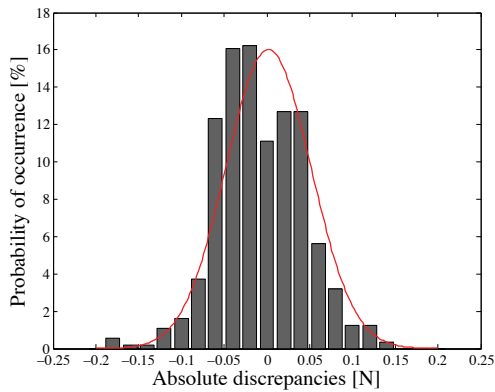


Figure 4.34 – Probability distribution of absolute discrepancies between the quadratic model and FEM

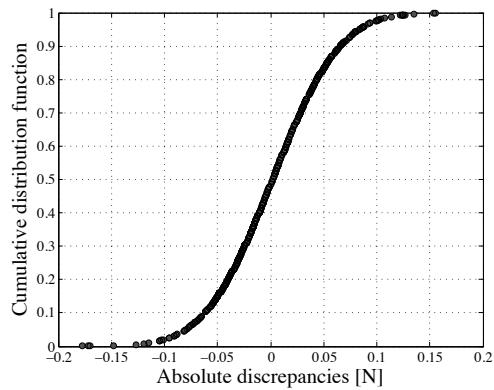


Figure 4.35 – Cumulative distribution function of absolute discrepancies

The analysis is repeated for the second quadratic model integrating real iron characteristics (Figures 4.36 and 4.37). Similar observations can be made and 89.4% of the errors are given between -0.1 N and 0.1 N. In both cases, the maximum is slightly shifted to the left creating a bias of the mean.

The discrepancies are finally shown relatively to the value of the force. As explained before, the largest errors appear for small force values and thus, their percentage gets even larger. Rare indeed are the discrepancies greater than 5%. 95.1% of the model points fit FEM with a relative error inferior to 5% for ideal iron experiments and 90.7% for real iron.

### 4.3. Design of experiments and parametrical modeling

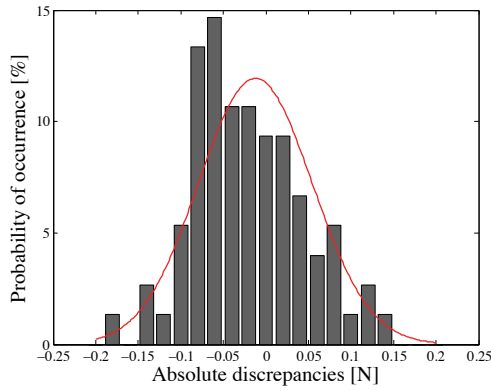


Figure 4.36 – Probability distribution of absolute discrepancies between quadratic model and FEM with saturation

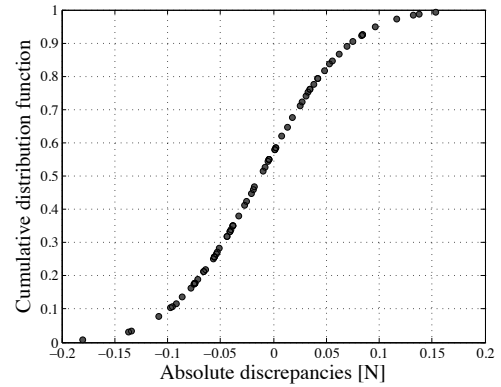


Figure 4.37 – Cumulative distribution function of absolute discrepancies with saturation

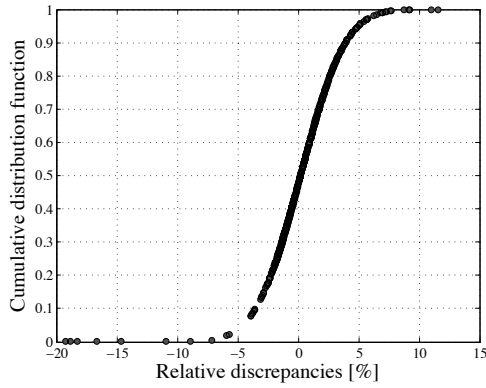


Figure 4.38 – Cumulative distribution function of relative discrepancies without saturation

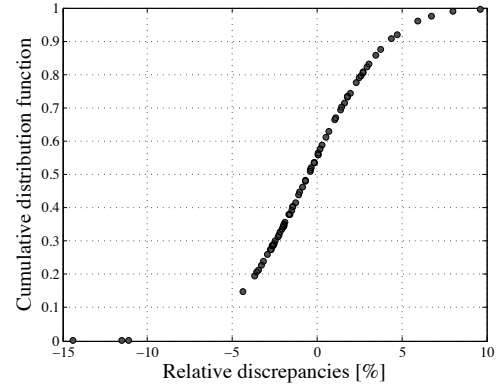


Figure 4.39 – Cumulative distribution function of relative discrepancies with saturation

Means, standard deviations, maximums and corresponding discrepancies of the quadratic models are summarized in Tables 4.9 and 4.10.

Table 4.9 – Discrepancy analysis of the quadratic models

	Ideal iron		Real iron	
	mean $\mu$	sigma $\sigma$	mean $\mu$	sigma $\sigma$
Absolute errors [N]	0.0018	0.0498	-0.0123	0.0669
Relative errors [%]	0.1962	2.9037	-0.5051	3.7155

Table 4.10 – Maximums and discrepancies with FEM of the quadratic models

Model	Max force [N]	Abs. discrepancy [N]	Rel. discrepancy [%]
Ideal iron	3.48	0.037	1.05
Real iron	2.93	0.074	2.53

In conclusion, the hybrid method mixing FEM and statistical DOE presented in this section is suitable for an accurate parametrical modeling of the force. Relative discrepancies stay as a majority within a 5 % range and go below 3 % for maximum values. It has to be mentioned that the numerous FEM simulations run in this chapter are used to validate the method and not to find the optimum. Indeed, once the method is recognized as accurate, the optimum is found using the model only and a few simulations around the optimal configuration are sufficient to confirm it. However in the present case, the numerous FEM simulations covering the entire experimental domain possess the second advantage of directly giving a geometry approaching the optimum which is kept without further analysis of the model. This geometry actually represents only the maximum among the FEM simulations run for validation. A proper optimization process should be computed on the parametrical model so as to get the real optimum of the function. However, as the present section aim is the validation of the parametrical modeling, this maximum is considered as an optimum. The proper optimization process will be addressed in section 4.5. The maximum force of the model obtained for the actuator in low position taking saturation into account is 2.93 N at 1 A. This value matches the maximum FEM result giving 2.86 N for the same dimensions:  $x_1 = 5$ ,  $x_2 = 10$ ,  $x_3 = 1$  mm. Compared with the initial actuator (Figure 4.6), it represents a force improvement of 27.4% (respectively 24.3% for FEM). Moreover, the total weight of the actuator decreases of 19.5%, from 22 g to 17.7 g according to FEM computations.

## 4.4 Design improvement

### 4.4.1 Linearization of the force profile

Once the force is optimized for the low position of the actuator, its profile is computed along the five millimeters of the travel. As already observed for the first version of the actuator, force is not exactly constant along the travel (Figure 4.6). Flux fringes and loops in the lower part of the airgap, largely discussed in the analytical modeling section (4.2.1), explain this variation. Completely removing fringes in such small actuators appears unfeasible. The solution is thus to make sure the level of fringes crossing the coil is as constant as possible along the travel. It is made possible thanks to three geometrical modifications presented in Figure 4.40: the introduction of a "mechanical offset" under the magnet ( $w_3$ ), saturation avoidance in the bottom housing part ( $w_2$ ) and a higher coil ( $h_c$  not visible here), increasing thus the total number of free factors to seven.

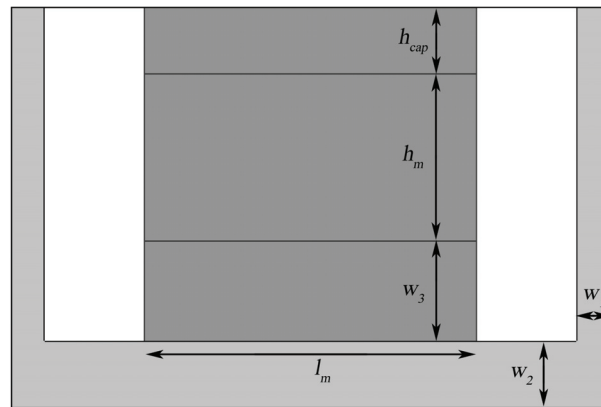


Figure 4.40 – Geometry improvements for linearization and new factors

In the specifications given in Table 4.1, an indicative value of 10 mm limits the actuator height. For the sake of improving the force linearity, it is decided to slightly increase this boundary. The geometry obtained in the previous section constitutes the base for the linearization. Its corresponding force profile computed with FEM goes up to 3.09 N and falls to 2.46 N, which represents a relative non-linearity of 20.5 % (Figure 4.41).

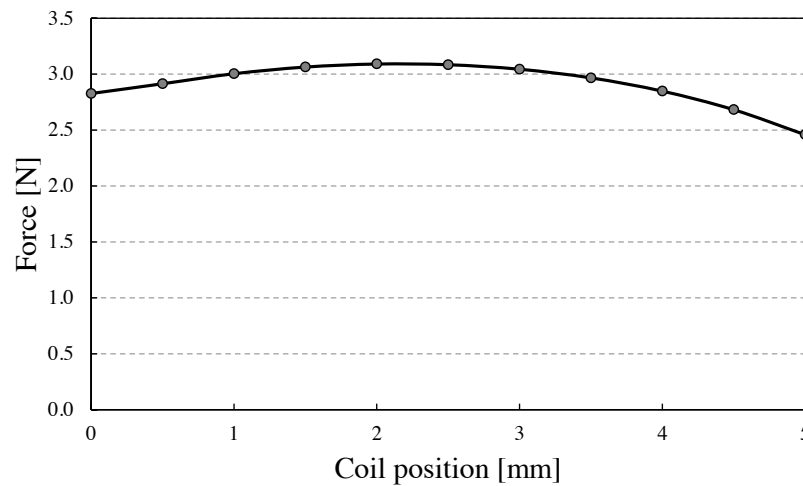


Figure 4.41 – Force profile corresponding to the optimal force geometry (4.3.5)

The criterion for linearization is the relative non-linearity defined as:

$$\epsilon_l = \frac{F_{max} - F_{min}}{F_{max}} \cdot 100 [\%] \quad (4.16)$$

The positive slope described by the first part of the curve is due to the retrieval of leaks overhanging the airgap. The second major effect decreasing the force characteristic for high positions of the coil is caused by the loss of the fringes appearing below the airgap. Both of these effects have to be attenuated to flatten the profile and to do so, the linearization is performed empirically using FEM for a better comprehension of the phenomena.

### Mechanical offset

Inserting an iron thickness  $w_3$  directly below the magnet shifts the force curve to the right (Figure 4.42). The coil travels thus longer before starting to lose significant flux components. It is clear that the introduction of this new thickness increases the total height of the actuator, leading to an increased number of turns. In Figure 4.42, the number of turns is however kept constant to illustrate the effect.

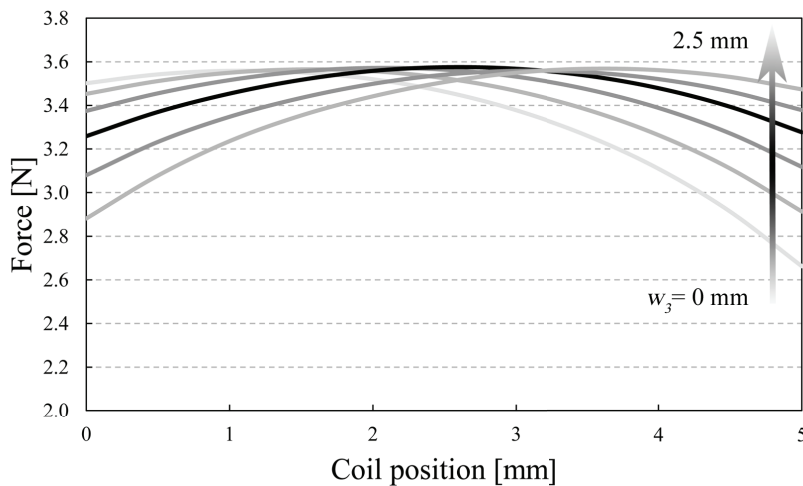


Figure 4.42 – Force profile shift provoked by a "mechanical offset"  $w_3$

### Saturation decrease in the base

The second intervention consists in adding an extra parameter  $w_2$  by distinguishing the thickness of the walls from the bottom thickness. Indeed, the iron section crossed by the flux in the bottom part of the housing gets smaller when approaching the center. A thickness of only 1 mm generates saturation that curves the flux lines in the lower airgap. Increasing  $w_2$  thus decreases the general leakage, avoids magnetic loops in the lower part of the airgap and cancels negative force components that could exist when the coil is down. Consequences are an increase of the force and the flattening of the first part of the curve (Figure 4.43). In the present case, the effect converges from  $w_2 = 2$  mm.

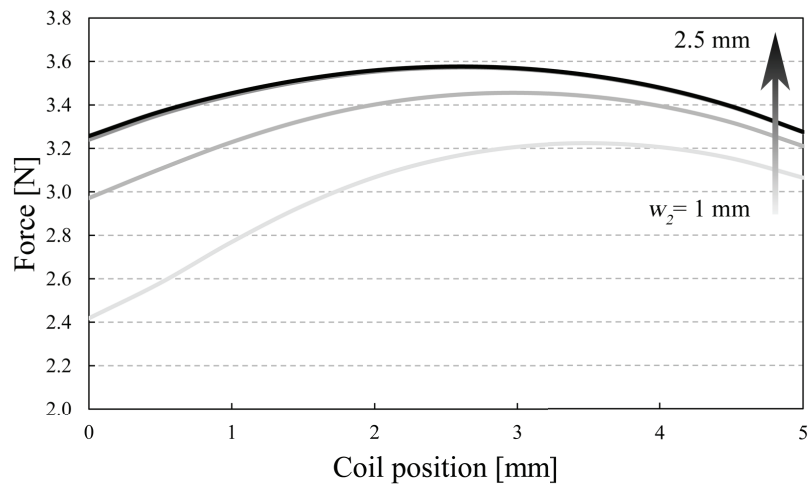


Figure 4.43 – Force profile shift provoked by an enlargement of the housing bottom  $w_2$

#### Upper fringes recovery

Finally, the coil height  $h_c$  and so the number of turns  $N$  are adapted so as to take advantage of the fringes overhanging the airgap, which flattens the left part of the force profile. Combining the three improvements presented above results in the force characteristic of Figure 4.44. The force varies between 3.63 and 3.76 N, corresponding to a relative non-linearity of 3.36 %. The actuator dimensions are summarized in Table 4.11.

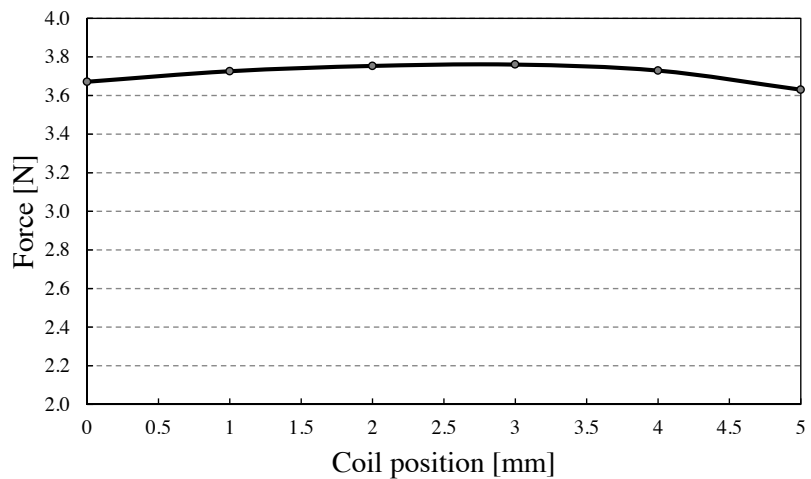


Figure 4.44 – Actuator force characteristic after linearization process

Table 4.11 – Actuator dimensions after linearization process [mm]

$h_m$	$l_m$	$h_{cap}$	$w_1$	$w_2$	$w_3$	$h_c$	$N [-]$
5	10	2	1	2	3	13	536

#### 4.4.2 Prototype

Following the linearization process, a second prototype is built. A plastic frame is added to support the winding, integrate a position sensor and guide the actuator (Figures 4.45 and 4.46). The frame is composed of two parts: the coil holder, moving inside the actuator and supporting the coil, and the external guidance sliding along the housing. The number of turns is inevitably reduced by the presence of the frame in comparison with a self-supporting coil. Indeed, the number of turns  $N$  decreases of 25 % to 400 and the new coil height  $h_c$  is 12.5 mm, increasing the relative non-linearity to 6.7 %. An additional board embedding a piezoresistive force sensor is mounted on the top of the actuator for testing purpose (Figure 4.45). The total weight including the force sensor is 28 g.

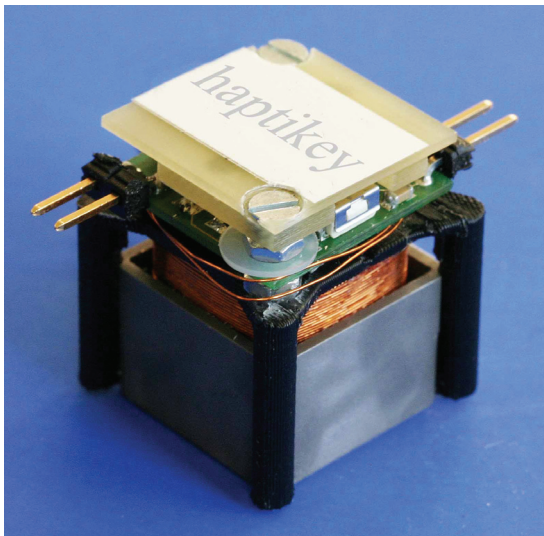


Figure 4.45 – Second prototype with embedded force sensor

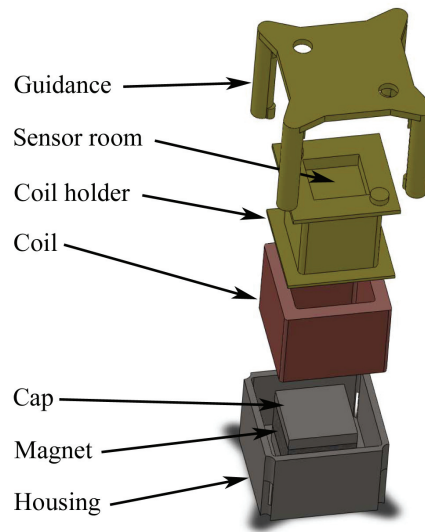


Figure 4.46 – Exploded view of the second prototype with guiding system

Unfortunately, this arrangement does not slide as smoothly as expected. In fact, the guidance is too loose and the tolerances of the coil are too large, leading to unwanted friction during the stroke. It can be observed on the comparison between measurements and FEM predictions at 0.5 A (Figure 4.47). The fit is quite good, but small variations disturb the profile, increasing the relative non-linearity to 11.8%.

In conclusion, despite parasitic friction attributed to the guidance, the increase of the number



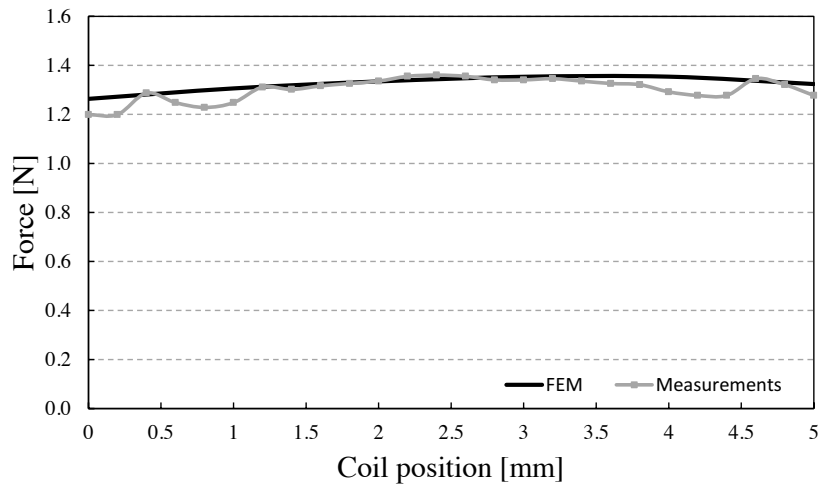


Figure 4.47 – Measurements vs FEM for the second prototype at 0.5 A

of geometrical factors to seven, allowing for three mechanical adaptations, greatly improves the linearity of the force. Precautions however have to be taken regarding the coil dimensions and tolerances which strongly influence the linearity. Moreover, Figure 4.47 confirms that FEM results match with measurements on manufactured prototypes and can be considered as reference.

## 4.5 Full parametrical setup

The method presented in section 4.3 provides a parametrical model of the force generated by an actuator using three-dimensional finite element simulations judiciously driven by the design of experiments. This method synthesizes a behavior but does not directly lead to an optimum. Moreover, the numerous phases of the design of experiments necessary to obtain a model from an initial geometry, jumping from finite elements to matrix computations and vice versa, can be confusing for the designer. For these reasons, the present section addresses a full parametrical setup covering the entire optimization process of short-stroke electromechanical actuators, from the initial to the optimal geometry, with only one software interface for each kind of actuator.

Many references related to the design of experiments together with finite element modeling can be found in literature, mainly for mechanical applications such as the deformation prediction of disc brakes [122] and microaccelerometers [123] or the design of steel wheels [124]. In the domain of ultrasonic motors, it has also been used to mechanically increase the magnitude of deformation [125, 126]. However, rare are the applications using this methodology in electromechanical engineering. Park and Min [127] propose to use 2D finite element modeling to design magnetic actuators with non-linear ferromagnetic materials but we could not find fully integrated optimization interfaces involving design of experiments and 3D FEM

for the design of electromagnetic actuators.

The aim of the full parametrical setup is thus to integrate and automate the entire optimization process. Its principle is summarized in the block diagram of Figure 4.48. Two main programs are used in the process. On one side, a technical computing software (Matlab) manages the sequence of events and on the other side, a finite element modeling software (Flux 3D) runs the simulations defined by the design of experiments.

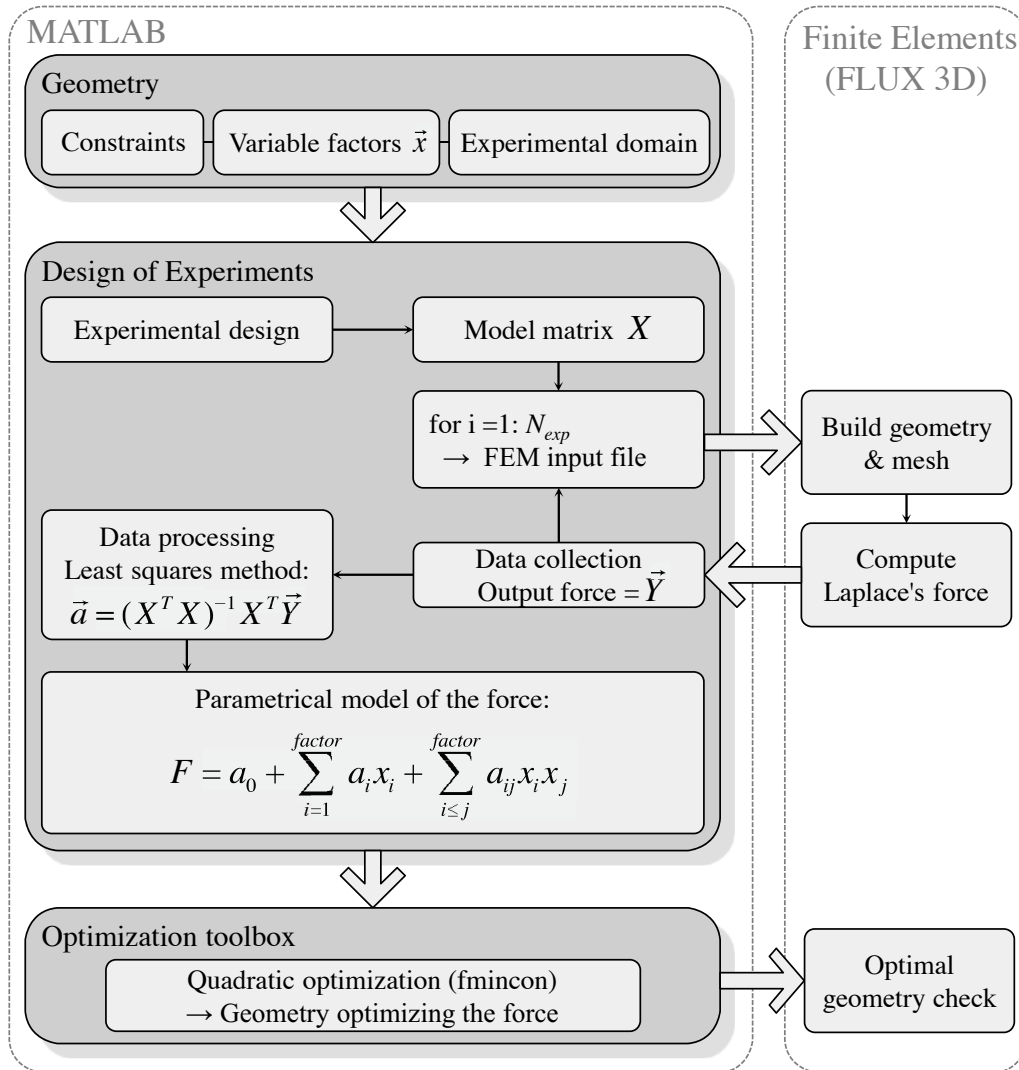


Figure 4.48 – Block diagram of the full parametrical setup

At first, the user enters the different geometry constraints and variable factors defining the experimental domain based on the actuator specifications. This can be done directly within a file or through a graphic user interface such as in Figure 4.49, specific to each actuator configuration, for a better ease of use.

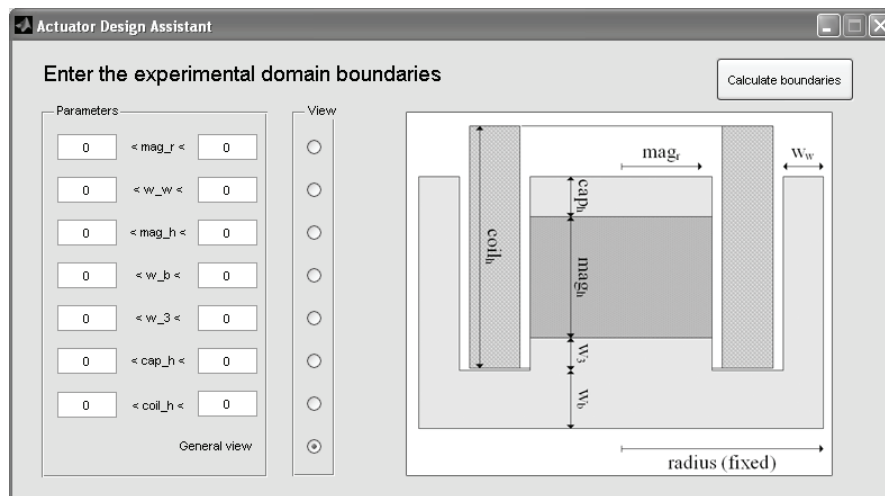


Figure 4.49 – Graphic user interface for the experimental domain definition

Then, according to a pre-defined design, the matrix of experiments is built with each of its rows corresponding to a geometry. As presented in the results of the square actuator modeling (4.3.4), a quadratic model with interactions is required so as to accurately interpolate the actuator force on the entire experimental domain. In order to have a large enough set of simulations at disposal, the composite design introduced in Figure 4.20 is selected. According to the chosen quadratic model and the matrix of experiments, the model matrix  $X$  is finally built.

For each actuator configuration contained in the experimental matrix, a text file is created and run by the finite element software in batch mode using a second programming language (Python). For each repetition of the loop, the force is saved in the output vector  $\vec{Y}$  and once all the simulations are completed, the obtained data is processed in Matlab and the parametrical model of the force is computed using the least squares method.

The last step consists in finding the geometry optimizing the force generated by the actuator. As the model is a quadratic polynomial with interactions, several well-trying solutions exist and are embedded in today's computation programs. In the present case, a Matlab function finding the minimum of constrained nonlinear multivariable polynomials is used (*fmincon*). Without going into detail, this tool computes the partial derivatives of the polynomial, starting from an initial condition  $\vec{x}_0$ , to converge towards an optimum. The fact that the force generated by the studied short-stroke electromechanical actuators approaches a quadratic behavior (section 4.3.4) avoids having local optimums and so, the solution provided by the optimization algorithm can directly be considered as a global optimum. Once the optimal geometric factors are known, a final finite element simulation is run for comparison with the value obtained with the optimization algorithm. If needed, additional simulations surrounding the optimal configuration within the experimental domain can be computed to confirm the optimum.

A great advantage of this optimization method is that it accepts non-linear constraints. Indeed, in addition to the geometrical boundaries entered by the user at the beginning of the process, it is possible to deal with a large variety of other constraints opening the way for multi-physic optimization. For instance, simple analytical models such as for the actuator weight or the thermal convection, which are not influenced by magnetic effects, can be introduced as new constraints. Moreover, similarly as for the force, alternative models obtained from the design of experiments like the non-linearity of the force along a displacement or elaborated thermal models can also be considered as constraints. In other words, the user can decide which part of the actuator model requires a precise knowledge of the magnetic behavior (provided by FEM) and which part does not.

### 4.6 Actuators

In order to demonstrate the efficiency of the global methodology addressed in this chapter and show the range of potential applications, several actuators are presented and optimized using the full parametrical setup.

#### 4.6.1 Cylindrical actuator

Often neglected in academic projects, the preparation for fabrication becomes necessary when one deals with systems composed of multiple actuators. Generally designated for final products, this last step also concerns prototypes involving numerous replications of a single element. It is notably the case for multi-finger haptic systems.

It is obviously possible to manufacture the actuator as presented in the end of the linearization process (4.4.1). However, companies and subcontractors will always put effort in the simplification of the system in terms of fabrication. Saving time and money is important for all and one should always look further and see how improvements oriented towards fabrication could be brought. In the case of the square actuator used until here, manufacturing square parts necessitates milling which is time consuming in comparison to bar turning. It is thus decided to switch to a cylindrical shape for the actuator (Figure 4.50), still with an external diameter of 18 mm.

Contrarily to the first square design for which the modeling is run on the down position of the actuator only, the non-linearity observed along the coil displacement (Figures 4.6, 4.41 and 4.47) will be taken into account for the following geometries. In order to integrate the non-linearity effect, it is decided to model the average force generated by the actuator along the travel (6 mm here). The fact of maximizing the average force indirectly limits the non-linearity and optimizes the global performance of the actuator.

Based on the linearization process (Figure 4.40), up to 7 geometrical factors are available for optimization: the housing thickness  $w_1$ , the bottom thickness  $w_2$ , the bump height  $w_3$ , the

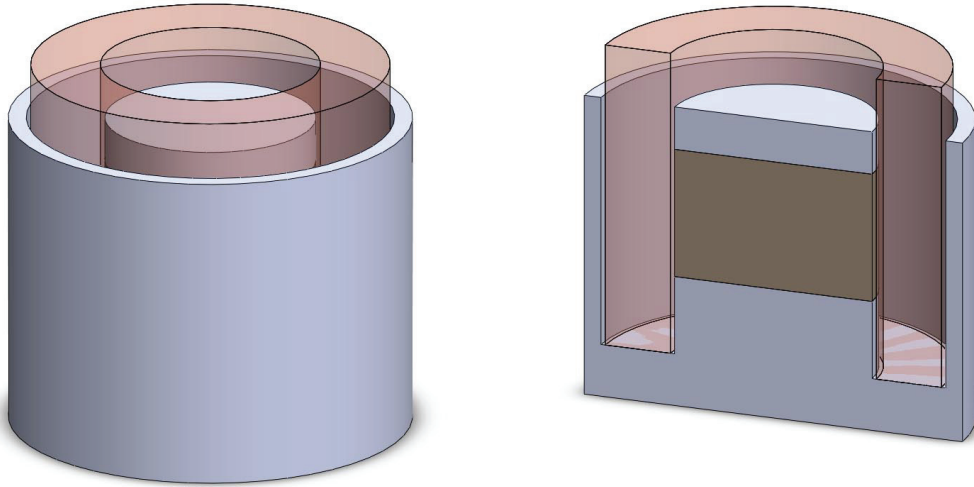


Figure 4.50 – Cylindrical actuator principle

magnet height  $h_m$  and diameter  $l_m$ , the height of the iron cap  $h_{cap}$  and the part of the coil overhanging the actuator housing  $h_c$ . In this subsection, three optimizations of the cylindrical actuator are run with respectively 3, 5 and 7 free factors for a current of 0.5 A (corresponding to a density  $j = 8 \text{ A/mm}^2$ ). Their role is mainly to show the accuracy of the method for various numbers of unknowns. For each configuration, a quadratic model with interactions is given and validated with FEM simulations and the optimal configuration is calculated.

### 3 factors

In the first configuration, 3 of the 7 geometrical parameters are considered as free factors and their boundaries are given in Table 4.12. The others, namely  $w_2$ ,  $w_3$ ,  $h_{cap}$  and  $h_c$  are fixed to respectively 2, 2.5, 2 and 2.5 mm.

Table 4.12 – Free factors for optimization

Factor	Geometrical dimension	Range [mm]
$x_1$	magnet radius ( $r_m$ )	[3-6]
$x_2$	housing thickness ( $w_1$ )	[0.8-2]
$x_3$	magnet height ( $h_m$ )	[3-6]

The full parametrical setup presented in section 4.5 is executed, generating a quadratic model of the average force with first order interactions. As the second order interactions turned out to be insignificant in the modeling of the square actuator ( $a_{123}$  in Figure 4.31), they are neglected here. The obtained model is illustrated with two histograms showing the value of

the parameters vector  $\vec{a}$ . Figure 4.51 contains the absolute values dominated by the average  $a_0$  and Figure 4.52 shows the ratio between the parameters and the average<sup>1</sup>. Similarly as for the initial square geometry (Figures 4.28 and 4.31), the housing thickness ( $a_2$ ) dominates the linear effects and the magnet radius ( $a_{11}$ ) dominates the quadratic effects. Regarding the interactions, the mutual effect brought by the magnet radius and the housing thickness ( $a_{12}$ ) is prevailing as both directly influence the number of turns participating to the force.

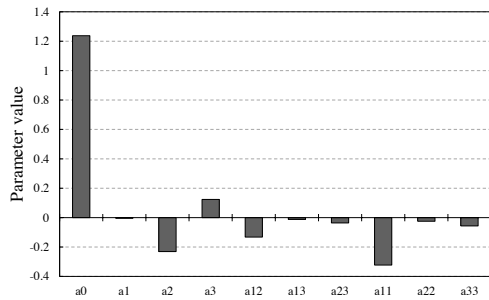


Figure 4.51 – Quadratic model parameters for 3 factors

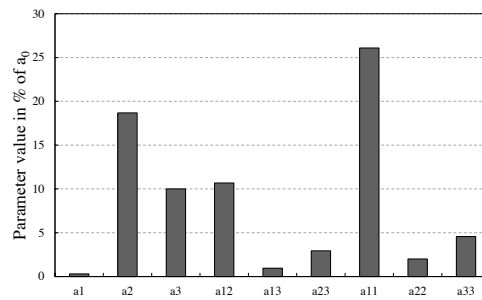


Figure 4.52 – Parameters in % of the average  $a_0$

In order to measure the accuracy of the obtained model, 48 simulations evenly distributed over the experimental domain are run with the finite element software (Figure 4.53). The model entirely fits the FEM simulations with absolute discrepancies lower than 0.1 N and 79.2 % of them are lower than 0.05 N. Regarding the errors relatively to the FEM values, 97.3 % are lower than 10 % and 81.3 % are lower than 5 %.

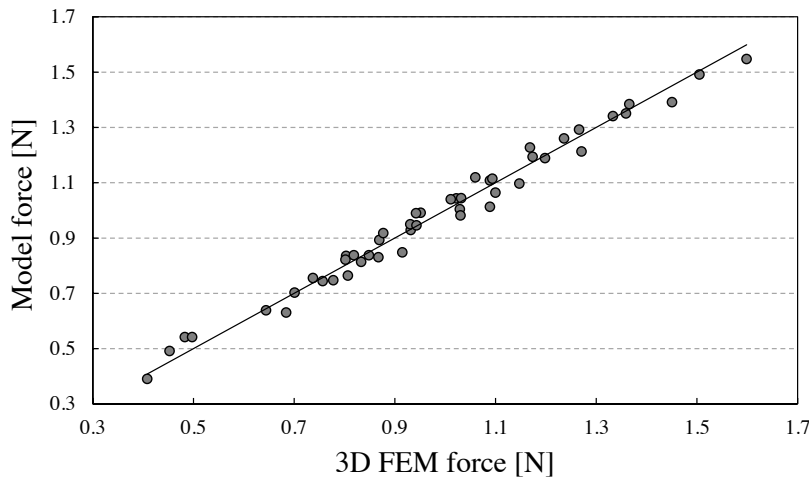


Figure 4.53 – Quadratic model vs FEM (48 simulations)

<sup>1</sup>The numerical values of the parameters vector  $\vec{a}$  are detailed in appendix A.2.1 for all the models studied in the present section.

### 5 factors

In the second configuration of the cylindrical actuator, 5 of the 7 geometrical parameters are taken as variable factors (Table 4.13) and  $h_{cap}$  and  $h_c$  are fixed to respectively 2 and 2.5 mm.

Table 4.13 – Free factors for optimization

Factor	Geometrical dimension	Range [mm]
$x_1$	magnet radius ( $r_m$ )	[3-6]
$x_2$	housing thickness ( $w_1$ )	[0.8-2]
$x_3$	magnet height ( $h_m$ )	[3-6]
$x_4$	bottom thickness ( $w_2$ )	[1-3]
$x_5$	bump height ( $w_3$ )	[1-4]

The twenty parameters of the quadratic model with interactions obtained with the parametrical setup are plot in percent of the average in Figure 4.54. The effect of the two additional factors  $x_4$  and  $x_5$  is limited but the linear effect of the latter, namely  $a_5$ , reaches 5 % anyway, which is not negligible.

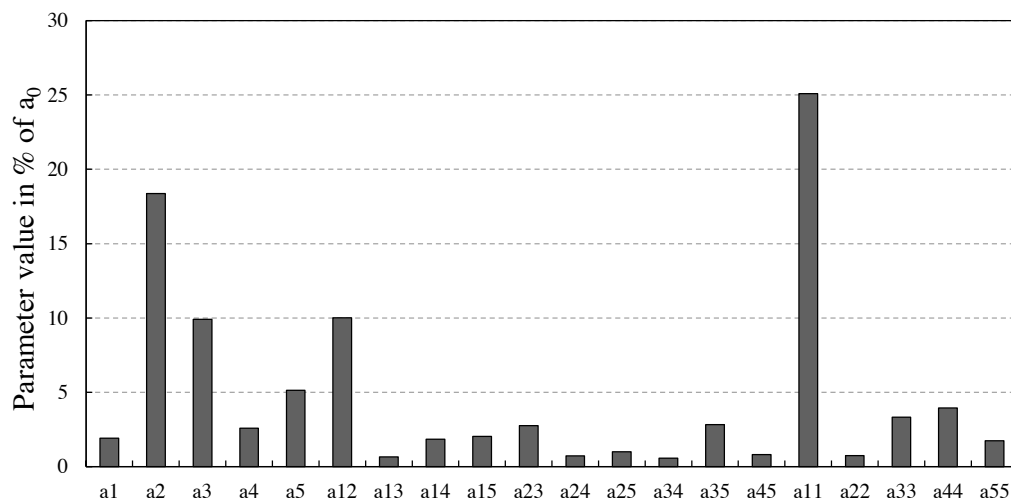


Figure 4.54 – Quadratic model parameters in % of the average  $a_0$  for 5 factors

The increasing number of free factors exponentially increases the number of simulations required for a validation using FEM simulations covering the entire experimental domain. To sidestep the problem, the validation is made by varying the parameters pair by pair and fixing the others in the middle of their range. The process gives a global overview of the model accuracy by allowing for the visualization of surfaces (Figure 4.55), in addition to the XY

representation (Figure 4.56).

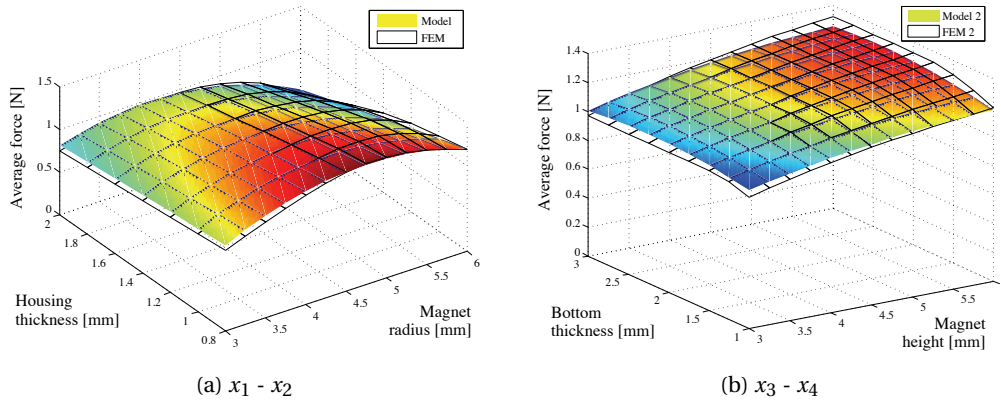


Figure 4.55 – Surface comparison between model and FEM when varying pairs of factors

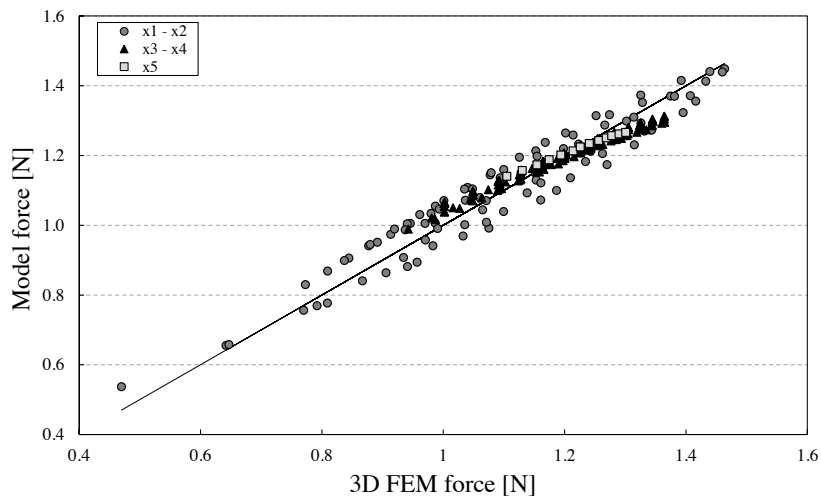


Figure 4.56 – FEM validation of the quadratic model when varying pairs of factors (221 simulations)

The fit is globally satisfying as shown in the XY representation (Figure 4.56). However, a closer look at Figure 4.55 (b) shows that for some specific plans, the matching between both surfaces does not seem optimal, showing linear discrepancies. This comes from the fact that the error is minimized for the entire experimental domain with the least squares method and so, less significant factors can punctually present unwanted errors. However, despite some local tendencies, the absolute error stays reasonable. Indeed, for all 221 simulations run for the pair validation, the relative error stays below 10 % and 78.3 % of them are lower than 5 %.



### 7 factors

The last cylindrical actuator configuration uses all the 7 factors of Table 4.14 for the optimization. The analysis of the model parameters of Figure 4.57 confirms that the linear effects of the two last factors  $x_6$  and  $x_7$ , respectively the iron cap height and the overhanging coil height, have to be taken into account in the modeling.

Table 4.14 – Free factors for optimization

Factor	Geometrical dimension	Range [mm]
$x_1$	magnet radius ( $r_m$ )	[3-6]
$x_2$	housing thickness ( $w_1$ )	[0.8-2]
$x_3$	magnet height ( $h_m$ )	[3-6]
$x_4$	bottom thickness ( $w_2$ )	[1-3]
$x_5$	bump height ( $w_3$ )	[1-4]
$x_6$	iron cap height ( $h_{cap}$ )	[1-3]
$x_7$	overhanging coil height ( $h_c$ )	[0-3]

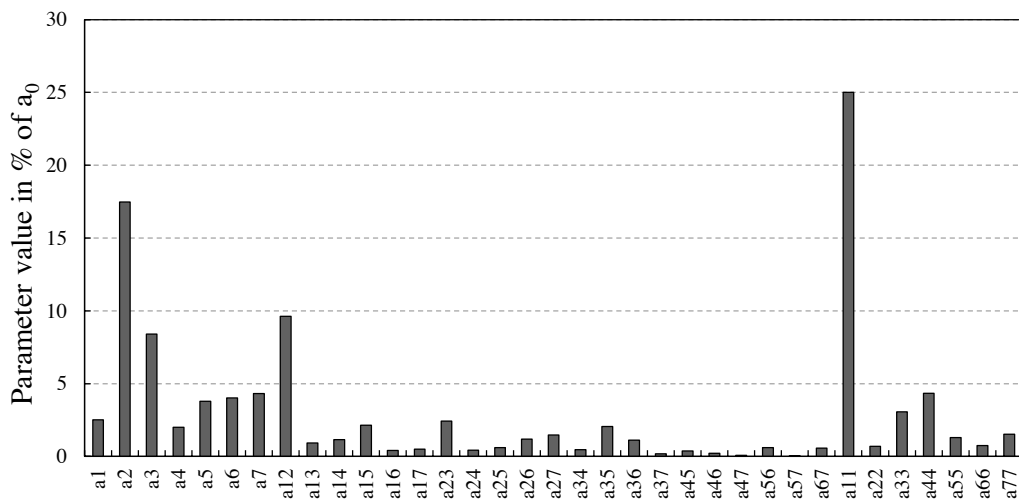


Figure 4.57 – Quadratic model parameters in % of the average  $a_0$  for 7 factors

Again, a pair validation composed of 325 simulations is used. Only 0.3 % of the model values differ from the FEM with more than 10 % and 16.3 % with more than 5 %. The same observation as previously for 5 factors can be made concerning the linear discrepancies for  $x_3 - x_4$  and  $x_5 - x_6$  (Figure 4.58).

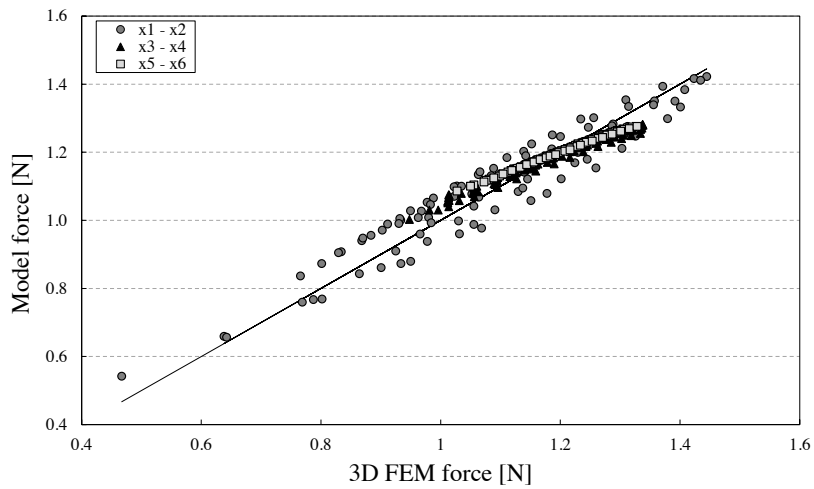


Figure 4.58 – FEM validation of the quadratic model when varying pairs of factors (332 simulations)

### Optimization

For each of the three models presented (3 - 5 - 7 factors), the value of the geometrical parameters representing the optimum obtained with the full parametrical setup are presented in Table 4.15. For each of them, a corresponding FEM simulation is run and absolute and relative discrepancies are calculated for the average force (Table 4.16).

Table 4.15 – Optimal actuator configurations

Model	$r_m$	$w_1$	$h_m$	$w_2$	$w_3$	$h_{cap}$	$h_c$
3 factors	4.77	0.8	6.0	2.0	2.5	2.0	2.5
5 factors	4.7	0.8	6.0	2.44	3.64	2.0	2.5
7 factors	4.63	0.8	6.0	2.39	3.5	3.0	3.0

Adding extra free factors to the optimization process slightly increases the average force. It is principally due to the fact that the boundaries of those additional factors increase the size of the experimental domain which results in greater forces. A side effect is that the modeling error increases with the number of free factors as shown in Table 4.16 for the optimal geometry. It is thus preferable to carefully select the most significant factors for an improved accuracy.

Table 4.16 – Average force resulting from the optimization process and comparison with FEM

Model	Model average force [N]	FEM average force [N]	Error [N]	Error [%]
3 factors	1.5578	1.6124	0.0546	3.39
5 factors	1.5870	1.6547	0.0677	4.09
7 factors	1.6150	1.7050	0.0900	5.28

#### 4.6.2 Square actuator II

In order to improve its performances, a new version of the square actuator is obtained by merging the initial square geometry with the cylindrical geometry. The second version of the square actuator presented in this subsection thus combines the high force density of the square actuator and the ease of manufacturing of the cylindrical actuator (Figure 4.59). The main advantage is that the part of the housing that is not facing the iron cap can be dug more largely, creating a discontinuity in alignment, so as to decrease the fringes responsible for the non-linearity under the airgap (Figure 4.12). Secondly, the airgap can be widened as the flux originally flowing through the outer walls concentrates in the corners (Figure 4.59 left) which offers a sufficient surface to avoid saturation and so decrease the non-linearity of the force. Similarly as for the cylindrical actuator, two models of the force, averaged on a 5 mm displacement, are established for 5 and 7 free factors. The minimum thickness of the walls below the airgap (Figure 4.59 right) is fixed at 0.1 mm for mechanical reasons making thus the factors identical as for the cylindrical actuator.

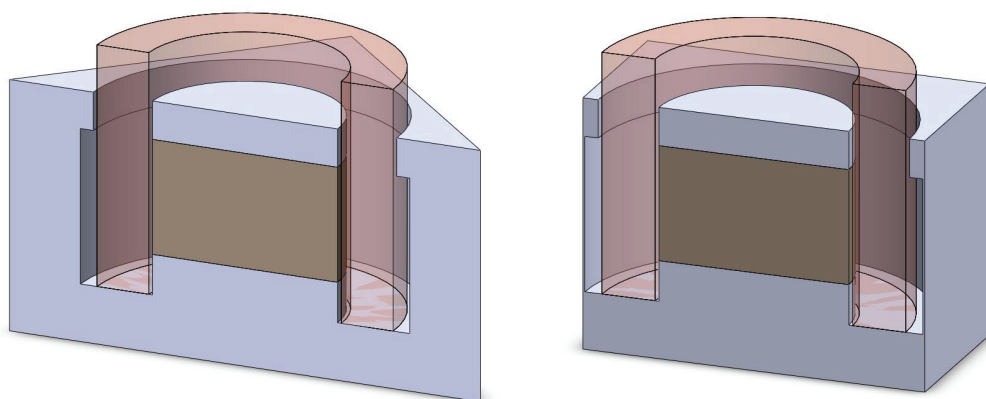


Figure 4.59 – Square actuator principle

## Chapter 4. Design methodology for linear short-stroke actuators

### 5 factors

The factors delimiting the experimental domain are summarized in Table 4.17. As for  $h_{cap}$  and  $h_c$ , they are fixed to respectively 2 and 2.5 mm.

Table 4.17 – Free factors for optimization

Factor	Geometrical dimension	Range [mm]
$x_1$	magnet radius ( $r_m$ )	[3-6]
$x_2$	housing thickness ( $w_1$ )	[0.8-2]
$x_3$	magnet height ( $h_m$ )	[3-6]
$x_4$	bottom thickness ( $w_2$ )	[1-3]
$x_5$	bump height ( $w_3$ )	[1-4]

The vector of parameters  $\vec{a}$  for the quadratic model with first order interactions (Figure 4.60) is without surprise similar to the cylindrical configuration.

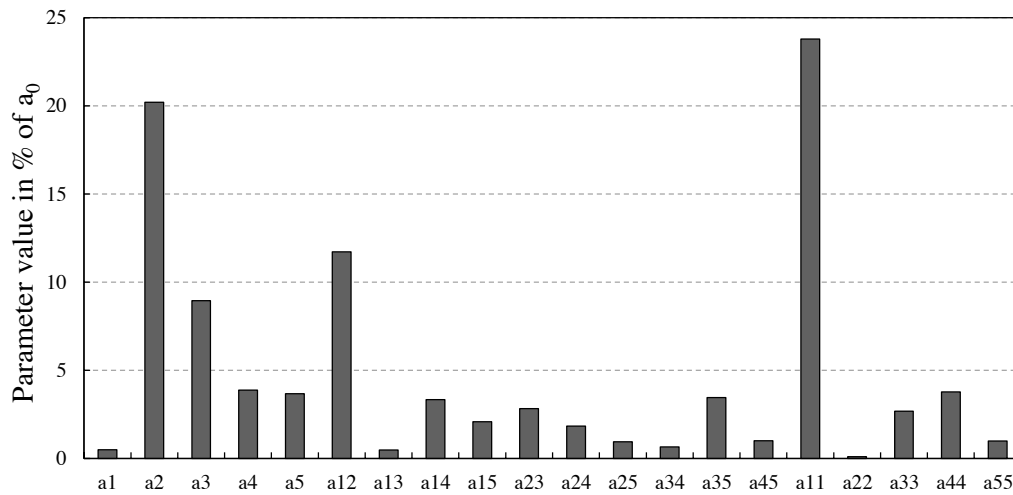


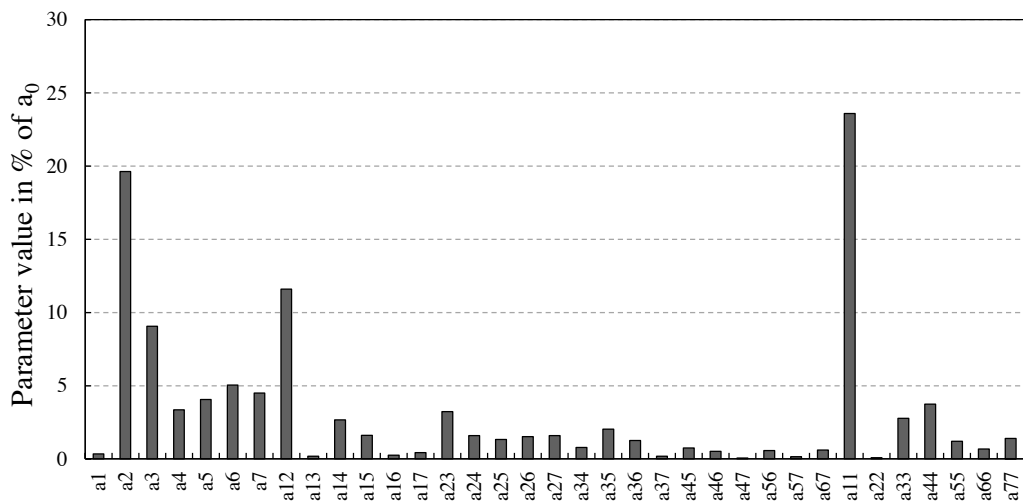
Figure 4.60 – Quadratic model parameters in % of the average  $a_0$  for 5 factors

### 7 factors

Ibid for 7 factors (Table 4.18 and Figure 4.61).

Table 4.18 – Free factors for optimization

Factor	Geometrical dimension	Range [mm]
$x_1$	magnet radius ( $r_m$ )	[3-6]
$x_2$	housing thickness ( $w_1$ )	[0.8-2]
$x_3$	magnet height ( $h_m$ )	[3-6]
$x_4$	bottom thickness ( $w_2$ )	[1-3]
$x_5$	bump height ( $w_3$ )	[1-4]
$x_6$	iron cap height ( $h_{cap}$ )	[1-3]
$x_7$	overhanging coil height ( $h_c$ )	[0-3]

Figure 4.61 – Quadratic model parameters in % of the average  $a_0$  for 7 factors

### Optimization

The properties of the optimal geometries obtained for 5 and 7 free factors are shown in Tables 4.19 and 4.20. The magnitude of the average force increases of respectively 5.3 and 8.1 % compared with the cylindrical actuator models. As for the discrepancies with the corresponding FEM simulations they stay in the same admissible order of magnitude.

For the present actuator configuration, no validation of the model using a grid of FEM simulations covering the entire domain is done. Instead, a star validation is directly run around the optimum obtained from the model. The principle of the star validation is presented in Figure 4.62 for 3 factors. Its aim is to run simulations on the main axes (two per factor), equidistant from the optimum which represents the center of the star and see if the obtained

Table 4.19 – Optimal actuator configurations

Model	$r_m$	$w_1$	$h_m$	$w_2$	$w_3$	$h_{cap}$	$h_c$
5 factors	4.99	0.8	6.0	3.0	2.11	2.0	2.5
7 factors	4.9	0.8	6.0	3.0	4.0	3.0	3.0

Table 4.20 – Average force resulting from the optimization process and comparison with FEM

Model	Model average force [N]	FEM average force [N]	Error [N]	Error [%]
5 factors	1.6707	1.6957	0.0250	1.47
7 factors	1.7452	1.8374	0.0922	5.02

geometry really maximizes the average force. In the case where a point of the star is outside the experimental domain, it is simply skipped.

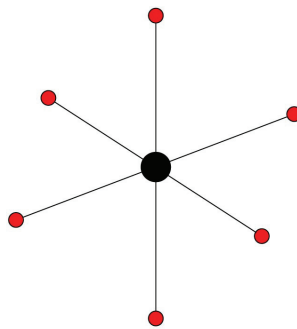


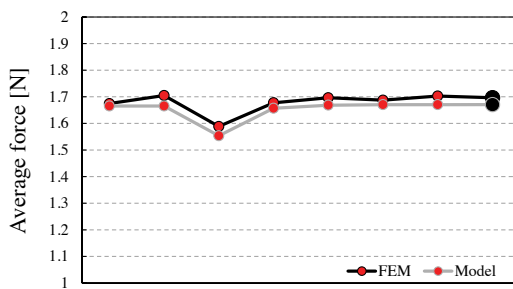
Figure 4.62 – Star validation principle for 3 factors (• = optimum)

A star validation with a radius of 0.2 mm is detailed hereinafter for the geometry obtained from the 5 factors model. The simulations surrounding the optimal geometry within the experimental domain are run using FEM. The geometrical parameters  $x_{1-5}$  are shown in Table 4.21. The first observation when plotting the average force is that the profile is not very steep around the optimum making it close to its neighbors (Figure 4.63 (a)). With the modeling discrepancy, it can happen that a surrounding value is equal or slightly higher than the optimum. The comparison between each point of the star and the optimal geometry (last column of Table 4.21) confirms this with two results greater than the optimum. However, the error stays below 0.5 % and can thus be tolerated. A second implementation of the star validation is executed with a radius of 0.5 mm showing similar results (Figure 4.63 (b)). The complete matrix is put in appendix A.2.2.

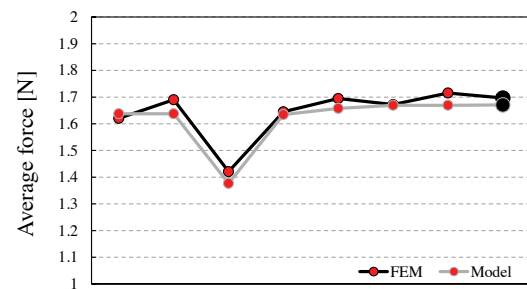
The same principle is applied to the 7 factors model and presented in Figure 4.64. As predicted in Table 4.20, the modeling error is slightly higher for 7 factors but the fit is generally good.

Table 4.21 – Dimensions [mm] and results of the star validation with a radius of 0.2 mm for the square actuator with 5 factors

$x_1$	$x_2$	$x_3$	$x_4$	$x_5$	$F$ model [N]	$F$ FEM [N]	Error with optimum [%]
4.79	0.8	6	3	2.11	1.665	1.675	1.29
5.19	0.8	6	3	2.11	1.665	1.705	-0.49
4.99	1.0	6	3	2.11	1.553	1.589	6.37
4.99	0.8	5.8	3	2.11	1.657	1.677	1.13
4.99	0.8	6	2.8	2.11	1.668	1.696	0.02
4.99	0.8	6	3	1.91	1.670	1.688	0.53
4.99	0.8	6	3	2.31	1.670	1.703	-0.37
4.99	0.8	6	3	2.11	1.671	1.697	optimum

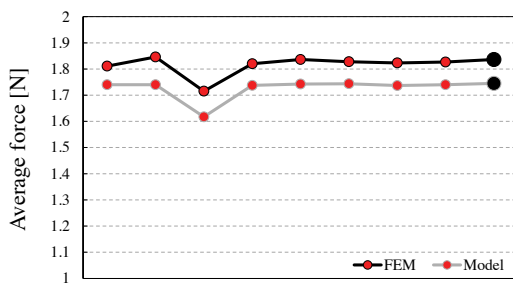


(a) 0.2 mm radius

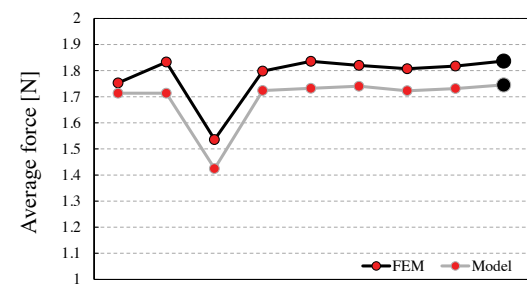


(b) 0.5 mm radius

Figure 4.63 – Average force of the star validation around the optimum (•) obtained respectively with the 5 factors model and FEM



(a) 0.2 mm radius



(b) 0.5 mm radius

Figure 4.64 – Average force of the star validation around the optimum (•) obtained respectively with the 7 factors model and FEM

## Chapter 4. Design methodology for linear short-stroke actuators

Despite the fact that a few surrounding simulations show better performances than both optimums (5 and 7 factors), the discrepancy stays below 1.11 % for the four star validations (see A.2.2 for details). It is acceptable and thus validates the method and the optimal geometries.

### 4.6.3 Fixed magnet actuators

Sometimes, the person in charge of the design of an actuator receives additional constraints. In the present case, in order to avoid the cost of a tailor-made magnet, the magnet is selected on the market in accordance with the previous optimizations: a cylindrical 10 x 5 mm NdFeB magnet. Starting from this point, both cylindrical and square actuators developed earlier are re-optimized with the 5 remaining factors (Table 4.22). The only difference in the boundaries is the wall thickness  $w_1$  that can go down to 0.5 mm.

Table 4.22 – Free factors for optimization

Factor	Geometrical dimension	Range [mm]
$x_1$	housing thickness ( $w_1$ )	[0.5-2]
$x_2$	bottom thickness ( $w_2$ )	[1-3]
$x_3$	bump height ( $w_3$ )	[1-4]
$x_4$	iron cap height ( $h_{cap}$ )	[1-3]
$x_5$	overhanging coil height ( $h_c$ )	[0-3]

The result of the optimizations (Tables 4.23 and 4.24) shows a decrease of the cylindrical actuator performance compared to the 7 factors optimum (-7.3 %) but an increase of the square actuator performance (+5.1 %). The former is logically worse due to the decrease of the magnet size. However, the enlargement of the airgap thanks to  $w_1$  increases the number of turns for the latter which, in addition, does not suffer from saturation compared to the cylindrical actuator.

Table 4.23 – Optimal actuator configurations

Model	$w_1$	$w_2$	$w_3$	$h_{cap}$	$h_c$
Cylindrical actuator	0.5	2.48	3.88	3.0	3.0
Square actuator	0.5	2.88	4.0	3.0	3.0



Table 4.24 – Average force resulting from the optimization process and comparison with FEM

Model	Model av. force [N]	FEM av. force [N]	Error [N]	Error [%]
Cylindrical actuator	1.6302	1.5810	0.0492	3.11
Square actuator	1.9218	1.9318	0.0100	0.52

### Prototypes

The prototypes corresponding to both optimums of Table 4.23 are finally built and mounted in plastic housings fabricated with a fast-prototyping 3D printer (Figures 4.65 and 4.68)<sup>2</sup>.

With an average force of 1.64 N, the measurements on the cylindrical actuator differ from the FEM value of Table 4.24 with 3.62 %. This discrepancy clearly appears in Figure 4.66 showing the force profile along the travel. Indeed, the measurements are more curved than FEM reaching an error of 5.3 % at 5 mm.

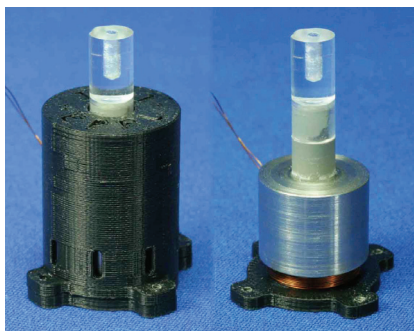


Figure 4.65 – Prototype of the cylindrical actuator

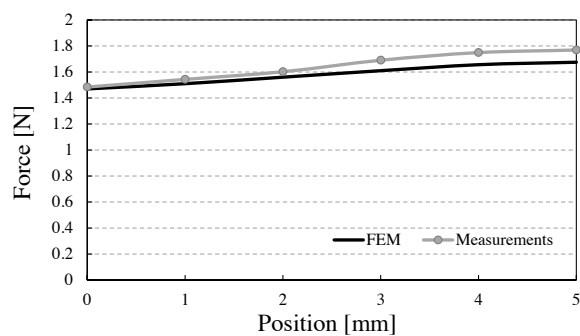


Figure 4.66 – Force profile comparison between FEM and measurements

The difference can be explained by the fact that the exact properties of the materials used for the prototype were not known during the modeling phase. For instance, the tolerance range of the magnetic remanence  $B_r$  (fixed at 1.26 T for the FEM simulations) goes up to 1.37 T in the magnet datasheet. Similarly for the iron characteristic for which the theoretical saturation level was set to 1.5 T but is actually closer to 1.1 T as shown in Figure 4.67 where the magnetic remanence and the iron saturation are set to respectively 1.37 and 1.1 T. Both curves match well and the residual discrepancy reaching a maximum of 3.37 % can be explained by mechanical tolerances and friction caused by the plastic housing.

The effect is even more important in the square configuration for which the error punctually reaches 16.3 % in the lowest position (Figure 4.69). Decreasing the iron saturation level to 1.1 T improves the results but not sufficiently to explain the force drop for the low positions of the

<sup>2</sup>Detailed pictures of the actuators parts are shown in appendix A.2.3.

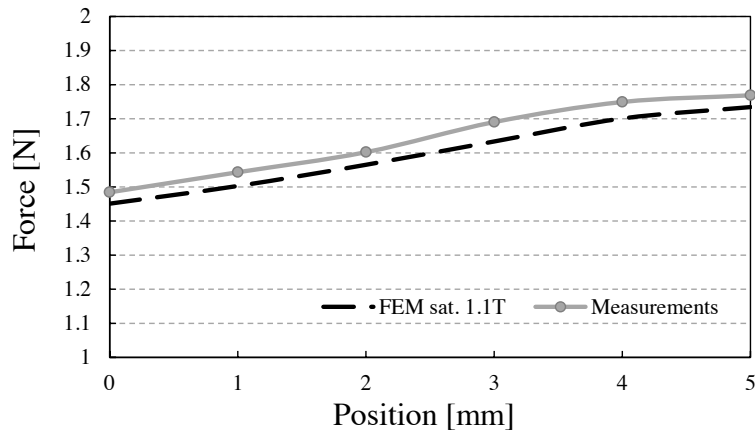


Figure 4.67 – Adaptation of iron saturation to 1.1 T and of magnetic remanence to 1.37 T

key. Indeed, the iron used for the square actuator is of lower magnetic quality corresponding to a saturation level below 1 T.

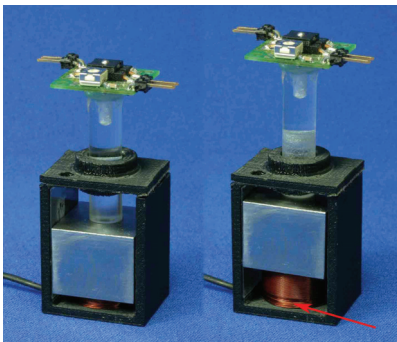


Figure 4.68 – Prototype of the square actuator

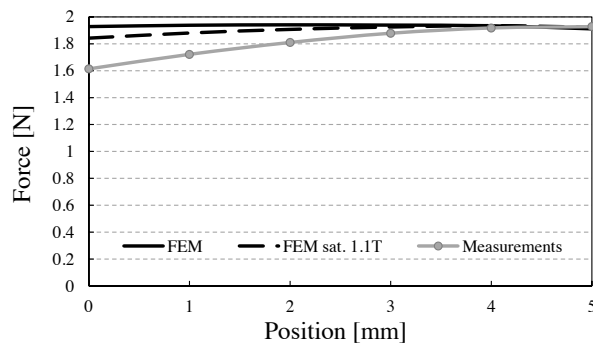


Figure 4.69 – Force profile comparison between FEM and measurements

In addition to the lower iron saturation, a non-homogeneous distribution of the turns within the coil disturbs the linearity of the force. In the realization of the square actuator, a lack of turns is clearly visible in the part of the coil overhanging the iron housing (red arrow in Figure 4.68). The result on the force profile is comparable to the use of a shorter coil ( $h_c$  decrease). Indeed, a FEM simulation with a 1 mm shorter coil but the same number of turns matches the measurements with a relative discrepancy lower than 2 % (Figure 4.70).

The measurements made on both prototypes of the subsection showed the necessity of knowing the characteristics of the materials at disposal for the manufacturing already at the beginning of the modeling process. Slight variations notably influencing the magnetic properties of iron play a role on the magnetic flux behavior which directly influences the linearity of the force profile for such miniature actuators.

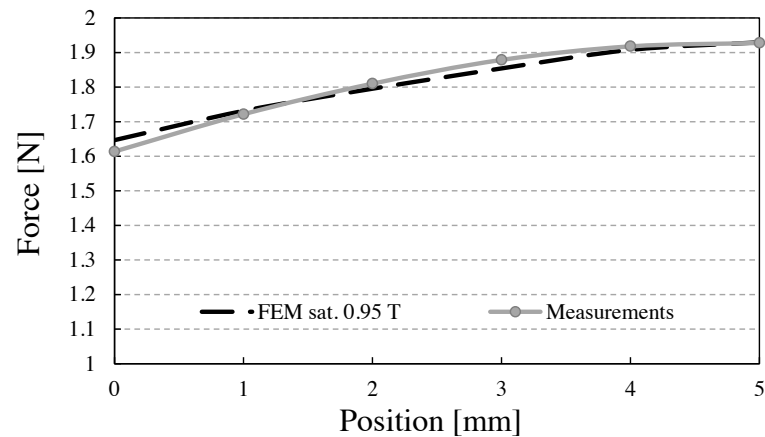


Figure 4.70 – FEM simulation of the square actuator with a 1 mm shorter coil and an iron saturation of 0.95 T

#### 4.6.4 Vibrotactile button

The vibrator addressed in this subsection is radically different from the previous actuators. Indeed, the idea is to design a flat linear electromagnetic actuator aimed to vibrate when subjected to an alternating current. It contains two main parts (Figure 4.71): a two-sided coil printed on a flex circuit board (0.1 mm thick) and a moving part composed of a ring magnet and an iron base whose role is to amplify the flux created by the magnet and guide it towards the center with the help of a central bump. When a current flows in the coil perpendicularly to the magnetic flux, Laplace's force is created between both parts. Supplying an alternating current in the coil thus generates a vibration. The simple configuration is due to the fact that the actuator needs to be as flat as possible.

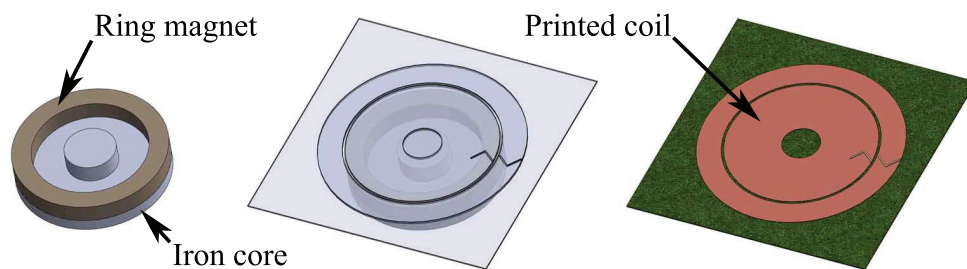


Figure 4.71 – Principle of the vibrotactile button

A ring magnet with an outer diameter of 12 mm, an inner diameter of 9 mm and a thickness of 1.5 mm is imposed by the application. The external diameter of the coil directly depends on the magnet and is set to 18 mm. It is to note that the sense of rotation of the current, set to 0.5 A for the optimization, changes above the magnet (arrows on Figure 4.71) in order to take advantage of the external magnetic fringes. As for the track width, it is limited by the

technology ( $150\ \mu m$ ) giving 23 turns on each side of the board. There is thus 3 free factors left for the optimization, namely the base thickness  $x_1$ , the central bump height  $x_2$  and its radius  $x_3$  outlined in Figure 4.72 and Table 4.25 with their experimental boundaries.

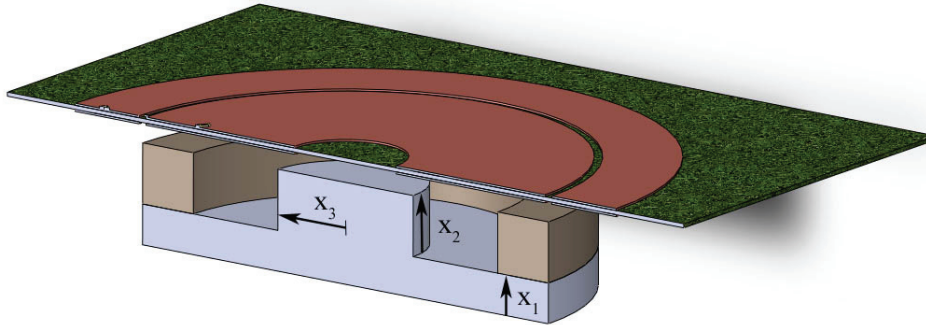


Figure 4.72 – Free factors for the vibrotactile button optimization

Table 4.25 – Free factors for optimization

Factor	Geometrical dimension	Range [mm]
$x_1$	base thickness	[0.5-2]
$x_2$	bump height	[0.5-2.5]
$x_3$	bump radius	[1-4]

The actuator is aimed to oscillate around a position and so, before launching the optimization process it is necessary to determine the optimal gap between the coil and the top of the magnet. Several FEM simulations are run for different positions of the coil giving 0.25 mm as the optimal gap (Figure 4.73). The full parametrical setup will thus be run for that position only.

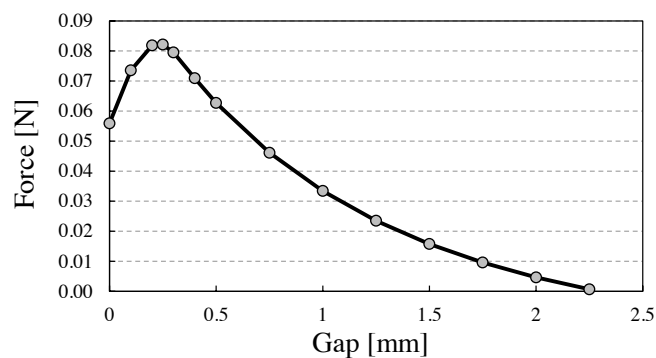


Figure 4.73 – Force characteristic of the vibrotactile button

The first model obtained for the experimental domain introduced in Table 4.25 is characterized by the parameters of Figure 4.74 (a). What comes directly in mind is that the bump height  $x_2$  is a dominant factor. Actually, it is due to the fact that the coil is placed 0.25 mm above the highest point of the magnetic part. Therefore, for the values of  $x_2$  that are greater than the magnet height, the coil gets away from the magnet and the force strongly decreases. The strong non-linearity brought by this effect caused an error of almost 10 % between the model optimum and the corresponding FEM simulation (Table 4.27). For that reason, a second model is computed with new boundaries for the bump height ( $x_2 = 0 - 1.5$  mm). The parameters of the second model are well-defined but clearly less significant showing that the response is not very hilly as shown in the surface representation of Figure 4.75. The error resulting from this second optimization process is almost divided by four and becomes acceptable (Table 4.27). The second optimum will thus be kept.

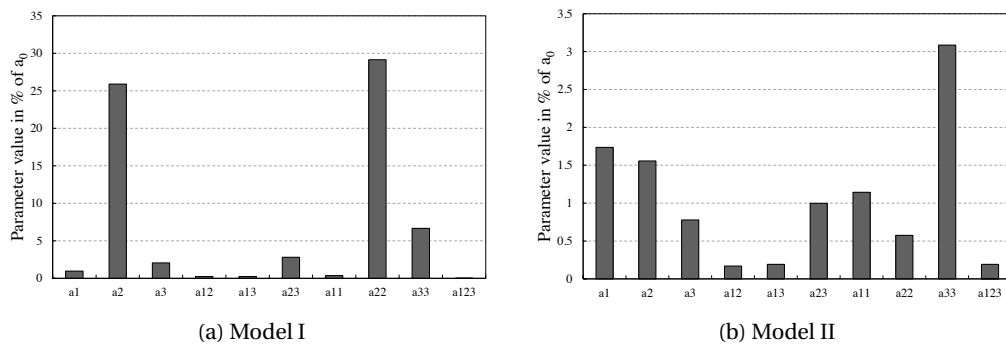


Figure 4.74 – Quadratic model parameters for 3 factors in % of the average  $a_0$

The parameters corresponding to the quadratic models I and II of the vibrator are shown in appendix A.2.4.

Table 4.26 – Optimal actuator configurations

Model	$x_1$	$x_2$	$x_3$
Model I	1.9998	1.0535	2.4272
Model II	1.8664	1.5	2.1571

Table 4.27 – Force resulting from the optimization process and comparison with FEM

Model	Model force [N]	FEM force [N]	Error [N]	Error [%]
Model I	0.1080	0.0983	0.0097	9.81
Model II	0.0989	0.1015	0.0026	2.57

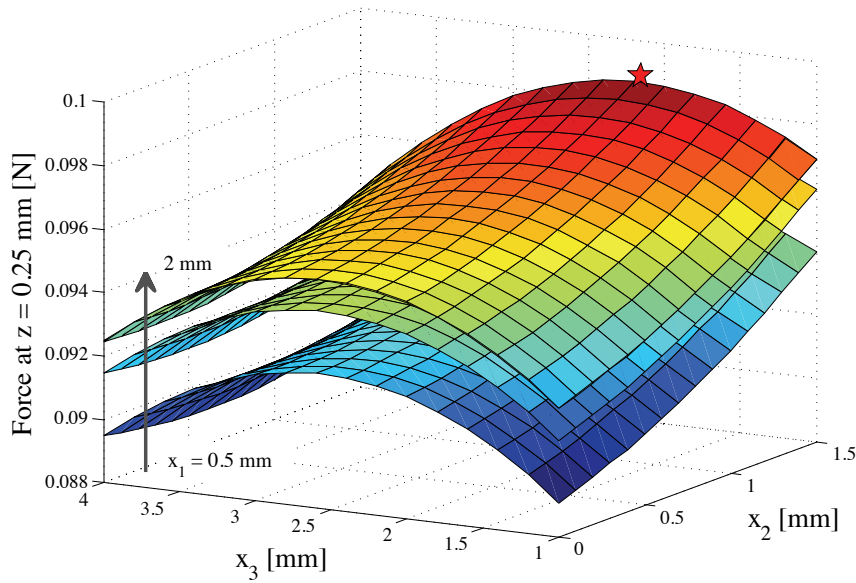


Figure 4.75 – Surface obtained with the quadratic model II for different base heights ( $x_1 = 0.5$ , 1, 1.5 and 2 mm, the two last being very close) and the optimum ( $\star$ )

## 4.7 Thermal analysis

Following the optimization of actuators presented in the previous section, a thermal analysis is completed to prevent any excessive heating. The seven configurations, including cylindrical (round) actuators (RA3-5-7), square actuators (SQ5-7) and fixed magnet actuators (RA5fix and SQ5fix) obtained in section 4.6 are simulated using finite element steady state thermal modeling.

### 4.7.1 Limiting elements

From the thermal point of view, two main components are critical in the design of electromagnetic actuators. First is the insulator covering the coil wires which, if overheated, can irreversibly lose its insulating properties, leading to the appearance of short-circuits between the turns. The maximum allowed temperature  $T_{max}$  is given by the insulation class of the wire. Two classes are mainly used for the manufacturing of motors and actuators: *B* with  $T_{max} = 130^\circ\text{C}$  and *F* with  $T_{max} = 155^\circ\text{C}$  [128]. For more safety, the lower limit of  $130^\circ\text{C}$  is chosen.

Concerning the magnets, they are characterized by an operating temperature over which it is not advised to work [129]. Between this operating temperature and the so-called Curie temperature  $T_C$  ( $310^\circ\text{C}$  for NdFeB magnets), the demagnetization is reversible and comes back to normal with a decrease of the temperature as long as no counter magnetic field is generated by the coil. Above  $T_C$ , the demagnetization is irreversible. For the selected magnets,

an operating temperature of 80°C is given by the manufacturer ([www.supermagnete.ch](http://www.supermagnete.ch)). It is thus necessary to make sure that the heating induced by the chosen current density does not exceed the above-cited value.

### 4.7.2 FEM steady state thermal analysis

The current of 0.5 A set for the optimization process of all actuators corresponds to a current density of 8 A/mm<sup>2</sup>. The first task is thus to calculate the Joule losses generated by each coil. The obtained values of between 3.18 and 4.30 W are given in Table 4.28. Then, the geometries are built with a finite element software and steady state thermal analysis are run.

Natural convection is assumed to occur over the external actuator surface with an ambient temperature  $T_{amb}$  of 20°C. Concerning the heat transfer coefficient  $h$ , a study of Markovic et al. [130] performed on small electric motors resulted in a value approaching 12 W/m<sup>2</sup>K (for a  $\varnothing 40 \times 65$  mm cylindrical motor) and increasing inversely with the motor diameter as also mentioned by Staton and So [131]. The actuators studied in this thesis, in addition of being even smaller, possess a self-supporting coil. The advantage of this kind of coils is that the surface available for convection is increased by more than 50 % due to the cylindrical shape of the wire directly in contact with the air. As a result, the apparent heat transfer coefficient increases compared to a plane surface usually modeled in FEM. Thanks to comparisons between measurements and simulations on the RA5fix model (presented later in Figure 4.78) the heat transfer coefficient  $h$  is set to 16 W/m<sup>2</sup>K. Conduction is then implemented through the airgap, between the coil and the ferromagnetic structure.

An example of temperature isovalues obtained with RA3 is shown in Figure 4.76 (a). It first tells us that the coil is always hotter than the rest of the structure ( $\sim 10$  % for RA and 16-20 % for SQ), whose temperature is almost homogeneous. This difference increases even more when the coil gets out of the structure ( $\sim 20$  % for RA and 30-40 % for SQ). Indeed, the higher the coil position, the larger is the convection area around it. The worst case scenario represented by the coil in the actuator will thus be studied with special care. As a first comparison between the seven models, an index giving the coil heating in degrees Celsius per Newton provided by the actuator is calculated (last column of Table 4.28). Clearly, the square actuators, taking advantage of the entire volume at disposal, are more efficient: between 21.5 % and 27.6 % relatively to their corresponding cylindrical actuator.

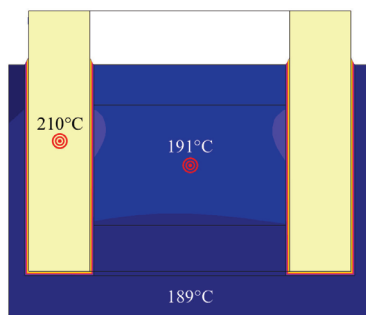
Two localized measurements (red targets in Figure 4.76 (a)), corresponding to the limiting elements of the actuator, namely the magnet and the coil, were made for the seven actuators with a current density of 8 A/mm<sup>2</sup> and a usage rate of 100 % (Figure 4.76 (b)). This result confirms the difference between high (5 mm) and low positions of the coil as well as between the coil and the magnet. One remarks that the temperature reached by the square actuators is systematically lower than round actuators, especially for SQ5.

The values displayed largely exceed those allowed by the materials. However, this graph is only

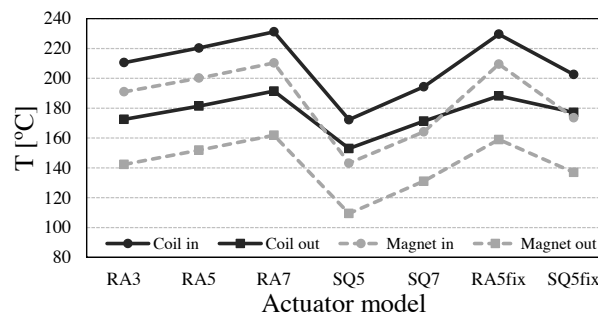
## Chapter 4. Design methodology for linear short-stroke actuators

Table 4.28 – Optimal actuators characteristics with  $N$  the number of turns,  $R$  the coil resistance,  $P$  the Joule losses and  $T/F$  the coil temperature over force ratio when the coil is inside the actuator

Model	$N$ [-]	$R$ [ $\Omega$ ]	$P$ [W]	$T/F$ [ $^{\circ}\text{C}/\text{N}$ ]
RA3	625	13.9	3.49	131
RA5	696	15.4	3.86	133
RA7	780	17.2	4.30	135
SQ5	560	12.7	3.18	101
SQ7	736	16.6	4.15	106
RA5fix	732	17.0	4.25	145
SQ5fix	738	17.1	4.29	105



(a) Thermics on RA3 (in)



(b) Values for the seven optimums

Figure 4.76 – Steady state thermal analysis of seven optimal actuator geometries for the two extreme positions of the coil (in and out) at full power ( $j = 8 \text{ A}/\text{mm}^2$ ). Temperature is measured on the red targets of (a) (coil and magnet).

indicative as it does not reflect the actual usage conditions of the actuators in multi-finger haptic applications.

In order to have an accurate feeling of the actual heating undergone by the actuators during their utilization, it is necessary to determine their usage rate. The main characteristic of multi-finger devices is to be composed of many actuators that generate a feedback only when the user presses on a key. The example of the computer keyboard is taken here as reference for the analysis. We firstly assume that the duration of a keystroke, including downwards and upwards displacements, is constant among the typists and corresponds to the average keystroke time of 77.2 ms measured by Rempel et al. [114]. Then, the number of occurrences of each character is calculated on a text sample constituted by the first two paragraphs of the present chapter. The "space" key arrives first with 15.1 % of the total characters, followed by



the "e" with 10.4 %. Based on the research of Karat et al. [132] and Ostrach [133], Table 4.29 helps understanding the final usage rate of the most frequently used keys. Most of the time, the typing rapidity is given in words per minute (WPM). It is here translated in characters per minute (CPM) by multiplying by a standard factor of 5 generally used to define a word [134]. The average time allowed for one character can then be calculated and compared to the 77.2 ms needed to physically press on a key (excluding displacements of the finger in the air). Based on this ratio, it is finally possible to give the global time ratio during which the "space" and "e" keys are meant to be active. With the hypothesis that a key is supplied at full power during its entire travel ( $j = 8 \text{ A/mm}^2$ ) and with the fact that the heating is an affine transformation relatively to the Joule losses  $P$ , it comes out that the worst case scenario of Table 4.29 is equivalent to less than 10 % of the total Joule losses calculated in Table 4.28.

Table 4.29 – Typing characteristics and usage rates for the most frequently used keys for different kind of users

	Composition	Transcription	Professional	Fastest
Words per minute	19	33	50	100
Characters per minute	95	165	250	500
Char. duration [s/character]	0.63	0.36	0.24	0.12
Ratio key active [%]	12.3	21.4	32.2	64.3
Usage rate "space" [%]	1.86	3.23	4.86	9.71
Usage rate "e" [%]	1.28	2.23	3.35	6.69

The usage rate of each model is thus adapted and the results are shown in Figure 4.77 for the coil and magnet temperatures when the coil is inside the actuator. It appears that at 10 %, the temperature stays below 40°C for both, largely below the limits of the materials. The magnet is clearly the limiting factor and the temperature exceeds its limit for most models above a rate of 40 %. However, this situation does not reflect reality and a sufficient safety margin is guaranteed for multi-finger applications.

Similarly, Figure 4.78 shows the behavior of the temperature when the current supplied in the coil is decreased, with the usage ratio kept at 100 %. Due to the definition of the Joule losses ( $RI^2$ ), the characteristic is quadratic and shows that the actuators could be constantly supplied with a current density approaching 5 A/mm<sup>2</sup> (60 % in Figure 4.78) for some models. In comparison, the current necessary to maintain the cylindrical actuator of Figure 4.65 in

## Chapter 4. Design methodology for linear short-stroke actuators

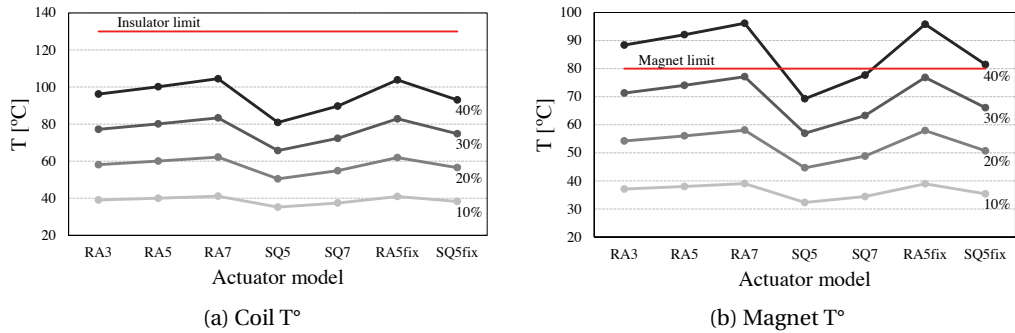


Figure 4.77 – Temperature of the actuator corresponding to different usage rates (coil in)

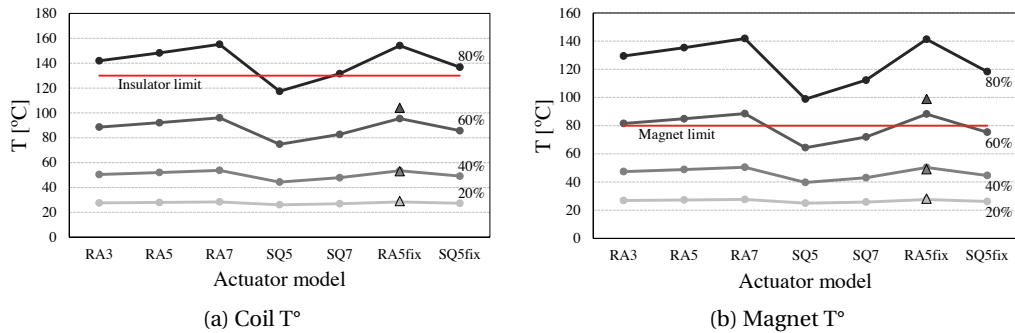


Figure 4.78 – Temperature of the actuator corresponding to different current levels (coil in) and comparison with measurements on the RA5fix prototype ( $\Delta$ )

its high position is 50 mA (i.e. 10 % of the maximum current) causing a heating of only 2°C above  $T_{amb}$ . Steady state measurements were made prior to the simulations on the RA5fix prototype in order to validate the heat transfer coefficient  $h$  of 16 W/m<sup>2</sup>K. The results are shown in Figure 4.78 with triangles standing for the measurements at respectively 20, 40 and 60 % of the maximum current of 0.5 A. The discrepancies observed at 60 % principally come from the fact that the coil resistance increases with the temperature which further increases the Joule losses.

Regarding the vibrotactile buttons designed in subsection 4.6.4, their winding resistances are two to three times lower than those shown in Table 4.28 for a similar current of 0.5 A, decreasing thus the Joule losses. The material on which the coils are printed, called Kapton<sup>®</sup>, possesses a thermal conductivity of 0.37 W/m·K, which is fourteen times higher than the air (www.dupont.com). Moreover, these vibrators are aimed to provide bursts of vibrations in response to a contact with the user's finger during a short period of time only. For these reasons, the heating will be even less critical than for the short-stroke actuators analyzed above. They will thus be considered as safe without further simulations.

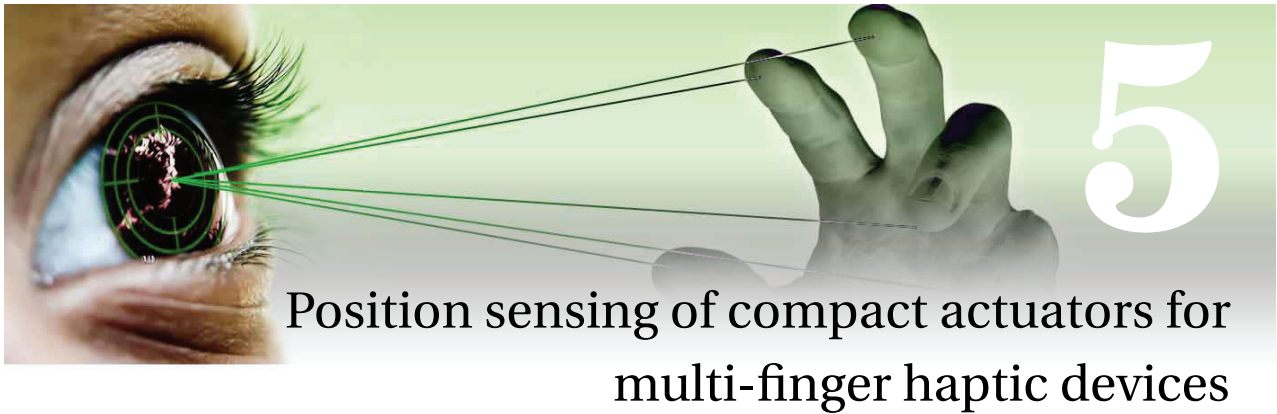
## 4.8 Summary

The development of innovative multi-finger haptic systems passes through the design of efficient compact actuators. In the case of electromagnetic actuators, small dimensions lead to an unusual behavior of the magnetic flux lines that are strongly affected by geometrical and material variations. It represents an issue that greatly complicates the elaboration of reliable analytical models. The present chapter thus focused on a new modeling methodology possessing qualities of accuracy, rapidity and adaptability. Indeed, the accuracy characterizing finite element modeling already convinced a large part of the scientific community and demonstrated a great flexibility of use. The appearance of 3D magnetic field analysis widened the scope for a large range of electromechanical applications even more. However, 3D finite element simulations are extremely time-consuming and strategies have to be found to limit their number during the optimization process. The main idea supported in the presented methodology is to take advantage of the design of experiments to judiciously select the simulations to be run within the experimental domain so as to be able to obtain a parametrical model of the desired objective function (the force in the present case). The careful choice of the design allows making a trade-off between computing time and accuracy of the parametrical model.

The use of quadratic models with interactions obtained from the composite design resulted in the efficient modeling of the force generated by numerous linear short-stroke actuators with up to seven geometrical free factors. Indeed, the relative discrepancy between the model and FEM is in general lower than 5 % and decreases for the geometries approaching the optimum. The advantage of the parametrical modeling is that its processing is facilitated in order to analytically find the optimum and moreover, additional non-linear constraints such as weight and temperature can be easily added to the optimization process in order to become multi-physic. The error finally obtained for all optimums is limited to a 5 % range, decreasing with the number of free factors.

Finally, the adaptability of the method is demonstrated by the modeling and optimization of a miniature linear vibrator whose discrepancy with FEM is lower than 3 %.





**Contents**

---

<b>5.1 Reassignment of existing sensors . . . . .</b>	<b>106</b>
5.1.1 Independent sensing method . . . . .	106
5.1.2 Hybrid sensing method . . . . .	109
<b>5.2 Self-sensing approach . . . . .</b>	<b>112</b>
<b>5.3 Back emf for position interpolation . . . . .</b>	<b>113</b>
5.3.1 Physiological considerations . . . . .	113
5.3.2 Back emf . . . . .	114
5.3.3 Free fall study . . . . .	115
5.3.4 Results . . . . .	117
<b>5.4 Oscillating RLC circuit . . . . .</b>	<b>120</b>
5.4.1 Coil properties . . . . .	120
5.4.2 Oscillating RLC circuit . . . . .	123
5.4.3 Simulation and numerical validation of the phenomenon . . . . .	126
5.4.4 Frequency adaptation . . . . .	130
5.4.5 Measurement method . . . . .	130
5.4.6 Results . . . . .	133
5.4.7 Improvements and design for self-sensing . . . . .	137
<b>5.5 Summary . . . . .</b>	<b>138</b>

---

Based on the recommendations introduced in section 3.3, the present chapter addresses four methods of position detection developed during the thesis. No sensor is properly designed, but techniques are proposed to measure the position of the mover by judiciously integrating, or not, existing sensors. The methods are classified according to their degree of self-sensing, meaning the level of interdependency between the sensor and the actuator. The first category gathers sensors that are completely independent from the actuator and are able to work even without the latter. Then, the so-called hybrid category takes advantage of intrinsic signals provided by the actuator but still necessitates the use of a sensor. Finally, pure self-sensing methods for which no sensor is required are presented.

### 5.1 Reassignment of existing sensors

#### 5.1.1 Independent sensing method

The principle of the first category is to add a fully functional sensing unit to the actuator. According to the specifications mentioned previously, optical and magnetoresistive sensors are well suited for this category<sup>1</sup>. Practically, a sensor slides along a graduated ruler and changes its output according to the pattern facing it. For optical systems, the sensor is generally an optical barrier (Figure 5.1 (a)) in which slides a ruler pierced with slits. The phototransistor is thus open or closed depending on the light that crosses the ruler. For magnetoresistive sensors, a comb made of iron plays the role of ruler and when the ferromagnetic material faces the sensor, the magnetic field produced by the latter increases and changes the resistance of the sensing element placed in a Wheatstone bridge. For both systems, a single sensor is not sufficient to discriminate the direction of movement. A second sensor is thus added, shifted from a quarter of period to form a quadrature encoder. Two square signals (or sinewave depending on the slit width) are obtained and allow for precise measurements of the position. So as to miniaturize the system and make it compatible with small actuators, a custom optical sensor is developed.

#### Custom single-photointerrupter sensor allowing for direction discrimination

Following the principle of the optical quadrature encoder, we developed a method to discriminate the direction of movement using only one optical barrier. Compared to existing detection methods using two photointerrupters shifted by a quarter of period required to detect the direction of movement, the present method uses only one photointerrupter decreasing thus the fabrication cost. The objective here is not to design a high-resolution sensor, but a low-cost sensor that could be easily adapted and manufactured depending on the application. The idea is to be able to print the ruler on a transparency film using a standard inkjet or laser printer. Of course, everyday printers are limited in resolution but they offer an excellent alternative for the fast prototyping of linear position sensors.

---

<sup>1</sup>e.g. [www.renishaw.com](http://www.renishaw.com)

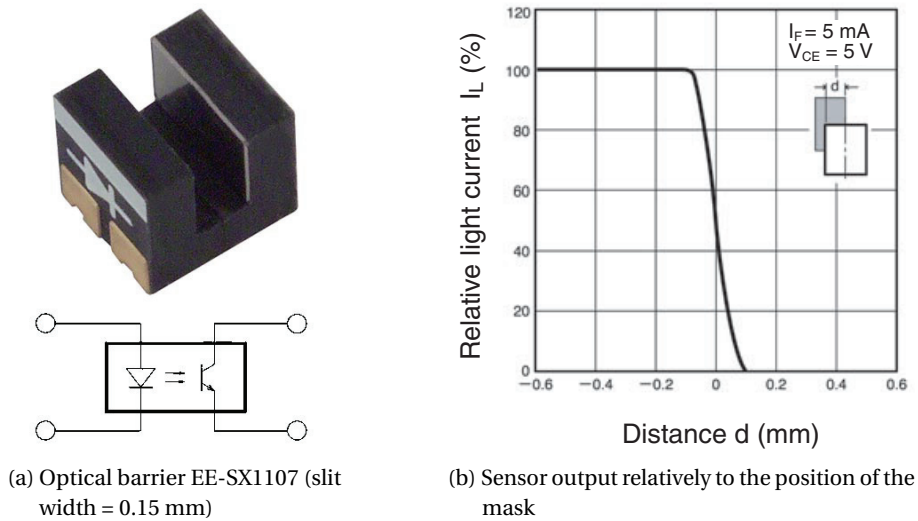


Figure 5.1 – Miniature photointerrupter from Omron Electronics Inc.

In order to discriminate the direction of movement, the method takes advantage of the transient part of an optical barrier. Indeed, when the phototransistor does not exactly face an opaque part of the ruler, the output becomes pseudo-linear as shown in Figure 5.1 (b) between -0.75 and +0.75 mm. To fake an incomplete covering of the sensor, the standard black and white pattern of the ruler is enhanced and alternates different levels of transparency (Figure 5.2 (a)). The output obtained with this kind of stripped pattern is presented in Figure 5.2 (b). Each black line pulls the output low and the magnitude of following oscillation depends on the grayscale value. Three different levels are necessary to avoid having a symmetry and so discriminate the direction of displacement. For each level, a comparator signals the transition and a pulse is generated to trigger a control interrupt.

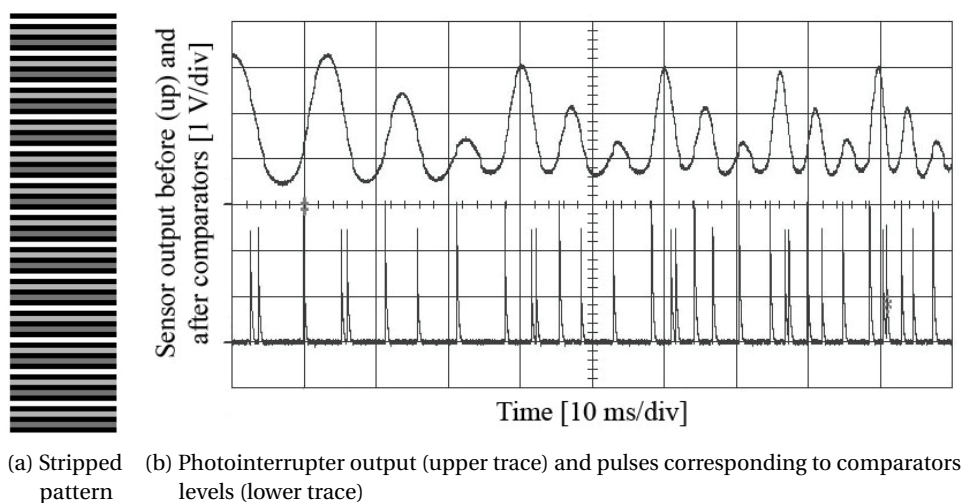


Figure 5.2 – Single-photointerrupter principle

At each pulse, the values of the two upper comparators, CMP1 and CMP2, are computed (Figure 5.3). When a (0 0) code corresponding to a black line is obtained, the previous binary code is saved and compared for the direction discrimination. The code in memory thus follows a (0 0) - (0 1) - (1 1) sequence in the forward direction.

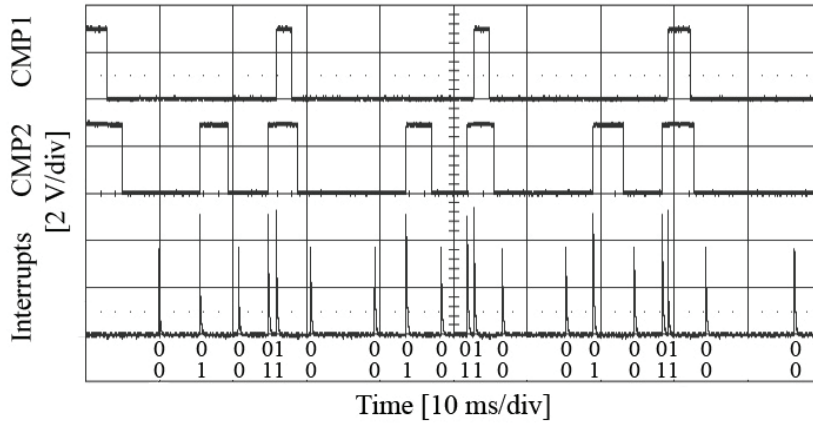


Figure 5.3 – Signal processing of the sensor output. At each pulse-triggered interrupt, the values of the two comparators (CMP1 and CMP2) are read and translated into a binary code

**Results**

Figure 5.4 shows the functional demonstrator built with the future aim to be integrated on the haptic glove developed at the laboratory (Figure 2.17 (a)).

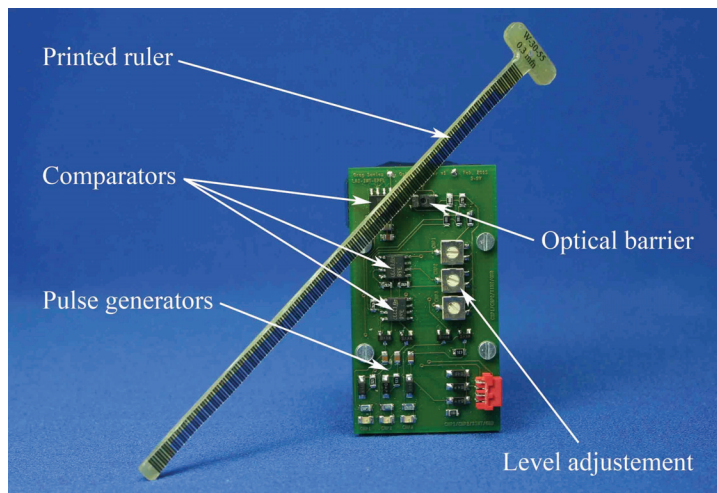


Figure 5.4 – Functional demonstrator of the single-photointerrupter optical sensor

The resolution of the sensor is limited by the width of the photointerrupter slit and defined by the stripped pattern (respectively 0.15 and 0.3 mm in the presented example). As for



the resolution of the detection of direction, it is divided by two as the check is made at every crossing of a black line. Again, that kind of sensor is not aimed to be used for high-resolution applications but has to be considered as an easily adaptable position sensor for fast prototyping. Indeed, once the electronic board is available, the user can simply design a ruler for each new application using any drawing software and printing it on a transparency film.

### 5.1.2 Hybrid sensing method

Hybrid sensing methods consist in taking advantage of physical quantities already present in the actuator. The term hybrid comes from the fact that a sensor needs to be added anyway so as to measure the intrinsic information. The nature of the measured quantity can vary a lot from one application to another but in any case, the sensor is closely related to the mechanical design. In the present subsection, the position of a linear short-stroke actuator, similar to those presented in the previous chapter, is measured. In this case, the magnetic flux density naturally present in the structure makes it an interesting candidate.

#### Linear Hall sensors for position measurement

In the particular case of the miniature actuator, the magnetic circuit surrounding the magnet is not ideal and leakage appears around the actuator. It is especially the case above the iron cap (Figure 4.5). As the flux density decreases with the distance to the actuator top, it can be used to determine the position of the mover. Tiny linear Hall sensors are particularly adapted to this operation and provide an output that is proportional to the flux density. The originality of the method is to use a Hall sensor for its linear characteristic instead of just for indicating a transition as it is usually the case in rotating brushless motor drives from the market. Moreover, one takes advantage of lost magnetic fringes which increases the faculty of integration even more and goes together with the idea of multi-finger haptic devices.

In order to illustrate the effect, the flux density is computed on the initial square geometry of the actuator using the finite elements on a two-dimensional grid overhanging the cap center (inset picture of Figure 5.5). The corresponding three-dimensional representation of the magnitude of flux density is shown in Figure 5.5. Two peaks clearly appear above the airgaps generating a large slope along the  $z$ -axis. However, the projections in the plan of Figure 5.6 show that the profile at these positions is strongly nonlinear ( $y = 5.4$  mm). It is thus decided to place the sensor on the central axis ( $y = 0$  mm) to increase the signal linearity. A similar analysis is run on a cylindrical actuator and the results, shown in appendix B.1.1, confirm the vertical behavior of the flux above the cap center (Figure B.2).

The flux density above the actuator center varies of 76 mT on the five first millimeters ( $y = 0$ ,  $z = 8-13$  in Figure 5.6). With a sensitivity of 13 V/T, the A1302 Hall sensor from Allegro<sup>®</sup> MicroSystems is a good candidate. It offers a theoretical bidirectional measurement range of 190 mT which represents a comfortable margin for the sensor location above the actuator.

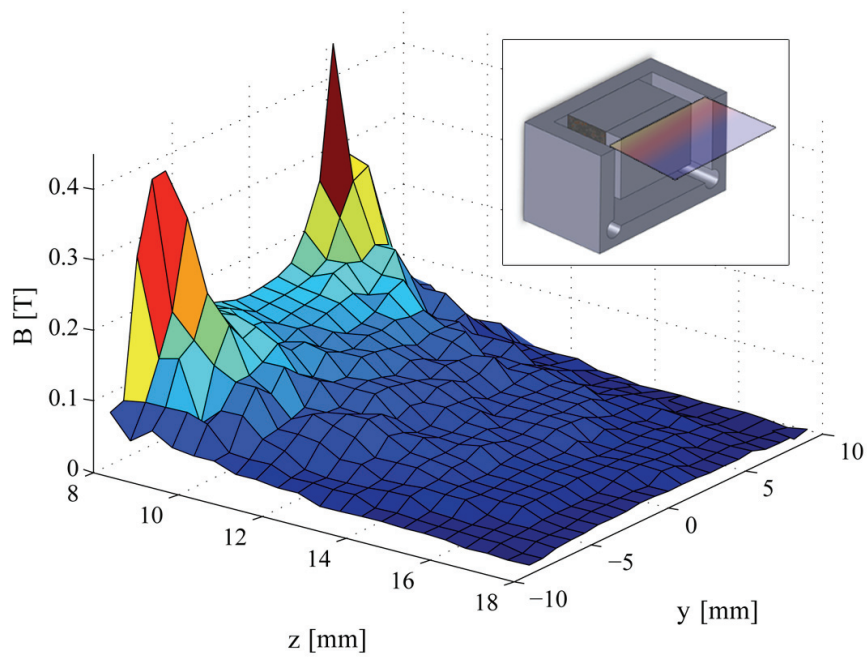


Figure 5.5 – Representation of the flux density  $B$  above the actuator initial square design (inset picture) ( $z = 8$  mm at the top of the cap)

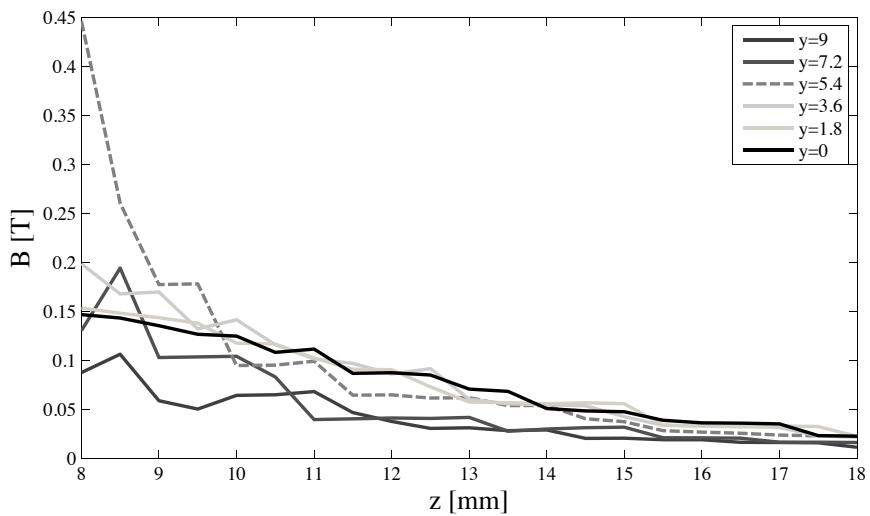


Figure 5.6 – Projections of the flux density characteristic along the  $z$ -axis

## Results

The prototype resulting from the linearization process presented in subsection 4.4.2 is studied before integrating the sensor. The flux density vertical component  $B_z$  is measured up to 15 mm above the cap using a teslameter (Figure 5.7). The profile describes an almost linear

behavior until 6 mm, before sensitivity decreases.

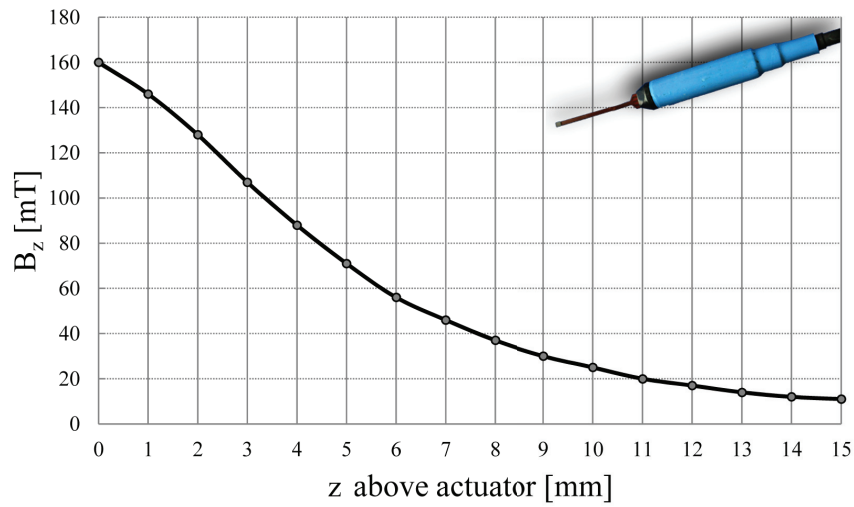


Figure 5.7 – Vertical component of the flux density above the actuator center with probe

A miniature electronic board including sensor and low-pass filter is mounted on the moving part (Figure 5.8). The output characteristic corresponding to a travel of 4.4 mm is shown in Figure 5.9 and presents a slight non-linearity. For this reason, a calibration is necessary in order to minimize the error.

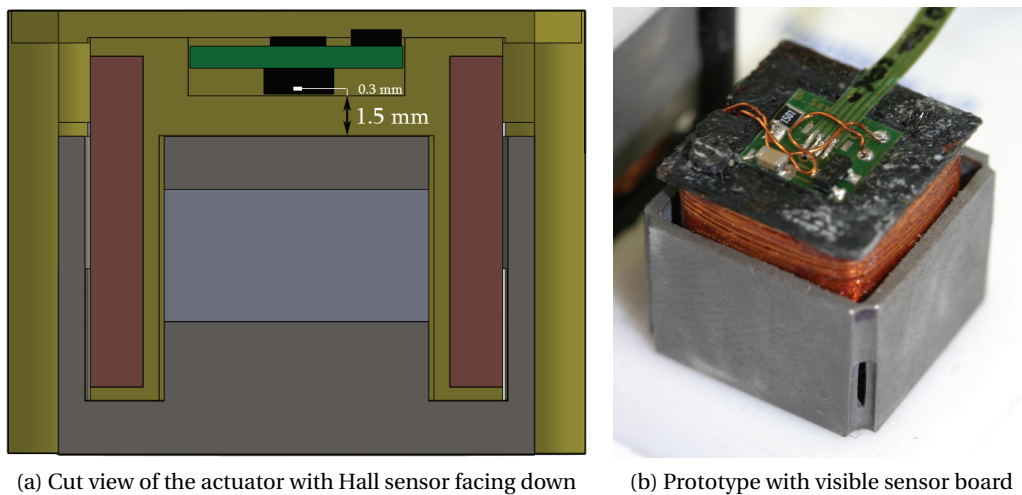


Figure 5.8 – Miniature Hall sensor board embedded in a square actuator

**Calibration and robustness**

The profile obtained with no current supplied in the coil can be matched by a quadratic polynomial (red trace in Figure 5.9). However, the calibration of devices integrating numerous

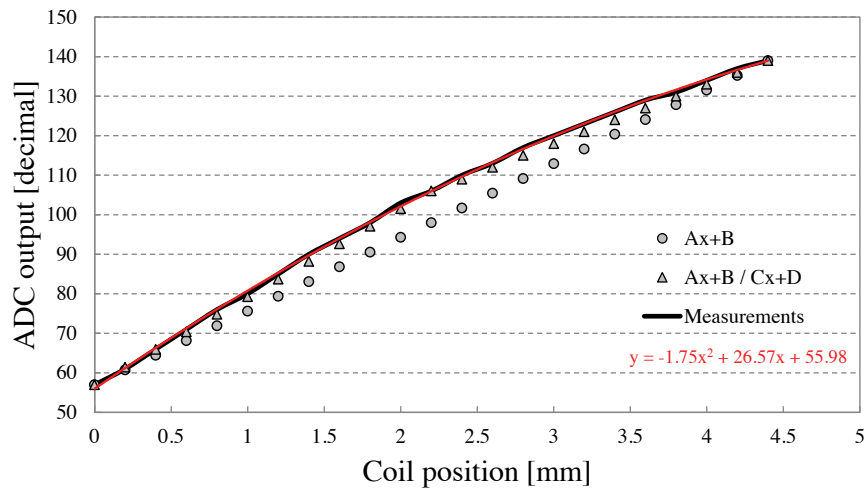


Figure 5.9 – Hall sensor measurements with linear interpolations and quadratic polynomial

actuators often represents a long and painful task. Avoiding or simplifying it can represent a non-negligible gain of time. Two different linear interpolations are thus proposed as potential alternatives in order to simplify the calibration. In both cases, only two measurements are required, one at the top and one at the bottom of the stroke. The first interpolation is a linear function between both ends ( $Ax + B$  in Figure 5.9). The error relatively to the full scale output (FSO) reaches 10 %. As an improvement, an offset is inserted in the middle of the travel. On each side, the function is split into two linear parts, decreasing the maximum relative error to 2.4 % ( $(Ax + B) / (Cx + D)$  in Figure 5.9). Both methods presented here necessitate knowing the total distance travelled by the coil. Should it be otherwise, a complete calibration with a reference position sensor would have to be set up.

Finally, a drawback observed with this position sensing method, where the sensor is directly surrounded by the coil, is a small variation of the output attributed to the magnetic flux generated by the coil when supplied with current (Appendix B.1.1). It is thus important to leave a distance between the sensor and the coil.

## 5.2 Self-sensing approach

In multi-finger haptic applications, each actuator is aimed to be controlled independently in force and position. The great number of actuators is often closely related to a limited space available for each sensory-motor unit. Self-sensing detection (no additional sensor) appears thus as a must. The principle is to take advantage of phenomena affecting the actuator coil itself. Many solutions have been developed for electrical machines with repetitive inductance characteristics (e.g. for rotary and linear permanent magnet synchronous motors [135] and [136]). The techniques developed at first for large machines are then adapted to

micro machines as summarized in [137]. Four phenomena are mainly used for detecting the position: back emf, magnetic anisotropy, eddy currents and magnetic saturation. All of them will not be explained in this section and interested readers are encouraged to refer to literature for further information.

The numerous methods developed for AC machines are not necessarily suitable for DC actuators and various alternatives are proposed. Notably in the domain of automotive, in which a luxury car can contain more than eighty electromechanical actuators driving wipers, lights, seats, mirrors, brakes, etc. . . , the suppression of position sensors is greatly appreciated. A first step towards the self-sensing of DC actuators was initiated by Consoli et al. [138] who propose to take advantage of the magnetic anisotropy of a rotating DC motor. The position is estimated by detecting periodical oscillations of the armature current caused by rotor slotting. The mechanical repetition is however not usable in linear short-stroke actuators.

In purely reluctant solenoid actuators, the impedance of the coil and particularly its inductance varies with the position of the plunger. This variation can be observed by measuring the current rise rate which is proportional to the coil impedance and thus allows sensing the position [139, 140]. The change in current slope is also used to drive electromechanical spring-mass actuators and industrial contactors either with pulse width modulation or simple DC supply [141, 142]. Hanson et al. [143] take advantage of the back emf induced in the coil of an actuator to estimate the position with an accuracy of 0.2 mm. Indeed, as it will be explained later, the back emf is proportional to the velocity of the moving part. Maridor et al. [144] even go a little further by superimposing a sinusoidal scan voltage to the main supply voltage. The additional high frequency signal allows exploiting the resonance phenomenon that magnifies the variation of inductance. Once filtered, the amplitude of the current oscillations is representative of the position.

The last method however has the drawback of requiring sophisticated filters and control that we would like to avoid. The challenge is here to develop a method to determine the mover position that would be simple enough to allow for a network of actuators to be controlled by a limited number of microcontrollers. Two self-sensing methods for electromagnetic short-stroke actuators are presented hereinafter. The first one uses the back emf to interpolate the position of the coil for displacements at constant acceleration and the second takes advantage of variations of the coil impedance at high frequency.

## 5.3 Back emf for position interpolation

### 5.3.1 Physiological considerations

The first method takes inspiration in the way the human being presses on a button. In this case, what better example than touch-typing when talking about multi-finger applications. As mentioned in Table 2.3, the maximum bandwidth with which the human finger can apply force and motion control comfortably is 5 to 10 Hz [31]. In comparison, the average down stroke of a

finger during touch-typing operations is, with 9.1 ms, ten to twenty times faster [114]. If so, the user's finger cannot react quickly enough and its behavior remains unchanged along the travel. In their study on control strategies for finger movement during touch-typing, Dennerlein et al. [145] demonstrated, using intramuscular electromyography, that the index movement can be dissociated into three phases. The first activity is initiated by the extensor muscle that lifts the finger before the keystroke. Potential energy is accumulated and converted into kinetic energy during the downswing. Once the downward movement has started, no activity of the extensor slows the movement down. Indeed, the extensor waits for the finger to hit the end stop of the key before deciding to lift it again. As for the flexor muscle, its contraction during the downstroke increases the stiffness of the finger joints, overcoming indirectly the keyswitch activation force. Moreover, a delay of 50 ms measured between the electrical stimulation and the effective onset of the force confirms that the action is too fast to be actively controlled. These arguments allow making the hypothesis of a constant force applied by the human finger during a keystroke. It means that if  $F_{finger}$  is constant, the acceleration directly depends on the force produced by the key  $F_{key}$  as stated by Newton in his second law:

$$\sum F = F_{finger} - F_{key} = m \cdot a \quad (5.1)$$

If no counterforce  $F_{key}$  is applied, the acceleration is constant. It is therefore possible to measure it at the very beginning of the stroke, when the current is not yet established and to estimate the mover position with a double integration of the acceleration.

### 5.3.2 Back emf

In order to measure the acceleration, a difference of speed over a given time is needed. The method presented here proposes to measure the velocity through the back electromotive force (back emf). Indeed, when using an actuator with no current supplied ( $i = 0$ ), the coil voltage  $U$  is reduced to a back emf  $e$  as follows:

$$U(t) = Ri(t) + L \cdot \frac{di(t)}{dt} + i(t) \cdot \frac{dL}{dt} + \frac{d\Psi_{cm}}{dt} = \frac{d\Psi_{cm}}{dt} \quad (5.2)$$

$$\Rightarrow \frac{d\Psi_{cm}}{dt} = \frac{d\Psi_{cm}}{dz} \cdot \frac{dz}{dt} = K \cdot v = e \quad (5.3)$$

where  $R$  is the coil resistance,  $L$  its self-inductance,  $\Psi_{cm}$  the total flux created by the magnet and crossing the coil and  $K$  the back emf constant.

The back emf is the variation of the magnetic flux created by the magnet and flowing through

### 5.3. Back emf for position interpolation

the coil over time. The actuators studied in this work, composed of a central, vertically polarized magnet, present the advantage of a  $\Psi_{cm}$  that is linear with the position. It is verified with a FEM simulation on the actuator resulting from section 4.4.1 by displacing the coil along the  $z$ -axis and computing the magnetic flux flowing into it. When the coil moves along the magnet, the variation of the flux created by the magnet, flowing vertically through the coil  $\Psi_{cm}$  is proportional to its position  $z$  (Figure 5.10). It is due to the fact that the flux density inside the magnet is constant. Since  $\Psi_{cm}/dz$  is a constant  $K$  (-4.3 Vs/m), the back emf is proportional to the velocity  $v$  (5.3).

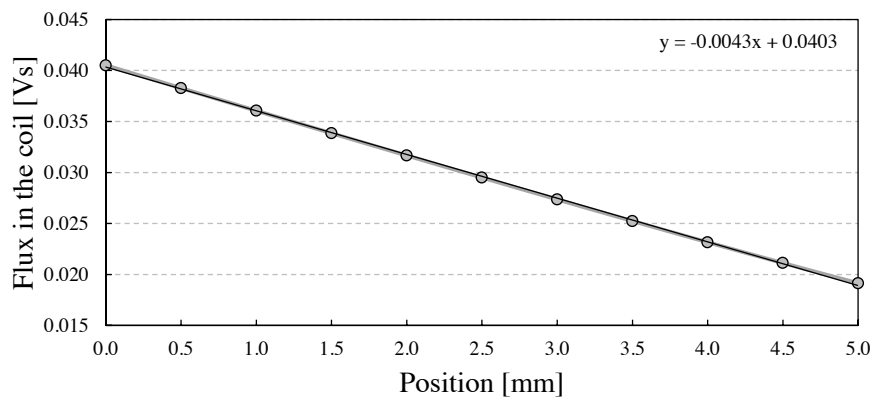


Figure 5.10 – Flux crossing the coil vs position

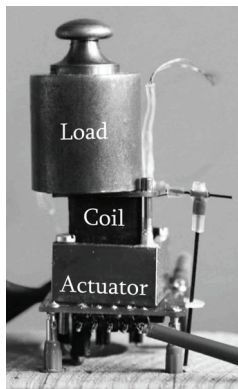
It is thus possible, by measuring the back emf, to get information about the coil velocity and then integrate it in order to get the position. However, as a single coil is aimed to be used to create the force and determine the position, tricks have to be found. Indeed, using this technique for continuous position sensing would require to quickly cut the power supply to the coil and to measure the back emf once the current is settled to zero. The time needed for the coil current to settle to zero and then establish again approaches 1 ms due to the values of  $R$  and  $L$ . Continuous measurements are therefore unrealizable without adding serious disturbances, considering an average down stroke time of approximately 10 ms [114].

#### 5.3.3 Free fall study

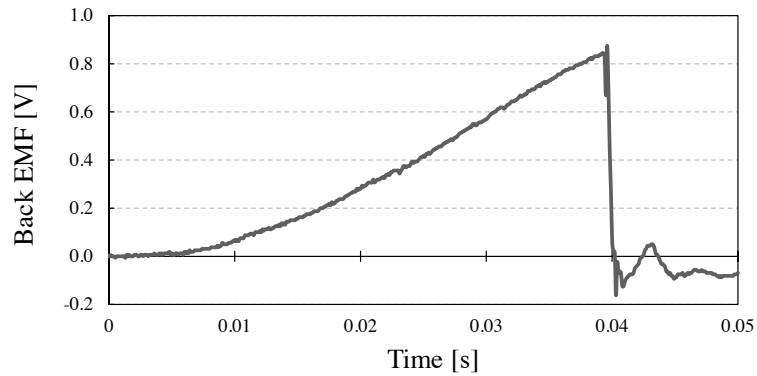
As mentioned in the previous subsection, if no counter force is applied, the acceleration is constant during a stroke, which is comparable to the free fall of a body subjected to gravity. The effect is thus observed by dropping a loaded coil from a 5 mm height (Figure 5.11 (a)).

As no external force is applied, the velocity is proportional to gravity:

$$v(t) = g \cdot t + v_0 \quad (5.4)$$



(a) Measurement setup with loaded coil



(b) Back emf during a free fall of the loaded coil

Figure 5.11 – Back emf measurement principle

In Figure 5.11 (b), representing a free fall, the back emf increases linearly during the fall, except for small disturbances at the beginning and just before the impact due to imperfect drops and parasitic wire forces. As expected, the measured voltage is proportional to the velocity, obtained by derivation of the position measured with an external position sensor (Figure 5.12).

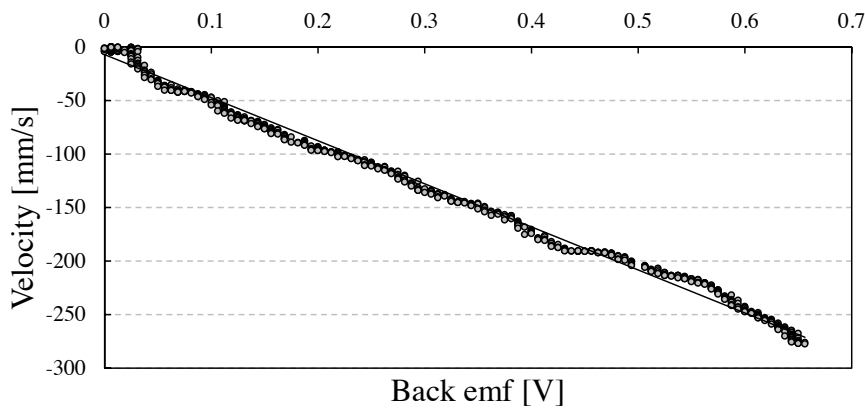


Figure 5.12 – Velocity vs back emf during a free fall

Figure 5.13 shows a zoom of the instrumentation amplifier output, alias the back emf produced by a free fall and summarizes the principle of the sensing method. In addition to the two back emf measurements responsible for the calculation of the acceleration, a trigger is introduced at the very beginning to notify the fall. The program runs until detecting a back emf value that rises above the threshold ( $e_0$ ). From there, a stroke is detected and acceleration can be measured. The second measurement  $e_1$  is taken a short while after the detection in order to avoid start disturbances. The third value  $e_2$  is finally recorded. Knowing the time between



both measurements ( $t_2 - t_1$ ), the acceleration  $a$  can be calculated:

$$a = \frac{\Delta v}{\Delta t} = \frac{v_2 - v_1}{t_2 - t_1} = \frac{1}{K} \cdot \frac{e_2 - e_1}{t_2 - t_1} \quad (5.5)$$

With the values of  $a$  and  $t_0$ , the key fall can be interpolated with:

$$z(t) = z_0 - \frac{1}{2} a \cdot (t - t_0)^2 \quad (5.6)$$

A delay  $t_2$  appears before the interpolation can catch up with the real position. However, the velocity at  $t_0$  is close to zero and hence the travelled distance is very limited ( $20 \mu\text{m}$  for 2 ms). Unwanted oscillations visible on the back emf above 0.4 V are simply due to the low common mode of the amplifier and do not disturb the measurements.

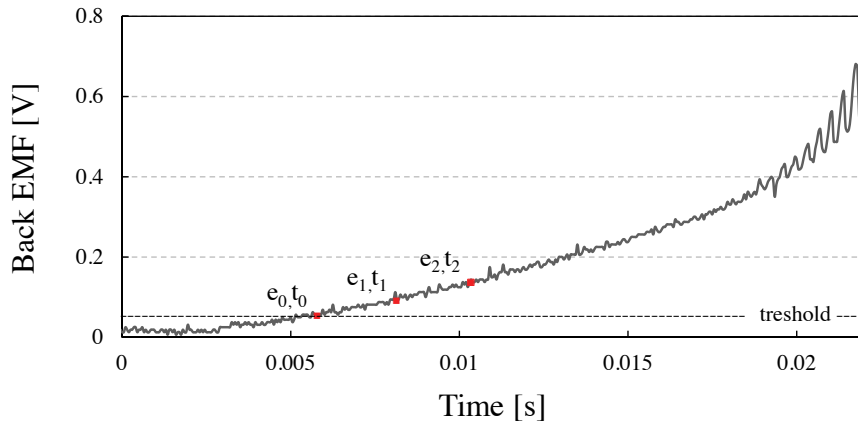


Figure 5.13 – Zoom on back emf from instrumentation amplifier output

#### 5.3.4 Results

- **Computer post-interpolation**

The back emf is at first processed with a computer to demonstrate the method accuracy. Different delays  $\Delta t$  from 1 to 5 ms are tested between the measurements.

A comparison between the interpolated position and the data measured with a precision CCD laser sensor shows that the curves match satisfactorily (Figure 5.14). Estimated profiles converge when the delay increases and the absolute error does not exceed 0.1 mm (0.06 mm for the moving average) (Figure 5.15). The acceleration computation with  $\Delta t = 1$  ms is a little less reliable. It comes from a small back emf difference at low speed which can be affected by the noise. It is thus important to choose a correct sampling

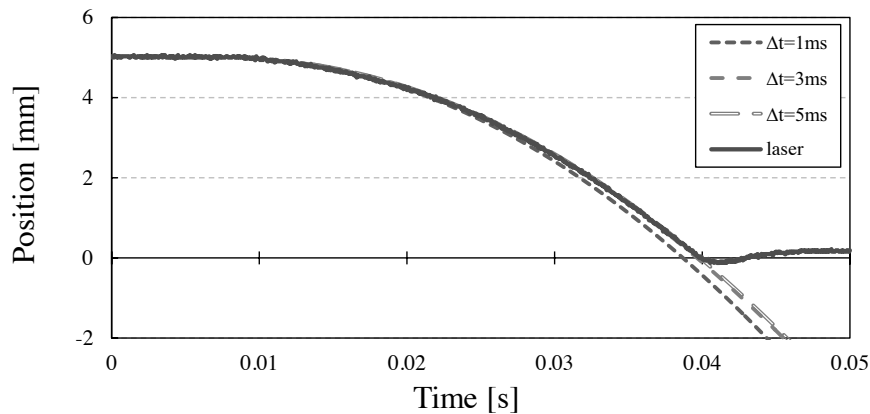


Figure 5.14 – Position interpolated from back emf data with different  $\Delta t$  vs position measured with a precision CCD laser sensor

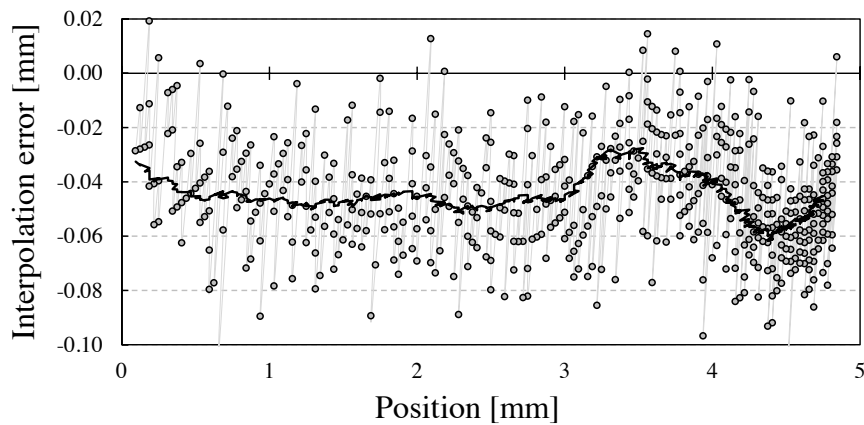


Figure 5.15 – Discrepancies between position measurement and interpolation and corresponding moving average

period to get efficient results. As for repeatability, it can vary due to noise and drop quality.

- **Embedded real-time interpolation**

The second phase consists in embedding the data processing within a microcontroller. The back emf is converted using an analog to digital converter and the position output is a PWM, low-pass filtered in order to get an analog value. Measurements are taken and the acceleration is calculated at the fall start. Then, the position is real-time interpolated and compared with the laser sensor data (Figure 5.16).

Interpolated and real positions are directly compared in Figure 5.17. Again, both profiles fit relatively well. The maximum absolute error approaches 0.3 mm (below 0.2 mm for the moving average, which represents 4 % of the full scale output).

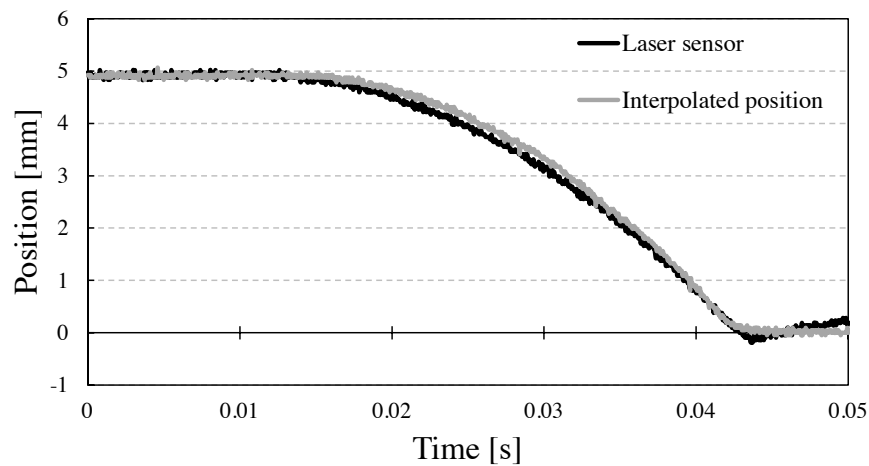


Figure 5.16 – Real time interpolated position from back emf data vs position measured with a precision CCD laser sensor

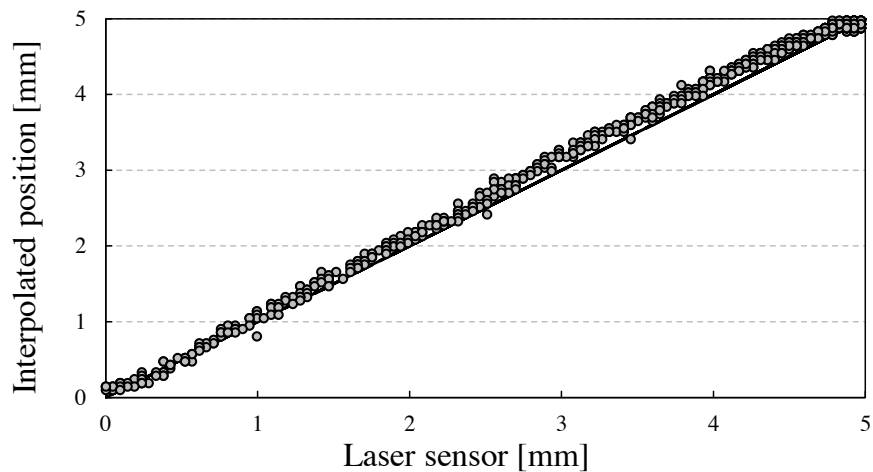


Figure 5.17 – Comparison between interpolated position and laser sensor data

### Discussion

The back emf method presented brings encouraging results [146]. The position of the mover can now be estimated all along a downstroke with the hypothesis of constant acceleration. A soft-landing control is thus made possible for electromagnetic actuators by slowing down the fall of a mover before the impact. Unfortunately, several studies aimed to provide a lumped-parameter model of the human fingertip showed that the way of typing and consequently the mechanical parameters strongly vary from one stroke to another [147, 148]. The uneven behavior of force and acceleration during a human stroke eliminates the chances for interpolation methods to succeed in all the tasks aimed to be accomplished by multi-finger haptic applications. A possibility would be to further this way by measuring both coil current and

voltage so as to actively measure the position deduced from the back emf as done in [143]. However, the aim of the present work being the simplification of the global sensory-motor system in order to integrate it in a network of actuators, this solution would not fit the objectives. Other principles will thus have to be studied in order to provide real-time position information. The research towards a self-sensing solution with light hardware and software requirements is thus transferred to a second method involving high frequency oscillations.

### 5.4 Oscillating RLC circuit

Plunging a coil in a ferromagnetic core has an influence on its own impedance, which further influences the electric signals. In this section, focus is put on this variation of impedance to implement a novel self-sensing method for position detection. Before looking at the electric signals themselves, the electrical properties of the coil are analyzed so as to get a better comprehension of the phenomenon.

#### 5.4.1 Coil properties

A coil is commonly modeled with a resistor  $R$  in series with the inductor  $L$  (Figure 5.18). This resistor represents the resistance of the wire itself and varies with the frequency due to high frequency effects (e.g. skin and proximity effects). In addition, as the conductors are very close to each other, electric charges can be accumulated within the winding. As a result, a capacitor  $C$  is added to the model in parallel to the inductor and resistor. This capacitor is generally omitted during control operations (PWM) as its role becomes only weighty at high frequency.

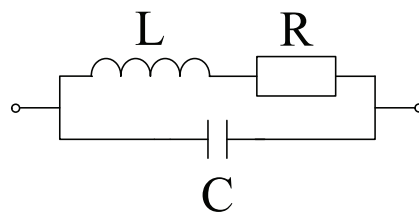


Figure 5.18 – Equivalent circuit of a wound coil

From a magnetic point of view, two main physical phenomena can influence the impedance of a coil [140]. On one hand, the fact of approaching a coil toward a ferromagnetic material increases its permeance, meaning that it becomes easier for the magnetic flux to flow due to the high magnetic permeability of iron [149]. As the inductance of a coil  $L$  is directly proportional to the permeance  $\Lambda$  (5.7), the former increases inversely to the distance with the

ferromagnetic material.

$$L = \frac{\Psi}{i} = N^2 \Lambda \quad (5.7)$$

with  $\Psi$  the total flux of the coil,  $i$  the current and  $N$  the number of turns.

On the other hand, an alternative current flowing in a coil generates a variable magnetic flux. When this flux crosses another conducting material, eddy currents are induced in the latter to counter the exciting magnetic field. As a result, the effect caused by eddy currents acts conversely to the variable reluctance effect and decreases the coil inductance  $L$ . The magnitude of both effects varies with the frequency and do not cancel each other as it will be presented later.

A side effect of the eddy currents are the Joule losses caused in the conductor placed at proximity [150]. These losses directly affect the real part of the coil impedance which is nothing else but  $R$ . The closer to a conductor the coil is, the more eddy currents are generated and the more the resistance increases. Both real and imaginary parts of the coil equivalent model are thus affected by the presence of a ferromagnetic body.

The short-stroke actuators designed in chapter 4 theoretically match the requirements presented above for the variation of impedance. Indeed, the coil is plunged inside a ferromagnetic core, which changes its inductance and resistance with the position. In order to confirm the possibility of using this physical principle for self-sensing, a frequency analysis of a prototype of cylindrical actuator is run. Figures 5.19 and 5.20 present the characteristics of inductance and respectively resistance of the coil along a frequency sweep for the two extreme positions of the coil (0 - 5 mm). Regarding the inductance, one remarks that below 20 kHz (barely visible on the graph) its value increases while the coil penetrates the core due to the increasing permeance as explained earlier. However higher in the frequency range, the eddy currents effect takes precedence on the permeability and the inductance decreases with the position. Above 800 kHz, a resonance phenomenon inverses the tendency again and the parasitic capacitor component becomes so preponderant that the equivalent circuit is capacitive (negative value of inductance).

As for the resistance, it increases when the coil is pushed inside the ferromagnetic core as explained by the eddy currents theory. However, beyond 400 kHz the tendency is inversed and the resonance peak strongly decreases with the position. The behavior of the coil impedance at very high frequency is mainly influenced by resonance phenomena which are yet partially unknown. Hence, it is preferable to stay below this resonance for a better understanding.

By looking at Figures 5.19 and 5.20, it comes out that there is a frequency  $f_0$  (400 kHz here) where the inductance decreases of almost 40 % while the resistance stays constant. At this point, both effects are clearly separated and the impedance variation is only due to a single

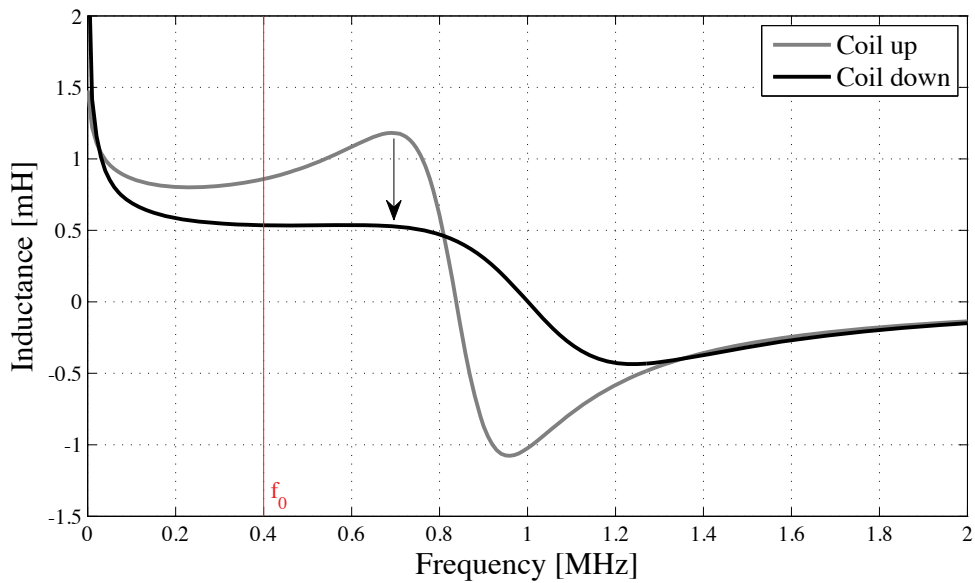


Figure 5.19 – Frequency characteristic of the inductance of a cylindrical short-stroke actuator coil at two extreme positions

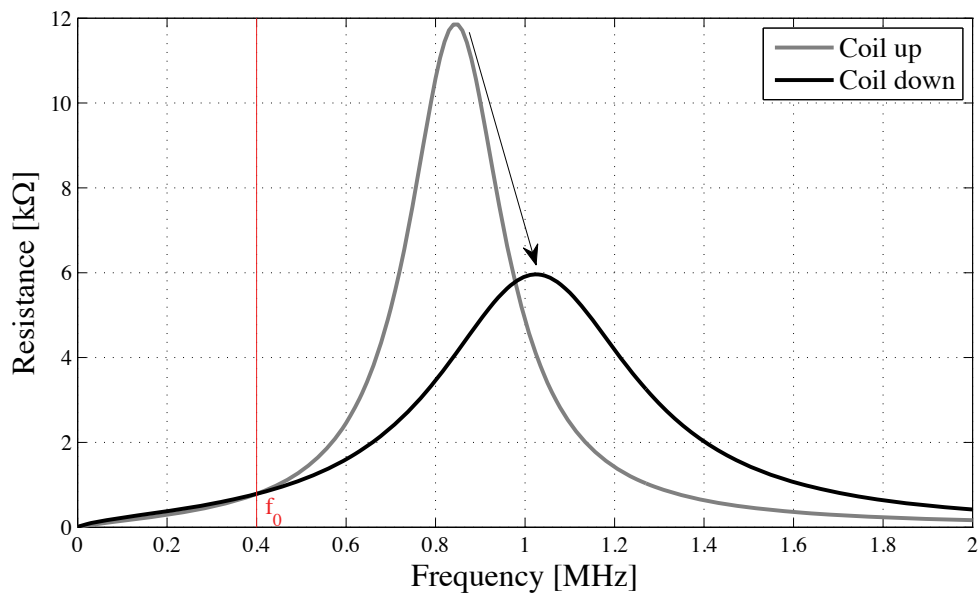


Figure 5.20 – Frequency characteristic of the resistance of a cylindrical short-stroke actuator coil at two extreme positions

parameter. The main challenge remains now to take advantage of the variation of inductance to measure the position. The idea is to passively generate oscillations at the frequency aforementioned and observe the effect on intrinsic electric signals. However, before analyzing the proper circuit of the actuator, a general review on oscillating circuits is presented.

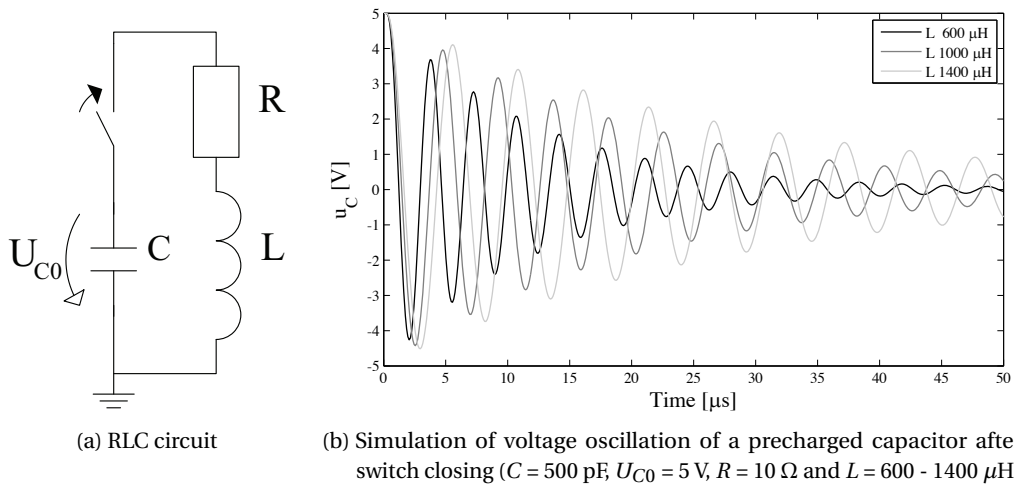


Figure 5.21 – Oscillating RLC circuit behavior

### 5.4.2 Oscillating RLC circuit

Kirchhoff's second law applied to a RLC circuit (Figure 5.21 (a)) is reduced to a second order differential equation as follows:

$$\ddot{i} + 2\lambda\dot{i} + \frac{1}{\omega_0^2}i = 0 \tag{5.8}$$

with  $\lambda = R/2L$  the attenuation describing the envelope of the oscillations and  $\omega_0 = 1/\sqrt{LC}$  the resonance frequency (details in appendix B.2.1).

In physical circuits the resistor is always different from zero and dissipates energy, which results in an attenuation of the oscillations. Three cases can appear depending on the damping factor  $\zeta$  defined as  $\frac{\lambda}{\omega_0}$ . The system is called critically damped at  $\zeta = 1$  when the overshoot is damped in a minimal time generating no oscillation at all. For values of  $\zeta > 1$ , the first peak is lower but takes more time to be cancelled. At the contrary, if  $\zeta < 1$ , the system is underdamped and the oscillations are gently attenuated following an exponential curve as shown in the simulations presented in Figure 5.21 (b) in which the capacitor is precharged at 5 V.

Indeed, if  $\lambda < \omega_0$  the solution presents exponentially decreasing oscillations given by:

$$i(t) = Ae^{-\lambda t} \sin(\omega_d t + \varphi) \tag{5.9}$$

with  $A$  and  $\varphi$  constants determined by the boundary conditions and  $\omega_d$  the actual frequency

of oscillation:

$$\omega_d = \sqrt{\omega_0^2 - \lambda^2} = \omega_0 \sqrt{1 - \zeta^2} \quad (5.10)$$

It is to note that the lower the damping, the closer to the resonance frequency  $\omega_d$  is.

As suggested in (5.9), the inductance of the circuit influences both amplitude and frequency of the oscillation. The simulation presented in Figure 5.21 where  $L$  varies between 600 and 1400  $\mu\text{H}$  confirms this statement.

With the aim of taking advantage of the variation of inductance observed during displacements of the coil within the actuator, modifications have to be made on the drive electronics. Theoretically, a coil is symbolized by a RLC circuit (Figure 5.18). However physically, the coil only possesses two connections and so, no oscillation can be created within it. In order to allow for an oscillation to be created, a second branch needs to be connected in parallel with the coil.

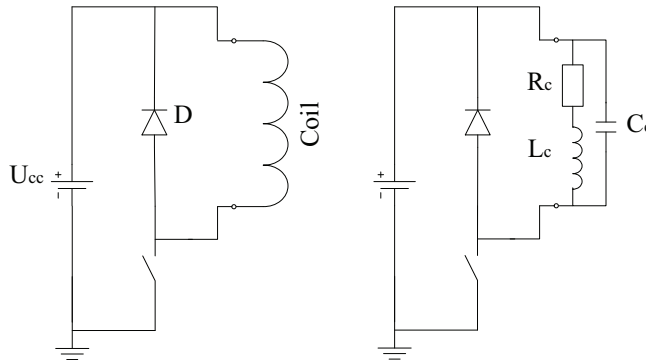


Figure 5.22 – Drive circuit principle for actuator and electrical model of a coil

The idea developed in this subsection consists in taking advantage of the branch composed of the freewheeling diode  $D$  responsible for the current extinction during off-phases of the transistor. In the present configuration (Figure 5.22), the current supplied in the coil disappears in the diode at the transistor extinction following a decreasing exponential. Used as is, the circuit behaves as a RL circuit with a time constant  $\tau = \frac{L}{R}$ . The circuit indeed works at the pulse width modulation (PWM) frequency driving the transistor (generally 20 kHz) which is too low to give importance to the effect of the tiny capacitor  $C_C$  which can almost be neglected ( $Z_C = \frac{1}{j\omega C_C}$ ). However, the current is so slowly cancelled in the RL loop that no significant difference can be observed. Two strategies are thus considered and simulated to reveal the change in inductance (Figure 5.23). In order to simplify the measurements and avoid adding a differential amplifier, voltage is measured between the transistor drain and the ground.



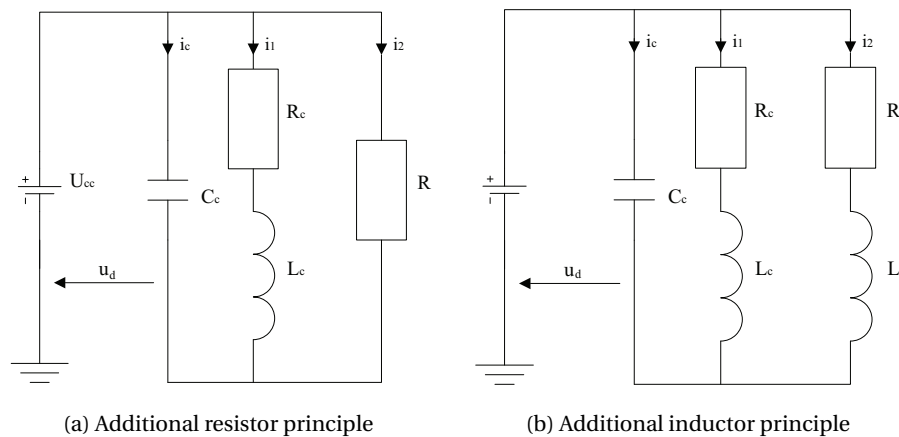


Figure 5.23 – Self-sensing measurement circuits for the simulation of the variable inductance effect

### RL circuit

The first possibility is to add a resistor in series with the free-wheeling diode to decrease the time constant  $\tau$  (Figure 5.23 (a)). To avoid perturbations generated by the transistor internal capacitor, simulations are run with a current  $I_{10}$  set in the coil inductor at  $t=0$  and the transistor is removed. In addition, the free-wheeling diode is considered as ideal and thus negligible. In this case, the current decreases more quickly which increases the voltage drop on the inductor which is proportional to the current derivative. Thereby the voltage on the transistor drain becomes measurable as shown in Figure 5.24, where a marked difference is observed depending on the inductance value. Despite a demonstrated potential, the main drawback of this solution is to narrow the effective control range of the PWM duty cycle. Indeed, the current is quickly cancelled during the transistor off-phase which results in a low current in the coil for the main part of the PWM range. A second drawback is that the measurement is strongly influenced by the initial value of the current  $I_{10}$  which we would like to avoid monitoring.

### RLC circuit

The second method investigated consists in creating an oscillating RLC circuit as introduced in Figure 5.21. As the coil itself is modeled by a capacitor in parallel with an inductor, one could add either an inductor or a capacitor in parallel with the coil to generate high frequency oscillations at the transistor shutting.

Removing the resistor  $R$  of Figure 5.23 (a) and adding a capacitor in parallel with the coil (but not in the diode branch) creates a RLC circuit. However, measurements on a test circuit revealed that the on-phases of the transistor are perturbed by the capacitor which shifts the impedance characteristic to the left and thus, does not allow the current creation in the coil resulting in very low forces (see appendix B.2.2). Oscillations are nevertheless well and truly

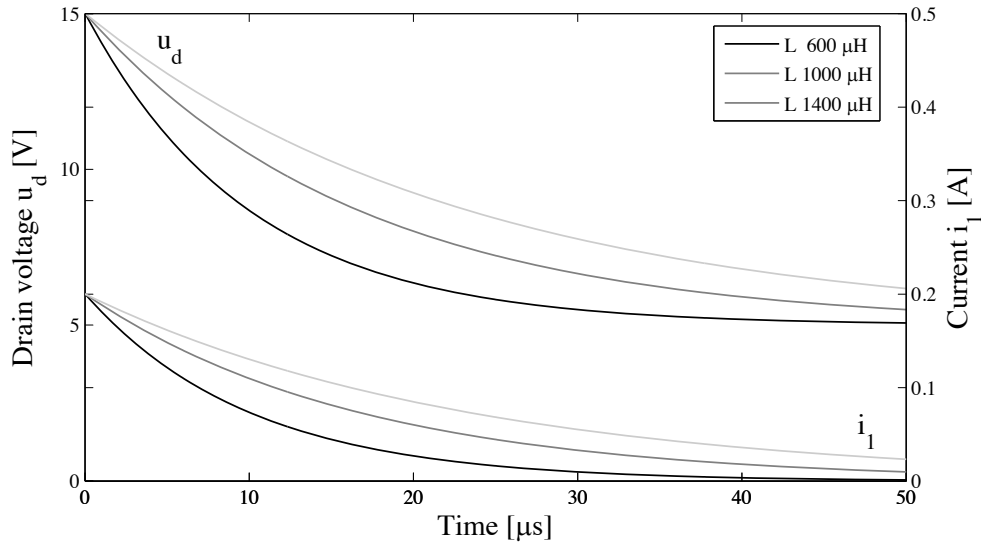


Figure 5.24 – Simulation of voltage and current decrease at the transistor shutting ( $C_C = 500$  pF,  $R_C = 10 \Omega$ ,  $L_C = 600 - 1400 \mu\text{H}$  and  $R = 50 \Omega$  with  $I_{10} = 0.2$  A)

present, which makes the method an eligible candidate for position sensing only, without active control of the force. Unfortunately the goal of the present section is to find a self-sensing method able to drive an actuator in closed-loop and not solely a new sensor.

The alternative option is to connect an inductor in the diode branch (represented by a  $R - L$  circuit in Figure 5.23 (b)). Like for the previous RL circuit, the initial current  $I_{10}$  decreases through the inductors ( $L + L_C$ ) and resistors ( $R + R_C$ ). However in this case, additional high frequency oscillations are superimposed, initiated by the coil capacitor and relayed by both inductors and notably the sensing element  $L_C$ . The small current oscillations of  $C_C$  are thus transformed into significant voltage oscillations in the inductors ( $u_L = L \cdot di/dt$ ) and their attenuation varies with the value of inductance. We have thus two superimposed circuits working in two different frequency domains. In order to get a better understanding of the circuit behavior, let us observe it in the frequency domain.

### 5.4.3 Simulation and numerical validation of the phenomenon

As presented in Figures 5.19 and 5.20, at a given position, the apparent values of  $R_C$  and  $L_C$  strongly vary with the frequency due to resonance phenomena. Thus, a distinction has to be made between the discharge of the coil current (RL circuit) and the generation of the oscillations (RLC circuit), happening at much higher frequency. Indeed the current extinction is synchronized with the PWM (generally 20-25 kHz) whereas the oscillations are generated ten to twenty times faster depending on the components value. The apparent value of the elements composing the circuit thus changes depending on the observed mode. Obviously, both phenomena happen simultaneously and are interconnected, however decoupled simulations

help explaining the functioning. In order to do so, the circuit of Figure 5.23 (b) is simulated twice, once at the inductor current discharge with low frequency components and once during oscillations initiated by the capacitor discharge with high frequency components (Table 5.1)<sup>2</sup>.

Table 5.1 – Parameters values for low and high frequency configurations of the RLC circuit based on measurements

Parameter	Low frequency	High frequency
$C_C$	500 pF	500 pF
$R_C$	10 $\Omega$	1 k $\Omega$
$L_C$	600 - 1400 $\mu$ H	600 - 1400 $\mu$ H
$R$	0.2 $\Omega$	10 $\Omega$
$L$	100 $\mu$ H	100 $\mu$ H
$U_{C0}$	0 V	5 V
$I_{10}$	0.2 A	0 A
$I_{20}$	-0.2 A	0 A

At the PWM frequency, the resistance of the circuit is low, close to DC conditions. After the transistor shutting, the current exponentially decreases in the RL circuit with a slow time constant  $\tau$  avoiding to kill the current creating Laplace's force too quickly (Figure 5.25). The duty cycle can thus be used efficiently on the entire range contrarily to the solution proposed in the RL circuit subsection (Figure 5.23 (a)). For the comprehension, it is important to note that only the initial current in the coil inductor  $I_{10}$  is simulated. In this configuration, the influence of the coil capacitor, barely visible with tiny oscillations on  $i_2$ , is negligible.

The oscillations finally appear in the high frequency configuration in which both coil and inductor resistances increase (Figure 5.26). The initial current is here set to zero in the inductors and only the capacitor is charged at  $U_{CC}$  at  $t=0$ . The discharge of the latter in both inductive branches generates important oscillations, whose attenuation and frequency vary with the coil inductance. The small value of the coil capacitor  $C_C$  allows it to be always charged at  $U_{CC}$  when the transistor shuts, improving the measurement repeatability. In this particular case, the reintroduction of the free-wheeling diode omitted for the simulations (Figure 5.22) would completely cancel the oscillations observed in Figure 5.26. However, as in reality it is superimposed with the decreasing current presented in the low frequency configuration, the direct current fluctuates but is always sufficient to keep the diode open. It is thus correct to simulate the high frequency effect without the free-wheeling diode.

The advantage of the solution integrating an additional inductance is that the position mea-

<sup>2</sup>For more clearness, only the resistor values  $R$  and  $R_C$  are adapted.

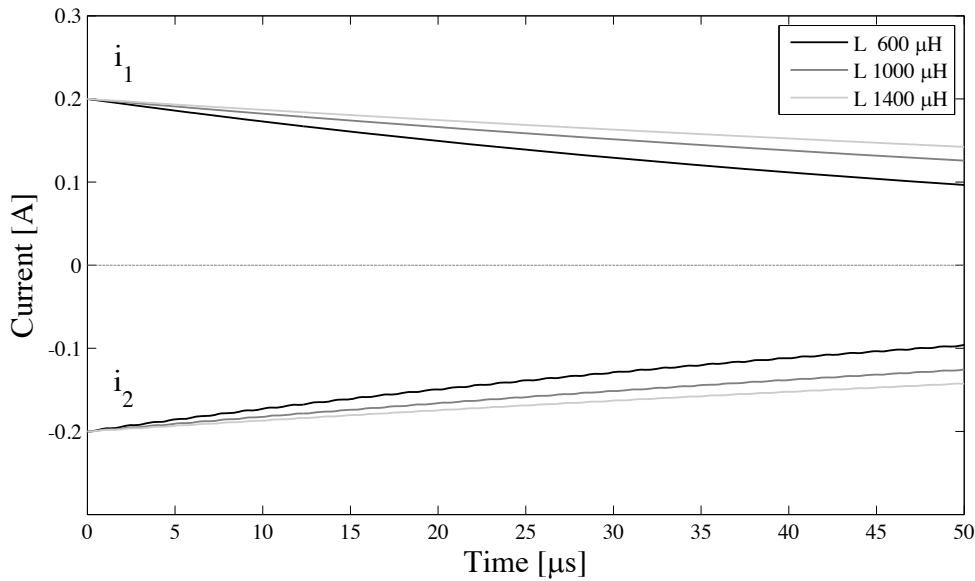


Figure 5.25 – Simulation of low frequency current decrease at transistor shutting ( $C_C = 500$  pF,  $R_C = 10$   $\Omega$ ,  $L_C = 600 - 1400$   $\mu$ H,  $R = 0.2$   $\Omega$  and  $L = 100$   $\mu$ H with  $I_{10} = 0.2$  A)

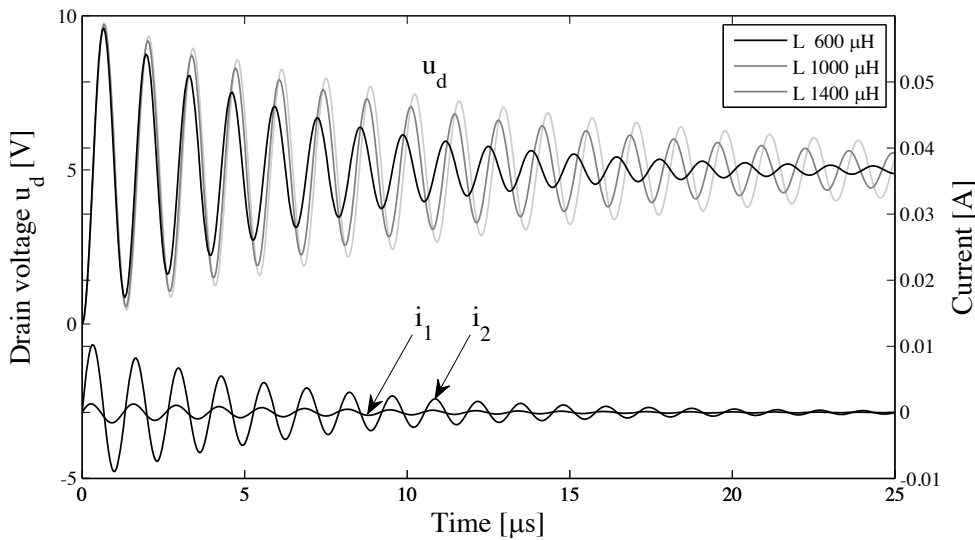


Figure 5.26 – Simulation of high frequency oscillations at transistor shutting ( $C_C = 500$  pF,  $R_C = 1$  k $\Omega$ ,  $L_C = 600 - 1400$   $\mu$ H,  $R = 10$   $\Omega$  and  $L = 100$   $\mu$ H with  $U_{C0} = 5$  V and  $I_{10} = I_{20} = 0$  A)

surement hardly influences the force creation and vice versa. On one hand, the current generated by the oscillations in the coil is so small that it does not influence the force, especially not for haptic applications (see  $i_1$  in Figure 5.26). On the other hand, the decrease of the current after transistor shutting only sees a tiny change in resistance attributed to the wire-wound inductor keeping thus a stable DC current in the coil for the creation of the force.

In order to confirm the simulations presented above and improve their understanding, an analytical model of the RLC circuit is established. Kirchhoff's second law applied to the circuit of Figure 5.23 (b) allows writing the third order differential equation below formulated as a function of  $i_2$  (details in appendix B.2.3):

$$i_2(R_C + R) + \dot{i}_2(R_C R C_C + L_C + L) + \ddot{i}_2(R_C L + R L_C) C_C + \dddot{i}_2 L_C L C_C = 0 \quad (5.11)$$

A numerical resolution of the differential equation (5.11) using Matlab produces the same results as for the current decrease simulation (Figure 5.25) as shown in Figure 5.27.

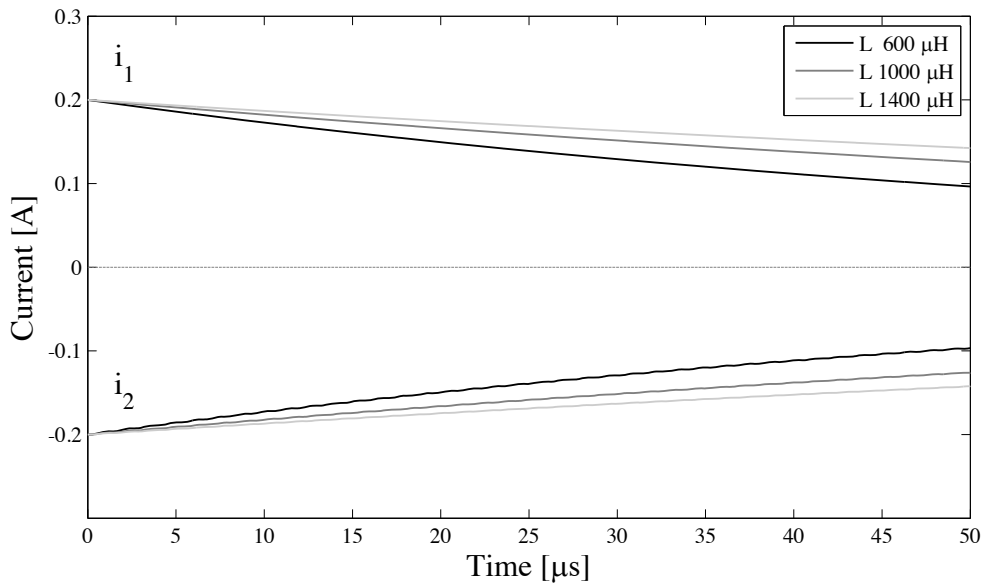


Figure 5.27 – Numerical resolution of low frequency current decrease at transistor shutting ( $C_C = 500$  pF,  $R_C = 10 \Omega$ ,  $L_C = 600 - 1400 \mu\text{H}$ ,  $R = 0.2 \Omega$  and  $L = 100 \mu\text{H}$  with  $I_{10} = 0.2$  A)

Then, in order to analyze the influence of the capacitor at high frequency, a second formulation of the system is established as a function of the coil voltage (appendix B.2.3). The system is solved in Matlab and once again, the results of Figure 5.28 correspond to the simulations of the circuit at high frequency (Figure 5.26). Tiny discrepancies are however visible on the phase of the drain voltage at  $25 \mu\text{s}$ , probably attributed to differences in software numerical resolution.

In the case of an electromagnetic actuator, the three parameters  $R_C$ ,  $L_C$  and  $C_C$  potentially vary with the position. What is interesting with the present method is that the capacitor variation only influences the frequency (see (5.8)) and not the attenuation. Measuring the difference in frequency would indeed cause problems as multiple parameters, namely  $L_C$  and  $C_C$ , influence it. Ideally, it would be important to measure the attenuation at the frequency  $f_0$  mentioned in Figures 5.19 and 5.20 where the resistance stays constant and solely the inductance varies with the position.

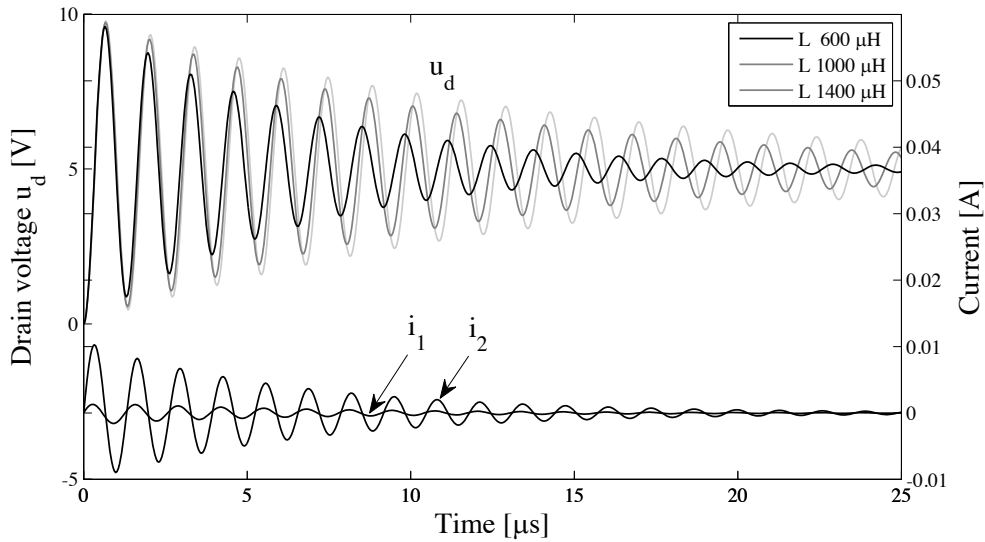


Figure 5.28 – Numerical resolution of high frequency oscillations at transistor shutting ( $C_C = 500 \text{ pF}$ ,  $R_C = 1 \text{ k}\Omega$ ,  $L_C = 600 - 1400 \text{ }\mu\text{H}$ ,  $R = 10 \text{ }\Omega$  and  $L = 100 \text{ }\mu\text{H}$  with  $U_{C0} = 5 \text{ V}$  and  $I_{10} = I_{20} = 0 \text{ A}$ )

#### 5.4.4 Frequency adaptation

In order to be dependent on the variation of inductance only, it is decided to target the  $f_0$  frequency to generate the oscillations on the transistor drain. As stated in (5.8), the pulsation  $\omega_0$  can be decreased by increasing either the inductance or the capacitance of the circuit. One step is already done with the addition of the second inductor  $L$ . However, in order to avoid adding a too large inductor that would be bulky and bury the variation of the coil inductance, there is the possibility of slightly increasing the circuit capacitance by connecting a small capacitor in parallel with the coil. Of course, this capacitor should remain as small as possible to avoid disturbing the creation of the current responsible for Laplace's force (as in Figure B.6, appendix B.2.2). The advantage is that the capacitor does not influence the attenuation ( $\lambda = R/2L$ ). In addition, attention should be paid to the choice of the transistor, the output capacitor of which influences the circuit behavior. A trade-off thus has to be made between the capacitor, the inductor and the transistor to get the most of the measurements.

Figures 5.29 and 5.30 show the influence of the additional capacitor which shifts the inductance and resistance characteristics to the left and decreases the resonance effect on the latter. This artefact can thus be used to fine-tune the frequency of the oscillations and the sensibility of the attenuation.

#### 5.4.5 Measurement method

Now that the presence of the oscillation phenomenon is known, a method has to be found to measure it. A first possibility would be to concentrate on a single oscillation and measure

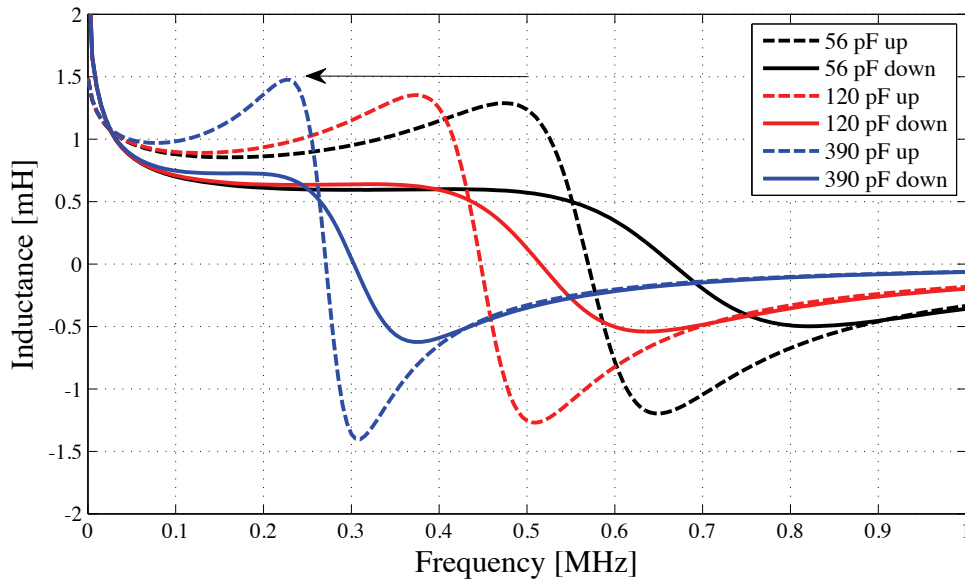


Figure 5.29 – Influence on the coil inductance caused by an additional capacitor in parallel

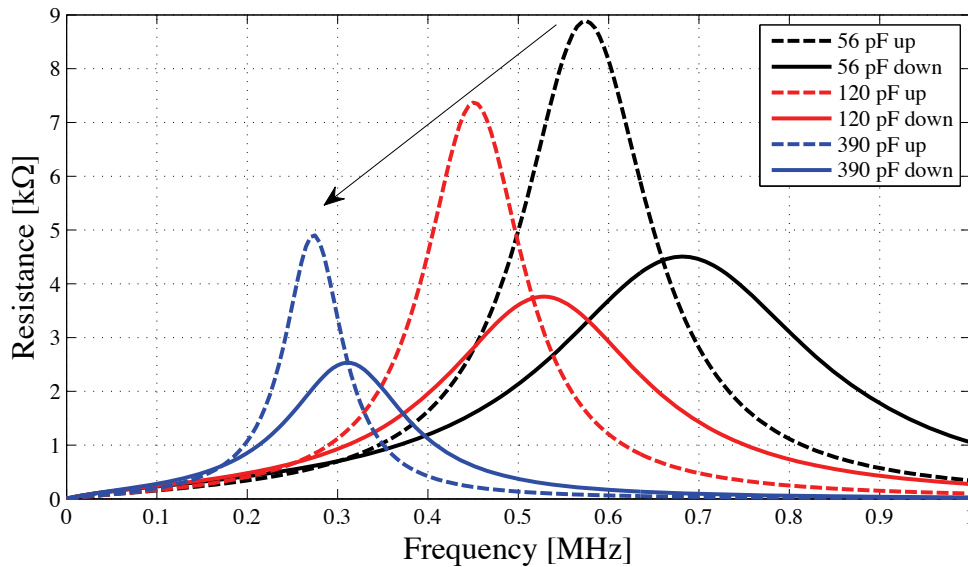


Figure 5.30 – Influence on the coil resistance caused by an additional capacitor in parallel

its magnitude at a given time within the PWM period (e.g. Figure B.5). In that case, the main drawback is that the oscillation frequency is so high that an ultra-fine resolution of the clock is required to get a reasonable measurement range for the position. An option to sidestep the problem would be to decrease the frequency of the oscillation in order to have only one oscillation per PWM period and thus be able to easily measure the drain voltage at a given time (Figure 5.31). However, as already mentioned earlier, when the oscillation frequency approaches the PWM frequency, the effect of the resonance on the impedance is important,

preventing the creation of the current responsible for the force. In that case, the advantage of the independence between high and low frequency circuits is lost.

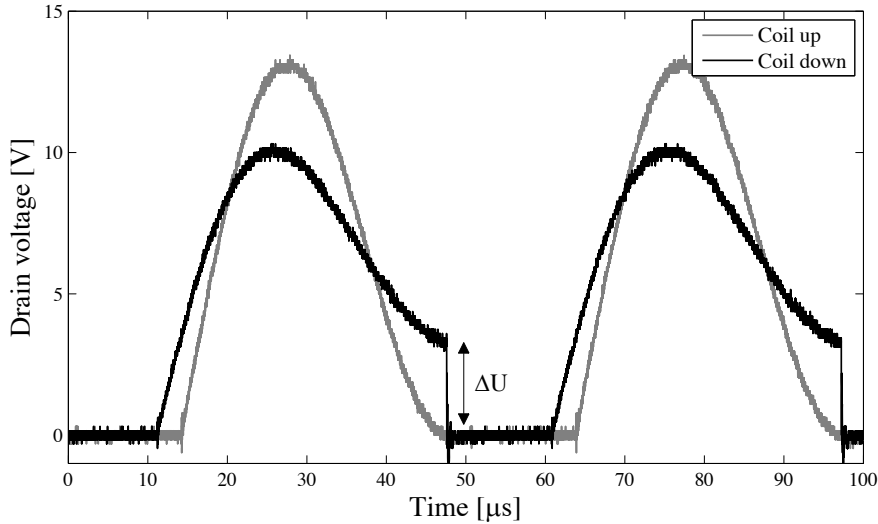


Figure 5.31 – Drain voltage characteristic with a 33 nF capacitor in parallel with the coil

The preferred solution is to measure the attenuation  $\lambda$  represented by the envelope of the high frequency oscillations. In order to do so, a filter circuit is implemented to create an image of the attenuation (Figure 5.32). The oscillations being isometric around  $U_{CC}$  (Figure 5.28), the signal is at first limited at this value by a Zener diode allowing the envelop to be revealed. A RC low-pass filter is then applied giving an output  $u_{lp}$  in  $1 - e^{-\lambda}$ . A simple comparator is finally used as a microcontroller input to stop a counter. The value of the position is given by the time between the transistor extinction and the interrupt triggered by the magnitude of the drain voltage envelope. It is to note that a follower circuit is added at the beginning of the signal processing to avoid disturbing the sensing RLC circuit.

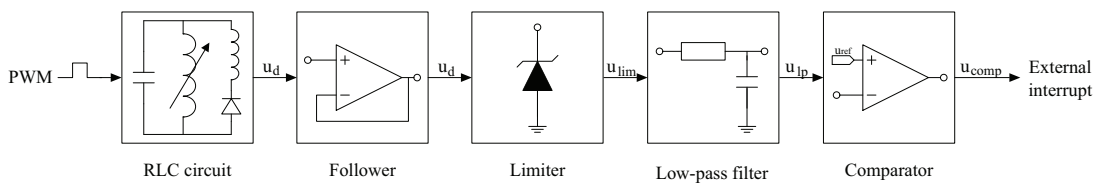


Figure 5.32 – Self-sensing measurement principle

Figure 5.33 shows the drain voltage obtained in the simulation of Figure 5.26 at different stages of the filter until getting the final  $u_{comp}$  used to trigger the microcontroller external interrupt. The variation of inductance results in a  $5 \mu s$  delay representative of the coil position. As for the design of the low-pass filter, it is a trade-off between a significant difference in time (high cutoff frequency) and the cancelling of the residual oscillations (low cutoff frequency).



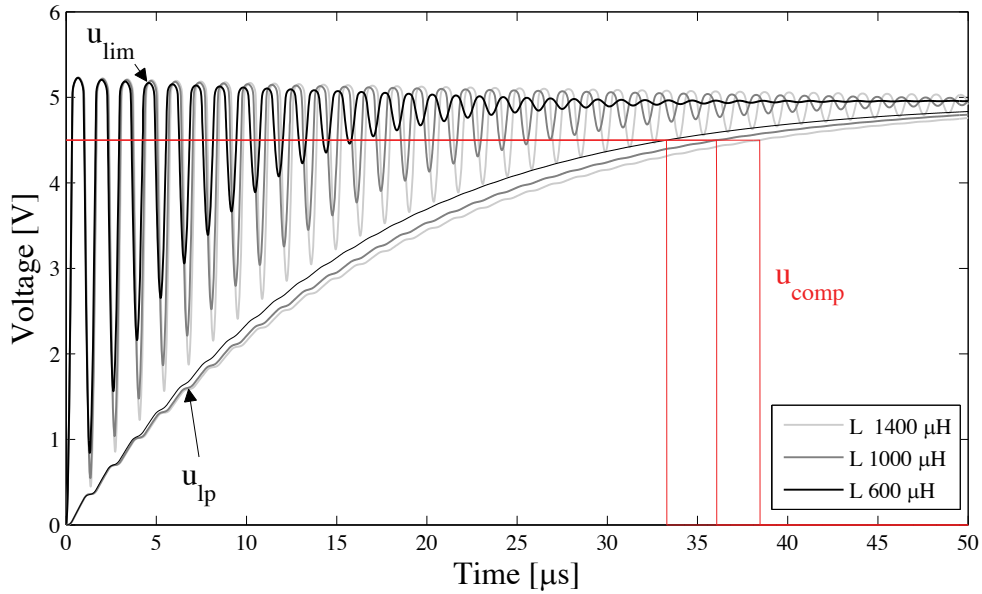


Figure 5.33 – Drain voltage after voltage limiter  $u_{lim}$  (5.1 V), low-pass filter  $u_{lp}$  (12 kHz) and comparator  $u_{comp}$  (4.5 V)

#### 5.4.6 Results

All the elements of the induced high frequency oscillations method developed in the previous subsection are assembled and applied to a circuit driving a cylindrical short-stroke actuator designed in chapter 4. The measured values of the components used in the circuit are summarized in Table 5.2. The signal processing principle introduced in Figure 5.32 requires two operational amplifiers, a Zener diode and a RC filter. The circuit is quite basic, however the first operational amplifier used as a follower needs to be fast enough to avoid perturbing the drain voltage  $u_d$ . Always with the aim of reducing the hardware requirements for multi-finger haptic applications, a trick is found to group the three first blocks (i.e. follower, limiter and low-pass filter) in a single electronic component. The integration of a slow low-cost operational amplifier as follower at the beginning of the chain avoids adding the two following blocks. Indeed, as the amplifier is supplied at  $U_{CC}$  (5 V), the part of the oscillations rising above that value are cut similarly as if a limiting diode was used. Then, the fact that the operational amplifier output swing starts decreasing from 5 kHz due to a restrained bandwidth (see appendix B.2.3, Figure B.7), the low-pass filter can be omitted. Moreover, the second operational amplifier used as final comparator doubles the low-pass filter effect brought by the narrow bandwidth. In conclusion, a single LM358 package containing two operational amplifiers is used to provide a unique time-based signal to the microcontroller for the position detection.

The initial oscillating drain voltage is thus transformed in a simple logic signal to trigger the microcontroller interrupt as presented in Figure 5.34. A first remark has to be made on the first voltage peak observed on  $u_d$ . Indeed, at the transistor shutting, the abrupt change in the

Table 5.2 – Measured values of the components used in the final test bench

$C_C$	$R_C$	$L_C$ (down - up)	$R$	$L$	$C$
52 pF	14 $\Omega$	438 - 645 $\mu$ H	0.7 $\Omega$	100 $\mu$ H	390 pF

current derivative bursts the voltage measured at the drain ( $u_L = L \frac{di}{dt}$ ). In order to protect the input of the follower circuit, a Zener diode is added in parallel with the transistor, between the drain and the ground. Its value is chosen as high as the operational amplifier allows, quickly killing the voltage peak and avoiding disturbing the high frequency oscillations. The second remark concerns the rise and fall times of the comparator output  $u_{comp}$ . The introduction of a faster operational amplifier would make its edges vertical, however as the interrupt is triggered at a fixed voltage,  $u_{comp}$  slope does not disturb the functioning. The measurable value  $\Delta t$  appears at the fall of  $u_{comp}$ , between the curves corresponding to the extreme positions of the actuator (red and pink).

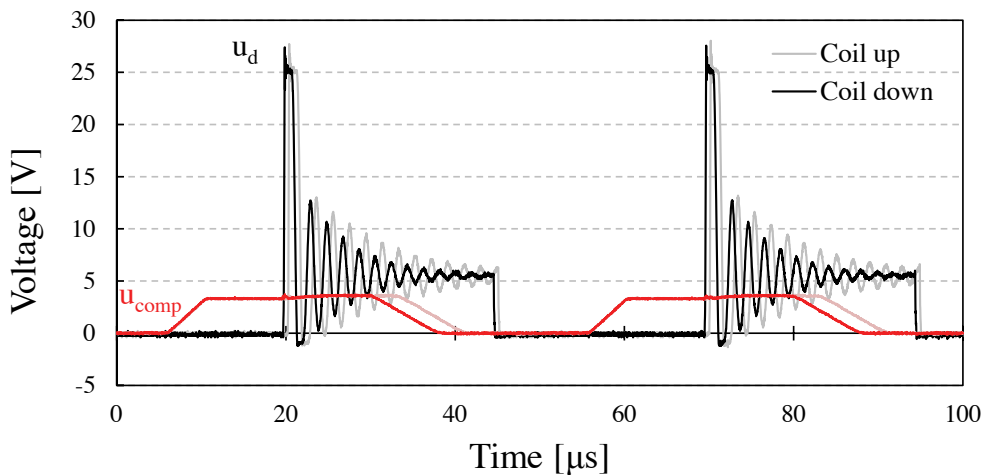


Figure 5.34 – Drain voltage measurements  $u_d$  and the corresponding signals triggering the microcontroller external interrupt  $u_{comp}$  for high and low positions of the coil

Dynamic position measurements are performed on the cylindrical actuator using a precise laser sensor for reference. The self-sensing algorithm converts the time difference  $\Delta t$ , reaching 2.8  $\mu$ s (Figure B.8), in an output PWM duty cycle which, once low-pass filtered, gives the position in volts. As shown in Figure 5.35, the fit between the laser sensor (black trace) and the self-sensing (grey trace) is good. However, a closer look allows distinguishing slight differences between both traces.

Indeed, the plot of the self-sensing values versus the laser position presents a non-linearity of the response (Figure 5.36). The characteristic can clearly be separated into an upper linear part (interpolated in red) and a lower quadratic part (interpolated in yellow). That discontinuity can be attributed to the geometry of the actuator. In the higher part, the coil plunges within

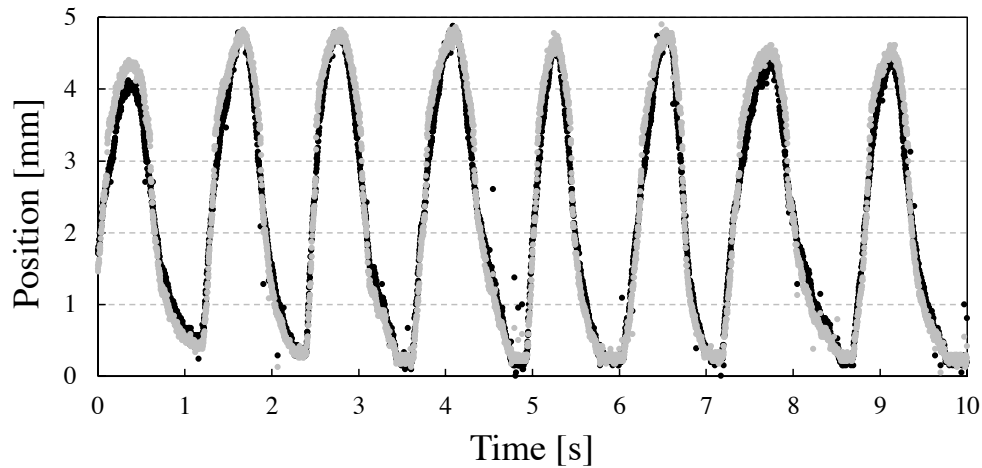


Figure 5.35 – Dynamic measurements of the coil position with a reference laser sensor (black) and the self-sensing algorithm output (grey) supplied with a PWM duty cycle of 50 %

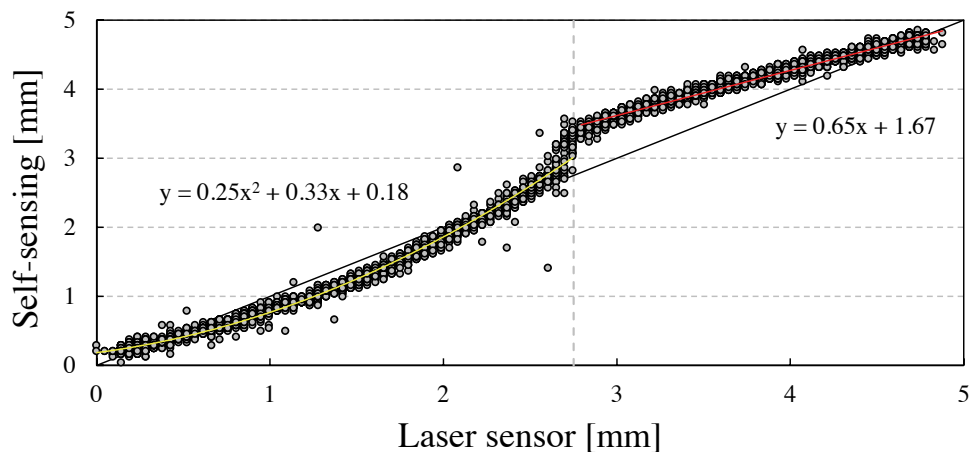


Figure 5.36 – Detailed comparison between self-sensing and laser sensor values during dynamic displacements of the coil (PWM 50 %). The profile can be split in two parts, modeled with a quadratic polynomial for the lower part (yellow) and a linear function for the upper part (red).

the iron housing and surrounds the magnet. As the magnetic permeability of the magnet is very low (comparable to air), approaching a coil does not change its inductance contrarily to approaching a ferromagnetic material. The effect of the magnet is thus limited to the eddy currents phenomenon (which is weak in the actuator walls). However, in the 3 last millimeters of the stroke, the coil penetrates both an external iron housing and an internal iron core in the form of a little bump inserted below the magnet for force linearization purpose. The permeance effect is thus reinforced. In addition, the closer to the bottom the coil is, the more important the eddy currents are, which increases even more the quadratic component of the

profile. As for the little gap between both curves responsible for errors up to half a millimeter, it comes from a residual oscillation affecting the follower circuit output due to the imperfect low-pass filter created by the operational amplifier (Figure 5.37).

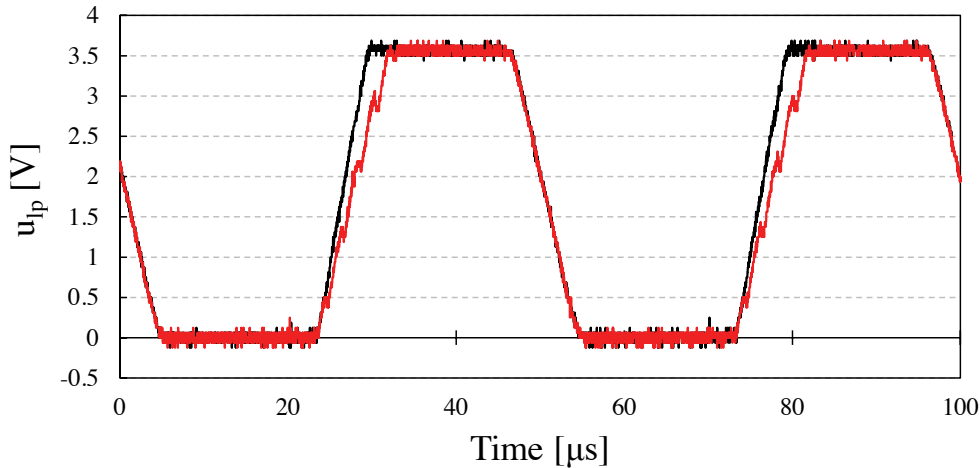


Figure 5.37 – Residual oscillations on the drain voltage for high positions (red)

The goal of the self-sensing method presented in this section being the integration in a closed-loop control, it is necessary to study its behavior over the power supply range. A discrete sweep of the PWM duty cycle is run and the interrupt time  $\Delta t$  is measured relatively to the lowest position offset measured at the beginning of each dynamic phase (Figure 5.38).

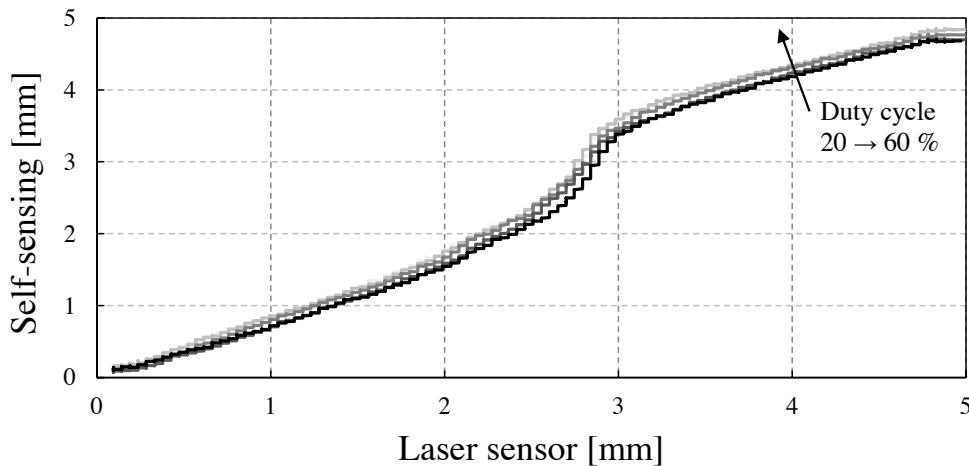


Figure 5.38 – Influence of the PWM duty cycle on the position detection during dynamic displacements of the coil (a moving average filter is used for a better clearness)

As predicted by the theoretical analysis of the circuit at low and high frequency, the influence of the current level barely influences the attenuation. The maximum discrepancy indeed does not generally exceed 0.2 mm and could be decreased using a digital offset. Figure 5.38 only presents the curves for duty cycles between 20 and 60 %. The reason is that the method,

used as is, is limited in its range between 18 and 67 %. The upper limit is set by the time the oscillation takes to be sufficiently damped for an efficient measurement through the low-pass filter. This limit could be increased by accelerating the signal damping but with the drawback of losing resolution on the position. As for the lower limit, it is defined by the operational amplifier rise and fall times, which could be easily improved by increasing the operational amplifier performance. However, as the first 10 to 20 % of the supplied energy is generally used to counter the gravity acting on the actuator, an enhancement this way is not necessary.

An additional tiny linear offset is directly attributed to the width of the first voltage peak  $u_d$  (Figure 5.39). The difference is only of five counter increments per 10 % step ( $0.17 \mu\text{s}$ ) on the whole range between 20 and 70 % and can be corrected by introducing a software offset.

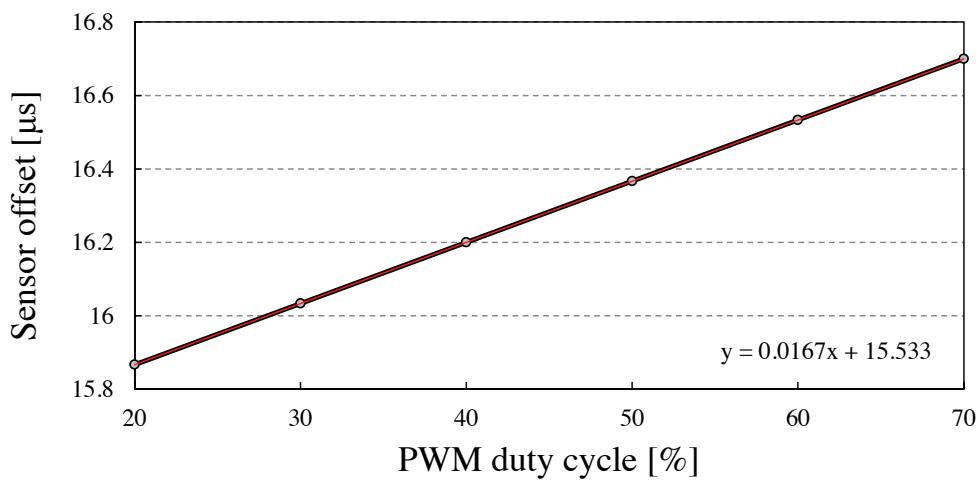


Figure 5.39 – Values of the counter at the lowest actuator position (sensor offset) for different duty cycles

In conclusion, a first strategy to use the presented self-sensing method in a closed-loop control consists in limiting the useful range of the PWM to  $\sim 70$  % if the application tolerates it. If not, a second strategy proposes to decrease the frequency of position measurements. Indeed, a position update rate of 1 kHz is sufficient to guarantee a smooth feeling to the user. It is thus possible to use one period over twenty to measure the position at a fixed duty cycle (e.g. 50 %) and still profit of the entire force range.

#### 5.4.7 Improvements and design for self-sensing

Regarding the possible improvements for the self-sensing method using induced high frequency oscillations, three main axes can be considered depending on the final application specifications.

- In the case where hardware modifications have to be avoided, a software linearization of the position characteristic appears as a must. Indeed, with the help of the calibration of

Figure 5.36, the position profile generated by the self-sensing algorithm can be entered as a look-up table within the microcontroller improving thus the sensing resolution. With neither additional electronic components nor modifications on the actuator, this solution represents the one minimizing the cost.

- The electronics introduced in Figure 5.32 can also be enhanced by introducing faster operational amplifiers capable of accurately following the high frequency oscillations. Coupled with a proper low-pass filter, either passive or active, the amplifiers allow for a widening of the measurement range within the PWM duty cycle. In addition, a tunable low-pass filter allows cancelling potential residual oscillations observed in Figure 5.37, improving thus the output linearity. In that case, the improvement of the sensing electronics goes with an increase of the cost and bulk that needs to be justified by the requirements of the application, but can be easily operated if needed.
- Finally, an improvement of the sensitivity and linearity of the position detection can be obtained by directly modifying the actuator geometry. The principle, called design for self-sensing, consists in thinking about the impedance variations of the coil during its travel, already at the actuator design stage. Reducing the wire section, for example, increases the three elements of the coil equivalent model. As for the thickness and position of the ferromagnetic material surrounding the coil, it plays a major role in the variation of impedance. However, conflicts can appear between the linearization of the force and the impedance characteristic. It is notably the case with the cylindrical actuator used for the dynamic measurements of Figure 5.35 where the iron bump added below the magnet for force linearization purpose generates a non-linearity of the position characteristic (Figure 5.36). A trade-off thus has to be made depending on the application requirements.

### 5.5 Summary

The diversity of potential applications in multi-finger haptics makes it difficult to provide a universal solution for the detection of the position. As introduced in section 3.3, the main properties required are a limited volume, a low cost of integration (including sensor and electronics), avoiding parasitic forces and rapidity. Despite building a general framework, these basic requirements leave a certain liberty to the developer. In order to guide him towards a solution that corresponds to the needs for a given application, four methods for position sensing are proposed, all distinct regarding their hardware and performance. They are classified according to their degree of hardware abstraction.

The first method can be characterized as standalone in a sense that its functioning is completely independent from any actuator and can be quickly adapted to different applications. It proposes to use a single optical barrier to measure the position and discriminate the direction of movement. The idea is to play with different levels of transparency of a ruler to increment or decrement the position. The advantage of this solution is to allow the user to simply design

the desired ruler with any drawing software and print it on a transparency film depending on his needs. Contrarily to traditional optical quadrature encoders, this method allows discriminating the direction of displacement with only one photointerrupter thanks to a ruler pattern alternating three levels of transparency. The method does not pretend to exhibit a high resolution but should be rather used as a tool for the fast prototyping of low-cost optical sensors in the research environment.

A first step in the merging between the actuator and the sensor is reached with the so-called hybrid sensing. Indeed, this method proposes to take advantage of physical quantities intrinsically present within or around the mechanical structure to detect the position of the mobile unit. In the case of the electromagnetic short-stroke actuators presented in the previous chapter, the magnetic flux density naturally appears as an eligible candidate. The trick is to place a miniature linear Hall sensor, interdependent with the coil, to measure the magnetic leakage of the actuator magnet. As the magnetic flux density decreases with the distance to the actuator, the output of the Hall sensor is proportional to the coil position. The repetitiveness and compact size of the method is however affected by the need for a calibration to counter a slight non-linearity of the position characteristic.

Finally, a total abstraction of the physical position sensor is reached with two self-sensing methods. In this case, the actuator becomes the sensor and the position information is directly extracted from intrinsic physical quantities of the coil such as current or voltage. The first method proposes to interpolate the position of the coil during a stroke using the back emf. Indeed, when a conductor moves within a magnetic flux, an induced voltage is created. In the case of an electromagnetic short-stroke actuator, the back emf is directly proportional to the coil velocity. Two back emf measurements made at the beginning of a fall allow calculating the acceleration and then interpolating the position. The method, used as is, necessitates a constant acceleration to produce a correct estimation of the position. It is by example possible to interpolate the free fall of a load subjected to gravity in order to generate a soft-landing. However, the human finger behavior during touch-typing operations is uneven and a constant acceleration cannot be guaranteed in all cases. Solutions exist to sidestep the problem, for instance by measuring both current and voltage, increasing thus the complexity of the position detection setup. However, the position detection for multi-finger haptic devices requires opting for a simplification of both hardware and software to allow for an efficient control of networks of actuators. For this reason, a new approach is investigated.

The last technique suggests taking advantage of the variation of the coil impedance when the latter plunges in the ferromagnetic core of the actuator. The principle lies in the generation of high frequency oscillations at the transistor shutting. Adding a wire-wound inductor in the free-wheeling diode branch in parallel with the coil creates a new circuit that works differently depending on the observed frequency domain. On one hand, at the PWM frequency, the current present in the coil at the transistor shutting only sees a little change in inductance due to the additional inductor and slowly decreases during the off-phase following an exponential. On the other hand, the fact that the coil conductors are close to each other can be modeled by a

small capacitor that charges when the transistor is on. At the transistor shutting, the discharge of this capacitor creates a RLC circuit oscillating at high frequency. The position information is then extracted from the damping of these oscillations that are proportional to the coil impedance. The advantage of this method is that the high frequency oscillations induced for the position detection are independent from the main supply current and so, barely influence the creation of the force. In addition, the modifications brought to the electronics are weak and low-cost variants are possible. Finally, a single microcontroller input only is needed and the algorithm is extremely light, which matches with the course of action towards the simplifications required by multi-finger haptic applications.

The originality of the two self-sensing methods presented resides in the fact that they can be applied to short-stroke actuators with non-repetitive inductance characteristics which has rarely been treated in literature up to know. In addition, required hardware and software resources have been reduced to the minimum, always with the aim of being able to drive as many actuators as possible. The proposed methods thus go against the current trend requiring always more complexity, which is clearly incompatible with multi-finger haptic devices.





# Multi-finger haptic applications

**Contents**

---

<b>6.1 Haptic Keyboard</b>	<b>142</b>
6.1.1 Actuator	142
6.1.2 Control	144
6.1.3 Communication	147
6.1.4 Prototypes	149
6.1.5 Software user interface	152
<b>6.2 VibKey Pad</b>	<b>155</b>
6.2.1 Capacitive touch sensor	156
6.2.2 Vibrator	157
6.2.3 Control	158
6.2.4 Prototypes	160

---

Introduced in chapter 3, the different parts constituting a multi-finger haptic device were largely discussed in chapters 4 and 5. First, the design methodology for electromagnetic actuators resulted in the optimization of miniature short-stroke actuators and vibrotactile buttons. Then, in order to measure the position of these linear actuators, several measurement techniques were presented, by reassigning existing sensors or developing innovative self-sensing methods. The present chapter naturally follows these results and takes advantage of some of these tools to design multi-finger haptic applications. Control, communication and software user interface aspects being specific to each system, they will be outlined together

with each application. Two devices are presented hereinafter: the Haptic Keyboard and the VibKey Pad.

In collaboration with Logitech Europe SA, a fully programmable force feedback keyboard is developed allowing the user to freely change the touch sensation provided in response to finger strokes. Mainly for research purpose, this keyboard is aimed to help understand and improve the typing comfort. Then, in order to fill in the lack of physical acknowledgement generated by the tactile buttons integrated in more and more consumer electronic devices, a small vibrator is used to improve the user's experience. Embedded in a four buttons remote, each vibrotactile button is able to provide tactile and auditory feedbacks to acknowledge finger contact.

### 6.1 Haptic Keyboard

The appearance of the first personal computers in the mid-seventies marked a turn in the data processing world and, more broadly speaking, in the people's daily life. In everyone's mind, the term "PC" includes not only the computer itself, but also peripherals like the screen, the mouse and the keyboard. It is in fact the latter that will represent the center of attention of the present section. The keyboard, which appeared way before the computer if one considers its ancestor, the writing machine, went through generations without significant change.

In the present application, it is proposed to improve the typing experience of the user by designing a novel haptic keyboard with the aim of providing an adaptable force feedback in response to human strokes. In order to make it possible, small linear actuators introduced in chapter 4 are fitted under each key in order to replace the rubber domes and scissors currently used in the keyboards of the market. The user will thus be able to tune the force feedback of the keys according to his wishes, whether he prefers hard or soft keys, smooth or rough sensation or even a buckling spring-like feeling.

Developing a device with as many actuators represents a real challenge from both hardware and software points of view. The next subsections thus provide an overview of the main features constituting the haptic keyboard, namely actuation, control and communication directly following from the general introduction given in chapter 3. Finally, two prototypes are fabricated: the Haptic Pad and the Haptic Keyboard integrating respectively 16 and 64 programmable keys. Moreover, in order to improve user-friendliness, a graphic interface is developed allowing the user to define his own force profiles and upload them in the keyboard.

#### 6.1.1 Actuator

##### Adaptations for manufacture

With its 64 programmable keys, the Haptic Keyboard is an excellent example for which the actuators have to be designed with an eye towards a simplification of the fabrication process.

As introduced in subsection 4.6.1, the cylindrical actuator goes this way with a simplified manufacturing compared to the square actuator. Moreover, its optimization showed that the specifications given in Table 4.1 and corresponding to those of a haptic keyboard key are fulfilled (Tables 4.15 and 4.16).

A well-known drawback of electrodynamic systems is the connection. Indeed, the moving coil needs to be connected to the power supply and in addition of being bulky, repeated movements can lead to break the wires in the worst case scenario. In the keyboard example, connecting all the keys could rapidly become a nightmare. This is the reason why it is decided to turn the actuator upside-down, passing from an electrodynamic to an electromagnetic configuration (Figure 6.1). All coils are fixed on the main board, avoiding the presence of intertwined wires moving relatively to each other. The density of the array thus increases and all the electronics can be mounted on a single board.

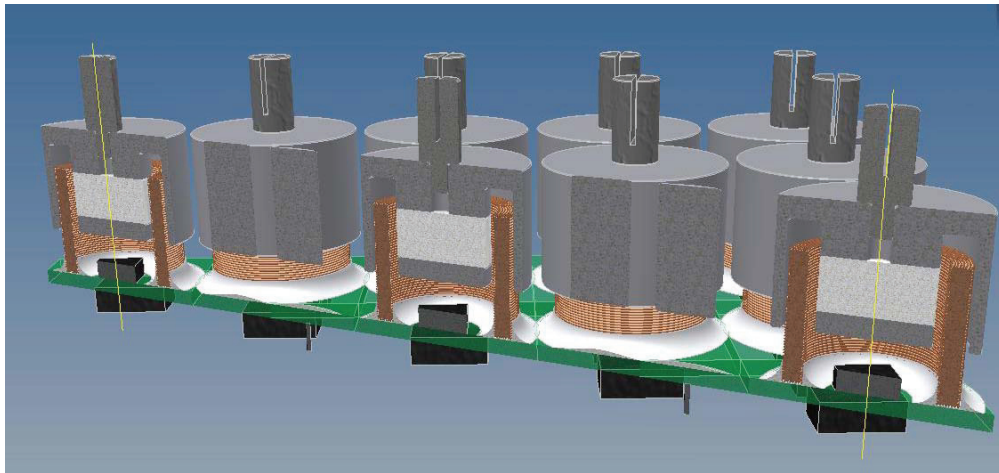


Figure 6.1 – Electromagnetic actuators array with the coils fixed on the main board

The main difference between both configurations is the moving inertia. Electrodynamic actuators were initially chosen because of their excellent dynamics made possible thanks to the lightweight of the coil. The electromagnetic configuration displacing the mass of the iron housing plus the magnet is thus slower. However, in the present case of miniature actuators, the additional weight is limited and the dynamics still guarantees to be faster than the human finger (see appendix C.1.1).

For the integration of the actuators inside the keyboard, the idea is to take benefit from the excellent guideway provided by existing Logitech keyboards. The choice fell on the MX™ 5500 keyboard for the Haptic Pad and on the MX™ 3200 for the Haptic Keyboard<sup>1</sup>, both guaranteeing a key travel of 4.4 mm. This travel represents one of the largest on the market, which allows for the implementation of various touch sensations. The second advantage is that the bottom of each key is pierced with a slot (Figure 6.2), allowing the moving part of the

<sup>1</sup>A QWERTY layout was required for the Haptic Keyboard for testing purpose in the USA.

## Chapter 6. Multi-finger haptic applications

---

actuator to be simply plugged in using a small plastic adapter (Figure 6.3).

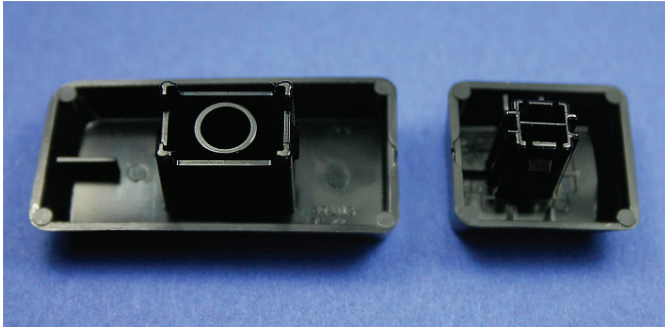


Figure 6.2 – Guideway of MX™ 5500 keys



Figure 6.3 – Key adapters with and without slit

Finally, an O-ring is glued on the actuator moving part to damp the shock of the key hitting the bottom case (Figure 6.4) and the coils are inserted inside the actuators before being fixed to the main electronic board for aligning reasons (Figure 6.5).

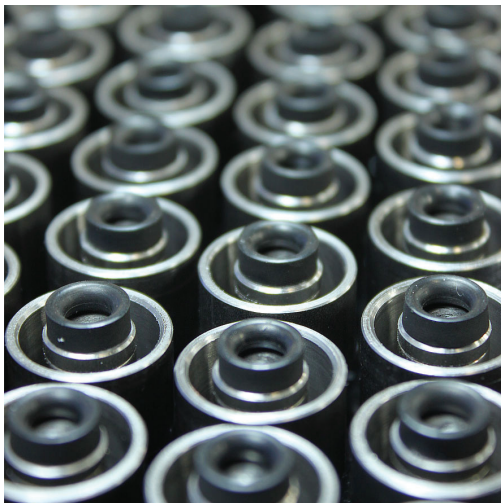


Figure 6.4 – O-rings mounted on actuators

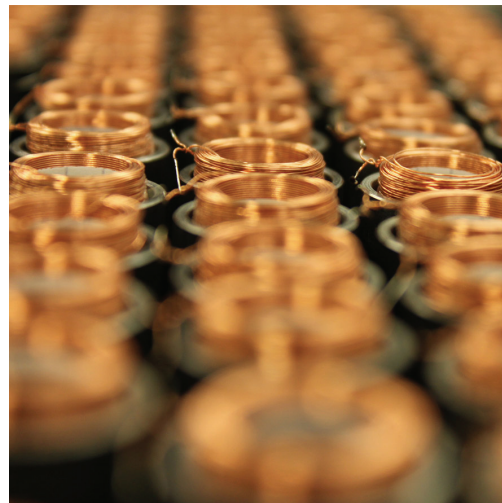


Figure 6.5 – Preparation for the gluing of the coils

### 6.1.2 Control

The control strategy adopted for the Haptic Keyboard is summarized in Figure 6.6. The right hand side shows the closed-loop control for a single actuator and the left hand side represents the block control strategy.

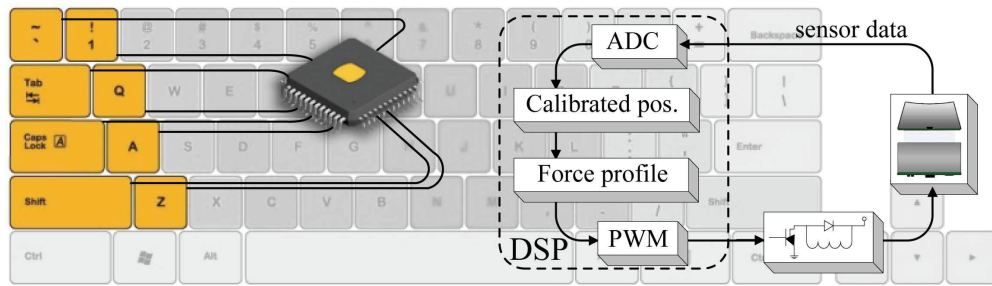


Figure 6.6 – Block control strategy and closed-loop principle for a single key

### Position detection

Linear Hall sensors [151] are chosen to monitor the position of the keys. As introduced in subsection 5.1.2, their small size, repeatability and straightforward data processing make them ideal for the realization of a force feedback keyboard. Moreover, the new upside-down configuration of the actuators allows them to be simply soldered on a single electronic board, in the center of each coil (Figure 6.7).

In order to reduce the overall power consumption, springs can be placed around the sensors. Their role is to carry the own weight of the actuators moving part ensuring thus a high position of the keys even when the keyboard is not powered (Figure 6.8). Indeed, maintaining the 64 keys of the Haptic Keyboard high without springs would necessitate 4.2 A under 5 V (21 W) just for the support (65 mA per key).

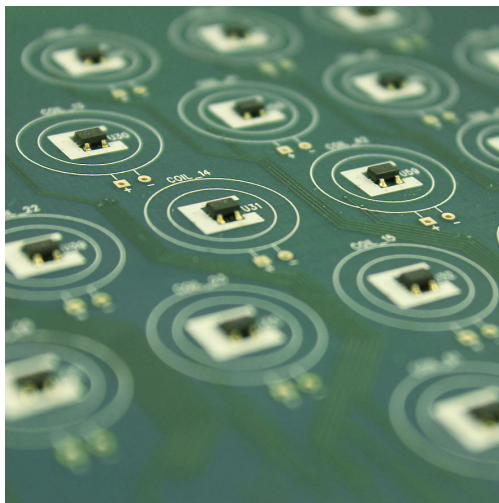


Figure 6.7 – Detailed view of the Hall sensors

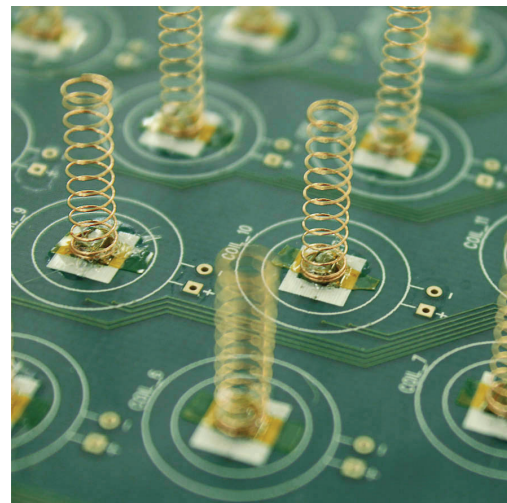


Figure 6.8 – Sensors insulation and supporting springs



**Single key control**

Optimizing the control efficiency of a multitude of actuators necessitates decreasing the number of computations. If the memory is sufficient, look-up tables are an excellent alternative for rapid executions. In the present case, the specifications require a resolution of 0.1 mm according to the human sensitivity, meaning that a vector of 45 elements is necessary to characterize the force along the 4.4 mm of the keyboard travel.

Two look-up tables are used to control an actuator, one for the position and one for the force (Figure 6.9). First, the value measured by the sensor in Volts is converted into digital data. Then, the position information is obtained with the element of the first look-up table corresponding to the digital value of the sensor. As the sensor output is not linear, this first vector contains more elements than the second to guarantee the minimal resolution. Finally, the PWM duty cycle controlling the magnitude of the force is the element of the second look-up table corresponding to the position information of the first table.

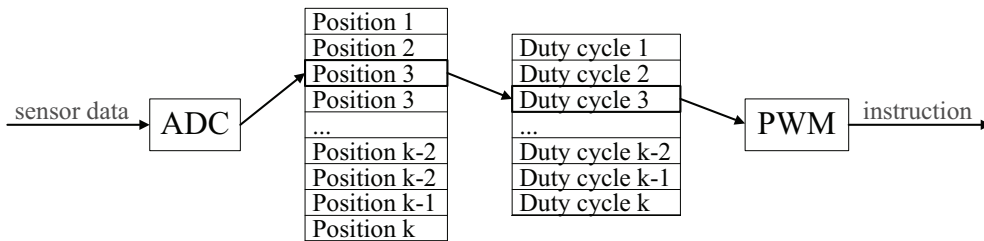


Figure 6.9 – DSP control principle for a single key

The vector containing the position information is hardware-dependent and thus implemented during the calibration process. In order to cancel mechanical and assembly discrepancies between actuators, each key is supposed to have its own look-up table. At the contrary, all keys connected to a microcontroller can follow the same force profile, created by the user according to his needs.

**Array control**

Independently controlling the 64 actuators composing the Haptic Keyboard represents a real challenge. The strategy introduced in section 3.4 consisting in putting multiple microcontrollers in parallel is implemented. Each microcontroller controls eight keys distinguishable by their color in Figure 6.10. This configuration presents the advantage of allowing the grouping of keys depending on their role. For instance, the keys standing for functions like *Ctrl*, *Alt* and *Space* can be implemented with a force profile distinct from the one controlling normal letters with still one force profile per DSP. Or, clusters of keys can be formed according to the finger that hit them more often so as to evenly allocate tasks between microcontrollers.



Figure 6.10 – Distribution of the groups of keys

The DSP chosen for the Haptic Keyboard is a Piccolo F28027 from Texas Instruments [152]. Running at 60 MHz, it possesses 8 PWM channels and 13 analog to digital converter channels (ADC) for position measurement. In addition, they are sold in a relatively small package (10 x 10 mm<sup>2</sup>) which facilitates their integration.

### 6.1.3 Communication

As mentioned in section 3.5, a bidirectional communication is required between the keyboard and the computer so as to be able to modify the touch sensation anytime. Regarding the physical connection between the keyboard and the PC, the microcontrollers used do not possess a direct USB port for communication. A serial universal asynchronous receiver transmitter (UART) is used instead and connected to a FT232R chip from Future Technology Devices International Ltd. [153] that emulates a virtual ComPort via the USB port to communicate with the PC (Figure 6.11).

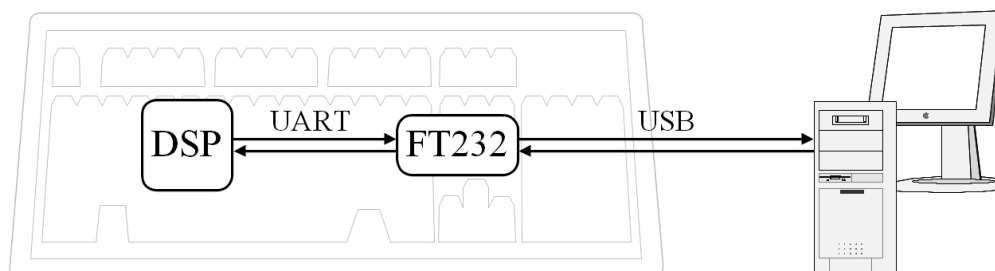


Figure 6.11 – Communication between keyboard and computer

#### Towards computer

In this direction, the initial role of the keyboard must be kept. The characters hit by the user are thus transmitted to the computer via USB. The major improvement is here the possibility of defining the position of the key at which the character is sent. Indeed, as the position of each

key is continuously measured, the threshold at which a stroke is considered as completed can be modified depending on the user wishes. Once the threshold is reached, the corresponding microcontroller sends the ASCII code corresponding to the key.

The presence of several microcontrollers in parallel requires a priority management that remains to be addressed. While typing, a single character needs to be sent at a time. Thus, in order to avoid adding an additional master DSP in the keyboard to deal with the collision issue, a passive priority selector is implemented (Figure 6.12). A cascade of OR gates gives the voice to who wants to speak avoiding short circuits. It is clear that two simultaneous hits would lead to the transmission of erroneous characters. However, this represents an error of the user and the character displayed by traditional keyboards in that case is wrong half the time. The priority selector will thus be used as presented.

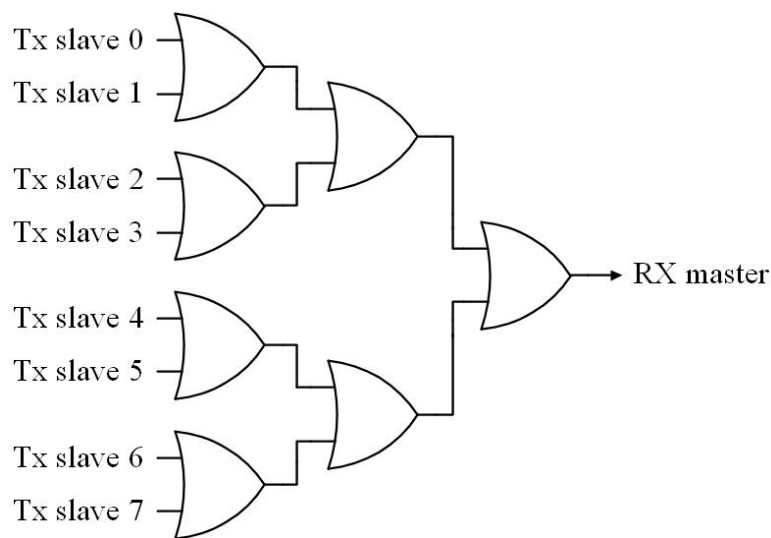


Figure 6.12 – Passive priority selector composed of a cascade of OR gates for the characters transmission

### Towards keyboard

Concerning the force control of the keyboard, it could be done without communication with the computer. Indeed, the position measured by the sensor is directly converted inside the microcontroller and the force profile is also stocked inside so as to increase reactivity. However, it has been decided to give the opportunity to the user to change the force characteristic anytime he wants. A means of conveying the elements of a force vector is thus implemented.

In addition to the transmission of the force profile, the user can select the microcontroller he wants to program. The advantage, already presented in section 6.1.2, allows for groups of keys to be characterized by a distinct force profile. To do so, the remaining control output signals of the RS232 emulated by the FTDI chip, namely Data Terminal Ready (DTR) and



Request To Send (RTS), are used to actively select the microcontroller to be programmed. In a first stage, a binary ripples counter counts the number of DTR pulses corresponding to the microcontroller to be programmed and converts them into a binary signal (Figure 6.13). Three bits are sufficient for eight microcontrollers. Then, these bits control a multiplexer that guides the data (Tx master) toward the desired microcontroller (Rx slave 0-7). Finally, RTS plays the role of reset in the end of the communication.

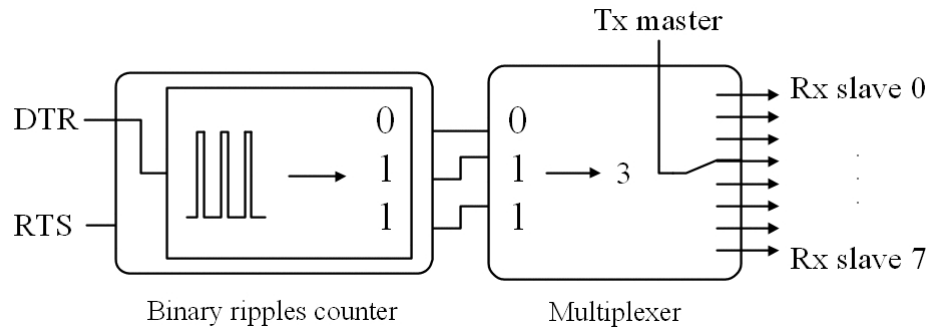


Figure 6.13 – Microcontroller selector for force profile upload

#### 6.1.4 Prototypes

##### Haptic Pad

The first prototype integrating 16 programmable actuators is the Haptic Pad. Everything is built around a single electronic board fixed on the bottom case (Figure 6.14). The board itself integrates all the functions discussed in the previous subsections. At the foreground lay two microcontrollers responsible for the control of eight actuators each. The right hand side is dedicated to communication, including passive priority detector, microcontroller selector, virtual ComPort emulator (FT232) and USB plug. Regarding the position detection, the Hall sensors are visible on the top side of the board while the filters as well as the transistors are placed on the back side. Finally, the self-supporting coils are directly glued on the board, facing the keys of the top case. Optional springs are also visible on the picture but will be removed for the Haptic Pad for a better usage flexibility.

The Haptic Pad is integrated under a MX™ 5500 keyboard from Logitech (Figure 6.15). The idea is here to keep the main part of the keyboard unchanged so as to be able to compare the touch sensation provided by the programmable keys with the existing rubber dome feeling and still take advantage of the original wireless connection of the keyboard. The moving parts of the actuators are thus plugged under the 16 keys of the numeric pad on the right hand side, facing the electronic board holding the coils. Finally, a 5 V AC/DC converter is added under the keyboard to power the actuators (see Figure C.1 in appendix C.1.2).

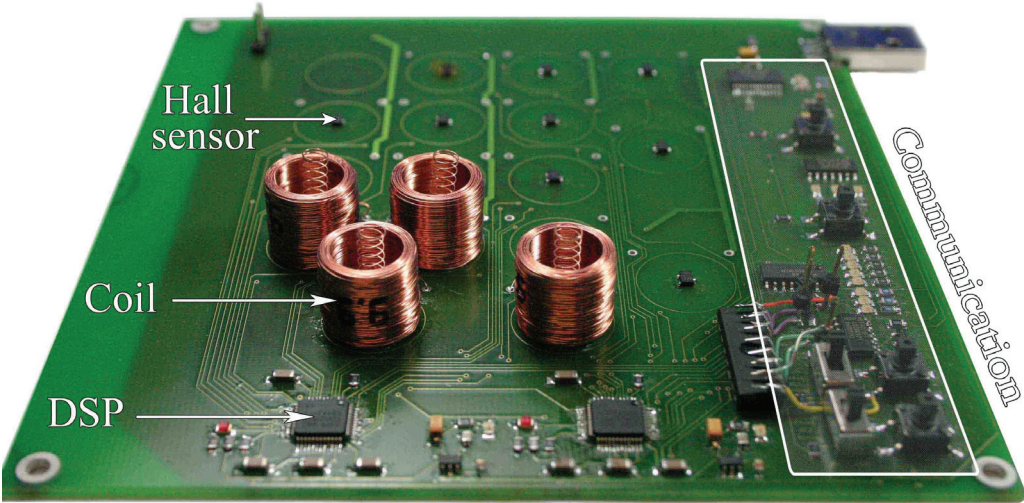


Figure 6.14 – Haptic Pad electronic board



Figure 6.15 – The Haptic Pad and its user interface

**Haptic Keyboard**

The Haptic Keyboard is very similar to the Haptic Pad in its conception. Indeed, the latter is designed in such a way that a block of eight keys can simply be repeated so as to get the desired number of keys following the distribution of Figure 6.10. This modularity greatly facilitates the design of the new electronic board.

For the second prototype, only the top case of the MX™ 3200 is kept and 64 actuators are plugged under the keys of the central pad (including the arrows) (Figure 6.16).



Figure 6.16 – Top case of the Haptic Keyboard with actuators plugged in

The coils are then inserted inside the actuators as in Figure 6.5. Some glue is delicately spread on their base and the electronic board is pressed and locked against the top case. The obtained bottom case is shown in Figure 6.17. The electronic board is screwed on a rigid aluminum base and all the electronic components, except for the Hall sensors are located on the back side of the board (see appendix C.1.2). The assembly represents a real mechanical challenge to correctly align all the keys together and needs to be done with precaution.

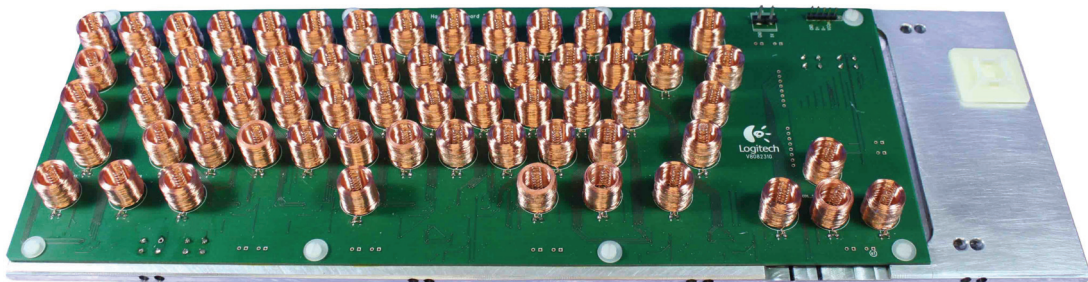


Figure 6.17 – Assembled bottom case of the Haptic Keyboard

An additional function is added to the keyboard in order to make its use even more flexible. An inclined plan mechanism allows the user to modify the depth of travel of the entire keyboard (Figure 6.18). Two rotating knobs located on the sides are attached, using a cable, to inclined plans supporting the pins connected to the bottom case. Turning the knobs slides the plans, which raises the main board, decreasing thus the travel. The new travel is automatically detected by the keyboard by taking measurements on pre-defined keys.



Figure 6.18 – Haptic Keyboard front view with travel modification mechanism

Finally, both prototypes are capable of detecting if a key is pressed and provide a force feedback to the user following a pre-defined profile.

### 6.1.5 Software user interface

In order to make the Haptic Keyboard more user-friendly, a software user interface (SWUI) is developed. Its role is to offer a graphic interface representing a bridge between the user's wishes and the keyboard. The two main tasks of the SWUI follow those presented in subsection 6.1.3, namely displaying the characters hit on the keyboard and, in the other way, uploading force profiles to the different microcontrollers.

#### SWUI for Haptic Keyboard

The Haptic Keyboard graphic interface is shown in Figure 6.19 with its nine different parts.

1. The first part (1 in Figure 6.19) allows the user to connect the graphic interface to the keyboard by opening a COM port. The port is selected among available ports and connected by clicking on the button on the right hand side.
2. All eight microcontrollers of the keyboard can be independently selected to receive the force profile displayed in the graph below. The group of keys controlled by the chosen DSP is highlighted in the picture on the right. It is also possible to upload the force vector in all microcontrollers in a row by ticking *All* before clicking the *Send Force Profile* button.
3. The force versus position characteristic is plotted here. The maximum displacement is limited to 4.4 mm corresponding to the travel of the keyboard adapted for the project. A point is displayed every 0.2 mm to avoid overloading the graph, however a linear interpolation increases the resolution to 0.1 mm. Each point can be adjusted by clicking on it and dragging it along the vertical axis. The force is however limited to 1 N to match the specifications.



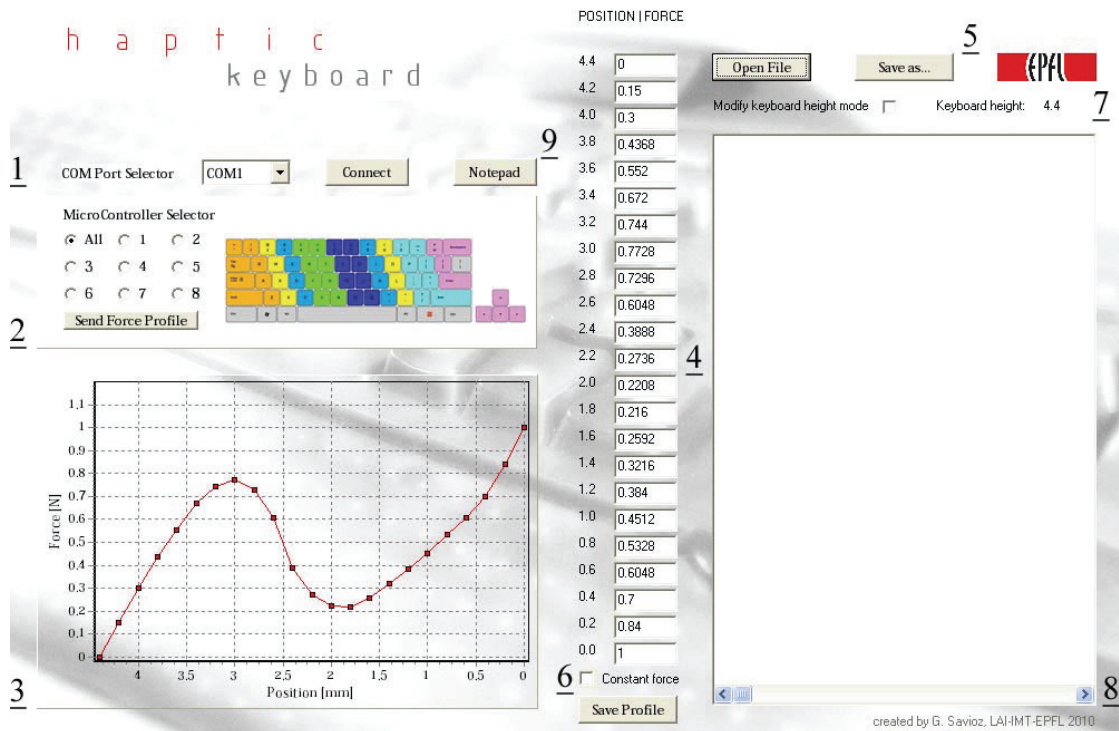


Figure 6.19 – Software User Interface for Haptic Keyboard

4. In the central part, the discrete values of the force vector face their corresponding position. The possibility is left to the user to type the force magnitude directly in the box which instantly modifies the profile on the left.
5. The SWUI offers the possibility to open existing force profiles stocked in .txt files with *Open File* and save new profiles by clicking on *Save as. ...* The modifications applied to the opened profile can be saved by clicking on *Save Profile*.
6. Two additional features appearing under the form of check boxes allow modifying the force profile. The first one called *Constant force mode* generates a constant force feedback no matter the position. Like shown in Figure 6.20, all points, except those above the maximum travel, are aligned with the point corresponding to the very bottom position (0 mm). Only this value can now be modified or dragged.
7. The second mode that can be selected by the user is the *Keyboard height modification mode* (Figure 6.21). If ticked, the position of the bottom case is continuously updated and displayed on the right hand side. Decreasing the keys travel with the mechanism of Figure 6.18 imposes an adaptation of the force profile. Indeed, if nothing is done, the keyboard would react as if all the keys were pressed simultaneously, resulting in excessive current consumption and thereby damaging the AC/DC converter. For this reason, no current should be supplied in the keys when they are up. To avoid the

## Chapter 6. Multi-finger haptic applications

problem, the points of the force profile above the maximum travel are automatically set to zero.

8. A HyperTerminal window is appended to the right hand side of the SWUI. The characters hit by the user as well as miscellaneous control information can thus be displayed in it.
9. Printing the text directly in the HyperTerminal window is very convenient for simple tests but suffers from a lack of functionality when considering the entire keyboard. Indeed, the HyperTerminal first role being the communication with, among other, peripherals via serial port (COMx), many control keys are not implemented. Notably *Ctrl*, *Alt*, *Windows* and the four arrow keys have no effect when pressed in the HyperTerminal interface. This does not really reflect normal typing conditions and so, the possibility is offered to open a Notepad window. As the characters typed on the Haptic Keyboard are transmitted to the computer through a virtual serial port, they are interpreted and translated into Windows<sup>®</sup> commands by the software interface to be displayed on the Notepad. This additional hidden function also overcomes the issue of the multiple roles of the keys (e.g. with *Shift* and *Caps Lock*).

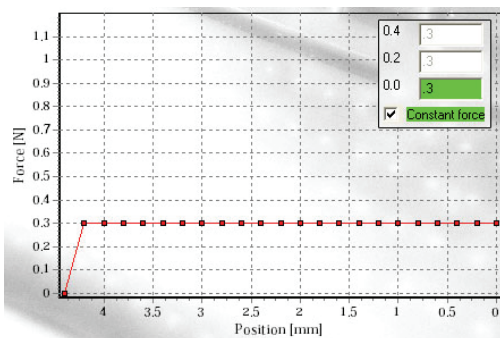


Figure 6.20 – Constant force mode

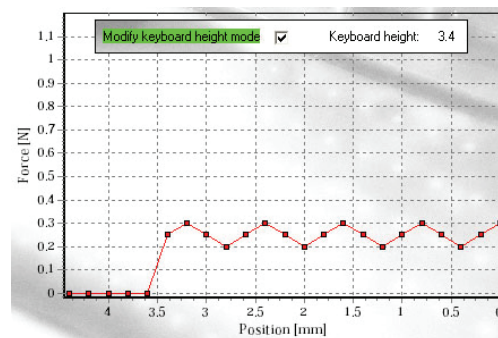


Figure 6.21 – Keyboard height modification mode

### SWUI for Haptic Pad

A similar user interface is finally implemented for the Haptic Pad (Figure 6.22).

As the springs supporting the weight of the actuators are removed in the Haptic Pad for more flexibility, a small offset current needs to be supplied in the coils to fulfill this role. A new feature thus allows inserting a manual offset that shifts the force profile up.

In addition to the Notepad window, the user can directly open and work with the calculator thanks to a dedicated button.

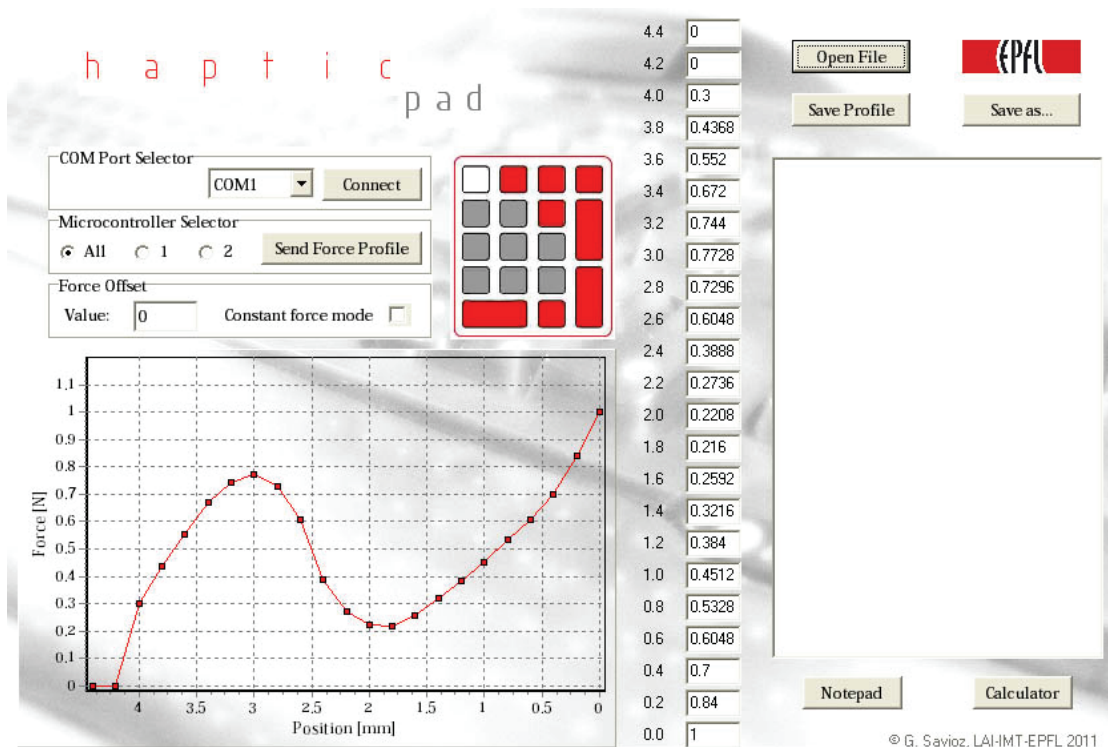


Figure 6.22 – Software User Interface for Haptic Pad

## 6.2 VibKey Pad

Buttons are the simplest and most used devices for a user to interact with a machine, whether it is a washing machine, a lamp or a computer. On most of these devices, the user gets a physical validation that his action has been transmitted to the system, for example with a displacement, a click or a sound. However, more and more, tactile surfaces tend to replace mechanical switches, especially in today's home electronics (mp3 players, alarm clocks, ...). Since the user does not get any physical feedback, it can sometimes be difficult for him to know if he correctly pressed the button or not. It is even truer for blind people. This annoying situation can even become dangerous in a car when the driver wants to set the position of the heating located on the central console. The aim of the present application is thus to design a new kind of actuator capable of playing the role of a standard tactile sensor coupled with a physical feedback in the form of a localized vibration (Figure 6.23).

The vibrotactile button designed in subsection 4.6.4 represents the central part of the device (Figure 6.24). A vibration is generated by the alternating displacements of the moving part composed of a ring magnet and its iron base, and is transmitted to the thin board on which a flat coil is printed. As for the coil, it is also be used as a capacitive touch sensor to detect the contact with a fingertip.

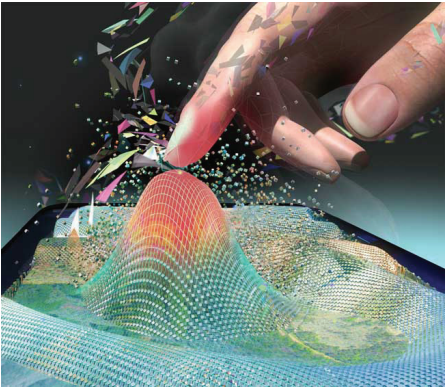


Figure 6.23 – Touch feedback [154]

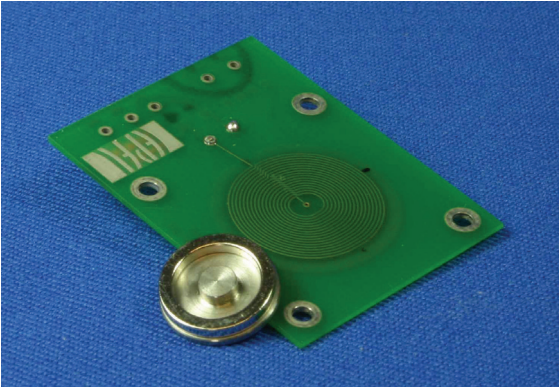


Figure 6.24 – Prototype of a vibrotactile button (VibKey)

**6.2.1 Capacitive touch sensor**

The change in capacitance of a conducting surface induced by a contact or proximity with another conducting material inspired numerous works [155–157] and led to all kinds of sensors. Indeed, capacitive sensors, whose main advantage is their low-cost, have a wide variety of uses such as the measurement of pressure [158], liquid level [159], position [160], humidity [161], etc . . . . Among them, the capacitive touch sensor slowly tends to replace the traditional mechanical switch in a wide range of consumer products.

When a fingertip approaches a conductive surface supplied with a constant voltage, it acts as a virtual ground. Indeed, the human finger is filled with conductive electrolytes and covered by the skin which plays the role of a dielectric [162]. As a result, the conductive plate behaves as a capacitor with charges being accumulated on both sides of the contact area (Figure 6.25).

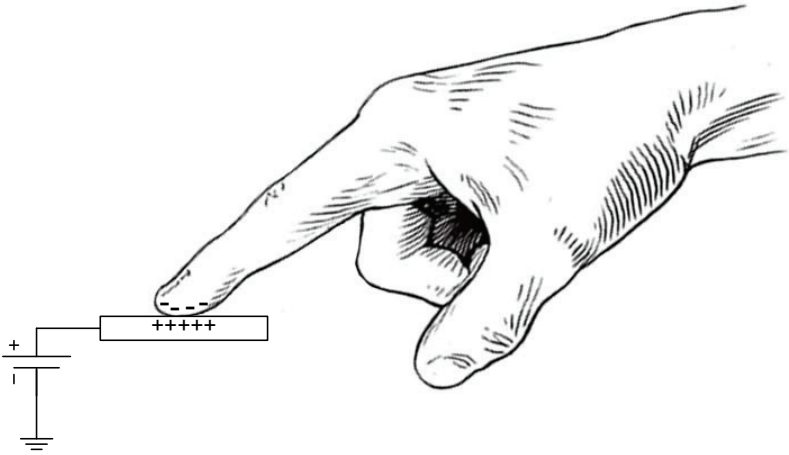


Figure 6.25 – Capacitive effect on fingertip



The important variation in capacitance provoked by the presence of the finger can be observed by measuring the time constant  $\tau$  describing the charge of a capacitor in a RC circuit:

$$\tau = RC \quad (6.1)$$

The simple circuit of Figure 6.26 allows measuring the time between the switch opening and the time when the capacitor voltage  $U_c$  reaches a reference value [163]. The contact with a finger at that time generates large differences in the rise time as shown in the measurements made on a printed coil (Figure 6.27). Then, the switch closes and the charges accumulated in the sensing device disappear in the ground ( $U_c = 0$ ) and so on.

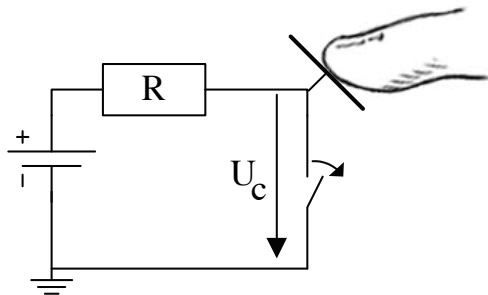


Figure 6.26 – Charge circuit principle of a capacitive touch surface

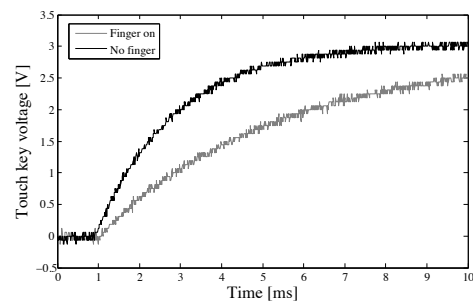


Figure 6.27 – Effect of the presence of a finger on the capacitor charge

The coil, printed on a thin electronic board is aimed to play the role of sensing area. Its size thus has to be determined in accordance with physiological data of the human fingertip in order to be more efficient. When pressing on his finger, a person deforms the fingertip pulp which spreads on the surface until becoming stable for forces above 6 N [147]. Beyond, the fingertip behaves as a stiff member. According to two studies from Westling and Johansson [11] and Fujita and Ohmori [164], the maximum contact area converges slightly above 200 mm<sup>2</sup> on hard materials. This value, corresponding to a radius of 8 mm will be taken as the reference for the size of the coil.

### 6.2.2 Vibrator

From the actuation point of view, the goal is to maximize the sensitivity to high frequency vibrations. The conclusion of subsection 2.2.4 mentions that the best efficiency is obtained for frequencies between 250 and 300 Hz applied to a surface approaching 300 mm<sup>2</sup>. Actually, in the case of a fingertip, there is no need to be larger than the contact area but it is preferable to cover it entirely so as to take advantage of the spatial integration of the Pacinian corpuscles [28]. The external radius of 8 mm for the coil, corresponding to the average size of a human

fingertip contact area, is thus confirmed.

Then, to take benefit of the outer magnetic fringes of the ring magnet for the force creation, it is chosen in the market with a radius of 6 mm as explained in the actuator design and the winding direction of the turns is inverted above the magnet (4.6.4).

Regarding the actuator optimization, the sensitivity to vibrations is usually given in decibels corresponding to the displacement of the skin (Figure 2.8). However, as the skin displacement is related to the force applied by the finger [11], it was decided to optimize the force provided by the actuator. As Westling and Johansson showed in their study on grasping [11], a force of 0.5 N already compresses the pulp of more than 1 mm. The 0.1 N resulting from the optimization process of subsection 4.6.4 are thus sufficient to reach the minimal sensitivity threshold of 15 nm given in Figure 2.8 at 300 Hz. A prototype of the vibrotactile button is shown in Figure 6.24.

### 6.2.3 Control

The main objective of the present application is to combine the features of a tactile sensor and a linear vibrator using a single actuator. Similarly, the control hardware is required to fulfill both actions. It is realized by integrating the sensing electronics of Figure 6.26 within a H-bridge generally used for the bidirectional control of DC actuators and motors (Figure 6.28). During the sensing phase, the two top transistors of the H-bridge stay open and both low transistors commute simultaneously between open and closed states. In the closed state, the coil is connected to the ground and its capacitance is emptied, but when the transistors are open, the coil is totally isolated by the transistors and slowly charges through the 330 k $\Omega$  resistor. It is thus possible to measure the voltage rise time directly on the coil. This signal is used to drive an additional transistor that triggers an external interrupt of the microcontroller.

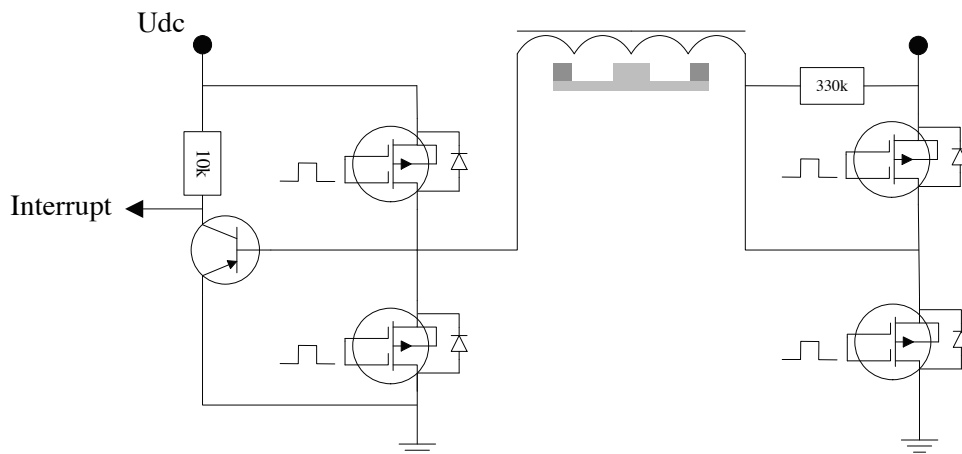


Figure 6.28 – Control circuit for the vibrotactile button

The block diagram of Figure 6.29 details the execution of the program. During the sensing

mode, the sequence presented above is repeated until detecting the presence of a finger. In case of contact, the control switches to the actuation mode during which the diagonal transistors alternate between ON and OFF states for a short period of time giving thus a physical acknowledgement to the user. Then, the presence of the finger is checked again by entering the sensing mode and so on.

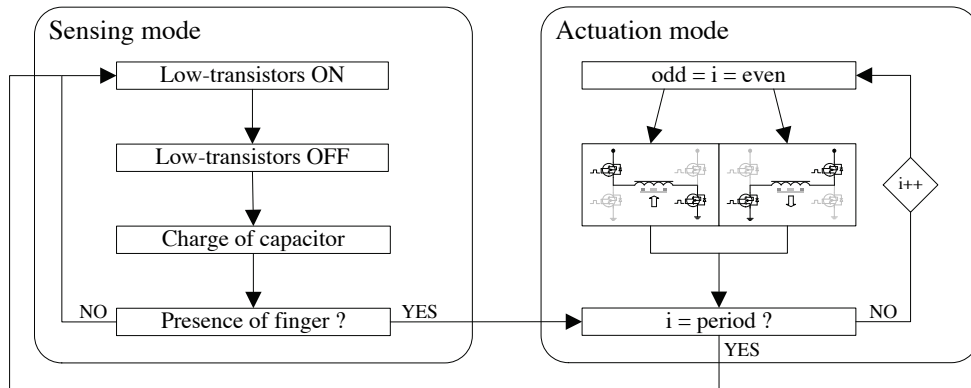


Figure 6.29 – Block diagram detailing the execution of the vibrotactile button program

DC motors and actuators are usually driven with two-state pulse width modulation signals similar to the one applied to a single vibrotactile button and shown in Figure 6.30 (a). However, at the frequency of 300 Hz optimizing the human sensitivity to vibrations, the presence of numerous odd harmonics, revealed by the discrete Fourier transform of Figure 6.30 (b) generates audible noise. Depending on the application, this noise can be useful to provide an additional feedback to the user. The VibKey Pad is thus able to combine up to three feedbacks, namely tactile, audible and visual (LEDs) depending on the user's wishes.

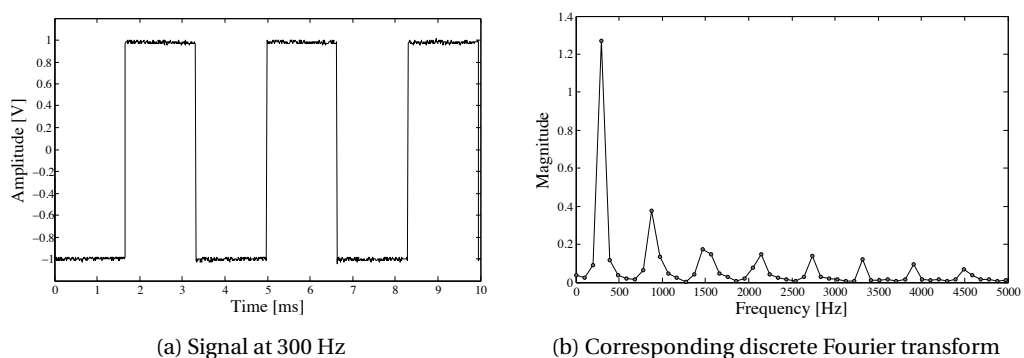


Figure 6.30 – Simple square control

If undesired, it is possible to get rid of the noise generated by the harmonics of the square signal by implementing an enhanced sinusoidal control (Figure 6.31). The spectral analysis shows that only the fundamental frequency stays, generating a very weak sound at 300 Hz.

## Chapter 6. Multi-finger haptic applications

It sounds like the noise characteristic of old communication devices and does not disturb the utilization. To illustrate this difference, measurements made on a speaker successively supplied with a square and a sinusoidal signal presented a difference of 15 dB. The sound provided by the square signal is thus 32 times louder than the one generated by the sinus.

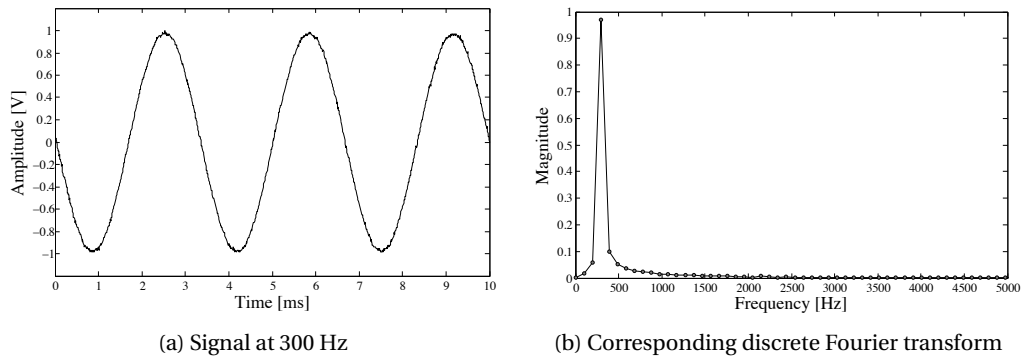


Figure 6.31 – Enhanced sinusoidal control

It is to note that the fundamental frequency of the square signal is about 30 % higher than for the sinus, resulting in a more important feeling of the vibration by the user.

### 6.2.4 Prototypes

Two prototypes, called VibKey Pads, are finally built based on the same electronics (Figures 6.32 and 6.34). Both take the form of a remote control integrating four vibrotactile buttons reacting to the contact with a finger. Figure 6.33 shows the back side of the first prototype in which the moving masses are visible on the left hand side and the electronics on the right hand side. In addition to the microcontroller and the four integrated H-bridges, a FT232R chip from Future Technology Devices International Ltd. is used to emulate a virtual serial port on the computer. The VibKey Pad is thus powered through a mini-USB cable and communicates with serial commands. Finally, four LEDs are located in the center of the pad to provide a visual feedback to the user.

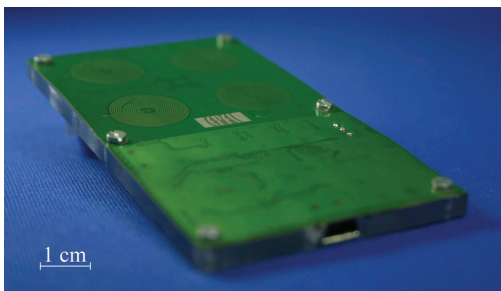


Figure 6.32 – Rigid VibKey Pad prototype

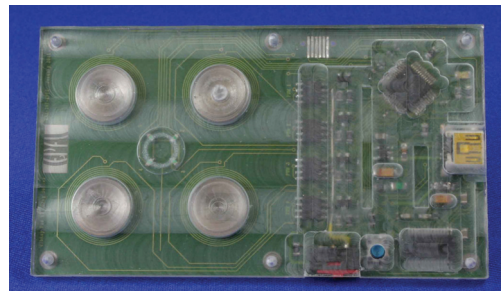


Figure 6.33 – Back side of the VibKey Pad

The coils are printed on a 0.1 mm thick board allowing for a direct transmission of the vibrations to the fingertip. Contrarily to existing devices like smartphones where an off-centered mass fixed to a DC motor (Figure 2.18) generates a vibration that propagates in the entire rigid structure, the vibration is here localized under the finger. An indirect advantage is that the board can be mounted on flexible supports allowing for the design of bendable devices. The second prototype of the VibKey Pad shown in Figure 6.34 is precisely stick on a foam layer that can be easily deformed and still provide a haptic feedback to the user.

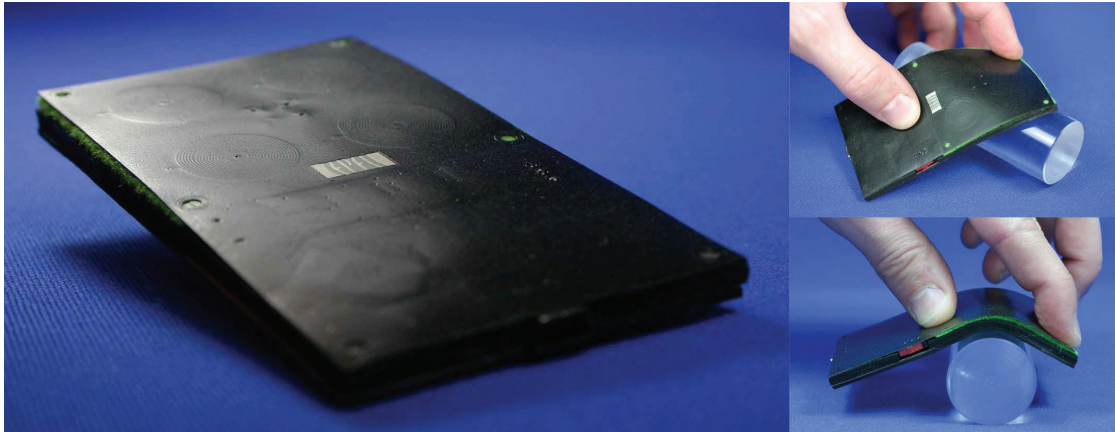
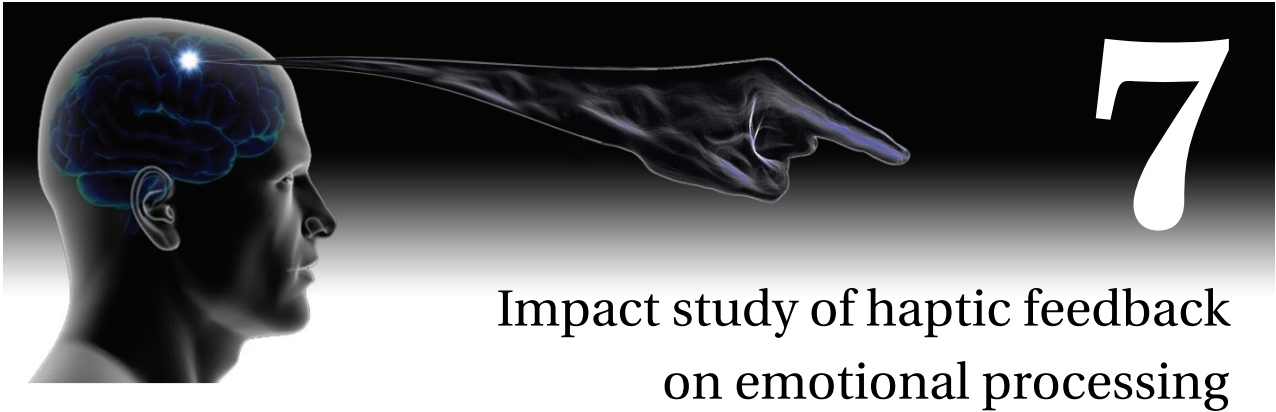


Figure 6.34 – Flexible VibKey Pad prototype





**Contents**

---

<b>7.1 Context</b> .....	<b>163</b>
<b>7.2 Objectives</b> .....	<b>167</b>
<b>7.3 Method</b> .....	<b>168</b>
7.3.1 Participants and apparatus .....	168
7.3.2 Procedure and experimental design .....	168
<b>7.4 Results</b> .....	<b>171</b>
7.4.1 Identification part .....	171
7.4.2 Effect on emotional processing .....	174
<b>7.5 Discussion</b> .....	<b>179</b>

---

**7.1 Context**

The omnipresence of advanced communication devices in today's society is aimed at bringing the people closer and enlarging their network. However, despite an exponential increase in the number of interlocutors and the quantity of information, the richness of interactions decreases. The computer and its numerous applications using the internet is a very representative example. Indeed, most of the communications pass through the keyboard and the screen

and suffer from a serious lack of reality from the point of view of the human being. Thus, the emotional dimension essentially brought by nonverbal signals is completely skipped, sometimes leading to misunderstandings. Following the design of multi-finger haptic devices addressed in the present thesis, the introduction of kinesthetic information in human-machine interactions is investigated.

Naturally, the human being adapts some of his behaviors depending on his mood. The most visible sign of emotion being observed on the face of the person, other nonverbal cues also appear to convey emotions. Several studies already demonstrated that the emotions felt by the user are translated physically. In particular, Park and al. [165] studied the direct relation between the frustration induced by an experiment on the computer and the pressure applied by the user on the touch pad. Emotions and haptics are thus psychophysiologicaly linked. The idea is now to reply to these physical inputs and to close what Höök calls the *affective loop* [166]. The proper affective loop implies that the system replies to emotional signs with visual, auditory or haptic feedbacks.

The affective pen developed by Alonso et al. [167] goes this way and proposes to influence the user's stress during handwriting operations using a haptic feedback. In humans, the stress manifests itself through the manipulation of objects and particularly rock and roll movements which are directly sensed by the affective pen. The pen then responds to these bodily expressions by adding friction in the rotation of the pen tip (roll) and displacing its center of mass (rock) in order to create a relaxing experience. The principle of affective loop is also used to improve the performance during tutoring tasks [168] and in medical applications in which emotions are directly extracted from speech processing [169]. The haptic sensation is until here generated as a response to user's actions. It can also be voluntarily provided by the machine to induce an emotion or a reaction of the user. All the processes involving emotions during computer operations are gathered under the term of *affective computing* [170].

Numerous studies on the human brain showed that the simultaneous presentation of multi-sensory signals allows for lower threshold, faster and more accurate detection [171–173]. This statement thus encourages even more the introduction of the haptic feedback in computer peripherals. A recent research conducted jointly between the Queen's University of Kingston, Ontario and the Carnegie Mellon University demonstrated the possibility of haptically discriminating facial expressions of emotion (FEEs) only by touching live faces [174] or by touching faces reconstituted using 2D raised-lines [175] with a performance well above chance. Vision alone is however still more reliable, reaching accuracies between 60 and 100 % for the six basic FEEs widely used in research, namely anger, fear, happiness, sadness, disgust and surprise. Following these results, Bonnet et al. [176] improved the visual recognition of emotions on virtual faces by adding a kinesthetic feedback generated by the Novint Falcon (Figure 2.11 (a)). During the experiment, the user had to consider the emotional haptic feedback as coming from another person. Concerning the force feedbacks themselves, slow stimuli with important amplitudes as well as fast stimuli with very low vertical amplitudes were considered as positive. At the contrary, slow stimuli oriented horizontally toward the user were considered



as negative. During the emotions recognition phase, not all feedbacks were beneficial but some like swinging (for joy), pulling (for fear), pushing (for disgust) and agitation (for anger) were indicating an improvement in the identification of facial expressions, showing thus the importance of the cues selection. In the end, 95 % of the participants declared preferring the multimodal configuration.

Following the same idea, the introduction of haptic feedbacks in computer peripherals provides an additional nonverbal communication to enrich online interactions. Researchers from the Tokyo Institute of Technology [177] succeeded in conveying emotions and therefore influencing subject's feelings during online negotiations even between people from different cultures (Japanese and Chinese) using the Phantom Omni (Figure 2.11 (b)). During the study, 75 % of the participants admitted having a tendency to fit into the other negotiator's mind.

Besides the trading side of the internet, instant messaging (IM) becomes more and more important for the new generations. IM takes the form of chatting platforms where people exchange short messages often including intimate information. All attempts to fill in the lack of emotional content usually contained in nonverbal communication were enthusiastically received by the users, opening the way for the introduction of haptic feedback. Indeed, audio or visual extensions such as earcons [178] and emoticons (☺ ☹) are well accepted and largely used in IM. As touch is a powerful support for emotional content, Rovers and van Essen [179, 180] introduced the term of *hapticon* defined as "small force and vibration patterns that can be used to communicate emotions and feelings". Using either eccentric masses on DC motors (Figure 2.18) or force feedback joysticks (Figure 2.10 (b)), haptic patterns are designed in order to convey emotions (e.g. Figure 7.1). When the users were asked to design their own hapticons with a specific design tool, they showed difficulties to generate intended feelings and strongly used the library of samples. In other words, the transition between an emotion and its corresponding tactile feeling is not an easy task and requires training. Even the relation between a force profile and its corresponding sensation is not obvious and comes in the course of time.






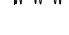



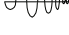


Icon	Emoticon	Meaning	Hapticon
	: )	regular smile	
	: D	big smile	
	: (	sad face	
	; -)	wink	
	( k )	kiss	
	: \$	embarrassed	

Figure 7.1 – Some emoticons and proposed hapticons [179]

With the aim of providing always more efficient haptic feedbacks, some research teams have

## Chapter 7. Impact study of haptic feedback on emotional processing

developed their own devices to enrich social interactions. For instance, Neviarouskaya et al. [181] directly extract emotions from short messages by interpreting their content and translate them into haptic feedbacks. Their system called iFeel\_IM! interfaces the 3D virtual world Second Life (secondlife.com) and integrates different kinds of haptic devices specifically developed to provide well-targeted feedbacks. The HaptiHug, for example, simulates a hugging by tensing a belt placed around the user's chest using a couple of motors (Figure 7.2). Likewise, a virtual heart beat is generated by a flat speaker transmitting vibrations to the chest (Figure 7.3).

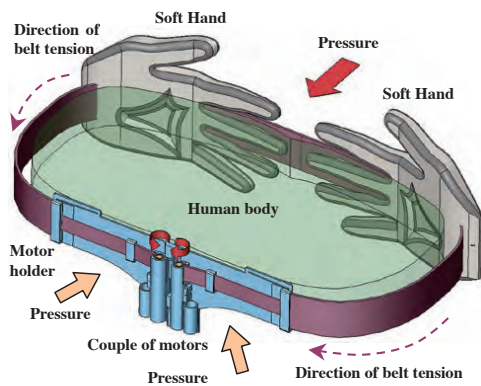


Figure 7.2 – The wearable HaptiHug imitates a realistic hugging [181]

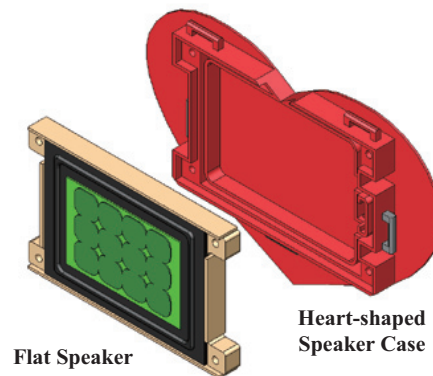


Figure 7.3 – The HaptiHeart simulates different heartbeat patterns

Despite encouraging results, the iFeel\_IM! system is bulky and can represent an obstacle for occasional users. For that reason, other groups are developing compact devices aimed at conveying emotions via new tactile languages. Benali-Khoujda et al. [182] designed a novel vibrotactile interface composed of a 8 x 8 matrix of micro electromagnetic actuators (Figure 7.4) able to generate different tactile patterns (waves, line sweeps, shutter, etc ...) in order to communicate emotional information. The difficulty is again to match tactile sensations with emotions. While feelings like urgency, stress, pain and affection were relatively well recognized, relaxation, for instance, was perceived as unpleasant by the subject. In this case, the noise generated by the tactile display is suspected to influence the user's opinion.

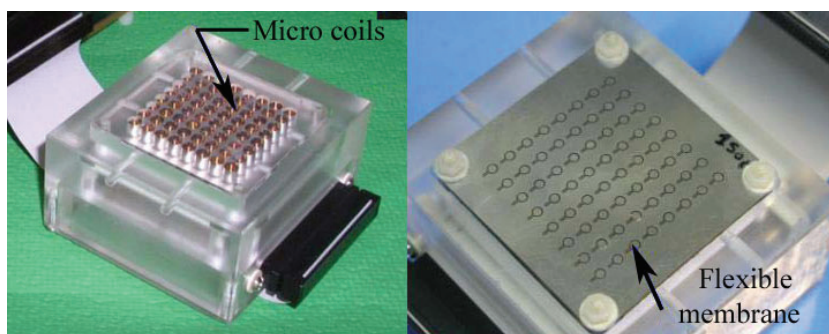


Figure 7.4 – VITAL vibrotactile interface [183]

Salminen et al. [184] pursue a similar objective with a friction based fingertip stimulator. The haptic information is created by the rotation of a cylinder under the user's finger by varying its direction of rotation, continuity and burst length. A total of 12 different stimuli were presented pair by pair and the user had to determine whether they were different or not. The overall error for this exercise was 13 % (for a total of 11 x 528 pairs). The second part consisted in rating the 12 stimuli following four emotional criteria namely pleasantness, arousal, approachability and dominance so as to show that even simple haptic stimulations can convey emotional information. The results presented the rotation style (discontinuous or continuous i.e. with or without still phases between direction switchings) as predominant. In the end, they suggest using continuous stimuli, perceived as more arousing and dominating, instead of discontinuous stimuli which are too pleasant and approachable to efficiently draw the user's attention.

## 7.2 Objectives

The main objective pursued in this chapter is the conveyance of kinesthetic information through human fingers using linear short-stroke actuators. The idea is to take advantage of the Haptic Pad presented in chapter 6 and "hijack" it in order to haptically communicate with the user, similarly to what Rovers and van Essen did with hapticons [179, 180]. The initial aim of a force feedback keyboard is to improve the user's comfort by modifying the keys make force. However, the stroke of a finger during typing operations is short and so is the time needed to press down a key. The maximum bandwidth with which the human finger demands the force input signals to be presented for meaningful perception is 30 Hz according to Table 2.3. With an average down stroke time approaching 10 ms [114], the typist's finger acts as a mechanical low-pass filter. Therefore, all the irregularities that could physically happen along the key travel are absorbed by the fingertip pulp and ignored by the sensory system. The only difference eventually felt by the user concerns the total energy overcome during the stroke. Indeed, the Pacinian corpuscles responsible for the detection of vibrations are capable of temporal integration [28, 78] allowing discriminating the overall force level. With these considerations, one notices that most of the kinesthetic information contained in the force profile is lost during normal typing due to the human hand physiology. A slower utilization of such kind of haptic devices is thus recommended to make the most of it.

Elaborated force profiles are thus implemented within the Haptic Pad and the user is asked to identify them by slowly pressing on the keys. In case of success, it would open the way for a new tactile communication language. Then, similarly as in the study of Bonnet et al. [176], we will try to influence the emotional processing of participants by providing haptic clues. For this part of the experiment conducted in collaboration with the University Service of Child and Adolescent Psychiatry in Lausanne (SUPEA - CHUV<sup>1</sup>), the performance in emotions recognition is aimed to be improved by introducing additional sensory signals complementing the visual perception. In their research, the psychologists from the SUPEA deal with the

---

<sup>1</sup>Service Universitaire de Psychiatrie de l'Enfant et de l'Adolescent du Centre Hospitalier Universitaire Vaudois

appearance of psychiatric disorders affecting children and adolescents between 0 and 18 years old and focus a part of their work on psychosis mainly affecting young people (13-18 years old). The contact with reality of psychotic adolescents is disturbed and they present symptoms going from difficulties to concentrate and follow a conversation up to hallucinations [185]. Their emotional behavior is also modified as reflected in a recent review of literature reporting that patients with schizophrenia demonstrate impairment in emotion expression, and recognition in facial domains [186]. Furthermore, the duration of schizophrenia is related to the deficits in emotion recognition as chronic patients suffering from negative symptoms are more impaired than less chronic patients [187–189], indicating the importance to intervene early in the time-course of schizophrenia. These disorders are thus not a fatality and they can, in some cases, be treated if rapidly detected. With the future aim of improving the emotional processing of psychotic adolescents, a first pilot experiment on healthy subjects is conducted to measure the effect of additional tactile information in the emotional processing.

### 7.3 Method

#### 7.3.1 Participants and apparatus

Seventeen experimentally naive participants (7 females, 10 males) took part in the study (mean age 29 years, range 24-39 years). Three of them were left-handed and fourteen were right-handed. The participants belong to two distinct groups: nine PhD students from different laboratories with various engineering backgrounds and eight psychologists. The experiment, split in two main parts, uses the Haptic Pad presented in subsection 6.1.4.

#### 7.3.2 Procedure and experimental design

##### Identification part

During the first part, the user is asked to identify eight different force profiles (Figure 7.5) implemented on the keys 1 to 8 of the numeric pad without looking at the profiles. The goal of this initial part is to familiarize the participant with the haptic feedback and determine his ability to identify and express the distinctive features of each profile. This habituation part is important in a sense that the human being is not used to experiment such kind of short-stroke force feedbacks and possesses different fingertip sensibilities. While some people are immediately able to recognize and differentiate the profiles, others need more time to catch the details. This effect has already been highlighted by Poupyrev and Maruyama [79] while introducing a vibrating feedback in a PDA touch screen using piezoelectric elements. Some time is thus given at the beginning of the experiment to freely touch all the keys and compare them before starting the test. As mentioned earlier, the user would not feel anything during normal typing operations due to the limited bandwidth of the human fingertip sensitivity. It is thus explained that for this exercise, the Haptic Pad does not have to be considered as a keyboard, but more as a tool to communicate tactile information. As a result, the user is asked

to slowly and smoothly press on the keys, several times if needed, to be able to efficiently perceive the force profiles. A control of the finger is necessary during the entire stroke to avoid missing tactile features.

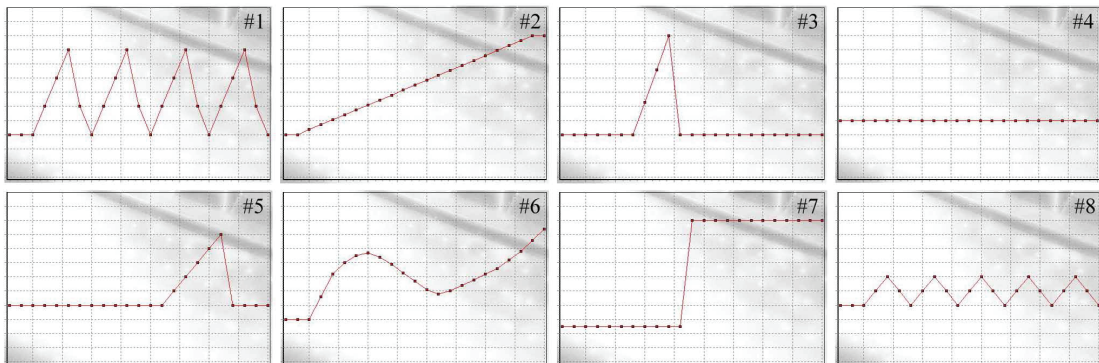


Figure 7.5 – Force profiles implemented on keys 1-8 of the Haptic Pad for identification

When the participant is ready, he receives a sheet of paper with eight blank graphs. His first task consists in drawing the force profiles corresponding to what he feels. In accordance with the conclusions of the work of Rovers and van Essen on hapticons [179, 180], it is expected to be very difficult for the participants to correctly translate touch sensations. In order to anticipate the problem, the participant is also asked to express, with words, a physical correspondence for each key. In addition, two examples of force profile are shown and explained to the participant (without saying that they correspond to implemented profiles) to guide them during the drawing phase (#6, #7 and #3 for the group of psychologists). A ranking of the five more memorable and differentiable keys is finally established by the subject. In a second step, the eight force profiles of Figure 7.5 are mixed up and presented to the participant, his task being to assign each profile to a single key.

It is to note that the eight force profiles constituting the basis of the experiment result from a pretest made by an undergraduate student and a PhD student who were confronted to sixteen initial profiles. Their excellent results in the drawing task (12/16 and 13/16) and in the matching part (14/16) were encouraging.

### Effect on emotional processing

Once the user is comfortable with the haptic feedback, starts the second part of the experiment related to the emotional processing. During this phase, faces showing four different emotions namely happiness, sadness, anger and fear are displayed on the computer and the participant is asked to select as fast and correctly as possible the emotion corresponding to what he sees. Ten different faces, each presenting the four emotions (e.g. Figure 7.6) are integrated in the experiment coded with the E-prime software from Psychology Software Tools Inc.



Figure 7.6 – Example of faces displayed during the emotional experiment<sup>2</sup>

The answers are given on the four keys of the Haptic Pad covered with an emoticon sticker on top, symbolizing an emotion (Figure 7.7). In addition to the answer, the program measures the time between the apparition of the face and the hit.

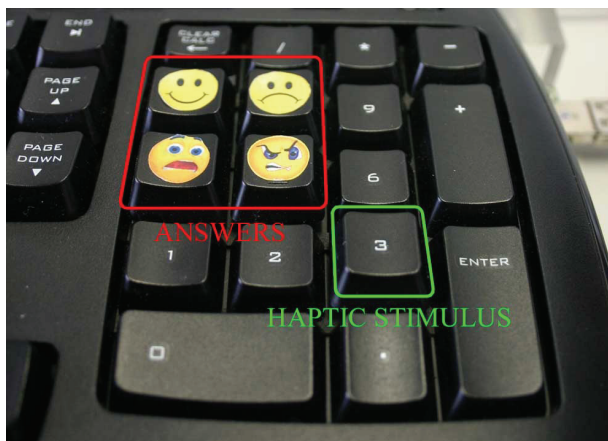


Figure 7.7 – Haptic Pad setup for the recognition of emotions

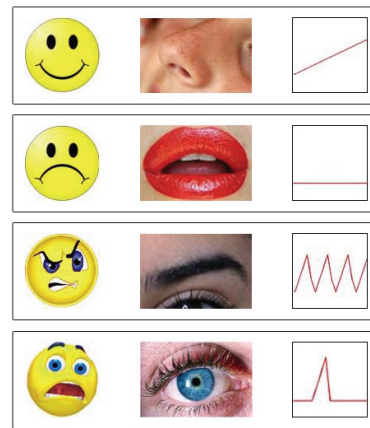


Figure 7.8 – Correspondence between emotions, visual and haptic clues

The emotions recognition block is repeated four times for a total of 160 trials. For each additional block, one or several clues are provided to the participant with the purpose of improving his performance both in rapidity and efficiency (Figure 7.9). During the second execution, a visual clue briefly appears on the screen (1 s) before the apparition of the face presenting the emotion. The user is told that the visual clue might help him finding the emotion but it is not mentioned how it could be helpful. By experience, we know that the expression of certain emotions manifest itself on specific parts of the face. The visual clue is thus aimed to focus the participant's attention on this specific part of the face. Indeed, the mouth often takes the shape of an upside-down U on sad faces, angry people frown their

<sup>2</sup>To avoid integrating cultural aspects, only white models were displayed during the experiment. However, for copyright reasons, only a few models are available for publication.



eyebrows and scared people are distinguishable by wide open eyes. Happiness being the most obvious emotion [175], the nose, located in the middle of the face, is assigned to it by default. The visual clues corresponding to the four emotions are presented in the central column of Figure 7.8.

The third execution integrates a tactile clue in the beginning of each trial. Four different clues are selected out of the identification part and associated to the emotions (Figure 7.8). The haptic information is conveyed through key number 3 (Figure 7.7) on which the participant is asked to press slowly. This time, a single hit is allowed. The participant then chooses one of the four force profiles by pressing on the key with the corresponding profile (v, b, n or m). The rest of the trial is similar to the previous execution with the presentation of the visual clue, the face and finally the answer.

In the last part, only the tactile clue, related to the following emotion, is presented before the apparition of the face. Finally, it has to be noted that before each part, a short training presenting four faces is done by the participant to avoid surprises.

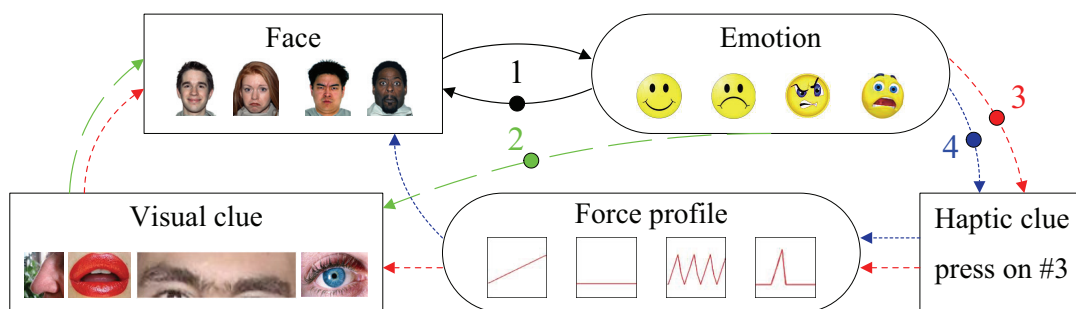


Figure 7.9 – Block diagram presenting the four parts of the experiment: 1. without clue, 2. visual clue, 3. visuo-tactile clues and 4. tactile clue only (• = start)

## 7.4 Results

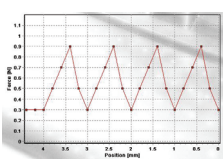
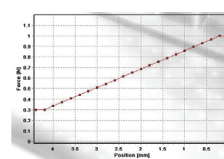
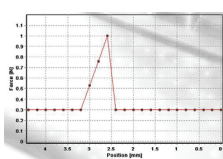
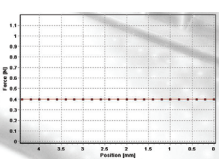
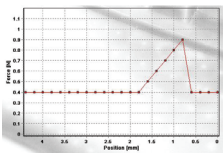
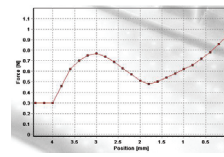
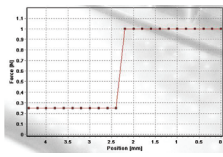
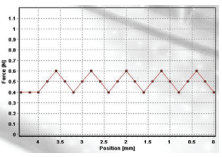
### 7.4.1 Identification part

The first indicators showing the general level of identification of haptic sensations are the words translating the users' feelings. A summary of the expressions used by the participants to describe the profiles is given in Table 7.1. The large peaks of key 1 are generally well distinguished through words like "clicks and stairs" and are assimilated to a roughness of the guideway. A resembling roughness is reported for key 8, however as its amplitude is lower, some people do not perceive the irregularities and describe it as "continuous". The three profiles (#3, #5 and #6) mimicking different clicks are relatively well sensed. The bottom click of key 5 reminds sensations of usual mechanical switches like "press stud, mouse and remote control button". Keys 3 and 6 are closer to each other and assimilated to computer keys. However, key 6 is correctly perceived as more "round" while key 3 is clearly harder to

## Chapter 7. Impact study of haptic feedback on emotional processing

overcome. Key 7 is probably one of the most distinguishable but also the most difficult to describe. Indeed, the threshold is sometimes well recognized and described as a "cork on water" but participants also sensed "vibrations". These vibrations come from the abrupt rise of the force profile which, coupled to the finger elasticity, generates oscillations around the central position and noise, reported as "disturbing" by the users. Finally, keys 2 and 4 are described as "soft, smooth, constant and pleasant". As for their difference, key 2 is clearly tagged as a "spring" whereas key 4 appears as "constant" even non-existent.

Table 7.1 – Summarized results of the descriptive part of the force profiles identification

#1	#2	#3	#4
			
Grip, stick-slip, clicks, rough, stairs	spring, soft, constant, smooth	computer key, click, obstacle to overcome, stuck key	constant, smooth, nothing, pleasant
#5	#6	#7	#8
			
Press stud, end click (mouse), remote control button, not pushing in entirely	round click, standard key, keyboard, light click	threshold, large stiffness in the end, cork on water, vibration, disturbing	scraper, friction, continuous, rough, rack rail

Besides the descriptive part, the participants were asked to draw what they feel on a blank chart. Three qualitative criteria, namely intensity, shape and position, are set to quantify the score allocated to each subject. The average result for the 17 participants of the experiment is 5.32/8 (66.5 %) (Figure 7.10). Understanding a force profile being easier for the participants with an engineering background, a distinction will be done between both groups when relevant. Subjects 1-9 will thus be referred to as *engineers* or *group 1* and subjects 10-17 to as *psychologists* or *group 2*. As expected, it is significantly easier for group 1 to link a haptic feeling with a force profile (79.2 %) compared to group 2 (52.3 %) ( $t(15) = 3.92, p \leq .001$ )<sup>3</sup>.

<sup>3</sup>Repeated measures ANOVA [190] are run on the data with the Statistical Package for the Social Sciences (SPSS) to determine whether or not the improvements are significant.



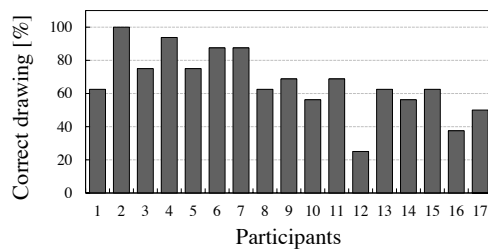


Figure 7.10 – Percentage of correct profiles drawing per participant

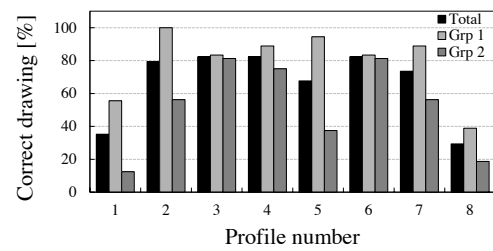


Figure 7.11 – Percentage of correct drawing of each profile for the distinct groups (all, engineers and psychologists)

The results presented in detail for each profile (Figure 7.11) show that half of them are drawn correctly over 80 % and three quarters of them over 67 %. A 2 x 8 ANOVA integrating the group effect highlights the existence of differences between the profiles ( $F(7, 105) = 6.96, p \leq .001$ ). This discrepancy can notably be attributed to the difficulty of the participants in drawing rough profiles which differ significantly from all other profiles in pairwise comparisons (#1 and #8 are different from #2, #3, #4, #6 and #7,  $p \leq .01$ , and from #5,  $p \leq .05$ ). The discrepancies between both groups ( $F(1, 15) = 15.42, p \leq .001$ ) are clearly visible on profiles such as the spring (#2) for which engineers have a useful background but are almost null for the clicks (#3, #6) and constant (#4) profiles. Despite the variation in performance observed between both groups, the interaction between group and profile effects is not significant ( $F(7, 105) = 1.51, p \geq .10$ ) meaning that the engineers and the psychologists globally present difficulties in identifying the same profiles.

In a second stage, the force profiles of Figure 7.5 are presented in disorder to the participant who is required to match each key with its corresponding profile. The average result is 4.82/8 (60.3 %) for the 17 subjects. Again, the difference between both groups is significant: 77.8 % for group 1 (1-9) and 40.6 % for group 2 (10-17) ( $t(15) = 3.38, p \leq .01$ ), visible on Figure 7.12 and showing a necessary learning and habituation to the haptic feedback. In order to demonstrate the influence of learning, the matching phase is repeated a second time, either directly after the experiment or several weeks later, with the participants of group 1 who did not obtained 8/8. The second series of results represented with dots in Figure 7.12 shows an improvement of 21.4 % (to 94.4 %) for the selected group ( $t(8) = 3.02, p \leq .05$ ).

A glance at the results detailed for each profile (Figure 7.13) shows two main differences with the drawing part. Firstly, elaborated profiles such as the sawtooth profiles (#1 and #8), the details of which were hardly interpretable, are more efficiently identified (#1 and #8 are only different from #5 and #6,  $p \leq .05$ ). Secondly, the profiles corresponding to variations of the click (#3, #5 and #6) are often mixed up due to their similarity ( $p \geq .30$ ). Globally, the difference between the profiles is significant ( $F(7, 105) = 3.41, p \leq .01$ ) but again, the interaction group-profile is not ( $F(7, 105) = 1.10, p \geq .30$ ).

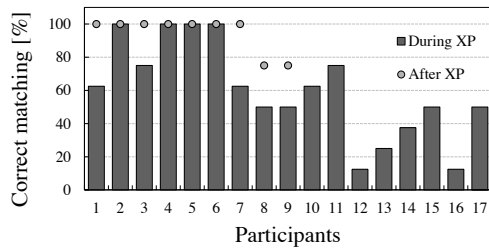


Figure 7.12 – Percentage of correct profiles matching per participant during and after the experiment

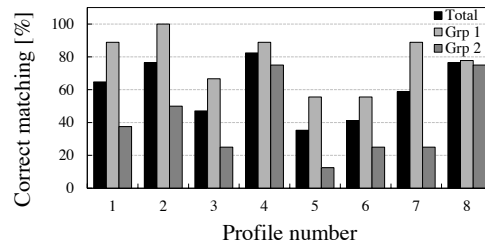


Figure 7.13 – Percentage of correct matching of each profile for the distinct groups (all, engineers and psychologists)

Finally, the ranking of the five more memorable keys shown in Figure 7.14 places profiles #2, #3, #4 and #7 in the lead. A second ranking taking the order given by the subject into account by adding weights to the profiles (5 for the first, 4 for the second and so on) confirms this list but places #7 slightly behind.

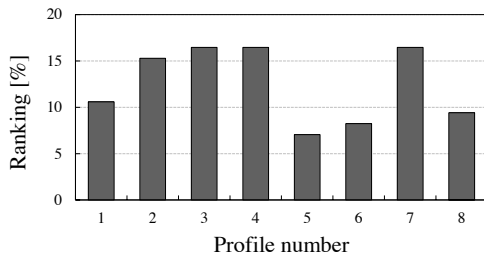


Figure 7.14 – Results of the ranking of the five more memorable touch sensations

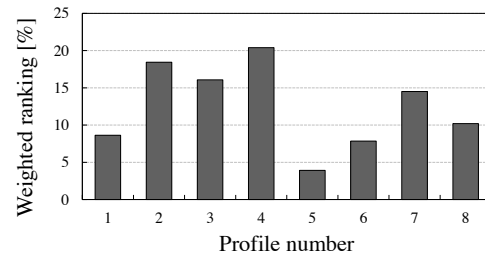


Figure 7.15 – Weighted ranking of the five more memorable touch sensations

### 7.4.2 Effect on emotional processing

Fifteen people participated in the second part of the experiment on emotional processing, eight from group 1 and seven from group 2. The accuracy with which the emotions are recognized and the response time represent the two measurements taken during the experiment. A difference between the engineers and the psychologists appeared to be significant for the accuracy measures ( $t(13) = 3.25, p \leq .01$ ) but not for the response time. However, a closer look emotion per emotion revealed that the only emotion to present a significant difference in accuracy is fear ( $t(13) = 2.34, p \leq .05$ ). The group will thus be considered as a covariable in this particular case only (accuracy - fear) and will be ignored for the rest of the results.

The accuracy of emotions recognition averaged on the four conditions, namely without clue, with visual, tactile and visuo-tactile clues, is summarized in Table 7.2. All four emotions are identified with high accuracies exceeding 80 %, anger being the lowest with 80.0 % and as ex-

pected [175], happiness being the most obvious with 97.4 %. Contrarily to the first experiment, group 2 achieved better results, probably due to the fact that they are regularly confronted to emotional processes in their work.

Table 7.2 – Overall accuracy of emotions recognition averaged on the four conditions [%]

Sample	Fear	Anger	Happiness	Sadness	Total
All	84.7	80.0	97.4	88.0	87.5
Group 1	77.5	75.0	96.3	86.3	83.8
Group 2	92.9	85.7	98.6	90.0	91.8

The effect of the addition of different clues before the presentation of the emotion is illustrated in Figures 7.16 and 7.17. The average accuracy for the four emotions shows a slight improvement for all three conditions compared to the reference with "no clue" (Figure 7.16). However, the overall accuracy is so high for the healthy pilot sample that the enhancement is inevitably limited and thus, not statistically significant. A detailed look, emotion by emotion (Figure 7.17), shows that the visual clue improves the identification in every case (values in Table 7.3), which results in a narrower standard error compared to tactile and visuo-tactile clues (bars in Figure 7.16). As for the tactile clue, it helps for some emotions like sadness but does not for anger. It is to note that the sawtooth profile ("peaks") attributed to anger was not ranked among the top memorable sensations in Figures 7.14 and 7.15. Indeed, the better the force profile was ranked by the participants, the more important is the improvement in emotions recognition. Finally, both visual and tactile clues presented together do not seem to sum the effects of individual clues. At the contrary, the diversity of information to be processed by the human brain seems to penalize the accuracy when both clues are individually beneficial (e.g. happiness and sadness).

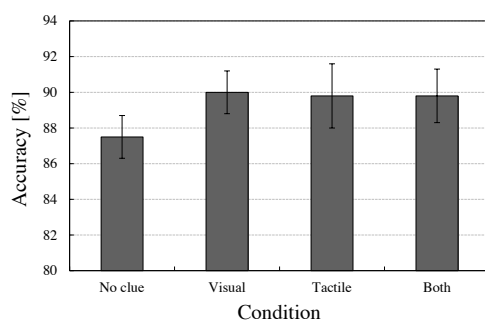


Figure 7.16 – Average accuracy of emotions recognition during the four conditions with standard errors

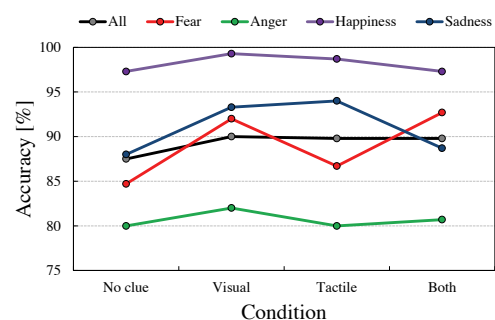


Figure 7.17 – Detail per emotion

## Chapter 7. Impact study of haptic feedback on emotional processing

Table 7.3 – Detailed accuracy of emotions recognition during the four conditions [%] and corresponding improvements relatively to the first condition

Condition	Fear	Anger	Happiness	Sadness	Total
<b>No clue</b>	84.7	80.0	97.3	88.0	87.5
<b>Visual</b>	92.0	82.0	99.3	93.3	90.0
Gain [%]	8.6	2.5	2.1	6.0	2.9
<b>Tactile</b>	86.7	80.0	98.7	94.0	89.8
Gain [%]	2.4	0.0	1.4	6.8	2.6
<b>Both</b>	92.7	80.7	97.3	88.7	89.8
Gain [%]	9.4	0.9	0.0	0.8	2.6

Regarding the response time, the introduction of visual and tactile clues, individually presented, results in a significant improvement in both cases (Figure 7.18). Indeed, the visual clue significantly decreases the response time compared to the reference (12.2 %,  $p = .017$ ) and the tactile clue even more (25.8 %,  $p = .000$ ). The enhancement brought by the haptic information is even significant compared to all other conditions (to visual: 15.5 %,  $p = .003$  and to visuo-tactile: 22.7 %,  $p = .000$ ). A detailed view per emotion confirms the improvement in all cases (Figure 7.19, values in Table 7.4). Again, happiness is identified the most rapidly and anger is globally the slowest, even if the curves are close to each other. Similarly as for the accuracy, the "peaks" profile is related to the lowest improvement (i.e. anger) and the magnitude of the improvement is directly related to the ranking of Figures 7.14 and 7.15. The feeling that several clues stimulating different senses simultaneously are counterproductive is confirmed for the reaction time by the last condition mixing both visual and tactile clues.

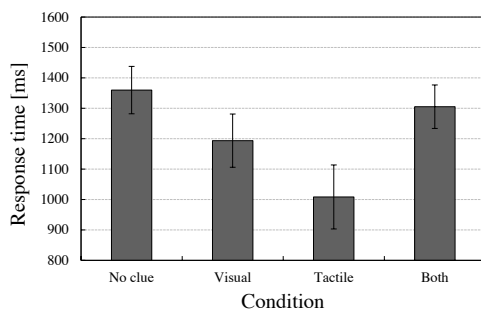


Figure 7.18 – Average response time during the four conditions with standard error bars

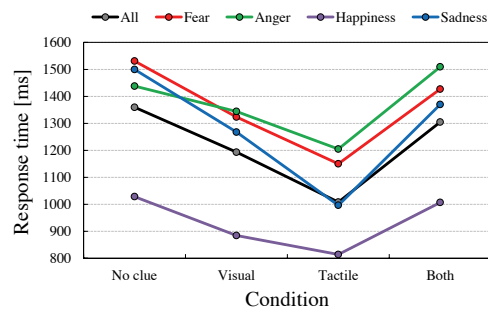


Figure 7.19 – Detail per emotion

By isolating the experiment with the tactile clue only, it comes out that the ranking of the relative improvements observed in both accuracy (Table 7.3) and response time (Table 7.4)

Table 7.4 – Detailed response times during the four conditions [ms] and corresponding improvements relatively to the first condition

Condition	Fear	Anger	Happiness	Sadness	Total
<b>No clue</b>	1531.0	1438.1	1028.6	1499.7	1359.8
<b>Visual</b>	1323.8	1344.3	884.6	1267.8	1193.5
Gain [%]	13.5	6.5	14.0	15.5	12.2
<i>p</i>	.064	.354	.001	.011	.017
<b>Tactile</b>	1150.2	1204.9	814.3	996.5	1008.4
Gain [%]	24.9	16.2	20.8	33.6	25.8
<i>p</i>	.004	.118	.001	.001	.000
<b>Both</b>	1427.3	1509.4	1007.0	1370.0	1305.1
Gain [%]	6.8	-5.0	2.1	8.6	4.0
<i>p</i>	.301	.501	.752	.218	.413

places sadness first, followed by fear, happiness and finally anger. The ranking of the corresponding force profiles, namely "constant", "click", "spring" and "peaks", tallies with the results obtained during the initial identification part where profiles #4, #3 and #2 (respectively "constant", "click" and "spring") obtained better drawings (Figure 7.11) and rankings (Figures 7.14 and 7.15) than profile #1 ("peaks").

For a better understanding of the relative variation of the improvement from one emotion to the other, a brief analysis of the accuracy of force profiles recognition during the two last executions of the emotional experiment (tactile and visuo-tactile conditions) is presented. Each emotion being associated to a dedicated force profile (Figure 7.8), the differences in haptic identification further influence the quality of the emotional processing. The accuracy of emotions recognition (Table 7.2) is left aside and only the accuracy in force profile detection is considered. Table 7.5 shows the results for both tactile and visuo-tactile conditions. The average of both conditions presents the "spring", "constant" and "click" profiles as well identified with results higher than 80 %. The "peaks" profile is once again misinterpreted.

The detailed answers obtained each time one of the four force profiles is presented to the participant are shown in Figure 7.20. They help understand the different levels of improvement obtained in the emotions recognition with tactile clue (Tables 7.3 and 7.4). Indeed, the most important improvement relatively to the "no clue" condition is attributed to sadness associated to the "constant" profile (Figure 7.20 (c)) which is globally well identified (85.3 %) despite a slight confusion with the "spring" profile (8.0 %) due to the absence of irregularities along the travel. Similarly, the "spring" profile (b) is clearly discriminated (92.0 %), however the natural

## Chapter 7. Impact study of haptic feedback on emotional processing

Table 7.5 – Overall accuracy of force profiles recognition under different conditions [%]

Condition	Click	Spring	Constant	Peaks	Total
Ass. emotion	Fear	Happiness	Sadness	Anger	
Tactile	82.0	92.0	85.3	64.6	81.0
Both	80.0	76.0	80.6	66.7	75.8
Mean	81.0	84.0	83.0	65.7	78.4

facility to identify happiness makes it difficult to importantly improve the performance for this emotion. The confusion is however more present for the two last profiles. Indeed, in 18.0 % of the cases, the participant answered "peaks" instead of "click" (a). As they are allowed to press only once on the key, some people might think they have missed some peaks and answer with caution. The effect is even more obvious for the last profile (d), where 35.5 % of the subjects confused the "peaks" and the "click" profiles ( $p \geq .10$ ).

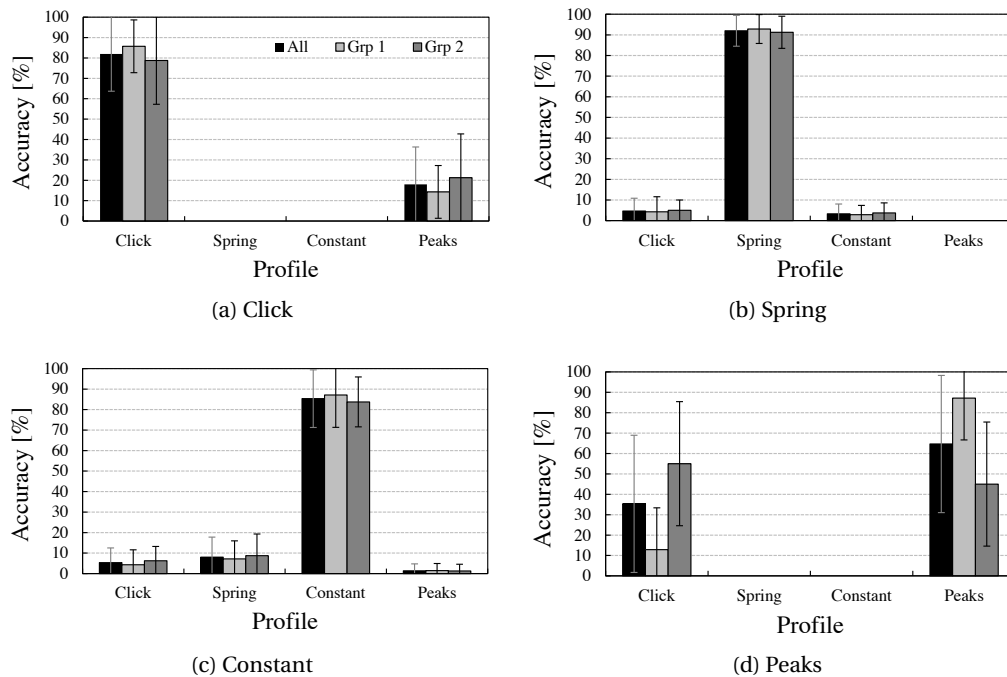


Figure 7.20 – Detail of the answers given for the four different haptic clues during the tactile part

This effect matches with the bad results obtained by the former during the identification experiment (Figures 7.11 and 7.13) and explains that the lowest improvements are obtained with the corresponding emotion (i.e. anger in Tables 7.3 and 7.4). It can be explained by the fact that if the person does not control his finger in position, it is charged in force to overcome

the first obstacle and directly transforms the potential energy into kinetic energy and thus masks the following peaks, similarly as a car would do on bumps. For this last profile, one finally remarks the important difference between groups 1 and 2, already present in Figures 7.11 and 7.13, which can be explained by fact that the engineers were more aware of the necessity of slowly displacing one's finger all along the stroke to feel all the details.

Similarly, the detail of the answers given during the visuo-tactile part is visible in appendix D (Figure D.1).

## 7.5 Discussion

The results obtained during the pilot experiment presented in this chapter show an increase of the participants' performance during emotional processing tasks attributed to the introduction of additional haptic and visual clues, individually presented. The response time is notably significantly shortened confirming thus the idea introduced by Salminen et al. [184] that even simple haptic stimuli can convey emotional content. The present study strengthens the fact that the visual recognition of emotions can be improved using a haptic feedback, which has also been supported by Bonnet et al. [176] in their research using large 3D movements. Following our study, a simplification of the haptic feedback can thus be considered. The use of multi-finger haptic devices integrating miniature short-stroke actuators actually allows conveying haptic information opening the way for affective computing operations.

In the case of the present pilot study involving healthy subjects, the accuracy of emotions recognition is not significantly improved with the introduction of sensory clues<sup>4</sup>, contrarily to the response time. However, the positive tendency notably appearing with visual and some tactile clues could become significant when working with psychotic youths who suffer from difficulties in identifying visual emotions. Indeed, significantly increasing accuracies reaching 90 % or more is difficult but could become conceivable when starting with lower initial scores, like it should probably be the case for the final target sample.

The improvements observed in the recognition of visual emotions are notably attributed to the efficient identification and discrimination of various haptic stimuli in the form of unidirectional force profiles generated by linear actuators. The accuracy, well above chance, with which up to eight different force profiles were identified during descriptive, drawing and matching parts is really encouraging and pushes towards an enlargement of the panel of stimuli. The force feedback hapticons developed could then be integrated in online conversations so as to enrich the interactions with nonverbal communication, going thus together with the popular trend of social networking and instant messaging.

Since the human being is not used to such kind of haptic feedback [180] and all people are not equally sensitive, a period of adaptation is necessary to feel the subtleties of each stimulus. The results of the identification part indeed presented large discrepancies between participants,

---

<sup>4</sup>Except for fear  $F(3, 39) = 4.36, p \leq .01$

## Chapter 7. Impact study of haptic feedback on emotional processing

---

from 25 to 100 % for the drawing and from 12.5 to 100 % for the matching exercise. The difference observed between the engineers (group 1: 79.2 % and 77.8 %) and the psychologists (group 2: 52.3 % and 40.6 %) is very interesting and highlights the fact that initiated people are more inclined to perceive and translate profile specificities. The importance of the learning process is even more clearly brought to light by a second iteration of the matching part completed by the subjects of group 1, directly in the end of the entire experiment or a few days later. The promising improvement of 21.4 % of the percentage of correct answers can also partly be due to the fact that the participants were more relaxed during the second iteration which was not executed directly after the painful exercise of drawing which might have slightly disturbed the results of the matching part. The last evidence of the rapid assimilation of the different haptic stimuli is the accuracy of force profile identification obtained in the emotional processing part. Except for the "peaks" profile which was hardly recognized by group 2, the profiles were correctly identified at more than 80 % and the differences between both groups almost disappeared.

All haptic stimuli were not equally recognized. The ranking by the participants of the eight proposed profiles (Figures 7.14 and 7.15) indicates that very simple profiles possessing only a single marked discontinuity (e.g. #3 and #7) or even no discontinuity at all (e.g. #2 and #4) are more likely to be identified. At the contrary, sawtooth profiles consisting in a repetition of irregularities and simulating different roughnesses (e.g. #1 and #8) are less memorable, especially for people with no engineering background. Moreover, the degree with which a profile is felt and identified directly influences the performance during the recognition of visual emotions. Indeed, when ranking the relative improvements obtained with the tactile clue in accuracy and response time (Tables 7.3 and 7.4), one remarks that the corresponding force profiles ("constant", "click", "spring" and "peaks") are ordered in the same way as it has been done during the first identification part (Figures 7.11 and 7.14). Thus, the better the haptic information is assimilated, the better the emotional processing is.

Concerning the noise, as already experienced by Benali-Khoudja et al. with their tactile display [182], the presence of parasitic sounds generated here by the actuator switching during elastic oscillations of the finger around a position at which the force profile is abrupt (principally #7) influences the user's judgment. 47 % of the participants answered positively to the question "Does the noise represent an inconvenience? Would it be preferable to wear a hearing protector headset?". In order to block this noise, Salminen et al. precisely run their experiments using a hearing protector headset [184], however in the present case, once the desired force profiles will be determined, efforts will be put to remove the noise by improving the control software.

Finally, it has to be noted that whereas visual and haptic clues are beneficial when individually presented, they become inefficient if presented simultaneously. Providing more than a single clue for the identification of emotions is counterproductive and seems to cancel the gain generated by each individual clue. Indeed, increasing the number of clues increases the number of cognitive processes involved which thus affects the performance. This statement is consistent with the research of Baumeister et al. in which controlled cognitive processes



are described as a limited resource [191–194]. According to their work, the different features of self-regulation, or self-control, including emotions, cognition and behavior depend upon the same resources and therefore, only a limited number of operations are allowed at a time. Several experiments showed that the fact of subjecting people to an initial act of self-control, notably involving an emotional activation, further impairs the performance during the second act of control. For instance, Schmeichel et al. [195] reported reasoning and thinking issues in subjects who were first asked to regulate their emotions when watching upsetting footage. Following the same idea, Urben [196] demonstrated an impairment of arithmetic tasks results in children after inducing frustration through unpredictable and unwanted delays imposed between trials. In the experiment presented in the present chapter, the treatment of a single clue, visual or haptic, does not involve a control process from the user and thus still allows for an improvement of the performance. However, by giving two consecutive clues, we force the participant to control the information and thus limit the resources available for the emotional processing which has the effect of canceling the benefit brought by the clues individually presented.

### **Outlook**

The drawing part being notably very demanding for the subject's concentration, the proper identification part will be separated from the emotional part for the next steps of the study. Following the encouraging results brought by the first pilot experiment, the identification part will be furthered with the aim of increasing the number of available haptic sensations. For instance by comparing different profiles with different intensities in pairs and by asking the participant to distinguish whether they are the same or different similarly as what Salminen et al. did with the rotating fingertip stimulator [184]. The distinctive features of each force profile will be listed so as to be able to give a general rule for the design of efficient short-stroke force feedbacks. Then, with an eye towards the development of linear hapticons for instant messaging and online chatting, the emotional content conveyed by the haptic sensations will be studied for a direct utilization [176, 182, 184].

As for the advantage brought by tactile (and visual) clues during emotions recognition tasks, the performance improvement observed on healthy subjects, notably on the response time, is encouraging and will thus be repeated on a sample of psychotic adolescents. As mentioned earlier, the improvement is expected to be even greater as the room for improvement increases with the difficulty of these adolescents to discern emotions. Indeed, with the hypothesis of a lower initial accuracy in emotions recognition, the contribution of tactile (and visual) clues is expected to increase and hopefully become significant. Regarding the experiment itself, small modifications will have to be brought. Firstly, the identification part will be replaced by a more playful habituation phase in order to make the participant used to the force feedback without being too boring. Then, based on the enhanced identification experiment, the four (or more) more memorable force profiles will be chosen in order to maximize the chance of improvement in emotions recognition. The emotional aspect conveyed by each force profile will also be

## **Chapter 7. Impact study of haptic feedback on emotional processing**

---

taken into account to fit with the corresponding emotion. With these modifications, we hope to be able to bring a little help to the psychotic adolescents to overcome their difficulties in expressing and identifying emotions during social interactions.



# 8

## Conclusion and outlook

The present thesis addresses a multidisciplinary system approach for multi-finger haptic devices which responds to an increasing demand for tactile comfort, non-verbal communication and interactive manipulation of the digital information. The strength of this work is, above all, to present a methodology that assembles a large set of technologies and proposes innovative solutions in order to design fully integrated haptic devices destined to research as well as to industry. In order to guide the designer towards adapted solutions, a detailed introduction on the human hand physiology is provided in preamble. Following that, general considerations on the different elements constituting a multi-finger haptic device are provided and several innovative tools required for their development are presented. These tools, notably handling the modeling and optimization of miniature short-stroke actuators as well as their position detection, are intended to be used by future developers and are thus presented in a generic manner in order to be easily adaptable to different kinds of applications. As for illustration of the methodology, fully functional prototypes such as the Haptic Keyboard and the VibKey Pad are designed and fabricated, giving an overview of the possibilities offered by multi-finger haptic devices.

### **8.1 Main results and innovative contributions**

Even if the methodology is presented as global, the scientific innovations actually making the originality of the thesis are targeted on the optimization of miniature electromagnetic short-stroke actuators as well as the development of innovative solutions for position detection. The original contributions are summarized hereinafter:

- An *accurate modeling of miniature short-stroke electromagnetic actuators* was made possible thanks to the combination of 3D finite element modeling (FEM) and design of experiments (DOE). The non-conventional behavior of magnetic flux lines in miniature actuators with relatively large airgaps led us to avoid simplified analytical models and use the reliable results of finite elements. The long computation times required by 3D FEM are balanced by the use of selective DOE making the modeling methodology easily adaptable, rapid and accurate.
- The parametrical model of the force provided by the modeling methodology was then integrated in a *full parametrical setup* possessing a single user interface. After entering the constraints defining the experimental domain, the program automatically runs the modeling process and then optimizes the force generated by the actuator using a conventional algorithm. The advantage of the parametrical optimization is that complementary non-linear constraints can be added so as to become multi-physic.
- Several original position measurement techniques using existing sensors were developed including a low-cost *custom single-photointerrupter sensor allowing for direction discrimination* for fast-prototyping and a *hybrid sensing method using tiny Hall sensors* and taking advantage of the leaks of the main actuator magnet.
- Two innovative self-sensing methods successfully allowed measuring the position of the mover of linear short-stroke actuators. The first solution estimates the position of the coil by *measuring the acceleration through the back emf*. However, a constant acceleration is required which strongly restrains the application scope. The second solution allows for a real-time measurement of the position thanks to a *passive oscillating RLC circuit* influenced by the variation of the coil impedance. All the solutions presented are low-cost, compact and require few computation resources.

In addition to the purely mechatronic side of the thesis, the results obtained from an experiment run by a sample of population pave the way for novel man-machine interactions:

- The encouraging results obtained during a force profiles identification phase lay the *first stones of a new tactile language*. The experiment showed the benefit of habituation in haptic feedback and demonstrated a clear discrimination capacity of the participants.
- The pilot experiment run in collaboration with the SUPEA - CHUV achieved in a *significant improvement of the subjects' performance during emotions recognition tasks* attributed to tactile clues provided by the Haptic Pad. These results bring a serious hope to help psychotic adolescents and learn from their disorders.

The scientific content of the thesis resulted in the publication of several papers presented in international conferences and a magazine paper. Both self-sensing methods have notably been presented in Tokyo (ICEMS 2009 [146]) and in Taiwan (AIM 2012 [197]). The modeling of

a miniature short-stroke actuator for a haptic key (ECCE 09, San Jose [198] and IEEE Industry Applications Magazine [199]) and the entire development of the Haptic Keyboard (ICEMS 2011, Beijing [200]) retrace the major scientific contributions brought to the design of multi-finger haptic devices.

## 8.2 Outlook

Labeled as "mechatronic", the present thesis covers a large scope and touches various domains in order to be finally coherent with the design methodology for multi-finger haptic devices. The advantage of multidisciplinary however avoids having an in-depth vision of every technological aspect, which leaves a door open to a series of further researches:

- Additional extensions could be brought to the full parametrical setup in order to provide a complete multi-physic interface for the optimization of short-stroke electromagnetic actuators. The idea would be to integrate secondary models, such as weight, temperature or design for self-sensing in the form of non-linear constraints for the final optimization.
- Besides the different electromagnetic actuators modeled in the present thesis, it would be interesting to enlarge the scope and test the applicability of the methodology on alternative technologies such as the smart materials and particularly the magnetorheological fluid actuator for haptic glove presented in Montréal (AIM 2010 [76]).
- Concerning the self-sensing, we recommend deepening the research on the induced oscillations method so as to explore its limits in resolution and robustness. Indeed, the promising results obtained with such an economical solution in terms of hardware and software resources should definitely retain our attention for future applications.
- Regarding the use of multi-finger haptic devices, it seems important to continue seeking after potential applications allowing for new developments. From our point of view, the opportunities offered by on-line communication, gaming and assistance to the blind fully justify an enlargement of the force profiles library started in the identification phase of the psychological experiment. Proposing a new tactile language to computer users will not be an easy task. It is the reason why appealing applications need to be implemented first to inform the potential users about the possibilities offered by multi-finger haptic applications.
- The use of the VibKey Pad could also be investigated for psychological studies in order to determine the influence of different vibration patterns on the performance during computer-related tasks. The interest would also be to see if the kinesthetic sense is more helpful than the tactile sense or inversely.
- Finally, the encouraging results obtained with the sample of healthy participants during the emotions recognition task of the psychological study confirms the hunch that haptics

## **Chapter 8. Conclusion and outlook**

---

can help in specific cognitive operations. From these results should flow the decision of starting a larger study on psychotic adolescents in order to determine if our expectations for better results when working with emotionally impaired people can be confirmed.

In conclusion, it is clear that the methods presented all along the thesis, notably for the design of actuators and the detection of the position, are likely to be used in various other domains that are not mentioned here for coherence reasons, such as robotics, automotive, etc. . .



## Contents

---

<b>A.1 Optimization tools</b> . . . . .	<b>187</b>
A.1.1 Design of experiments . . . . .	187
<b>A.2 Actuators</b> . . . . .	<b>190</b>
A.2.1 Cylindrical actuator . . . . .	190
A.2.2 Square actuator II . . . . .	191
A.2.3 Fixed magnet actuators . . . . .	194
A.2.4 Vibrotactile button . . . . .	195

---

## A.1 Optimization tools

### A.1.1 Design of experiments

#### Designs from literature

A non-exhaustive list of existing designs is presented hereinafter in order to help understand the functioning of the design of experiments:

- **Hadamard designs**, known as **Plackett & Burman designs** in English literature, are two-level matrices made of very few experiments whose role is to screen the main effects

of a system. The very limited data set does not allow for an accurate description of models with interactions. Proper Hadamard matrices only exist for number of runs  $N_e$  that are multiples of 4 and can estimate up to  $N_e-1$  factors. The second row of the matrix, called generator, can be found in literature [201]. It is a combination of '+' and '-' corresponding to 1 and -1. The  $N_e-2$  following rows are circular permutations of the generator. The first row is finally filled with '+'.

- The advantage brought by the **full factorial design** proposed by Fischer consists in varying multiple factors simultaneously [120]. Two and three-level factorial designs exist. Considering only the extremities of the experimental domain defines a two-level design (Figure A.1 left). Middle points are added to obtain three levels (Figure A.1 right). The total number of experiments is obtained by multiplying all levels together (2· 2 and 3· 3 respectively). Two levels will be used for the presentation of the design. The number of experiments in this case is given by:

$$N_e = 2^k \tag{A.1}$$

with k the number of factors.

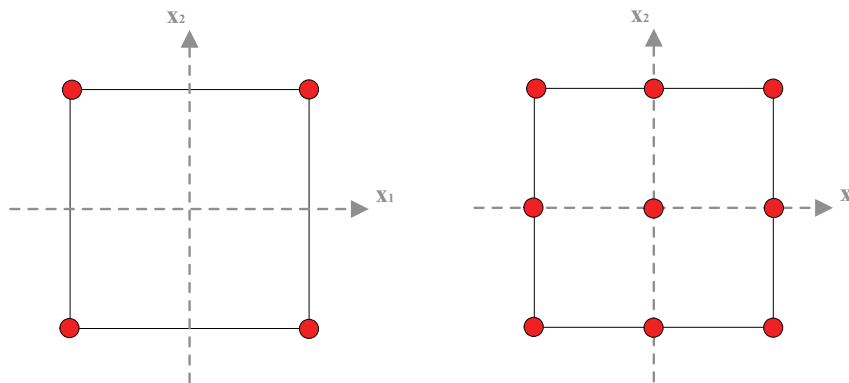


Figure A.1 – Two and three-level factorial designs for two factors  $x_1$  and  $x_2$

- The **fractional design** is an improvement of the factorial design in a sense that it avoids an exponential expansion of the number of experiments with the number of factors. Indeed, increasing the number of factors increases the number of interactions between them. With two inputs, there is only one interaction  $x_1x_2$ , but three factors already give four interactions  $x_1x_2$ ,  $x_1x_3$ ,  $x_2x_3$  and  $x_1x_2x_3$  and so on. High levels of interaction can often be neglected and leave space for new factors instead. In the full factorial design, all parameters are estimated independently due to the property of orthogonality. In the fractional case, adding extra factors generates interactions between parameters which cancels this property. However, as soon as high level interactions can be neglected, orthogonality can be considered again [201].



- An **equiradial design** consists in placing all experimental points at a predefined distance around the experimental domain center. A well-known equiradial design is the Doehlert matrix, represented by a hexagon capable of covering the domain with translations (Figure A.2). The advantage of such configuration is that the matrix of points can move over the experimental domain, which makes it a candidate for optimization processes.

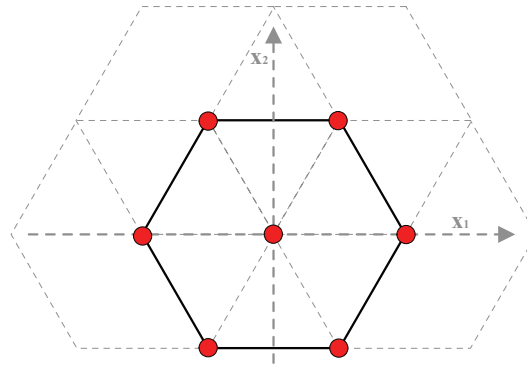


Figure A.2 – Doehlert hexagonal matrix for two factors  $x_1$  and  $x_2$

- Following the same idea, the **composite design** mixes a factorial design with a star design (Figure A.3). Like for equiradial designs, all points of the star design are arranged on a sphere of diameter  $\alpha$  around the center. Experimental errors are detected by repeating measurements on the central point. However, in the case of FEM, these discrepancies are negligible and a single central simulation is sufficient.

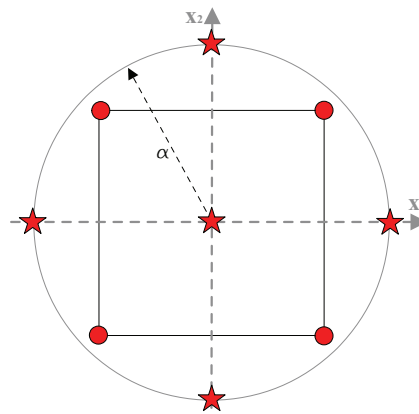


Figure A.3 – Composite design for two factors  $x_1$  and  $x_2$

The list of standard designs presented above is not exhaustive but gives a good overview of what can be found in literature. More information is available in the following references: [120, 201–203].

## A.2 Actuators

### A.2.1 Cylindrical actuator

The parameters value for the quadratic models with first order interactions are shown in Table A.1 for 3 factors, in Table A.2 for 5 factors and in Table A.3 for 7 factors.

Table A.1 – Quadratic model of the cylindrical actuator with first order interactions for 3 factors

$a_0$	$a_1$	$a_2$	$a_3$	$a_{12}$	$a_{13}$	$a_{23}$	$a_{11}$	$a_{22}$	$a_{33}$
1.24	0.00	-0.23	0.12	-0.13	-0.01	-0.04	-0.32	-0.03	-0.06

Table A.2 – Quadratic model of the cylindrical actuator with first order interactions for 5 factors

$a_0$	$a_1$	$a_2$	$a_3$	$a_4$	$a_5$	$a_{12}$	$a_{13}$	$a_{14}$	$a_{15}$	$a_{23}$
1.22	-0.02	-0.22	0.12	0.03	0.06	-0.12	-0.01	0.02	-0.02	-0.03
$a_{24}$	$a_{25}$	$a_{34}$	$a_{35}$	$a_{45}$	$a_{11}$	$a_{22}$	$a_{33}$	$a_{44}$	$a_{55}$	
-0.01	-0.01	0.01	-0.03	-0.01	-0.31	-0.01	-0.04	-0.05	-0.02	

Table A.3 – Quadratic model of the cylindrical actuator with first order interactions for 7 factors

$a_0$	$a_1$	$a_2$	$a_3$	$a_4$	$a_5$	$a_6$	$a_7$	$a_{12}$
1.21	-0.03	-0.21	0.10	0.02	0.05	0.05	0.05	-0.12
$a_{13}$	$a_{14}$	$a_{15}$	$a_{16}$	$a_{17}$	$a_{23}$	$a_{24}$	$a_{25}$	$a_{26}$
-0.01	0.01	-0.03	0.00	-0.01	-0.03	-0.01	-0.01	-0.01
$a_{27}$	$a_{34}$	$a_{35}$	$a_{36}$	$a_{37}$	$a_{45}$	$a_{46}$	$a_{47}$	$a_{56}$
-0.02	0.01	-0.03	-0.01	0.00	0.00	0.00	0.00	-0.01
$a_{57}$	$a_{67}$	$a_{11}$	$a_{22}$	$a_{33}$	$a_{44}$	$a_{55}$	$a_{66}$	$a_{77}$
0.00	-0.01	-0.30	-0.01	-0.04	-0.05	-0.02	-0.01	-0.02

**A.2.2 Square actuator II**

The parameters value for the quadratic models with first order interactions are shown in Table A.4 for 5 factors and in Table A.5 for 7 factors.

Table A.4 – Quadratic model of the square actuator with first order interactions for 5 factors

$a_0$	$a_1$	$a_2$	$a_3$	$a_4$	$a_5$	$a_{12}$	$a_{13}$	$a_{14}$	$a_{15}$	$a_{23}$
1.24	0.01	-0.25	0.11	0.05	0.05	-0.15	-0.01	0.04	-0.03	-0.04
$a_{24}$	$a_{25}$	$a_{34}$	$a_{35}$	$a_{45}$	$a_{11}$	$a_{22}$	$a_{33}$	$a_{44}$	$a_{55}$	
-0.02	-0.01	0.01	-0.04	-0.01	-0.30	0.00	-0.03	-0.05	-0.01	

Table A.5 – Quadratic model of the square actuator with first order interactions for 7 factors

$a_0$	$a_1$	$a_2$	$a_3$	$a_4$	$a_5$	$a_6$	$a_7$	$a_{12}$
1.21	0.00	-0.24	0.11	0.04	0.05	0.06	0.05	-0.14
$a_{13}$	$a_{14}$	$a_{15}$	$a_{16}$	$a_{17}$	$a_{23}$	$a_{24}$	$a_{25}$	$a_{26}$
0.00	0.03	-0.02	0.00	-0.01	-0.04	-0.02	-0.02	-0.02
$a_{27}$	$a_{34}$	$a_{35}$	$a_{36}$	$a_{37}$	$a_{45}$	$a_{46}$	$a_{47}$	$a_{56}$
-0.02	0.01	-0.02	-0.02	0.00	0.01	0.01	0.00	-0.01
$a_{57}$	$a_{67}$	$a_{11}$	$a_{22}$	$a_{33}$	$a_{44}$	$a_{55}$	$a_{66}$	$a_{77}$
0.00	-0.01	-0.28	0.00	-0.03	-0.05	-0.01	-0.01	-0.02

**Star validation**

The matrix for the star validation of the 5 factors model with a radius of 0.5 mm is presented in Table A.6 for the square actuator.

Similarly, the star validation is applied to the 7 factors model with two different radii of 0.2 and 0.5 mm (Tables A.7 and A.8)

## Appendix A. Actuators

Table A.6 – Dimensions [mm] and results of the star validation with a radius of 0.5 mm for the square actuator with 5 factors

$x_1$	$x_2$	$x_3$	$x_4$	$x_5$	$F$ model [N]	$F$ FEM [N]	Error with optimum [%]
4.49	0.8	6	3	2.11	1.638	1.620	4.48
5.49	0.8	6	3	2.11	1.638	1.690	0.37
4.99	1.3	6	3	2.11	1.377	1.421	16.25
4.99	0.8	5.5	3	2.11	1.635	1.645	3.04
4.99	0.8	6	2.5	2.11	1.658	1.695	0.11
4.99	0.8	6	3	1.61	1.669	1.672	1.44
4.99	0.8	6	3	2.61	1.669	1.715	-1.11
4.99	0.8	6	3	2.11	1.671	1.697	optimum

Table A.7 – Dimensions [mm] and results of the star validation with a radius of 0.2 mm for the square actuator with 7 factors

$x_1$	$x_2$	$x_3$	$x_4$	$x_5$	$x_6$	$x_7$	$F$ model [N]	$F$ FEM [N]	Error with opt. [%]
4.7	0.8	6	3	4	3	3	1.740	1.811	1.4
5.1	0.8	6	3	4	3	3	1.740	1.846	-0.5
4.9	1	6	3	4	3	3	1.617	1.715	6.6
4.9	0.8	5.8	3	4	3	3	1.738	1.820	0.91
4.9	0.8	6	2.8	4	3	3	1.743	1.836	0
4.9	0.8	6	3	3.8	3	3	1.744	1.828	0.49
4.9	0.8	6	3	4	2.8	3	1.737	1.823	0.74
4.9	0.8	6	3	4	3	2.8	1.740	1.827	0.53
4.9	0.8	6	3	4	3	3	1.745	1.837	optimum

Table A.8 – Dimensions [mm] and results of the star validation with a radius of 0.5 mm for the square actuator with 7 factors

$x_1$	$x_2$	$x_3$	$x_4$	$x_5$	$x_6$	$x_7$	$F$ model [N]	$F$ FEM [N]	Error with opt. [%]
4.4	0.8	6	3	4	3	3	1.714	1.753	4.55
5.4	0.8	6	3	4	3	3	1.714	1.833	0.2
4.9	1.3	6	3	4	3	3	1.424	1.536	16.37
4.9	0.8	5.5	3	4	3	3	1.724	1.798	2.08
4.9	0.8	6	2.5	4	3	3	1.732	1.836	0.05
4.9	0.8	6	3	3.5	3	3	1.740	1.820	0.9
4.9	0.8	6	3	4	2.5	3	1.723	1.807	1.59
4.9	0.8	6	3	4	3	2.5	1.731	1.817	1.04
4.9	0.8	6	3	4	3	3	1.745	1.837	optimum

## Appendix A. Actuators

### A.2.3 Fixed magnet actuators

The parameters value for the quadratic models with first order interactions are shown in Table A.9 for the cylindrical actuator and in Table A.10 for the square actuator.

Table A.9 – Quadratic model of the cylindrical actuator with first order interactions for the fixed magnet configuration

$a_0$	$a_1$	$a_2$	$a_3$	$a_4$	$a_5$	$a_{12}$	$a_{13}$	$a_{14}$	$a_{15}$	$a_{23}$
1.34	-0.25	0.06	0.02	0.06	0.08	0.01	0.00	-0.01	-0.03	0.01
$a_{24}$	$a_{25}$	$a_{34}$	$a_{35}$	$a_{45}$	$a_{11}$	$a_{22}$	$a_{33}$	$a_{44}$	$a_{55}$	
0.00	0.00	-0.01	0.00	0.00	-0.13	-0.07	-0.01	0.00	-0.02	

Table A.10 – Quadratic model of the square actuator with first order interactions for the fixed magnet configuration

$a_0$	$a_1$	$a_2$	$a_3$	$a_4$	$a_5$	$a_{12}$	$a_{13}$	$a_{14}$	$a_{15}$	$a_{23}$
1.34	-0.34	0.08	0.04	0.08	0.08	-0.02	-0.02	-0.02	-0.03	0.02
$a_{24}$	$a_{25}$	$a_{34}$	$a_{35}$	$a_{45}$	$a_{11}$	$a_{22}$	$a_{33}$	$a_{44}$	$a_{55}$	
0.01	0.00	-0.01	0.00	-0.02	-0.01	-0.08	-0.01	-0.01	-0.02	

Detailed views of both fixed magnet prototypes (RA5 - SQ5) are shown in Figures A.4 and A.5.



Figure A.4 – Cylindrical actuator parts

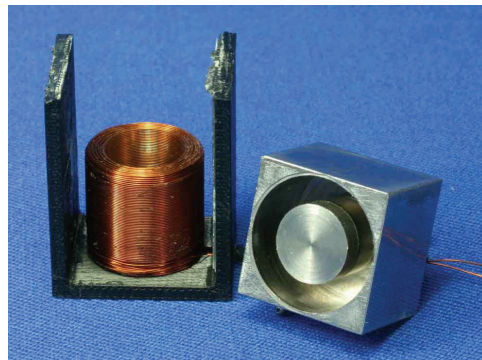


Figure A.5 – Square actuator parts

### A.2.4 Vibrotactile button

The parameters value for the quadratic models I and II with first order interactions are shown in Tables A.11 and A.11 for the vibrotactile button.

Table A.11 – Quadratic model I of the vibrator with interactions for 3 factors

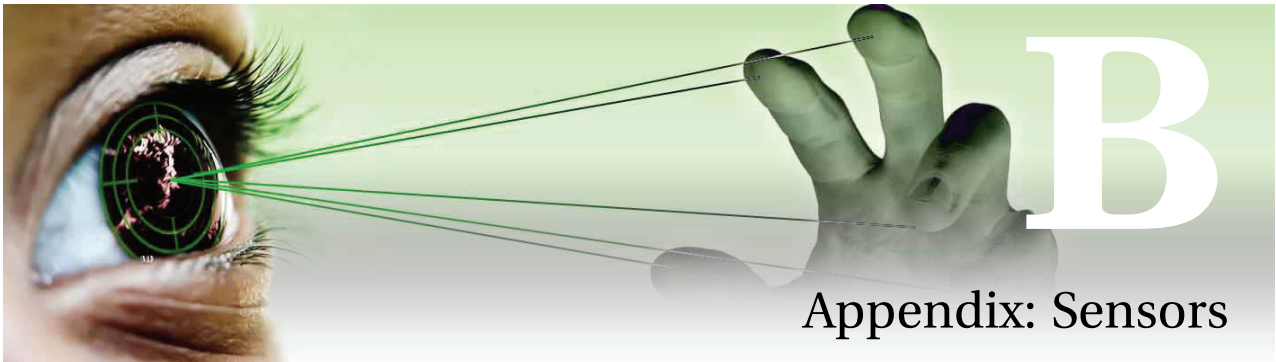
$a_0$	$a_1$	$a_2$	$a_3$	$a_{12}$	$a_{13}$	$a_{23}$	$a_{11}$	$a_{22}$	$a_{33}$
0.1007	1e-3	-2.61e-2	-2.1e-3	-2e-4	2e4	-2.8e-3	4e-4	-2.93e-2	-6.7e-3

Table A.12 – Quadratic model II of the vibrator with interactions for 3 factors

$a_0$	$a_1$	$a_2$	$a_3$	$a_{12}$	$a_{13}$	$a_{23}$	$a_{11}$	$a_{22}$	$a_{33}$
0.0958	1.7e-3	1.5e-3	-7e-4	2e-4	2e-4	-1e-3	-1.1e-3	6e-4	-3e-3







**Contents**

---

**B.1 Hybrid sensing method . . . . . 197**

    B.1.1 Linear Hall sensors for position measurement . . . . . 197

**B.2 Self-sensing approach . . . . . 199**

    B.2.1 Oscillating RLC circuit . . . . . 199

    B.2.2 RLC circuit with parallel capacitor . . . . . 199

    B.2.3 RLC circuit with parallel inductor . . . . . 200

---

**B.1 Hybrid sensing method**

**B.1.1 Linear Hall sensors for position measurement**

**Application on the cylindrical actuator**

The same FEM analysis as in Figure 5.5 is run on a cylindrical actuator (Figure B.1). FEM computations on a 2D grid overhanging the actuator confirm that the flux density is vertical above the center (Figure B.2).

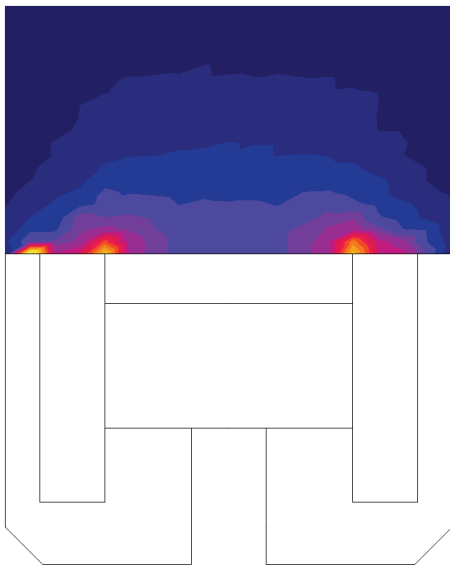


Figure B.1 – Flux density on a 2D grid overhanging a cylindrical actuator

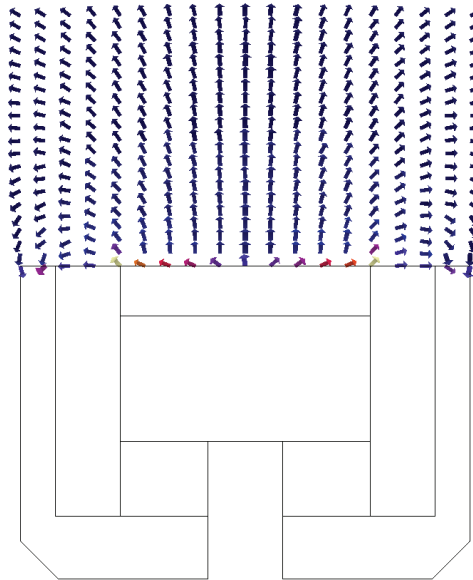


Figure B.2 – Flux density vectors above the actuator

**Calibration and robustness: effect of the current on position measurement**

A drawback observed with this position sensing method, where the sensor is placed directly in the coil, is the slight variation of the output with the power supplied for force creation. A small rotation of the curve is observed in Figure B.3. The increase of coil resistance due to iron losses and the magnetic field created by the coil itself can explain this effect.

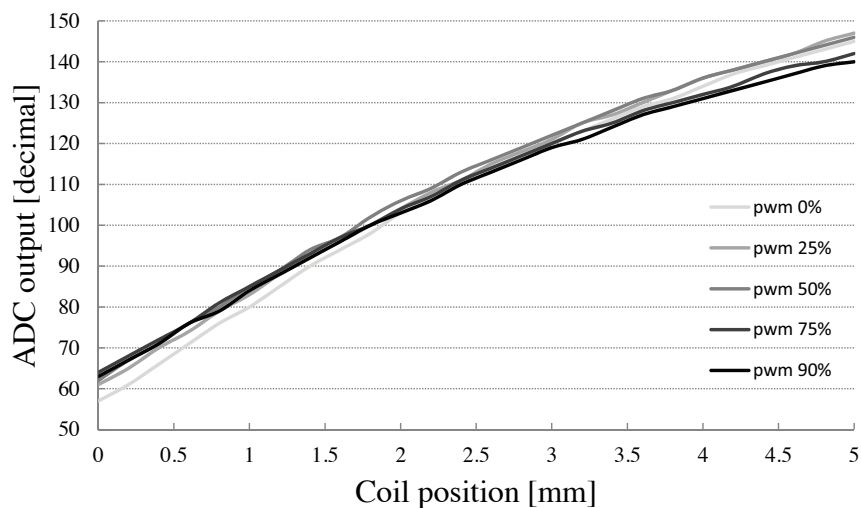


Figure B.3 – Hall sensor output variation related to PWM duty cycle

## B.2 Self-sensing approach

### B.2.1 Oscillating RLC circuit

Kirchhoff's second law applied to a RLC circuit (Figure 5.21 (a)) gives:

$$\frac{1}{C} \int i(t) dt + Ri(t) + L \frac{di(t)}{dt} = 0 \quad (\text{B.1})$$

Which becomes by derivation, a second order differential equation:

$$\frac{1}{C} i(t) + R \frac{di(t)}{dt} + L \frac{d^2 i(t)}{dt^2} = 0 \quad (\text{B.2})$$

that can be formulated as:

$$\ddot{i} + 2\lambda \dot{i} + \frac{1}{\omega_0^2} i = 0 \quad (\text{B.3})$$

with  $\lambda = \frac{R}{2L}$  the attenuation describing the envelope of the oscillations and  $\omega_0 = \frac{1}{\sqrt{LC}}$  the resonance frequency.

### B.2.2 RLC circuit with parallel capacitor

These measurements were made in the framework of a semester project [204]. A capacitor is connected in parallel with the actuator coil creating thus an oscillating circuit. A free-wheeling diode and three Zener diodes are connected so as to kill the current and still allow for oscillations to be created (Figure B.4). The measurements show a variation of both damping and frequency with the position of the actuator (Figure B.5). However, as the current can hardly establish within the coil due to the capacitor, it is only useful for position measurements and cannot be used for an efficient force control.

The problem can be explained by the analysis of the total impedance. Indeed, when a large capacitor (relatively to the coil capacitor  $C_C$ ) is connected in parallel with the coil, the impedance characteristic is shifted to the left as presented in Figure B.6 (the actuator used here is the same as for Figures 5.19 and 5.20). The resonance thus gets closer and closer to the PWM frequency which avoids the current to be created. In this configuration, the capacitor needs to be large in order to observe a significant variation of the oscillations. The method is thus an excellent candidate for position detection only but does not allow generating a force feedback.

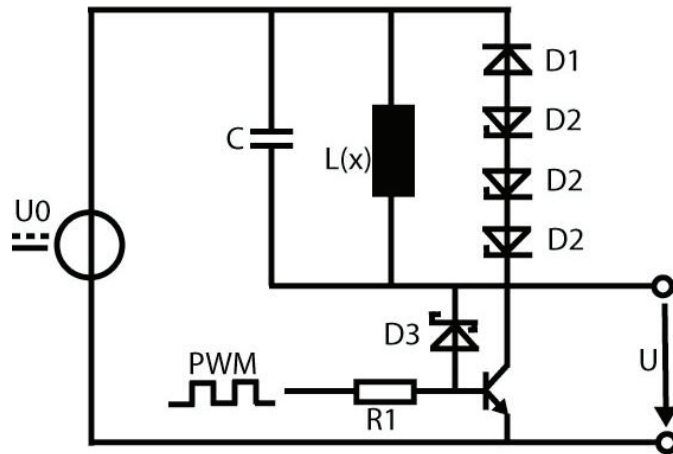


Figure B.4 – Test circuit with parallel capacitor ( $R1 = 270 \Omega$ ,  $C = 417 \text{ pF}$ ,  $D1 = \text{LN4147}$ ,  $D2 = 1\text{N4740A}$ ,  $D3 = \text{SB140}$ , Transistor =  $\text{BC337-25}$ ,  $U0 = 10 \text{ V}$ ,  $\text{PWM} = 20 \text{ kHz}$ ,  $50 \%$ ,  $L(x)$  represents the coil of the actuator)

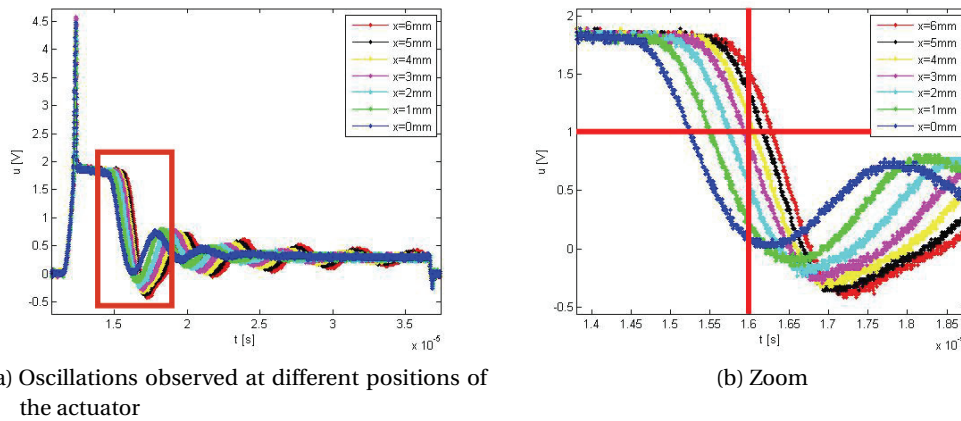


Figure B.5 – Measurements made on the circuit of Figure B.4 with a prototype of actuator (Figure 4.45)

### B.2.3 RLC circuit with parallel inductor

Kirchhoff's second law applied to the circuit of Figure 5.23 (b) allows writing the two following loop equations:

$$R_C i_1 + L_C \frac{di_1}{dt} - R i_2 - L \frac{di_2}{dt} = 0 \tag{B.4}$$

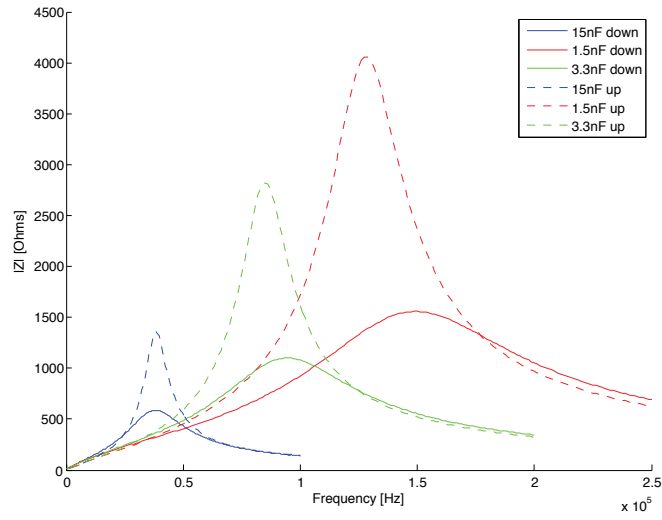


Figure B.6 – Effect on the capacitor impedance connected in parallel with the coil

$$U_{C0} + \frac{1}{C_C} \int i_C dt - R i_2 - L \frac{d i_2}{dt} = 0 \quad (\text{B.5})$$

Which becomes by derivation:

$$\frac{1}{C_C} i_C - R \frac{d i_2}{dt} - L \frac{d^2 i_2}{dt^2} = 0 \quad (\text{B.6})$$

With the introduction of the equation of the currents:

$$i_C = -i_1 - i_2 \quad (\text{B.7})$$

(B.6) becomes:

$$\frac{1}{C_C} (i_1 + i_2) + R \frac{d i_2}{dt} + L \frac{d^2 i_2}{dt^2} = 0 \quad (\text{B.8})$$

The system represented by (B.4) and (B.8) is simplified in a third order differential equation

## Appendix B. Sensors

---

formulated as a function of  $i_2$ :

$$i_2(R_C + R) + \dot{i}_2(R_C R C_C + L_C + L) + \ddot{i}_2(R_C L + R L_C) C_C + \ddot{i}_2 L_C L C_C = 0 \quad (\text{B.9})$$

Then, in order to analyze the influence of the capacitor at high frequency, a second formulation of the system is established as a function of the coil voltage:

$$i_C = C_C \frac{du_C}{dt} \quad (\text{B.10})$$

$$u_C = R_C i_1 + L_C \frac{di_1}{dt} \quad (\text{B.11})$$

$$u_C = R i_2 + L \frac{di_2}{dt} \quad (\text{B.12})$$

By introducing the equation of the currents (B.7), the system can be formulated as:

$$u_C = -\frac{1}{C_C} (i_1 + i_2) \quad (\text{B.13})$$

$$\dot{i}_1 = \frac{1}{L_C} u_C - \frac{R_C}{L_C} i_1 \quad (\text{B.14})$$

$$\dot{i}_2 = \frac{1}{L} u_C - \frac{R}{L} i_2 \quad (\text{B.15})$$

With the initial conditions for the three unknown  $(u_C(0), i_1(0), i_2(0)) = (U_{C0}, I_{10}, I_{20})$ .

### Operational amplifier used for the measurements

Figure B.7 shows the output swing of the LM358 used for the measurement of the induced high frequency oscillations.

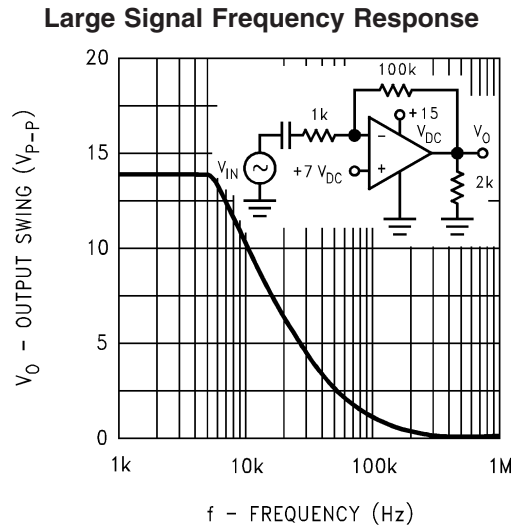


Figure B.7 – Output characteristic of the LM358 operational amplifier [205]

**Output linearity**

The variation of the induced oscillation damping representative of the position is measured in  $\Delta t$  and presented in Figure B.8. The maximum difference between the high and the low position of the coil obtained at the trigger of the external interrupt reaches  $2.8 \mu s$ . It represents 84 steps for a travel of 5 mm giving a theoretical resolution of  $60 \mu m$ .

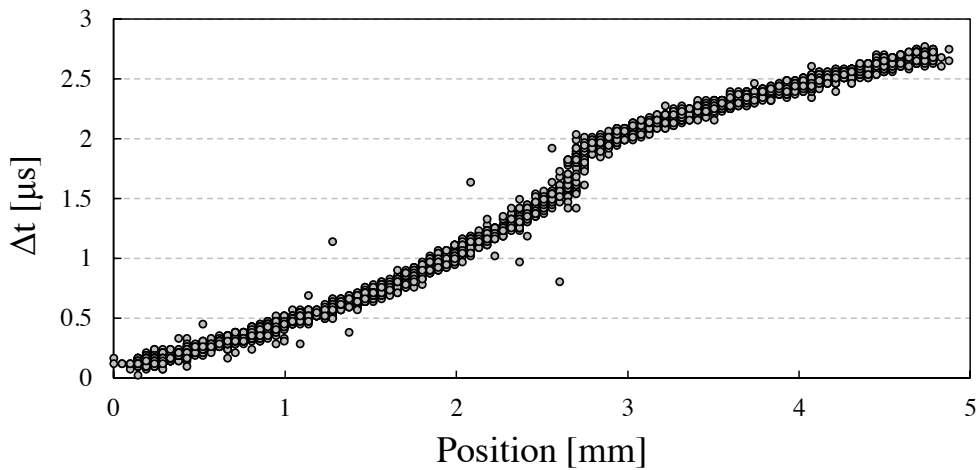


Figure B.8 – Measured time variation  $\Delta t$  versus position measured with an external laser sensor

The current extinction and the position measurement using high frequency oscillations are theoretically independent. However, the necessity of protecting the follower circuit using a limiting Zener diode disturbs the force characteristic (Figure B.9). Hopefully, the time needed to cut the first voltage peak is so short that the current decrease is limited (Figure B.10) and the force linearity is only slightly affected.

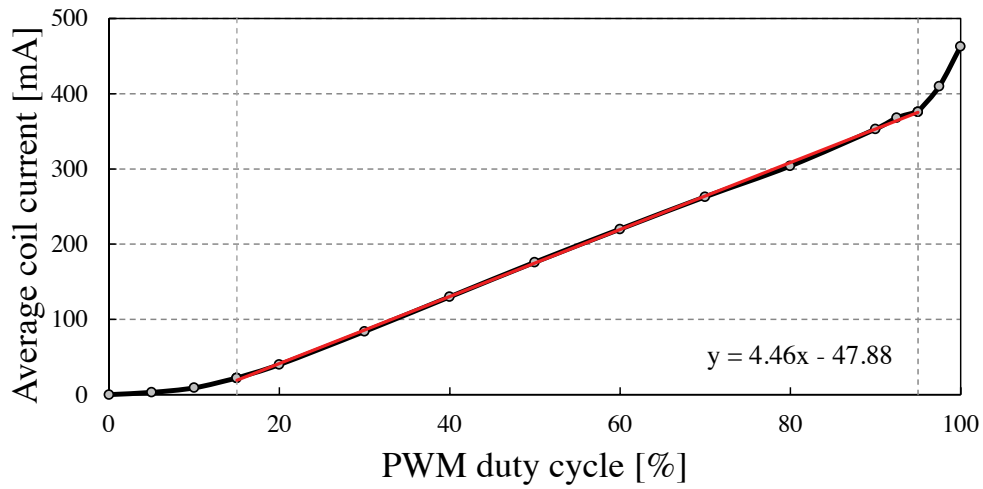


Figure B.9 – Current versus duty cycle characteristic measured on the complete self-sensing setup and its linear interpolation between 15 and 95 % (red)

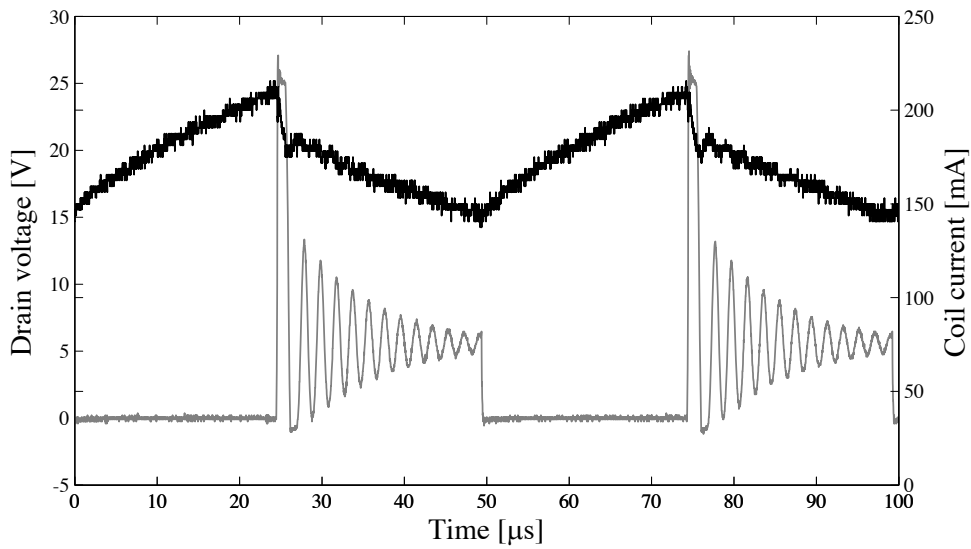


Figure B.10 – Current behavior (black) and drain voltage oscillations (grey) during normal PWM operations





**Contents**

---

<b>C.1 Haptic Pad and Haptic Keyboard . . . . .</b>	<b>205</b>
C.1.1 Actuator . . . . .	205
C.1.2 Prototypes . . . . .	207

---

**C.1 Haptic Pad and Haptic Keyboard**

**C.1.1 Actuator**

**Dynamics**

A brief comparison is run on the cylindrical actuator manufactured for the Haptic Keyboard to make sure the response of the electromagnetic version still satisfies dynamic specifications. The average down stroke duration of normal typing operations measured by Rempel & al. is 9.1 ms for a 3.5 mm travel [114]. The acceleration of the actuator should at least correspond to this value. A basic analysis based on Newton's second law of motion (C.1) allows for the calculation of the time needed to travel the distance. According to the specifications, a force  $F$  of 1 N is assumed to be produced by the actuator. It is the only force acting on it as gravity is

## Appendix C. Applications

---

supposed to be compensated.

$$F = m \cdot a \tag{C.1}$$

Knowing the moving mass  $m$ , acceleration  $a$  can be determined. Velocity  $v$  and position  $z$  can then be integrated as:

$$v(t) = a \cdot t + B \tag{C.2}$$

$$z(t) = a \cdot t^2 + B \cdot t + C \tag{C.3}$$

with the initial conditions  $z(0) = 0$  and  $v(0) = 0$ , time is given by:

$$t(z) = \sqrt{\frac{z}{a}} \tag{C.4}$$

The values obtained for both configurations are summarized in Table C.1.

Table C.1 – Dynamics of electrodynamic and electromagnetic configurations

Configuration	$m$ [g]	$a$ [ $m/s^2$ ]	$a$ [G]	$t(5 \text{ mm})$ [ms]	$t(3.5 \text{ mm})$ [ms]
Electrodynamic	4.8	208.3	21.2	4.9	4.1
Electromagnetic	16	62.5	6.4	8.9	7.5

The time needed to reach a given position is increased by more than 80% by switching configuration. However, the comparison with Rempel & al. average measurement on a 3.5 mm travel shows that the electromagnetic actuator is still 1.6 ms quicker (17.6%). Moreover, the role of a force feedback key being to counter human force, it would be sufficient for the actuator to follow the release of the finger. The average key release duration being 59.3 ms in accordance with [114], the margin is largely sufficient to adopt the electromagnetic configuration.

### C.1.2 Prototypes

#### Haptic Pad

The top view of the complete electronics of the Haptic Pad is shown in Figure C.1.

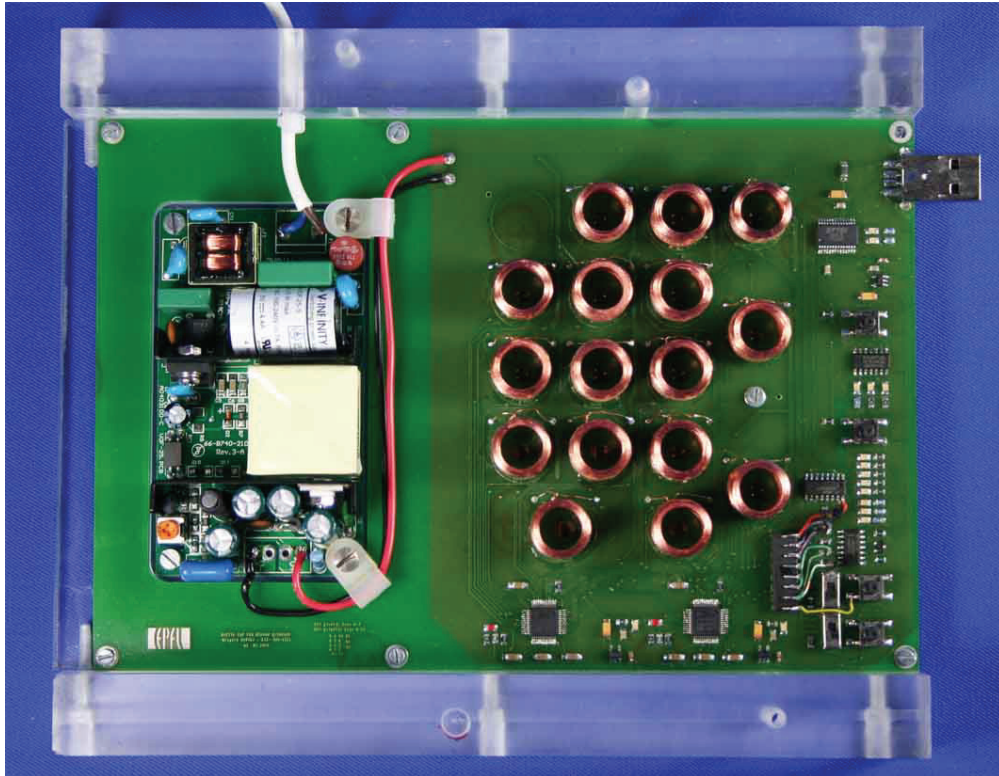


Figure C.1 – Top view of the Haptic Pad electronic board

#### Haptic Keyboard

The major part of the electronics is hidden on the back side of the board (Figure C.2). The communication block is concentrated on the top left-hand corner of the picture. The micro-controllers are dispatched at the bottom in accordance with the groups distribution (Figure C.3) and finally, facing the Hall sensors, transistors and low-pass filters for position measurement are grouped under each key (Figure C.4). The space left between the clusters of components will lean upon the bottom case.

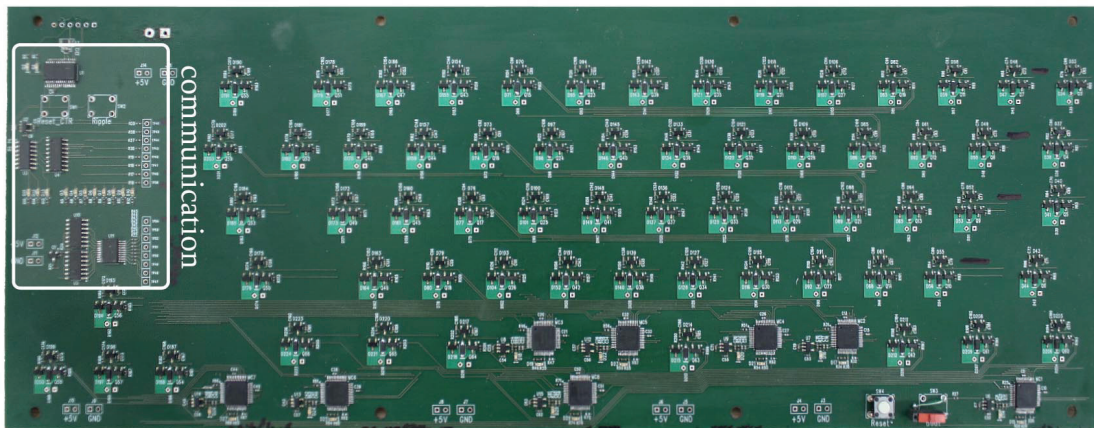


Figure C.2 – Back side of the Haptic Keyboard electronic board

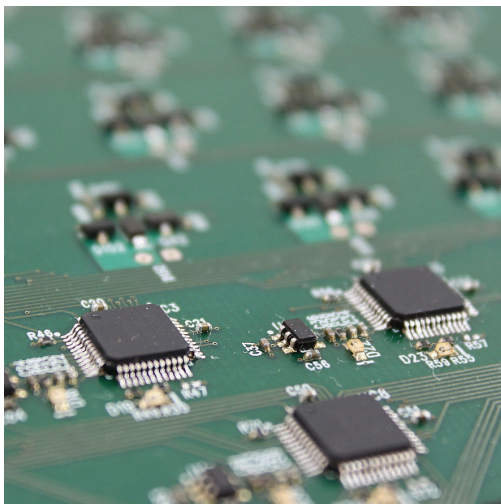


Figure C.3 – Detailed view of the micro-controllers

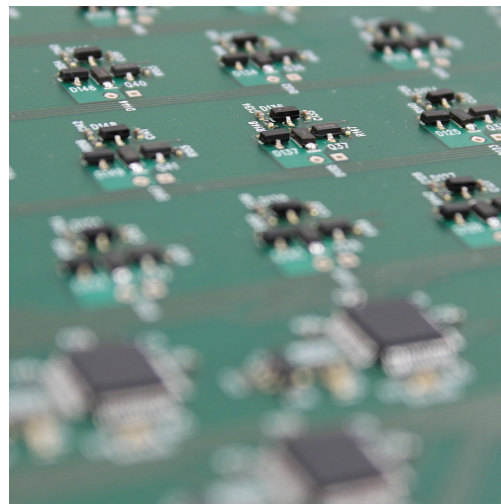


Figure C.4 – Driver circuits and position sensor filters



**Contents**

---

<b>D.1 Results</b> . . . . .	<b>209</b>
D.1.1 Effect on emotional processing . . . . .	209

---

**D.1 Results**

**D.1.1 Effect on emotional processing**

Similarly as for the tactile clue (Figure 7.20), the answers given for the four tactile clues during the visuo-tactile part give very good results for the "spring" and "constant" profiles, despite a slightly more important confusion between them (13-14 %) probably attributed to the additional processing brought by the visual information. Again, a more important confusion is observed between the "click" and "peaks" profiles. The accuracy with which the force profile is identified is directly related to the performance (Table 7.4).

**Appendix D. Impact study of haptic feedback on emotional processing**

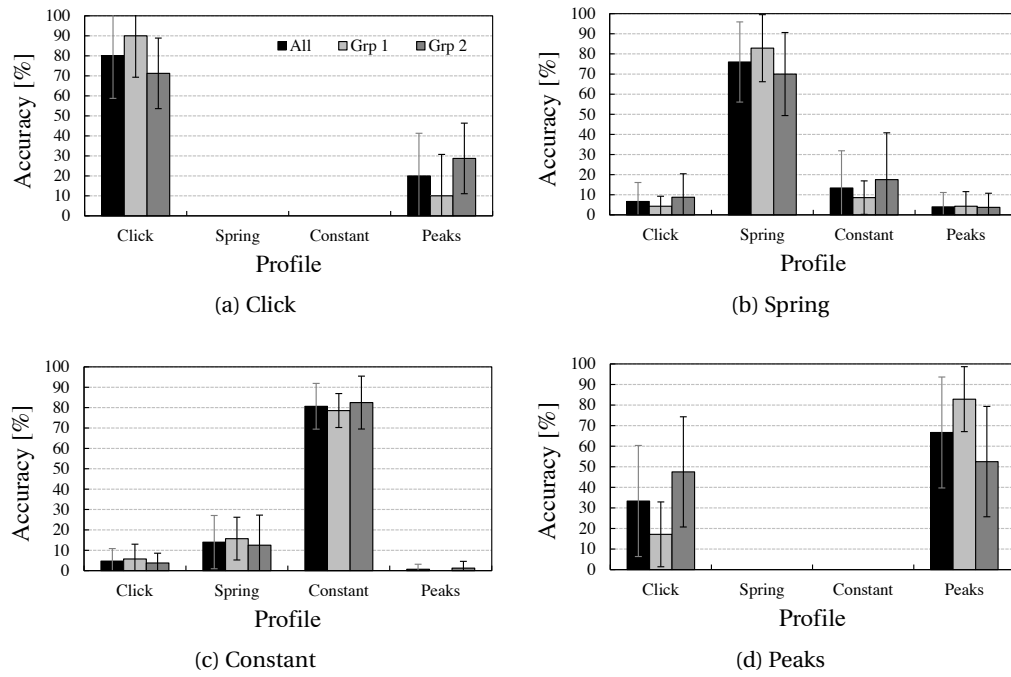


Figure D.1 – Detail of the answers given for the four different haptic clues during the visuo-tactile part

## Bibliography

- [1] CLVE, “Haptique,” tech. rep., Communication and Life in Virtual Environments (CLVE), 2000.
- [2] J. C. Craig and G. B. Rollman, “Somesthesia,” *Annual Review of Psychology*, vol. 50, pp. 305–331, 1999.
- [3] W. Penfield and T. Rasmussen, *The Cerebral Cortex of a Man: A Clinical Study of Localization of Function*. The Macmillan Company, New York, 1950.
- [4] Wikipedia, “Homonculus sensitif.,” 2011.
- [5] J. J. Gibson, “Observations on active touch,” *Psychological review*, vol. 69, pp. 477–491, 1962.
- [6] S. J. Lederman and R. L. Klatzky, “Haptic perception: A tutorial,” *Attention, Perception and Psychophysics*, vol. 71 (7), pp. 1439–1459, 2009.
- [7] M. Grunwald, *Human Haptic Perception. Basics and Applications*. Birkäuser Basel, 2008.
- [8] S. Najarian, J. Dargahi, and A. A. Mehrizi, *Artificial tactile sensing in biomedical engineering*. McGraw-Hill Professional, 2009.
- [9] M. Biet, “*Conception et contrôle d’actionneurs électro-actifs dédiés à la stimulation tactile*”. PhD thesis, Université des Sciences et Technologies de Lille, 2007.
- [10] B. G. Green, “Temperature perception and nociception,” *Journal of Neurobiology*, vol. 61, no. 1, pp. 13–29, 2004.
- [11] G. Westling and R. S. Johansson, “Responses in glabrous skin mechanoreceptors during precision grip in humans,” *Experimental Brain Research*, vol. 66, pp. 128–140, 1987.
- [12] A. B. Vallbo and R. S. Johansson, “Properties of cutaneous mechanoreceptors in the human hand related to touch sensation,” *Human Neurobiology*, vol. 3, pp. 3–14, 1984.
- [13] B. Vallbo and K.-E. Hagbarth, “Activity from skin mechanoreceptors recorded percutaneously in awake human subjects,” *Experimental Neurology*, vol. 21, no. 3, pp. 270 – 289, 1968.

## Bibliography

---

- [14] R. S. Johansson and A. B. Vallbo, "Tactile sensibility in the human hand: relative and absolute densities of four types of mechanoreceptive units in glabrous skin," *Journal of Physiology*, vol. 286, pp. 283–300, 1979.
- [15] R. Johansson and A. B. Vallbo, "Spatial properties of the population of mechanoreceptive units in the glabrous skin of the human hand," *Brain Research*, vol. 184, pp. 353–366, 1980.
- [16] R. Johansson, U. Landstroöm, and R. Lundstroöm, "Sensitivity to edges of mechanoreceptive afferent units innervating the glabrous skin of the human hand," *Brain Research*, vol. 244, no. 1, pp. 27 – 32, 1982.
- [17] R. S. Johansson, U. Landström, and R. Lundström, "Responses of mechanoreceptive afferent units in the glabrous skin of the human hand to sinusoidal skin displacements.," *Brain Research*, vol. 244, no. 1, pp. 17–25, 1982.
- [18] M. R. Chambers, K. H. Andres, M. von Dring, and A. Iggo, "The structure and function of the slowly adapting type II mechanoreceptor in hairy skin," *Experimental Physiology*, vol. 57, pp. 417–445, 1972.
- [19] R. S. Johansson and k. B. Vallbo, "Tactile sensory coding in the glabrous skin of the human hand," *Trends in Neurosciences*, vol. 6, no. January, pp. 27–32, 1983.
- [20] U. Lindblom, "Properties of touch receptors in distal glabrous skin of monkeys," *Journal of Neurophysiology*, vol. 28, pp. 966–985, 1965.
- [21] A. Iggo and A. R. Muir, "The structure and function of a slowly adapting touch corpuscle in hairy skin.," *The Journal of Physiology*, vol. 200, no. 3, pp. 763–796, 1969.
- [22] R. S. Johansson, "Tactile sensibility in the human hand: receptive field characteristics of mechanoreceptive units in the glabrous skin," *Journal of Physiology*, vol. 281, pp. 101–123, 1978.
- [23] S. Weinstein, *The skin senses*, ch. Intensive and extensive aspects of tactile sensitivity as a function of body part, sex, and laterality., pp. 195–222. Springfield IL: Thomas, 1968.
- [24] J. C. Stevens and W. Q. Patterson, "Dimensions of spatial acuity in the touch sense: Changes over the life span," *Somatosensory and Motor Research*, vol. 22, pp. 29–47, 1995.
- [25] M. M. Wickremaratchi and J. G. Llewelyn, "Effects of ageing on touch," *Prostgrad Medical Journal*, vol. 82, pp. 301–304, 2006.
- [26] C. E. Scherrick and R. W. Cholewiak, *Handbook of Perception and Human Performance*, ch. Cutaneous sensitivity. New York: John Wiley Series in Probability and Statistics, 1986.
- [27] S. J. Lederman, "Skin and touch," *Encyclopedia of Human Biology*, vol. 7, p. 55, 1991.



- [28] S. J. Bolanowski, G. A. Gescheider, R. T. Verrillo, and C. M. Checkosky, "Four channels mediate the mechanical aspects of touch," *Journal of Acoustical Society of America*, vol. 84, no. 5, pp. 1680–1694, 1988.
- [29] R. D. Frisina and G. A. Gescheider, "Comparison of child and adult vibrotactile thresholds as a function of frequency and duration," *Perception and Psychophysics*, vol. 22, pp. 100–103, 1977.
- [30] R. T. Verrillo, "Effects of contactor area on the vibrotactile threshold," *Journal of Acoustical Society of America*, vol. 35, pp. 1962–1966, 1963.
- [31] K. Shimoga, "Finger Force and Touch Feedback Issues in Dexterous Telemanipulation," in *Intelligent Robotic Systems for Space Exploration, Proceedings*, pp. 159–178, Oct 1992.
- [32] T. L. Brooks, "Telerobotic response requirements," in *Proceedings IEEE International Conference on Systems, Man and Cybernetics*, pp. 113–120, 1990.
- [33] R. S. Johansson and G. Westling, "Roles of glabrous skin receptors and sensorimotor memory in automatic control of precision grip when lifting rougher or more slippery objects," *Experimental Brain Research*, vol. 56, pp. 550–564, 1984.
- [34] H. Grant and C.-K. Lai, "Simulation modeling with artificial reality technology (smart): an integration of virtual reality and simulation modeling," in *Simulation Conference Proceedings, 1998. Winter*, vol. 1, pp. 437–441 vol.1, dec 1998.
- [35] R. Balaniuk and C. Laugier, "Haptic interfaces in generic virtual reality systems," in *Intelligent Robots and Systems, 2000. (IROS 2000). Proceedings. 2000 IEEE/RSJ International Conference on*, vol. 2, pp. 1310–1315 vol.2, 2000.
- [36] J. Rosen, B. Hannaford, M. MacFarlane, and M. Sinanan, "Force controlled and teleoperated endoscopic grasper for minimally invasive surgery-experimental performance evaluation," *Biomedical Engineering, IEEE Transactions on*, vol. 46, pp. 1212–1221, oct. 1999.
- [37] C. Basdogan, S. De, J. Kim, M. Muniyandi, H. Kim, and M. Srinivasan, "Haptics in minimally invasive surgical simulation and training," *Computer Graphics and Applications, IEEE*, vol. 24, pp. 56–64, march-april 2004.
- [38] V. Hayward, O. R. Astley, M. Cruz-Hernandez, D. Grant, and G. Robles-De-La-Torre, "Haptic Interfaces and Devices," *Sensor Review*, vol. 24, pp. 16–29, 2004.
- [39] R. Taylor and D. Stoianovici, "Medical robotics in computer-integrated surgery," *Robotics and Automation, IEEE Transactions on*, vol. 19, pp. 765–781, oct. 2003.
- [40] R. McColl, I. Brown, C. Seligman, F. Lim, and A. Alsaraira, "Haptic rendering perception studies for laparoscopic surgery simulation," in *Engineering in Medicine and Biology Society, 2006. EMBS '06. 28th Annual International Conference of the IEEE*, pp. 833–836, 30 2006-sept. 3 2006.

## Bibliography

---

- [41] N. Bajcinca, R. Cortesao, M. Hauschild, J. Bals, and G. Hirzinger, "Haptic control for steer-by-wire systems," in *Intelligent Robots and Systems, 2003. (IROS 2003). Proceedings. 2003 IEEE/RSJ International Conference on*, vol. 2, pp. 2004 – 2009 vol.2, 27-31 2003.
- [42] P. Yih and J. Gerdes, "Modification of vehicle handling characteristics via steer-by-wire," *Control Systems Technology, IEEE Transactions on*, vol. 13, pp. 965 – 976, nov. 2005.
- [43] S. Haggag, D. Alstrom, S. Cetinkunt, and A. Egelja, "Modeling, control, and validation of an electro-hydraulic steer-by-wire system for articulated vehicle applications," *Mechatronics, IEEE/ASME Transactions on*, vol. 10, pp. 688 – 692, dec. 2005.
- [44] G. Jenney, "Simple fly-by-wire actuator," in *Aerospace and Electronics Conference, 1991. NAECON 1991., Proceedings of the IEEE 1991 National*, pp. 522 –528 vol.2, may 1991.
- [45] J. Wang, J. Li, Y. Zhang, and S. Wang, "Design of an exoskeleton for index finger rehabilitation," in *Engineering in Medicine and Biology Society, 2009. EMBC 2009. Annual International Conference of the IEEE*, pp. 5957 –5960, sept. 2009.
- [46] S. Mohamaddan and T. Komeda, "Wire-driven mechanism for finger rehabilitation device," in *Mechatronics and Automation (ICMA), 2010 International Conference on*, pp. 1015 –1018, aug. 2010.
- [47] J. Veneman, R. Kruidhof, E. Hekman, R. Ekkelenkamp, E. Van Asseldonk, and H. van der Kooij, "Design and evaluation of the lopes exoskeleton robot for interactive gait rehabilitation," *Neural Systems and Rehabilitation Engineering, IEEE Transactions on*, vol. 15, pp. 379 –386, sept. 2007.
- [48] U. Mali and M. Munih, "Haptic interface for finger exercise and virtual rehabilitation," in *Biomedical Robotics and Biomechatronics, 2006. BioRob 2006. The First IEEE/RAS-EMBS International Conference on*, pp. 243 –248, feb. 2006.
- [49] D. Jack, R. Boian, A. Merians, M. Tremaine, G. Burdea, S. Adamovich, M. Recce, and H. Poizner, "Virtual reality-enhanced stroke rehabilitation," *Neural Systems and Rehabilitation Engineering, IEEE Transactions on*, vol. 9, pp. 308 –318, sept. 2001.
- [50] M. Bouri, Y. Stauffer, C. Schmitt, Y. Allemand, S. Gnemmi, R. Clavel, P. Metrailler, and R. Brodard, "The walktrainer: A robotic system for walking rehabilitation," in *Robotics and Biomimetics, 2006. ROBIO '06. IEEE International Conference on*, pp. 1616 –1621, dec. 2006.
- [51] P. Metrailler, V. Blanchard, I. Perrin, R. Brodard, R. Frischknecht, C. Schmitt, J. Fournier, M. Bouri, and R. Clavel, "Improvement of rehabilitation possibilities with the motion-maker tm," in *Biomedical Robotics and Biomechatronics, 2006. BioRob 2006. The First IEEE/RAS-EMBS International Conference on*, pp. 359 –364, feb. 2006.
- [52] J. Cole, *Pride and Daily Marathon*. MIT Press, 1995.

- [53] P. Lammertse, "Admittance control and impedance control - a dual," *FCS Control Systems*, 2004.
- [54] R. Haenni, "Joystick à Retour de Force," Master's thesis, Ecole Polytechnique Fédérale de Lausanne (EPFL-LAI), 2000.
- [55] H. Kudo, K. Suzumori, and T. Kanda, "Force feedback mouse with differential mechanism for omni-traveling," *Micro-NanoMechatronics and Human Science, 2007. MHS '07. International Symposium on*, pp. 430–435, Nov. 2007.
- [56] W. Li, B. Liu, P. Kosasih, and X. Zhang, "A 2-dof mr actuator joystick for virtual reality applications," *Sensors and Actuators A: Physical*, vol. 137, no. 2, pp. 308 – 320, 2007.
- [57] W. Park, S. Park, L. Kim, and S. Shin, "Haptic mouse interface actuated by an electromagnet," in *Complex, Intelligent and Software Intensive Systems (CISIS), 2011 International Conference on*, pp. 643 –646, 30 2011-july 2 2011.
- [58] B. Weinberg, J. Nikitzuk, A. Fisch, and C. Mavroidis, "Development of electro-rheological fluidic resistive actuators for haptic vehicular instrument controls," *Smart Materials and Structures*, vol. 14, pp. 1107–1119, 2005.
- [59] K. Hirota and M. Hirose, "Development of surface display," in *Virtual Reality Annual International Symposium, 1993., 1993 IEEE*, pp. 256 –262, sep 1993.
- [60] Q.-Z. Ang, B. Horan, Z. Najdovski, and S. Nahavandi, "Enabling multi-point haptic grasping in virtual environments," in *3D User Interfaces (3DUI), 2011 IEEE Symposium on*, pp. 55 –58, march 2011.
- [61] S. Choi, L. Walker, H. Z. Tan, S. Crittenden, and R. Reifengerger, "Force constancy and its effect on haptic perception of virtual surfaces," *ACM Transactions on Applied Perception*, vol. 2 (2), pp. 89–105, 2005.
- [62] S. Martin and N. Hillier, "Characterisation of the Novint Falcon haptic device for application as a robot manipulator," *Australasian Conference on Robotics and Automation (ACRA)*, Dec. 2009.
- [63] A. Panarese and B. B. Edin, "A modified low-cost haptic interface as a tool for complex tactile stimulation," *Medical Engineering & Physics*, vol. 33, no. 3, pp. 386 – 390, 2011.
- [64] S. Agili, D. Gaddipati, and T. Stewart, "Haptic system to simulate minimally invasive surgery," in *Industrial Electronics, 2006 IEEE International Symposium on*, vol. 1, pp. 453 –458, july 2006.
- [65] A. Talasaz, R. Patel, and M. Naish, "Haptics-enabled teleoperation for robot-assisted tumor localization," in *Robotics and Automation (ICRA), 2010 IEEE International Conference on*, pp. 5340 –5345, may 2010.

## Bibliography

---

- [66] C. Cadoz, L. Lisowski, and J.-L. Florens, "A Modular Feedback Keyboard," *Computer Music Journal*, vol. 14, pp. 47–50, 1990.
- [67] A. Luciani, C. Cadoz, and J. L. Florens, "The crm device: a force feedback gestural transducer to real-time computer animation," *Displays*, vol. 15, no. 3, pp. 149 – 155, 1994. Special Issue: Interactive Computer Animation.
- [68] E. Baudet, "Conception d'un Système à Retour de Force pour Instrument de Musique à Clavier," Master's thesis, Ecole Polytechnique Fédérale de Lausanne, Laboratoire d'Actionneurs Intégrés (EPFL-LAI), 2005.
- [69] R. Ansermot, "Conception et réalisation d'un système haptique pour instrument de musique à clavier transportable avec interface MIDI," Master's thesis, Laboratoire d'Actionneurs Intégrés, Ecole Polytechnique Fédérale de Lausanne (LAI - EPFL), 2008.
- [70] J. Lozada, X. Boutillon, and M. Hafez, "Modélisations mécanique de la touche de piano et de son imitation haptique," *18è Congrès Français de Mécanique*, 2007.
- [71] J. Martin, M. Latash, and V. Zatsiorsky, "Inverse piano technique for studying finger interaction during pressing tasks," in *EuroHaptics conference, 2009 and Symposium on Haptic Interfaces for Virtual Environment and Teleoperator Systems. World Haptics 2009. Third Joint*, pp. 395 –396, 18-20 2009.
- [72] S. Winter and M. Bouzit, "Use of magnetorheological fluid in a force feedback glove," *Neural Systems and Rehabilitation Engineering, IEEE Transactions on*, vol. 15, pp. 2 –8, march 2007.
- [73] J. Blake and H. Gurocak, "Haptic glove with mr brakes for virtual reality," *Mechatronics, IEEE/ASME Transactions on*, vol. 14, pp. 606 –615, oct. 2009.
- [74] H. Kawasaki, T. Furukawa, S. Ueki, and T. Mouri, "Virtual robot teaching in the assembly work environment for multi-fingered robots," in *Automation Congress, 2008. WAC 2008. World*, pp. 1 –7, 28 2008-oct. 2 2008.
- [75] T. Mouri, H. Kawasaki, and K. Umabayashi, "Developments of new anthropomorphic robot hand and its master slave system," in *Intelligent Robots and Systems, 2005. (IROS 2005). 2005 IEEE/RSJ International Conference on*, pp. 3225 – 3230, aug. 2005.
- [76] G. Savioz, V. Ruchet, and Y. Perriard, "Study of a miniature magnetorheological fluid actuator for haptic devices," in *Advanced Intelligent Mechatronics (AIM), 2010 IEEE/ASME International Conference on*, pp. 1197 –1202, july 2010.
- [77] M. Bouzit, G. Popescu, G. Burdea, and R. Boian, "The rutgers master ii-nd force feedback glove," in *Haptic Interfaces for Virtual Environment and Teleoperator Systems, 2002. HAPTICS 2002. Proceedings. 10th Symposium on*, pp. 145 –152, 2002.
- [78] S. J. Bensmaïa and M. Hollins, "Complex tactile waveform discrimination," *Journal of Acoustical Society of America*, vol. 108(3), pp. 1236–1245, Sept. 2000.

- [79] I. Poupyrev and S. Maruyama, "Tactile interfaces for small touch screens," in *In proceedings of ACM UIST 2003*, ACM, pp. 217–220, ACM Press, 2003.
- [80] T. Kaaresoja, L. M. Brown, and J. Linjama, "Snap-crackle-pop: Tactile feedback for mobile touch screens," in *in Proceedings of Eurohaptics 2006*, pp. 565–566, 2006.
- [81] R. Hughes and A. Forrest, "Perceptualisation using a tactile mouse," in *Visualization '96. Proceedings.*, pp. 181–188, 27 0-nov. 1 1996.
- [82] R. W. Lindeman, J. N. Templeman, J. L. Sibert, and J. R. Cutler, "Handling of virtual contact in immersive virtual environments: Beyond visuals," *Virtual Reality*, vol. 6(3), pp. 130–139, October, 2002.
- [83] L. Rincon-Gonzalez, J. P. Warren, D. M. Meller, and S. Helms Tillery, "Haptic interaction of touch and proprioception: Implications for neuroprosthetics," *Neural Systems and Rehabilitation Engineering, IEEE Transactions on*, vol. 19, pp. 490–500, oct. 2011.
- [84] K. Overvliet, J. Smeets, and E. Brenner, "The use of proprioception and tactile information in haptic search," *Acta Psychologica*, vol. 129, no. 1, pp. 83–90, 2008.
- [85] A. Frisoli, M. Solazzi, M. Reiner, and M. Bergamasco, "The contribution of cutaneous and kinesthetic sensory modalities in haptic perception of orientation," *Brain Research Bulletin*, vol. 85, no. 5, pp. 260–266, 2011.
- [86] M. Akamatzsu, S. Sato, and I. S. MacKenzie, "Multimodal Mouse: a Mouse-Type Device with Tactile and Force Display," *Presence*, vol. Vol. 3 No. 1, pp. 73–80, 1994.
- [87] D. A. Kontarinis and R. D. Howe, "Tactile display of vibratory information in teleoperation and virtual environments," *Presence*, vol. 4, pp. 387–402, 1996.
- [88] H. Z. Tan, N. I. Durlach, W. M. Rabinowitz, and C. M. Reed, "Information transmission with a multi-finger tactual display," *Perception & Psychophysics*, vol. 61(6), pp. 993–1008, 1996.
- [89] A. Israr, H. Z. Tan, and C. M. Reed, "Frequency and amplitude discrimination along the kinesthetic-cutaneous continuum in the presence of masking stimuli.," *Journal of the Acoustical Society of America*, vol. 120, no. 5 Pt 1, pp. 2789–2800, 2006.
- [90] A. Israr, P. H. Meckl, C. M. Reed, and H. Z. Tan, "Controller design and consonantal contrast coding using a multi-finger tactual display.," *Journal of the Acoustical Society of America*, vol. 125, no. 6, pp. 3925–3935, 2009.
- [91] M. Jian, S. Liu, and J. Dong, "3d surface texture synthesis based on wavelet transform," in *Computer Science and Computational Technology, 2008. ISCSCT '08. International Symposium on*, vol. 2, pp. 230–233, dec. 2008.

## Bibliography

---

- [92] G. Poling, J. Weisenberger, and T. Kerwin, "The role of multisensory feedback in haptic surface perception," in *Haptic Interfaces for Virtual Environment and Teleoperator Systems, 2003. HAPTICS 2003. Proceedings. 11th Symposium on*, pp. 187 – 194, march 2003.
- [93] E. Chubb, J. Colgate, and M. Peshkin, "Shiverpad: A glass haptic surface that produces shear force on a bare finger," *Haptics, IEEE Transactions on*, vol. 3, pp. 189 –198, july-sept. 2010.
- [94] Y. Ikei and M. Shiratori, "Textureexplorer: a tactile and force display for virtual textures," in *Haptic Interfaces for Virtual Environment and Teleoperator Systems, 2002. HAPTICS 2002. Proceedings. 10th Symposium on*, pp. 327 –334, 2002.
- [95] M. Benali-Khoudjal, M. Hafez, J.-M. Alexandre, J. Benachour, and A. Kheddar, "Thermal feedback model for virtual reality," in *Micromechatronics and Human Science, 2003. MHS 2003. Proceedings of 2003 International Symposium on*, pp. 153 – 158, oct. 2003.
- [96] R. T. Verrillo, S. J. Bolanowski, C. M. Checkosky, and F. McGlone, "Effects of hydration on tactile sensation," *Somatosensory & Motor Research*, vol. 15, pp. 93–108, 1998.
- [97] W. B. Tiest and A. Kappers, "Tactile perception of thermal diffusivity," *Attention, Perception and Psychophysics*, vol. 71, pp. 481–489, 2009.
- [98] C. R. Lacy and A. G. Kroll, "Cumulative Trauma Disorders in Office Workers," tech. rep., Public Employees Occupational Safety and Health Program, New Jersey, USA, Feb. 2003.
- [99] National Institute of Neurological Disorders and Stroke, "Repetitive motion disorders information page," tech. rep., US National Institutes of Health, Bethesda, MD 20892, October 2011.
- [100] D. Fergusson and J. Duncan, "Keyboard Design and Operating Posture," *Ergonomics*, vol. 17, pp. 731–744, 1974.
- [101] W. R. Hargreaves, "Comfort by Design: Selecting an Ergonomic Keyboard," *The Ergonomics Report*, 2008.
- [102] National Institute of Neurological Disorders and Stroke, "Carpal tunnel syndrome fact sheet," tech. rep., National Institutes of Health, Bethesda, MD 20892, September 2011.
- [103] "Self-reported work-related illness (SWI) and workplace injuries: Results from the Labour Force Survey (LFS)," tech. rep., UK Health and Safety Executive, October 2011.
- [104] "Repetitive strain injury (RSI) still blights british workers," tech. rep., The Chartered Society of Physiotherapy, 2009.
- [105] "Repetitive Motion Injuries and Days Away from Work in 2008," tech. rep., US Bureau of Labor Statistics, 2008.

- [106] S. S. Snibbe, K. E. MacLean, R. Shaw, J. Roderick, W. L. Verplank, and M. Scheeff, "Haptic techniques for media control," in *Proceedings of the 14th annual ACM symposium on User interface software and technology*, UIST '01, (New York, NY, USA), pp. 199–208, ACM, 2001.
- [107] M. Badescu, C. Wampler, and C. Mavroidis, "Rotary haptic knob for vehicular instrument controls," in *Haptic Interfaces for Virtual Environment and Teleoperator Systems, 2002. HAPTICS 2002. Proceedings. 10th Symposium on*, pp. 342–343, 2002.
- [108] C. Hasser and M. Cutkosky, "System identification of the human hand grasping a haptic knob," in *Haptic Interfaces for Virtual Environment and Teleoperator Systems, 2002. HAPTICS 2002. Proceedings. 10th Symposium on*, pp. 171–180, 2002.
- [109] J. M. Hollerbach, I. W. Hunter, and J. Ballantyne, "A comparative analysis of actuator technologies for robotics,," *The Robotics, Review 2*, pp. 299–342, 1992.
- [110] J. Madden, N. Vandesteeg, P. Anquetil, P. Madden, A. Takshi, R. Pytel, S. Lafontaine, P. Wieringa, and I. Hunter, "Artificial muscle technology: physical principles and naval prospects," *Oceanic Engineering, IEEE Journal of*, vol. 29, pp. 706–728, july 2004.
- [111] J. McBean and C. Breazeal, "Voice coil actuators for human-robot interaction," in *Intelligent Robots and Systems, 2004. (IROS 2004). Proceedings. 2004 IEEE/RSJ International Conference on*, vol. 1, pp. 852–858 vol.1, sept.-2 oct. 2004.
- [112] W. Kaal and S. Herold, "Electroactive polymer actuators in dynamic applications," *Mechatronics, IEEE/ASME Transactions on*, vol. 16, pp. 24–32, feb. 2011.
- [113] M. Leary, F. Schiavone, and A. Subic, "Lagging for control of shape memory alloy actuator response time," *Materials & Design*, vol. 31, no. 4, pp. 2124–2128, 2010. <ce:title>Design of Nanomaterials and Nanostructures</ce:title>.
- [114] D. Rempel, J. Dennerlein, C. D. Mote, Jr, and T. J. Armstrong, "A method of measuring fingertip loading during keyboard use," 1994.
- [115] M. De Volder, K. Yoshida, S. Yolota, and D. Reynaerts, "Electrorheologic liquid crystals in microsystems: Model and measurements," in *Nano/Micro Engineered and Molecular Systems, 2006. NEMS '06. 1st IEEE International Conference on*, pp. 236–241, jan. 2006.
- [116] M. Jufer, *Traité d'Electricité: Electromécanique*, vol. IX. Presses polytechniques et universitaires romandes, 3rd ed., 2004.
- [117] D. H. Chai, "Permeance model and reluctance force between toothed structure," *2nd Symposium on Incremental Motion Control System and Devices, University of Illinois*, pp. K1–K12, 1973.
- [118] L. W. Matsch, *Electromagnetic & electromechanical machines*. second edition ed., 1977.

## Bibliography

---

- [119] J. Maridor, M. Markovic, Y. Perriard, and D. Ladas, "Optimization design of a linear actuator using a genetic algorithm," pp. 1776–1781, may. 2009.
- [120] R. Fisher, *The design of experiment*. London: Collier Macmillian publishers, 9th edition ed., 1971.
- [121] C. Feneuille, D. Mathieu, and R. Phan-Thau-Luu, "Méthodologie de la recherche expérimentale. Tome I: outil mathématiques; Tome II: surface de réponse.," *Laboratoire de prospective réactionnelle et d'analyse de l'information*, 1983.
- [122] M. Nouby, D. Mathivanan, and K. Srinivasan, "A combined approach of complex eigenvalue analysis and design of experiments (DOE) to study disc brake squeal," *International Journal of Engineering, Science and Technology*, vol. 1, pp. 254–271, 2009.
- [123] Y. Gianchandani and S. Crary, "Parametric modeling of a microaccelerometer: comparing i- and d-optimal design of experiments for finite-element analysis," *Microelectromechanical Systems, Journal of*, vol. 7, pp. 274–282, jun 1998.
- [124] C. Schäfer and E. Finke, "Shape optimisation by design of experiments and finite element methodsan application of steel wheels," *Structural and Multidisciplinary Optimization*, vol. 36, pp. 477–491, 2008. 10.1007/s00158-007-0183-6.
- [125] J. Fernandez and Y. Perriard, "Sensitivity analysis and optimization of a standing wave ultrasonic linear motor," *Ultrasonics, Ferroelectrics and Frequency Control, IEEE Transactions on*, vol. 53, pp. 1352–1361, july 2006.
- [126] M. Flueckiger, J. M. Fernandez, and Y. Perriard, "Finite element method based design and optimisation methodology for piezoelectric ultrasonic motors," *Mathematics and Computers in Simulation*, vol. 81, no. 2, pp. 446–459, 2010. <ce:title>Modelling and Simulation of Electrical Machines, Converters and Power Systems</ce:title>.
- [127] S. Park and S. Min, "Design of magnetic actuator with nonlinear ferromagnetic materials using level-set based topology optimization," *Magnetics, IEEE Transactions on*, vol. 46, pp. 618–621, feb. 2010.
- [128] P. Dereumaux, "Classe d'isolation et échauffement des machines," tech. rep., Société industrielle de travaux électriques (SITELEC), 2001.
- [129] M.-D. Calin and E. Helerea, "Temperature influence on magnetic characteristics of ndfeb permanent magnets," in *Advanced Topics in Electrical Engineering (ATEE), 2011 7th International Symposium on*, pp. 1–6, may 2011.
- [130] M. Markovic, L. Saunders, and Y. Perriard, "Determination of the thermal convection coefficient for a small electric motor," in *Industry Applications Conference, 2006. 41st IAS Annual Meeting. Conference Record of the 2006 IEEE*, vol. 1, pp. 58–61, oct. 2006.



- [131] D. Staton and E. So, "Determination of optimal thermal parameters for brushless permanent magnet motor design," in *Industry Applications Conference, 1998. Thirty-Third IAS Annual Meeting. The 1998 IEEE*, vol. 1, pp. 41–49 vol.1, oct. 1998.
- [132] C.-M. Karat, C. Halverson, D. Horn, and J. Karat, "Patterns of entry and correction in large vocabulary continuous speech recognition systems," in *Proceedings of the SIGCHI conference on Human factors in computing systems: the CHI is the limit*, CHI '99, (New York, NY, USA), pp. 568–575, ACM, 1999.
- [133] T. R. Ostrach, "Typing speed: How fast is average," tech. rep., Five Star Staffing, Inc., Orlando, FL, 1997.
- [134] A. S. Arif and W. Stuerzlinger, "Analysis of text entry performance metrics," in *In Proc. IEEE TIC-STH 2009. IEEE*, pp. 100–105, 2009.
- [135] F. Bonvin, *Analyse et mise en oeuvre de méthodes de commande sans capteur pour moteurs synchrones à aimants permanents*. PhD thesis, Ecole Polytechnique Fédérale de Lausanne (EPFL), Lausanne, 2001.
- [136] J. Persson, *Innovative standstill position detection combined with sensorless control of synchronous motors*. PhD thesis, Ecole Polytechnique Fédérale de Lausanne (EPFL), Lausanne, 2005.
- [137] Y. Perriard, O. Scaglione, C. Koechli, and J. Persson, "Self-sensing methods to drive micro-machines," in *Physics of Semiconductor Devices, 2007. IWPSD 2007. International Workshop on*, pp. 639–644, dec. 2007.
- [138] A. Consoli, A. Bottiglieri, R. Letor, R. Ruggeri, A. Testa, and S. De Caro, "Sensorless position control of dc actuators for automotive applications," in *Industry Applications Conference, 2004. 39th IAS Annual Meeting. Conference Record of the 2004 IEEE*, vol. 2, pp. 1217–1224 vol.2, oct. 2004.
- [139] M. Rahman, N. Cheung, and K. W. Lim, "Position estimation in solenoid actuators," *Industry Applications, IEEE Transactions on*, vol. 32, pp. 552–559, may/jun 1996.
- [140] D. Pawelczak and H.-R. Trankler, "Sensorless position control of electromagnetic linear actuator," in *Instrumentation and Measurement Technology Conference, 2004. IMTC 04. Proceedings of the 21st IEEE*, vol. 1, pp. 372–376 Vol.1, may 2004.
- [141] C. Günselmann and J. Melbert, "Soft-landing control for sensorless electromagnetical spring-mass actuators," in *Power Electronics, Machines and Drives, 2004. (PEMD 2004). Second International Conference on (Conf. Publ. No. 498)*, vol. 2, pp. 715–718 Vol.2, march-2 april 2004.
- [142] A. Espinosa, J.-R. Ruiz, J. Cusido, and X. Morera, "Sensorless control and fault diagnosis of electromechanical contactors," *Industrial Electronics, IEEE Transactions on*, vol. 55, pp. 3742–3750, oct. 2008.

## Bibliography

---

- [143] B. Hanson, M. Brown, and J. Fisher, "Self sensing: closed-loop estimation for a linear electromagnetic actuator," in *American Control Conference, 2001. Proceedings of the 2001*, vol. 2, pp. 1650–1655 vol.2, 2001.
- [144] J. Maridor, N. Katic, Y. Perriard, and D. Ladas, "Sensorless position detection of a linear actuator using the resonance frequency," in *Electrical Machines and Systems, 2009. ICEMS 2009. International Conference on*, pp. 1–6, nov. 2009.
- [145] J. T. Dennerlein, C. D. Mote Jr., and D. M. Rempel, "Control strategies for finger movement during touch-typing the role of the extrinsic muscles during a keystroke," *Experimental Brain Research*, vol. 121, pp. 1–6, 1998.
- [146] G. Savioz and Y. Perriard, "Towards self-sensed drives in linear haptic systems," in *Electrical Machines and Systems, 2009. ICEMS 2009. International Conference on*, pp. 1–5, nov. 2009.
- [147] A. Z. Hajian and R. D. Howe, "Identification of the mechanical impedance at the human finger tip," *Journal of Biomechanical Engineering*, vol. 119, no. 1, pp. 109–114, 1997.
- [148] D. L. Jindrich, Y. Zhou, T. Becker, and J. T. Dennerlein, "Non-linear viscoelastic models predict fingertip pulp force-displacement characteristics during voluntary tapping," *Journal of biomechanics*, vol. 36, no. 4, pp. 497–503, 1 April 2003.
- [149] P. A. Passeraub, *An integrated inductive proximity sensor*. PhD thesis, Ecole Polytechnique Fédérale de Lausanne (EPFL), Lausanne, 1999.
- [150] P. Reghem, E. Destobbeleer, T. Derrey, and L. Protin, "Precision of an eddy current sensor with magnetic circuit losses," in *Industrial Electronics, Control and Instrumentation, 1994. IECON '94., 20th International Conference on*, vol. 2, pp. 915–919 vol.2, sep 1994.
- [151] Allegro MicroSystems Inc., *Continuous-Time Ratiometric Linear Hall Effect Sensors. A1301 and A1302*, May 2006.
- [152] Texas Instruments, *Piccolo Microcontrollers. TMS320F2802x, TMS320F2802xx MCUs*, November 2008.
- [153] Future Technology Devices International Ltd., *FT232R USB UART IC*, 2010.
- [154] J. Wood, "Illustration: Haptic devices "touch you back"." *Fortune*, 2009.
- [155] L. K. Baxter, *Capacitive sensors. Design and Applications*. IEEE Press Series on Electronics Technology, 1997.
- [156] W. Heerens, "Application of capacitance techniques in sensor design," *J. Phys. E: Sci. Instrum*, vol. 19, pp. 897–906, 1986.
- [157] R. Puers, "Capacitive sensors: when and how to use them," *Sensors and Actuators*, vol. A37-A38, pp. 93–105, 1993.

- [158] W. Ko and Q. Wang, "Touch mode capacitive pressure sensors for industrial applications," in *Micro Electro Mechanical Systems, 1997. MEMS '97, Proceedings, IEEE., Tenth Annual International Workshop on*, pp. 284–289, jan 1997.
- [159] C. Quintans, J. Marcos, and S. Perez, "Developing of low cost capacitive sensors for laboratory classes," in *Education Engineering (EDUCON), 2010 IEEE*, pp. 445–450, april 2010.
- [160] T. Chen, L. Chen, M. Pan, and L. Sun, "Application of a novel capacitive sensor in precise positioning systems," in *Industrial Electronics and Applications (ICIEA), 2011 6th IEEE Conference on*, pp. 1712–1715, june 2011.
- [161] A. Hassanzadeh, R. Lindquist, and A. Borghei, "Relative humidity measurement using capacitive sensors," in *Southeastcon, 2008. IEEE*, pp. 396–398, april 2008.
- [162] M. Lee, "The art of capacitive touch sensing," *Embedded.com*, 2007.
- [163] W. Banks, *Touch sensitive switch*. Byte Craft Limited, 2002.
- [164] K. Fujita and H. Ohmori, "A new softness display interface by dynamic fingertip contact area control," in *5th World Multiconference on Systemics, Cybernetics and Infomatics*, pp. 78–82, 2001.
- [165] N. Park, W. Zhu, Y. Jung, M. Mclaughlin, and S.-a. Jin, "Utility of haptic data in recognition of user state related work pressure and frustration (emotional arousal) method experimental design," *Analysis*, vol. 11, 2003.
- [166] K. Höök, "Affective loop experiences — what are they?," in *Proceedings of the 3rd international conference on Persuasive Technology, PERSUASIVE '08*, (Berlin, Heidelberg), pp. 1–12, Springer-Verlag, 2008.
- [167] M. Alonso, D. Keyson, and C. Hummels, "Roll and rock: Exploring the affective loop in a pen," in *Affective Computing and Intelligent Interaction and Workshops, 2009. ACII 2009. 3rd International Conference on*, pp. 1–2, sept. 2009.
- [168] D. Heylen, M. Vissers, R. O. D. Akker, and A. Nijholt, "Affective feedback in a tutoring system for procedural tasks," 2004.
- [169] Z. Ciota, "Audio-haptic feedback in speech processing," in *Haptic, Audio and Visual Environments and Games, 2007. HAVE 2007. IEEE International Workshop on*, pp. 67–70, oct. 2007.
- [170] R. W. Picard, *Affective computing*. Cambridge, Massachusetts: The MIT Press, 1997.
- [171] M. Hershenson, "Reaction time as a measure of intersensory facilitation," *Journal of Experimental Psychology*, vol. 63, no. 3, p. 289293, 1962.

## Bibliography

---

- [172] J. Miller, "Divided attention: Evidence for coactivation with redundant signals," *Cognitive Psychology*, vol. 14, no. 2, pp. 247 – 279, 1982.
- [173] M. Kinsbourne, "The multimodal mind: How the senses combine in the brain," *The multimodality of human communication: Theories, problems and applications*. New School University, New York., 2002.
- [174] S. J. Lederman, R. L. Klatzky, A. Abramowicz, K. Salsman, R. Kitada, and C. Hamilton, "Haptic recognition of static and dynamic expressions of emotion in the live face.," *Psychological Science*, vol. 18, no. 2, pp. 158–164, 2007.
- [175] S. Lederman, R. Klatzky, E. Rennert-May, J. Lee, K. Ng, and C. Hamilton, "Haptic processing of facial expressions of emotion in 2d raised-line drawings," *Haptics, IEEE Transactions on*, vol. 1, pp. 27 –38, jan.-june 2008.
- [176] D. Bonnet, M. Ammi, and J. Martin, "Improvement of the recognition of facial expressions with haptic feedback," in *Haptic Audio Visual Environments and Games (HAVE), 2011 IEEE International Workshop on*, pp. 81 –87, oct. 2011.
- [177] M. Chen, S. Okada, and K. Nitta, "Effectiveness of haptic interaction in online negotiation between chinese and japanese," in *Granular Computing (GrC), 2011 IEEE International Conference on*, pp. 111 –114, nov. 2011.
- [178] S. A. Brewster, P. C. Wright, and A. D. N. Edwards, "Experimentally derived guidelines for the creation of earcons," 1995.
- [179] A. Rovers and H. van Essen, "Him: a framework for haptic instant messaging," in *CHI '04 extended abstracts on Human factors in computing systems*, CHI EA '04, (New York, NY, USA), pp. 1313–1316, ACM, 2004.
- [180] L. Rovers and H. V. Essen, "Design and evaluation of hapticons for enriched instant messaging," in *Virtual Reality*, pp. 177–191, 2004.
- [181] A. Neviarouskaya, D. Tsetserukou, H. Prendinger, N. Kawakami, S. Tachi, and M. Ishizuka, "Emerging system for affectively charged interpersonal communication," in *ICCAS-SICE, 2009*, pp. 3376 –3381, aug. 2009.
- [182] M. Benali-Khoudja, M. Hafez, A. Sautour, and S. Jumpertz, "Towards a new tactile language to communicate emotions," in *Mechatronics and Automation, 2005 IEEE International Conference*, vol. 1, pp. 286 – 291 Vol. 1, july-1 aug. 2005.
- [183] M. Benali-Khoudja, M. Hafez, J.-M. Alexandre, A. Kheddar, and V. Moreau, "Vital: a new low-cost vibro-tactile display system," in *Robotics and Automation, 2004. Proceedings. ICRA '04. 2004 IEEE International Conference on*, vol. 1, pp. 721 – 726 Vol.1, april-1 may 2004.

- [184] K. Salminen, V. Surakka, J. Lylykangas, J. Raisamo, R. Saarinen, R. Raisamo, J. Rantala, and G. Evreinov, "Emotional and behavioral responses to haptic stimulation," in *Proceedings of the twenty-sixth annual SIGCHI conference on Human factors in computing systems*, CHI '08, (New York, NY, USA), pp. 1555–1562, ACM, 2008.
- [185] A. Abdel-Baki, "La psychose et son traitement," *Association Québécoise des Programmes pour Premiers Episodes Psychotiques*, <http://www.aqppep.com/fichiers/Lapsychoseetsontraitement.pdf>, 2012.
- [186] F. Trémeau, "A review of emotion deficits in schizophrenia," *Dialogues Clin. Neurosci.*, vol. 8, pp. 59–70, 2006.
- [187] M. Brüne, "Emotion recognition, 'theory of mind', and social behavior in schizophrenia," *Psychiatry Research*, vol. 133, no. 2, pp. 135 – 147, 2005.
- [188] K. T. Mueser, R. Doonan, D. L. Penn, J. J. Blanchard, A. S. Bellack, P. Nishith, and J. DeLeon, "Emotion recognition and social competence in chronic schizophrenia," *Journal of Abnormal Psychology*, vol. 105, no. 3, pp. 271–275, 1980.
- [189] D. L. Penn, W. Spaulding, D. Reed, and M. Sullivan, "The relationship of social cognition to ward behavior in chronic schizophrenia," *Schizophrenia Research*, vol. 20, no. 3, pp. 327 – 335, 1996.
- [190] Laerd Statistics, "Repeated measures anova," <https://statistics.laerd.com/statistical-guides/repeated-measures-anova-statistical-guide.php>, 2012.
- [191] R. F. Baumeister, "The self," *Handbook of Social Psychology*, vol. 4th ed., pp. 680–740, 1998.
- [192] R. Baumeister, K. D. Vohs, and D. Tice, "The strength model of self-control," *Current Directions in Psychological Science*, vol. 16, pp. 351–355, 2007.
- [193] M. Muraven and R. F. Baumeister, "Self-regulation and depletion of limited resources: Does self-control resemble a muscle?," *Psychological Bulletin*, vol. 126, pp. 247–259, 2000.
- [194] M. Muraven, D. M. Tice, and R. F. Baumeister, "Self-control as limited resource: regulatory depletion patterns," *Journal of Personality and Social Psychology*, vol. 74, no. 3, pp. 774–789, 1998.
- [195] B. J. Schmeichel, K. D. Vohs, R. F. Baumeister, and D. Vohs, "Intellectual performance and ego depletion: Role of the self in logical reasoning and other information processing," *Journal of Personality and Social Psychology*, pp. 33–46, 2003.
- [196] S. Urben, *L'inhibition d'une réponse dominante chez l'enfant: Développement et interaction avec les processus émotionnels*. PhD thesis, Université de Genève, Faculté de Psychologie et des Sciences de l'Éducation, 2011.

## Bibliography

---

- [197] G. Savioz and Y. Perriard, "Self-sensing of linear short-stroke actuators for multi-finger haptic interfaces using induced high frequency oscillations," *Advanced Intelligent Mechatronics (AIM), 2010 IEEE/ASME International Conference on*, 2012.
- [198] G. Savioz and Y. Perriard, "A miniature short stroke linear actuator and its position control for a haptic key," in *Energy Conversion Congress and Exposition, 2009. ECCE 2009. IEEE*, pp. 2441 –2446, sept. 2009.
- [199] G. Savioz and Y. Perriard, "Miniature short-stroke linear actuator," *Industry Applications Magazine, IEEE*, vol. 17, pp. 14 –19, nov.-dec. 2011.
- [200] G. Savioz, M. Markovic, and Y. Perriard, "Towards multi-finger haptic devices: A computer keyboard with adjustable force feedback," in *Electrical Machines and Systems (ICEMS), 2011 International Conference on*, pp. 1 –6, aug. 2011.
- [201] G. E. P. Box, J. S. Hunter, and W. G. Hunter, *Statistics for Experimenters: Design, Innovation, and Discovery, Second Edition* . Wiley Series in Probability and Statistics, 2005.
- [202] W. F. Smith, *Experimental Design for Formulation*. ASA-SIAM series on Statistics and applied Probability, 2005.
- [203] A. Saltelli, *Sensitivity analysis*. 2000.
- [204] M. Stöck, "PC-keyboard with force feedback: Sensorless position detection by current measurements," tech. rep., Laboratory of Integrated Actuators, Ecole Polytechnique Fédérale de Lausanne (LAI - EPFL), 2010.
- [205] Texas Instruments, *LM158/LM258/LM358/LM2904 Low power Dual Operational Amplifiers. Datasheet SNOSBT3G*, October 2005.

# Curriculum Vitae

Grégory SAVIOZ  
Born April 24, 1984  
Swiss Citizen  
gregory.savioz@a3.epfl.ch

## Studies and professional experience

- 2008 - 2012 Teaching assistant and Ph.D. student at the Integrated Actuators Laboratory (LAI), École Polytechnique Fédérale de Lausanne (EPFL), Switzerland.
- 2007 - 2008 Master project + R&D engineer at Overview Ltd., London, UK.
- 2003 - 2008 Master of Science in Microengineering, École Polytechnique Fédérale de Lausanne (EPFL), Switzerland.
- 1997 - 2003 High School Diploma in Economics, Bilingual (French/German), Sion, Switzerland.

## Publications

- G. Savioz and Y. Perriard. A miniature short stroke linear actuator and its position control for a haptic key. *Proceedings of the 2009 IEEE Energy Conversion Congress and Exposition (ECCE), San Jose, USA, Sept. 20-24, 2009.*
- G. Savioz and Y. Perriard. Towards self-sensed drives in linear haptic systems. *Proceedings of the 2009 IEEE International Conference on Electrical Machines and Systems (ICEMS), Tokyo, Japan, Nov. 15-18, 2009.*
- G. Savioz, V. Ruchet and Y. Perriard. Study of a miniature magnetorheological fluid actuator for haptic devices. *Proceedings of the 2010 IEEE/ASME International Conference on Advanced Intelligent Mechatronics (AIM), Montréal, Canada, July 6-9, 2010.*
- G. Savioz and Y. Perriard. Miniature Short-Stroke Linear Actuator. *IEEE Industry Applications Magazine, Issue 6, 2011.*
- G. Savioz, M. Markovic and Y. Perriard. Towards multi-finger haptic devices: A computer keyboard with adjustable force feedback. *Proceedings of the 2011 IEEE International Conference on Electrical Machines and Systems (ICEMS), Beijing, China, Aug. 20-23, 2011.*
- G. Savioz and Y. Perriard. Self-sensing of linear short-stroke actuators for multi-finger haptic interfaces using induced high frequency oscillations. *Proceedings of the 2012 IEEE/ASME International Conference on Advanced Intelligent Mechatronics (AIM), Taiwan, July 10-14, 2012.*